UNIVERSITY OF LEEDS

Development of Artificially Intelligent Reactors for Precision Polymer Synthesis

Clarissa Y. P. Wilding

Submitted in accordance with the requirements for the degree of
Doctor of Philosophy

The University of Leeds

Faculty of Engineering and Physical Sciences

School of Chemical and Process Engineering

January 2023

Abstract

The digitisation of chemistry has been a rapidly evolving field of research both in academia and industry in the last 20 years. Miniaturisation of equipment and increased computational power have aided in the evolution of the way chemists conduct and optimise their reactions. Pharmaceutical drugs and small-molecule industries have taken precedence when it comes to artificially intelligent reactor platforms. Flow chemistry has enabled the development of user-independent and modular platforms with interchangeable components. In polymer science, there has been a delay due to challenges associated with the accuracy of liquid handlers, the increasing viscosity, and the use of specialised characterisation equipment. In precision polymer synthesis, low molar mass dispersity and high conversions are targeted; however, this is not trivial in reversible deactivation radical polymerisation (RDRP); a trade-off in these objectives complicates optimisation. Prior to the work in this thesis, multi-objective optimisation algorithms had been used in a droplet flow reactor and a batch reactor; however, a completely operator-independent platform had not been reported. A mechanistic understanding of polymerisation techniques can assist polymer chemists in predicting the reaction space of interest. Current models require the use of software or programming abilities which are not always accessible. Efforts towards explicit quantitative equations for conversion exist for most RDRPs, including reversible addition-fragmentation chain transfer (RAFT). Full predictive equations for dispersity, that also account for termination, exist for atom transfer radical polymerisation (ATRP), nitroxide-mediated polymerisation (NMP), and cationic polymerisation, but this does not exist yet for RAFT. The aim of this thesis is to bridge the gap between polymer synthesis, kinetics, and autonomous self-optimisation. Bayesian optimisation will be used to facilitate high-throughput experimentation and will be applied to RAFT polymerisation. Furthermore, extensive reactor design will be applied that will lead to a platform capable of exploring a wider reaction space. A conversion model will be coupled to a newly completed equation for dispersity as a function of conversion, allowing for rapid *in-silico* kinetic modelling of RAFT. Inclusion of the model will also be used in tandem with the self-optimisation platform to direct reaction space exploration.

Intellectual Property

The candidate confirms that the work submitted is her own and that appropriate credit has been given where reference has been made to the work of others.

Chapter 2 includes data that were published in Knox, S. T.; Parkinson, S. J.; Wilding, C. Y. P.; Bourne, R. A.; Warren, N. J. Autonomous Polymer Synthesis Delivered by Multi-Objective Closed-Loop Optimisation. Polym. Chem. 2022, 13 (11), 1576–1585. CYPW contributed to improvements to software/data aquisition and experimentation. CYPW performed all optimisations in this chapter except that seen in Figure 2. For the statistical copolymerisation, PFPA was synthesised by Alexander Grimm from KIT.

All experimental work in Chapter 3 was performed by CYPW.

Chapter 4 is taken from Wilding, C. Y. P.; Knox, S. T.; Bourne, R. A.; Warren, N. J. Development and Experimental Validation of a Dispersity Model for In silico RAFT Polymerization. Macromolecules 2023, 56, 4, 1581–1591. Model developed and validated by CYPW. Graphical user interface for the model can be found at https://github.com/ClarissaYPWilding/KineticsModellerRAFT.

In Chapter 5, experimentation, software and model implementation conducted by CYPW.

Acknowledgements

First and foremost, I would like to thank my supervisors Nicholas Warren and Richard Bourne for giving me the opportunity to work on this project. The professional support and encouragement I have received has been truly appreciated. I also thank Stephen Knox for his support during my PhD, especially for reading through my papers, being there to bounce ideas off of, humouring my lab "inventions" and being there to vent to when the NMR was misbehaving. In addition, I thank the whole Warren group, iPRD and CPEG for listening to my practise talks, constructive comments, and advice which has benefited me greatly.

It is safe to say that if someone had said that there would have been a national lockdown during my PhD, I would have thought they were joking. However, I have met some wonderful people who are not just colleagues but friends. In particular, I would like to thank Jonny, Yaz, and El, who have been hugely supportive and enriched my PhD experience. Our conference karaoke escapades, singing and dancing along to '80's hits in the lab, and coffee breaks really made the days when things were not working better.

Finally, I would like to thank my family, particularly my parents Paul Harris and Lorraine Wilding, who have supported me throughout my education to have the opportunities they never had. I owe my motivation and hard working attitude to them.

Contents

5 Digitally Augmented Self-Optimisation of RAFT polymerisation 127

List of Figures

List of Tables

Acronyms

ACOMP automatic continuous online monitoring of polymerisation.

ACVA 4,4-Azobis(4-cyanovaleric acid).

AIBN Azobisisobutyronitrile.

BPR back pressure regulator.

CCTP catalytic chain transfer polymerisation.

CSIRO Commonwealth Scientific and Industrial Research Organisation.

DMAm dimethylacrylamide.

DOE design of experiments.

DTC dithiocarbonates.

EHI expected hypervolume improvement.

EPR electroparamagnetic resonance.

GCFID gas chromatography flame ionisation detection.

GPC/SEC gel permeation chromatography/ size exclusion chromatography.

HPLC high-performance liquid chromatography.

IR infrared.

IRT intermediate radical termination.

IRTO intermediate radical termination with oligomers.

IUPAC International Union of Pure and Applied Chemistry.

kMC kinetic monte carlo.

LAMs less activated monomers.

MA Methylacrylate.

MAMs more activated monomers.

MMA Methylmethacrylate.

MOAL multi-objective active learner.

MoM method of moments.

MS mass spectrometery.

MVMOO mixed Variable multi-objective optimisation.

nBUA n-butylacrylate.

NGSM II non-dominated genetic sorting algorithm 2.

NIPAM N-isopropyl acrylamide.

NMR nuclear magnetic resonance.

NMSIM nelder-mead simplex.

NVC N-Vinyl carbazole.

NVP N-Vinyl pyrrolidone.

OVAT one variable at a time.

ParEGO pareto efficient global optimisation.

PEEK polyether ether ketone.

PFA perfluoroalkoxy alkane.

ROMP ring-opening metathesis polymerisation.

RTD residence time distribution.

SF slow fragmentation.

SNOBFIT stable noisy optimisation by branch and fit.

St Styrene.

tBuAm Tert-butylacrylamide.

TS-EMO thompson sampling by efficient multi-objective optimisation.

TTC trithiocarbonates.

UV/Vis ultraviolet/ visible light.

VA044 2,2'-Azobis2-(2-imidazolin-2-yl)propanedihydrochloride.

VAc Vinyl acetate.

Chapter 1

Introduction

1.1 Polymerisation

Although, nature has been synthesising polymers since the origin of organic life through DNA/RNA and proteins, etc., we have gained the ability and understanding to synthesise non-naturally occurring polymers in the last few centuries.[1] In 1920, Staudinger defined polymers as the linkage of small molecules (monomers) to form large macromolecules (polymers). Although in 1833, Berzelius first used the term "polymer" to describe benzene, which he deemed a polymer of ethyne. In addition, he also recognised the existence of compounds with different numbers of atoms but identical elemental composition.[2] Nowadays, the Staudinger definition is predominantly used among polymer chemists.[3] The first man-made polymeric material was actually synthesised decades before polymers were defined and understood. Bakelite was the first thermoset polymer and was made in 1907 by condensing phenol and formaldehyde and is typically described as the origin of the plastic industry. Berthelot (1863) is often hailed the original polymer chemist, suggesting that "polymeric transformations" will occur when there is incomplete compounds or those which can add chlorine, hydrogen, or water. In addition, he also postulated routes of initiation, including heat or exotherms, a primary chemical reaction, and/or an intermediate species. This formed the foundations of what is known as polymerisation today.[4] In 1929, Carothers categorised polymers into condensation and addition polymers; dependent on how they are formed. Condensation polymers are defined as polymers formed from functional monomers where the reactive centre is the reactive functional group (ie, dicarboxylic acid and a diamine species).[5] As a consequence, a small molecule, such as water or an acid, is eliminated. On the other hand, addition polymers are those formed without the expulsion of a small molecule.

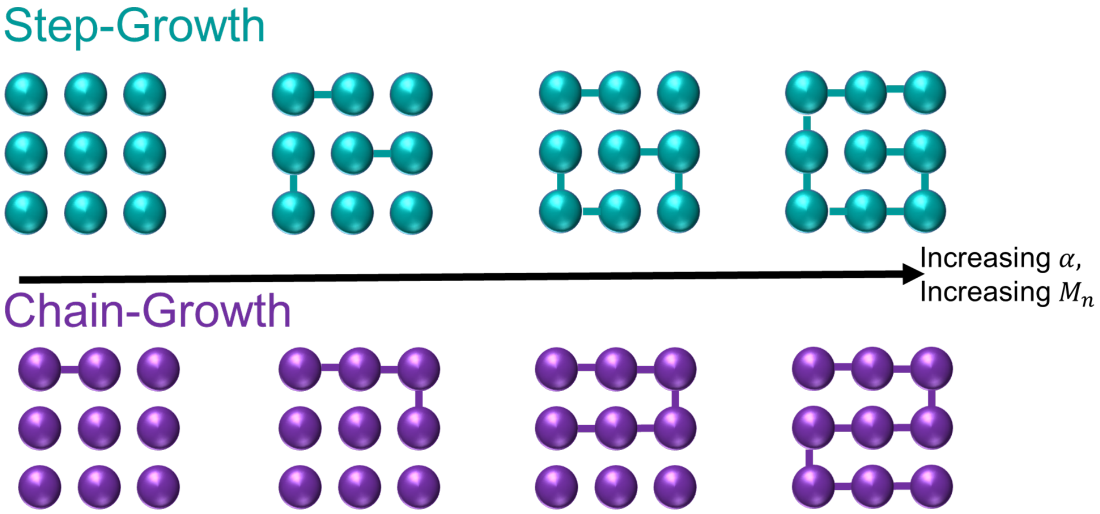

Figure 1.1: Comparison of the mechanism of step-growth (teal) and chain-growth polymerisation (purple) with increasing conversion [(α)] and average molecular weight (M_n).

The kinetics of condensation and addition polymerisation can exhibit different types of growth of the polymer chain. The growth of a polymer with respect to conversion is divided into step growth and chain growth, shown in Figure 1.1. In step-growth polymerisation the molecular weight increases slowly with conversion as oligomers are formed, then the molecular weight increases as oligomers join to form polymers. On the other hand, chain-growth results in an increase in molecular weight as each monomer is successively added to the polymer chain.[6] Due to the statistical nature of polymerisations, there is no single molecular weight produced by the reaction; instead, a distribution of molecular weights is observed, which is typically described by molar mass dispersity, Đ. Where Đ (Equation 1.1), is the ratio of the average weight molecular weight (Equation 1.3) to the average number molecular weight (Equation 1.2).

$$Đ = \frac{\bar{M_w}}{\bar{M_n}} \tag{1.1}$$

$$\bar{M_n} = \frac{\sum N_i M_i}{\sum N_i} \tag{1.2}$$

$$\bar{M_w} = \frac{\sum N_i M_i^2}{\sum N_i M_i} \tag{1.3}$$

Process Conditions

Process conditions can be engineered to facilitate rapid kinetics and tunable MWDs.Some polymerisations can be conducted in bulk/mass which means that any other reactive species are dissolved in the monomer. These are typically more "green" processes, as they require little or no purification and drying, and do not use potentially environmentally damaging solvents. However, these polymerisations can lead to loss of control due to potential exotherms and reduced heat transfer as a result of increased viscosity, especially in the case of chain-growth polymerisation. On the other hand, higher molecular weight polymers are not achieved until the later stages of the polymerisation (i.e. for step-growth polymerisation) - therefore, bulk polymerisation is better suited. Solution polymerisation techniques are commonly used for chain growth polymerisations. Conducting polymerisation in solution can help increased viscosity and heat transfer; however, it is important to consider the effect of transfer to the solvent as this may cause molecular weight distribution (MWD) broadening.[6] Typically, radical polymerisations can also be conducted under heterogeneous conditions. Precipitation polymerisation occurs when the starting reagents (e.g. monomer and initiator) are in solution until the polymer forms where they are then absorbed into the polymer - this could be in bulk or solution. Another type of polymerisation process is suspension, where the reagent species form a discontinuous phase and the solvent (e.g. water) is the continuous phase. The biphasic mixture is then agitated to suspend the monomer in droplets in the continuous phase, which can then form polymer within the droplets. The coalescence of the droplets can be prevented by the use of dispersants and surfactants. Finally, emulsion polymerisation is used as the medium for some chain-growth polymerisations. This is different from the case for suspension because an emulsion is formed immediately without agitation, and higher molecular weight polymers can be obtained without lowering the rate of polymerisation. In emulsion polymerisation, the initiator is not soluble in the monomer droplet; however, because of the low monomer concentration, the main site of polymerisation is not the continuous phase. Polymerisation actually occurs in the active micelles.[6] The effect of oxygen on polymerisation has been known for decades.[7] Metal-based polymerisation is typically effected by oxidation of the organometallic reagent. Radical-based polymerisation is effected as a result of radical scavenging capabilities of molecular oxygen via formation of a less reactive peroxyl radical. Ultimately, this causes rate retardation and can affect molecular weight as a result.[7] Physical doxygenation is often the standard method for removing molecular oxygen; methods include: degassing with an inert gas, freeze-pump-thaw by liquid nitrogen, and

/ or using a glovebox to ensure that no air gets to the reaction. Deoxygenation is not always feasible in the scale-up of polymers; thus, oxygen-tolerant polymerisations became a point of interest for polymer chemists.[8] Methods of improving oxygen tolerance include: transformation of ground-state oxygen (^{3}O) into singlet oxygen (^{1}O) using a photocatalyst, the use of a reactive oxygen reagent(e.g. ascorbic acid) and the use of enzymes such as glucose oxidase (GO_x) to form a non-radical species (H_2O_2). Alternatively, oxygen can also be used as a co-initiator using triethyl borane as an activator.[8]

Co-polymers

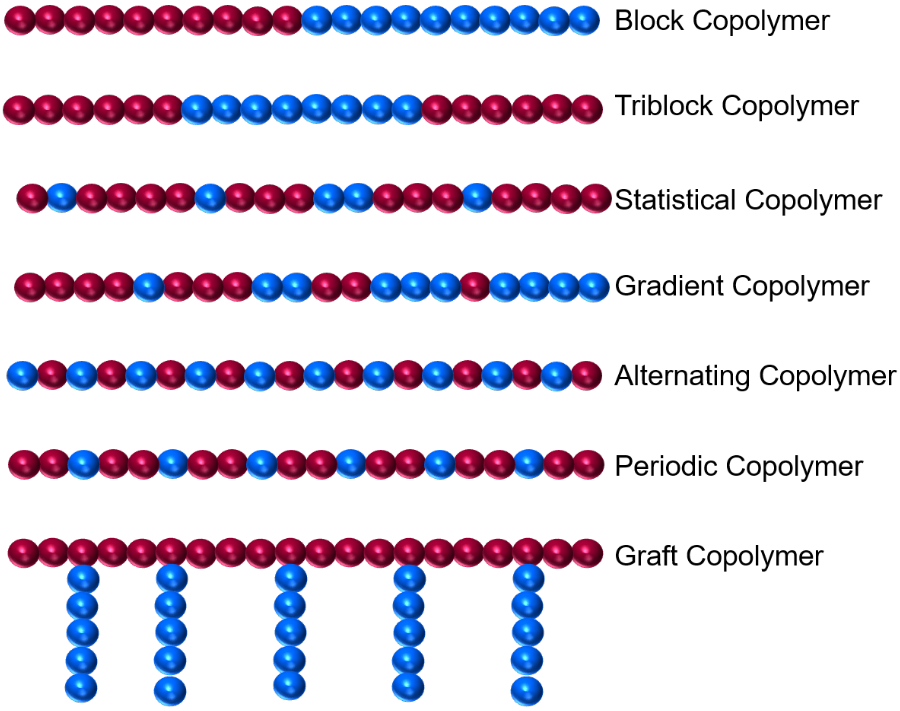

Figure 1.2: Comparison of different monomer arrangements in copolymers.

A homopolymer is a polymer containing a single monomer species, whereas a copolymer is defined as a polymer derived from more than one monomer species.[9] The arrangement of the monomers can affect the morphology and structure activity relationship of the resultant polymer. The nomenclature of a copolymer depends on the arrangement of the monomers, this is shown in Figure 1.2. The monomers in a copolymer may be in an alternating arrangement, known as an alternating polymer. If the sequence of monomers is random, this is known as a statistical copolymer. They can also have blocked arrangements of constitutionally different adjacent monomers (polymer with 2 blocks = diblock copolymer, 3 blocks = triblock copolymer, etc.) or have a periodic pattern of monomers that is repeated through the polymer. They may also have a gradient where the composition of the monomer increases or decreases along the chain, or be a graft polymer where another monomer branches from a linear chain of another.

From this point onwards, the focus will be on the polymerisation of vinyl monomers. The resonance and inductive properties of the substituent group on the C=C dictates the suitability of initiation by anionic, cationic, and/or radical initiators. Typically, electron-donating groups (e.g. alkoxy or alkyl groups) increase the C=C electron density, which enables initiation by cationic species, as the cation on the propagating species will be stabilised by resonance. Both cationic and anionic propagating species of alkenyl and phenyl-substituted monomers will be stabilised by the delocalisation of electrons. However, electron-withdrawing groups (e.g. carbonyls and amides) decrease the electron density on C=C, which aids initiation by anionic species only. Halogenated vinyls such as vinyl chloride can only be polymerised by radical polymerisation, due to inductive withdrawing and resonance-donating electronic properties. Almost any type of monomer can be polymerised by radical polymerisation, as radical initiators are labile and will attack the C=C bond.[6]

1.1.1 Ionic Polymerisation

Living Anionic

The seminal work reported by M.Swarc (1956) suggested that polymers that do not undergo termination are "living". He defined a living polymer as a polymer that has a reactive end group, where, as long as there is a supply of monomer, it will continue to grow and the molecular weight will increase.[10] The first instance of this demonstrated the use of sodium naphthalenide as an electron transfer initiator to polymerise styrene. Furthermore, they elucidated the mechanism through viscosity-kinetic studies.[11,12]

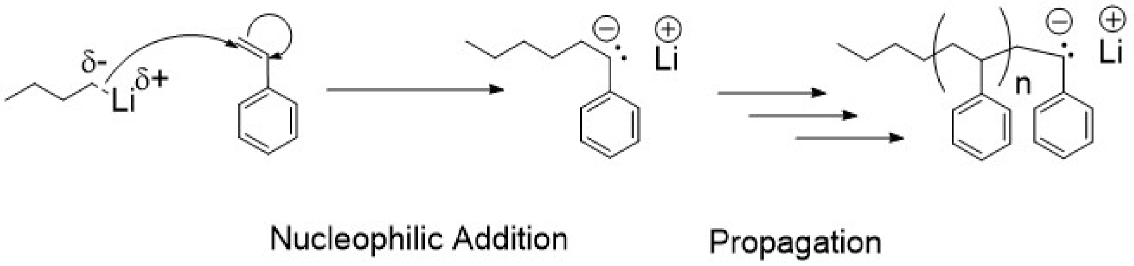

Figure 1.3: Schematic for Living Anionic Polymerisation using a linear alkyllithium species

Today, alkyllithium species are used as the initiator, which is possible because of the electronegativity causing polarisation of the carbon and lithium bond. The alkyllithium used should be compatible with the monomer and solvent polarity, and the types of alkyllithium species exhibit varying intermolecular aggregation. Polymerising styrene with nBuLi has been shown to exhibit rate retardation as a result of significant aggregation compared to sBuLi or tBuLi.[13] Living anionic polymerisation has been shown to provide the lowest dispersity of all polymerisation techniques with a molecular weight distribution described by a poisson distribution.[14]

Cationic Polymerisation

Cationic polymerisation is defined by the International Union of Pure and Applied Chemistry (IUPAC) as polymerisation in which the kinetic chain carrier is a cation.[9] To obtain a "living" character, initiation and propagation must be controlled.

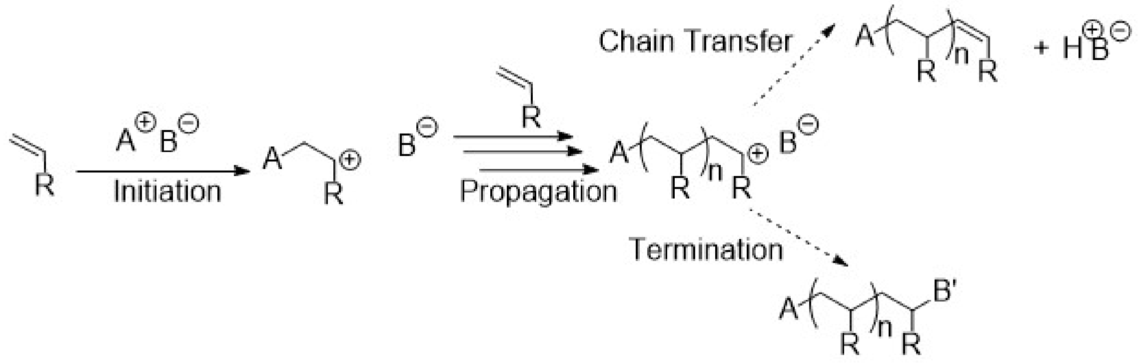

Figure 1.4: Schematic for cationic polymerisation using a linear alkyllithium species

Lewis acids are the most common initiators in cationic polymerisation with the rate being dependent on the strength of the Lewis acid. Cationic polymerisations using Lewis acids are rapid and typically conducted at low temperatures with a *protogen* (e.g. protic solvents) or with a *cationogen* (e.g. tertiary alkyl halide). It is more challenging to obtain the "living" character with cationic polymerisation due to the presence of an irreversible termination step, as seen in Figure 1.4.

1.1.2 Radical Polymerisation

The mechanism of radical polymerisation was investigated in the early 1900s. Stobbe and Posnjak (1909) explored the change in viscosity of the polymerisation of styrene to metastyrol (now named polystyrene) and discovered that fresh styrene polymerised much slower than styrene that had been left a few weeks. Thus, we now explain what we identified as the induction period.[15,16] Lautenschlager further explained this observation through the formation of peroxides as catalysts.[17] Swarc also defined polymers that can no longer react with the monomer even if there is monomer present as "dead polymers".[10] This section will cover traditional radical polymerisation as well as the developments in controlling radical polymerisation such as RDRP techniques.

Free Radical Polymerisation

Staudinger (1920) theorised that trivalent carbon atoms that we now call radicals were responsible for the formation of long-chain species, which he called a "Makromolekul". In addition, he proposed that the long chains would have a reactive end which proceeded to terminate or deactivate[3] At this point the mechanism was based on speculation, and it was not until 1929 when he then published a subsequent paper where this was addressed. Here he addressed a possible route for termination; such that, chains eventually terminate by ring formation.[18,19] A few years later, Staudinger and Kohlschutter (1931), suggested that acrylic acid polymerises through activation of the monomer and that the rate of addition is rapid; which we now call propagation.[20] Schulz (1935) suggested the presence of catalytic species to form the active monomeric species.[21] Flory then proceeded and concluded that propagating chains, can only terminate by bimolecular disproportionation and combination and that the rate of polymerisation is dependent on monomer and initiator concentration.[22]

The mechanism of FRP is well studied and each step has its own rate constant.[23] Initiation occurs typically by thermal or photochemical decomposition; the rate constants of decomposition,k_d, are widely available. Due to the unimolecular nature of the reaction, the kinetic rate constant can be extrapolated by monitoring the decay in the concentration of the initiator or by using a radical "trap" such as a monomer. Subsequently, the Arrhenius Equation can be applied at different temperatures to obtain the activation energies, E_a and the frequency factor, A.[23] The fraction of initiator radicals that are added to monomer species is known as the initiator efficiency, f. f is dependent on the functionalities of the initiator, the solvent used and whether there is the presence of oxygen - the lability of radical species may cause side reactions that can reduce the rate of polymerisation.[6]

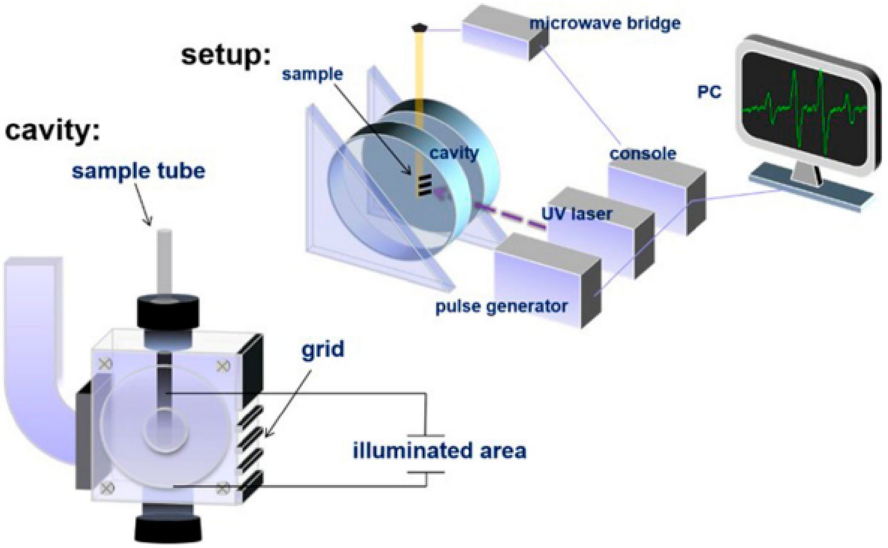

Figure 1.5: Schematic of a pulsed laser polymerisation setup taken from Buback *et al.*.[24] Reproduced with permission from The American Chemical Society, Copyright ©2016

Since the inception of FRP there has been a driving force led by IUPAC to benchmark rate constants to enable better modelling. Propagation and termination rate constants can be described by k_p and k_t, respectively, which are most commonly found through pulsed-laser polymerisation (PLP) techniques due to improved data quality. Prerequisite knowledge of the monomer concentration and the time between pulses of the laser is mandatory for the identification of k_p and k_t.[25] The apparatus used in PLP is shown in Figure 1.5. A laser pulse applied at a constant frequency initiates the polymerisation, and chain growth between each pulse is monitored by SEC such that the first pulse initiates the polymerisation and the following pulse quenches the polymerisation.[26] PLP has been coupled to a variety of analytical techniques, such as SEC and EPR, to detect macroradical concentration. SP-PLP-EPR which uses a single pulse (SP) of light to photo-dissociate the initiator has been used in conjunction with EPR to elucidate the chain-length dependence.[2725,28] Termination can occur by combination (k_{tc}), where the two propagating chains share their single electron or by disproportionation (k_{td}), where a hydrogen from one propagating chain is abstracted by the radical forming one saturated and one unsaturated chain.[6]

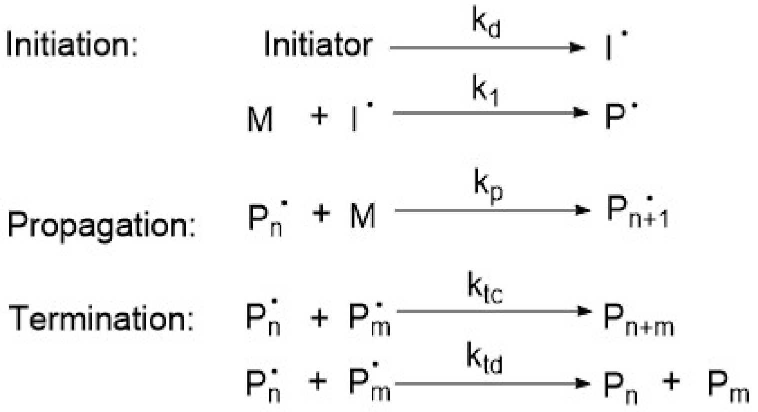

Figure 1.6: Kinetic mechanism of free-radical polymerisation, where k_p, k_t and k_d are the rate constants of propagation, termination and decomposition, respectively.

The overall rate of polymerisation, R_p is commonly denoted as Equation 1.4.

$$R_p = k_p[M]\sqrt{\frac{(2f[I]_0 e^{(-k_d t)})}{k_t}} \tag{1.4}$$

As a result of uncontrolled termination events, molecular weight distributions can be broad and asymmetric compared to a living anionic polymerisation - Đ can be large (>1.4).[29] Some vinyl monomers can exhibit autoacceleration of the polymerisation rate in both bulk and solution, causing a deviation from first-order kinetics. This phenomenon was first identified by Trommsdorff, Norrish, and Smith between 1948 and 1951 for the polymerisation of methyl methacrylate. They suggested that the increase in molecular weight was caused by a decrease in termination occurring at a certain viscosity. Furthermore, causing a decrease in the rate of diffusion of propagating chains. The termination rate of two vastly different chains will therefore be dominated by the shorter of the 2 terminating chains. This phenomenon was later coined the Trommsdorff-Nordish effect.[30,31] This effect can be reduced by using the aforementioned solution and heterogeneous process conditions, by lowering the temperature and/or using a species that holds the propagating species in an equilibrium.

1.1.3 Reversible Deactivation Radical Polymerisation Techniques

RDRP is defined by IUPAC as "Chain polymerisation, propagated by radicals that are deactivated reversibly, bringing them into active/dormant equilibria of which there might be more than one".[32] Between 1956-1990, Otsu and co-workers reported the use of dithiocarbamyl radicals as a mediating initiator species for the radical polymerisation of MMA and St, which they named iniferters. The propagating species has an iniferter end group that allows for controlled monomer insertion. This is a type of RDRP known as stable radical-mediated polymerisation (SRMP), where the mediating species is a radical[33] (i.e. there is reversible termination). The three most studied RDRP techniques, atom transfer radical polymerisation (ATRP),[34,35] nitroxide mediated polymerisation (NMP)[36,37] and reversible addition fragmentation chain transfer (RAFT)[38–40] all have well studied and well understood mechanisms.[41,42] These exhibit pseudo-first order kinetics, which is illustrated by a linear evolution in number average molecular weight (M_n) with conversion (α), and results in low Đ polymers (typically <1.20). These properties are a result of equilibration between the dormant species and propagating radicals; in the absence of this (for FRP) broader statistical distributions of molecular weights are observed.[42]

Nitroxide Mediated Polymerisation

NMP was first reported in 1984 in a patent application by Commonwealth Scientific Industrial Research Organisation (CSIRO),[43] it was then published in 1985 in a patent named "Free radical polymerisation and the produced polymers".[36] The name "nitroxide-mediated polymerisation" (NMP) is disputed by the IUPAC nomenclature where they encourage the name "aminoxyl-mediated radical polymerisation" (AMRP).[33] NMP is defined by IUPAC as "Stable-radical-mediated polymerisation in which the deactivation of the radicals involves reversible coupling with aminoxyl radicals".[32,33]

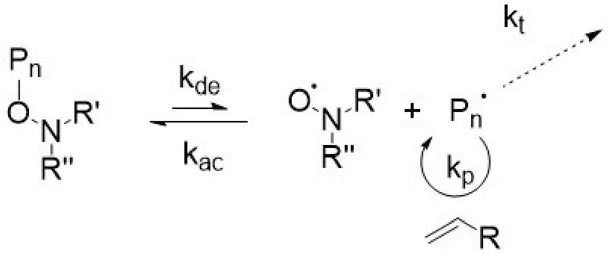

Figure 1.7: Mechanism for Nitroxide-Mediated Polymerisation where P_n is the propagating chain, k_{de} and k_{ac} are the rates of deactivation and activation, respectively

Atom Transfer Radical Polymerisation

In 1995, Matyjaszewski and co-workers demonstrated control over radical polymerisation through the use of copper metal complexes[34] and later that year Sawamoto and co-workers published similar work using Ruthenium metal complexes.[44]

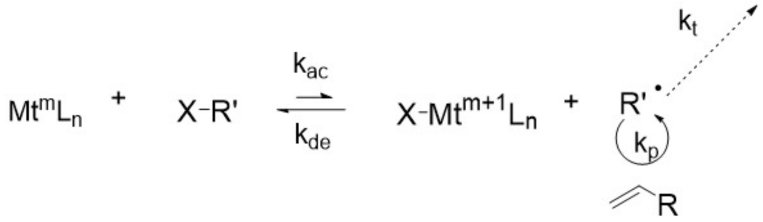

Figure 1.8: General mechanism for atom transfer radical polymerisation where P_n is the propagating chain, k_{de} and k_{ac} are the rates of deactivation and activation, respectively.

The mechanism of ATRP is extensively studied, the catalyst abstracts the halogen on the alkyl halide initiating species in a reversible redox reaction with the catalyst.[45] Since the seminal ATRP work, different transition metals such as Os, Mo, Cr, Re, Fe, Au, Rh, Ni, and Pd have been used. Stimuli responsive ATRP techniques have also been used. Photon-induced electron transfer ATRP (PET-ATRP) has also been demonstrated using 10-phenylphenothiazine and dihydrophenazine as catalysts, eliminating the need for metal complexes. High surface area electrodes have also been used as an electron source to convert the metal centre (Mt) from Mt (m + 1) back to Mt(m) to improve control in electrochemical ATRP (eATRP).[46] Charge separation has also been performed using piezoelectric nanoparticles that convert energy to electrons by sonication[46] Chemical reducers can also be added to reduce Mt (m + 1) in the presence of a low concentration of catalysts. In the presence of organic reducers such as ascorbic acid, this is known as activators regenerated by electron transfer (ARGET) ATRP. However, if a zero-valent metal is used, this is known as supplement activator and reducing agent (SARA) ATRP.[46] Initiator for continuous activator regeneration (ICAR) ATRP uses conventional thermal initiators at low temperature to release a small amount of deactivating species.

Reversible Addition-Fragmentation Chain Transfer

RAFT utilises sulphur containing compounds that can participate in reversible chain transfer.[29] RAFT was first reported by CSIRO in 1998, as a type of degenerative transfer radical polymerisation.[38] Thiocarbonyl species were identified from the chain-transfer capabilities of macromonomers. IUPAC defines RAFT as a "degenerate transfer radical polymerisation in which chain activation and chain deactivation involve a degenerative chain transfer process that occurs by a two-step addition-fragmentation mechanism".[32] Propagating radicals undergo addition to the CTA forming a radical adduct intermediate, which then decomposes to reform the CTA and a radical.

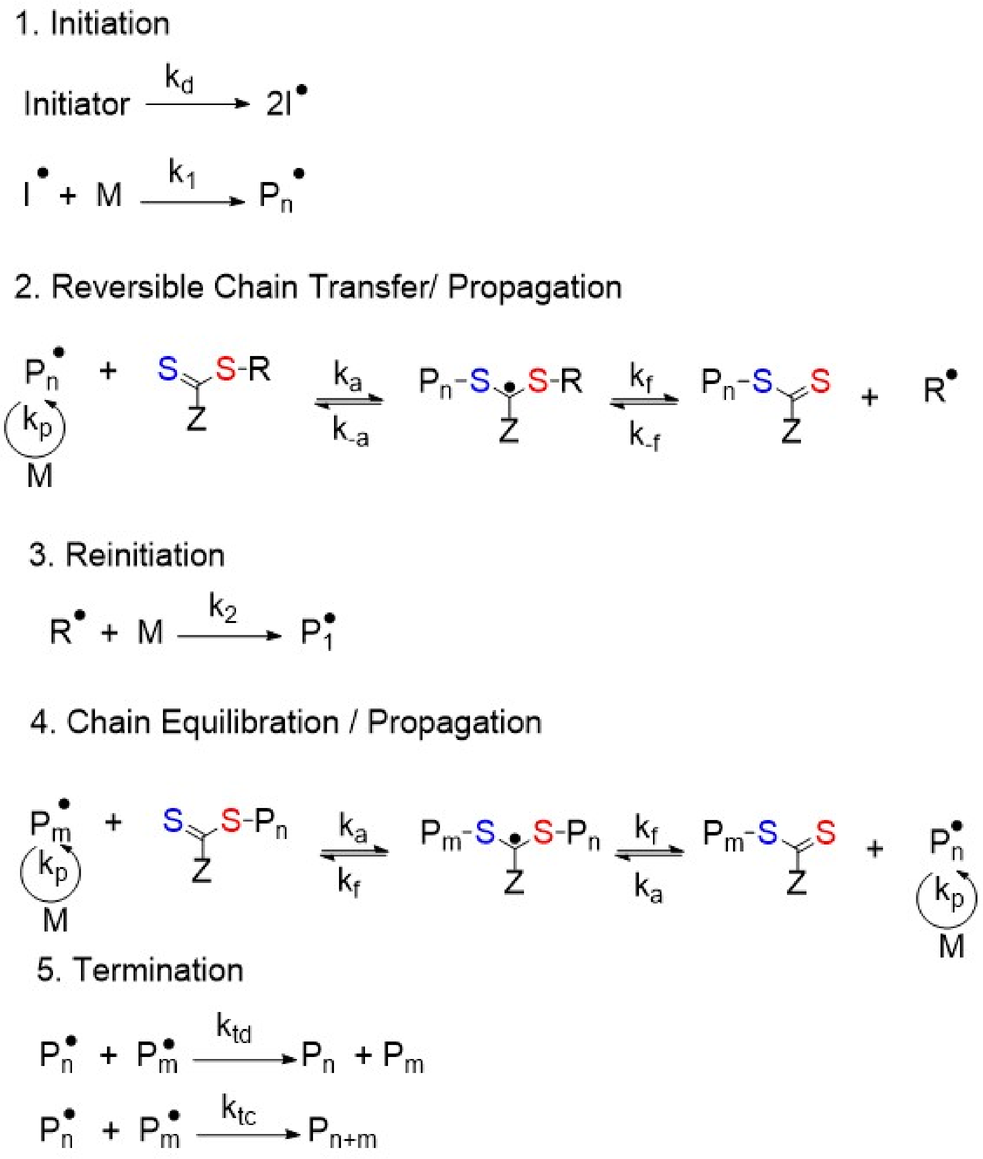

Figure 1.9: The general mechanism for RAFT where k_d, k_p, k_a, k_f, k_{-a}, k_{-f}, k_{td} and k_{tc} are the rates of initiator decomposition, propagation, forward addition, forward fragmentation, backwards addition, backwards fragmentation, termination by disproportionation, termination by coupling, respectively.

The two step equilibrium can be deconvoluted to account for the partitioning of the radical adduct intermediate between the starting materials, ϕ, using Equations 1.5 and 1.6.

$$k_{tr} = k_a \phi = k_a \left(\frac{k_f}{k_{-a} + k_f} \right) \tag{1.5}$$

$$k_{-tr} = k_{-f} \left(1 - \phi \right) = \frac{k_{-a}}{k_{-a} + k_f} \tag{1.6}$$

where k_{tr} and k_{-tr} are the rates of chain transfer. If $k_{tr} \left[P_r \right] \left[CTA_x \right] = k_{-tr} \left[P_r \right] \left[CTA_y \right]$ then the polymerisation is degenerate. If $k_{tr}\,[P_r]\,[CTA_x] > k_{-tr}\,[P_r]\,[CTA_y]$ then radicals are being produced by a mechanism other than initiator decomposition, the reverse suggests that propagating radicals are not only being consumed by termination.[47]

The compatibility of the RAFT agent is critical to control the polymerisation of certain monomers. The Z-group controls the rate of addition of propagating radicals (P_n) to the thiocarbonyl species and the rate of fragmentation of the radical adduct intermediate. The class of RAFT agent is moderated by the Z group, and RAFT categories include: dithiobenzoates, xanthates, trithiocarbonates, dithiocarbamates, and dithioesters. RAFT using xanthates is often referred to as macromolecular design by interchange of xanthate (MADIX). Typically, more-activated monomers (MAMs) are more compatible with trithiocarbonates and dithiobenzoates as the Z-group improves the stabilisation of the radical adduct intermediate, which increases the rate of addition of the propagating radical to the C=S bond. On the other hand, less-activated monomers (LAMs) are better suited to xanthates and dithiocarbamates, this affords labile radical adduct intermediates - that otherwise would be stable and able to undergo side reactions - increasing the rate of fragmentation. Presence of oxygen and nitrogen in the Z-group provides a lone pair of electrons that can delocalise in the S-C=S system, increasing the lability of the radical adduct intermediate. The R groups tend to have structures similar to those of the monomer or initiator radical and require a balance of sterics and radical stability. The effect of the R group is less prominent than the Z, but mediates: the rate of addition, leaving group ability of the R group in fragmentation and the rate of propagation. It is important to consider which monomer to make the macro-CTA from in block co-polymer synthesis - as a good leaving group enables more controlled polymerisation.[29,48] Chain-transfer describes the ratio of the rate of a transfer process involving the propagating chain (propagating radicals-solvent/propagating radicals-CTA) to the rate of propagation. The chain transfer coefficient C_{tr}, is frequently used to demonstrate the chain transfer activity of a RAFT agent or solvent. If the rate of transfer is greater than propagation then $C_{tr} > 1$, and vice versa. Transfer coefficients can be found by constructing a Mayo plot, this is a plot of the inverse of the DP against the inverse of the ratio of monomer to CTA or solvent concentration. Donald *et al.*[49] compared the efficacy of different plots to obtain C_{tr}. Mayo plots were compared to Smith plots is monitoring the concentration of monomer to CTA and plotting on a logarithmic scale, here the gradient would correspond to the transfer coefficient. Gilbert method[49] involved converting SEC data into number molecular weight distribution and expressing as a function of the DP.

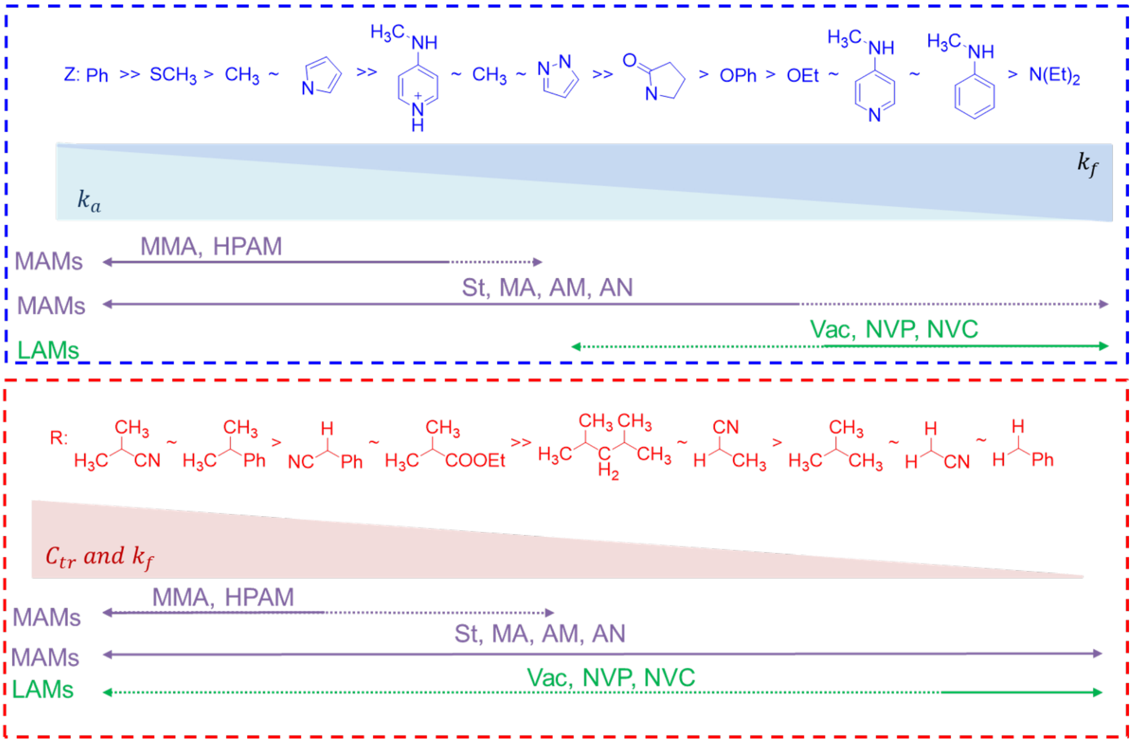

Figure 1.10: RAFT agent design and synthesis showing the effect of the Z and R groups on the rate coefficients for the polymerisation of MAMs and LAMs

Switchable RAFT agents are RAFT agents that have stimuli-dependent reactivity. These are of particular interest for the synthesis of block copolymers. For example, where the z group has a pyridine ring such as N-aryl-N-(4-pyridinyl)dithiocarbamate. Here, the RAFT agent affords good control over LAMs (VAc, NVP, and NVC), while upon the addition of a strong acid, the pyridine ring will be protonated to enable compatibility with MAMs (MMA, MA, and St).[50] Additionally, the use of porphyrin-cobalt complexes has been demonstrated by Belovskii and co-workers as early as 1981 to show regenerative chain transfer effects with methyl methacrylate,[51] offering control over polymerisation. This has been suggested to be sulphur-free RAFT and has been used by Haddleton and co-workers[52] for the emulsion polymerisation of methacrylic multi-block copolymers. The first step involved catalytic chain transfer polymerisation (CCTP), which generated a vinyl-terminated poly(methyl methacrylate) using a cobaloxime catalyst. The authors used macro-CTA to synthesise block copolymers with low dispersity.[52,53] Examples of electrochemically mediated RAFT (eRAFT) have also surfaced in the literature. Matyjaszewski and co-workers[54] successfully carried out eRAFT for the polymerisation of (meth)acrylates by producing aryl radicals as initiators by reducing benzoyl peroxide or 4-bromobenzenediazonium tetrafluoroborate. It was also reported that the electrochemical reduction of the standard RAFT agent itself led to carbanions. Furthermore, they concluded that eRAFT provided high conversions (>80 %) with narrow MWDs.[54] Deviations from the traditional free radical polymerisation rate are known as rate retardation.

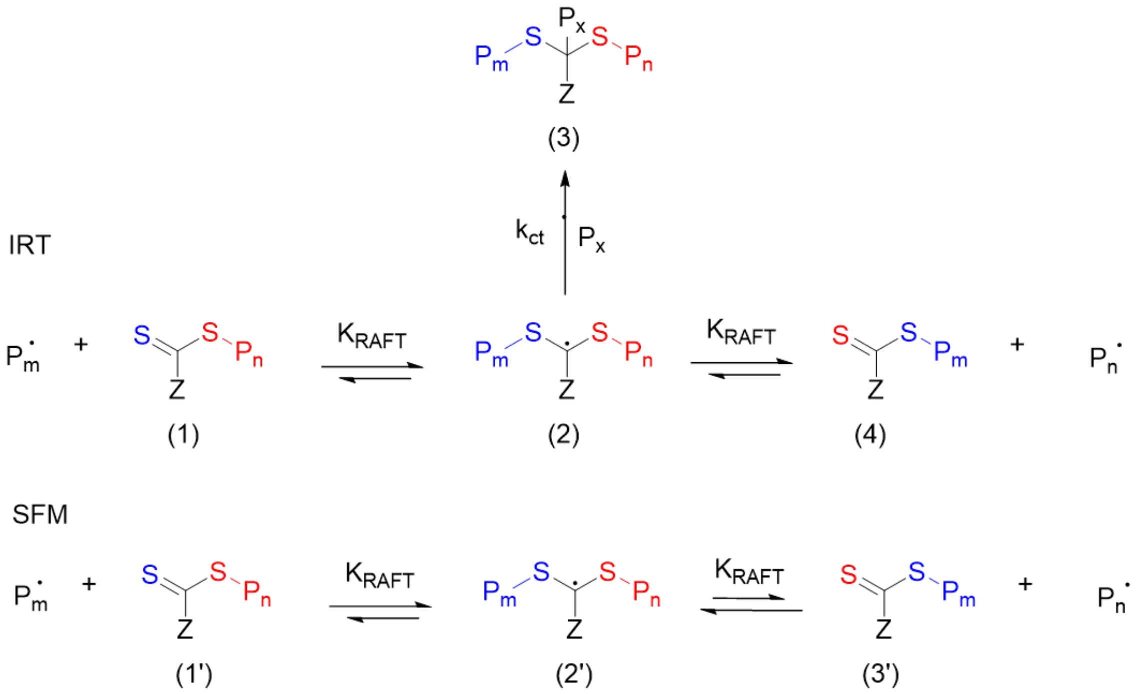

Figure 1.11: Comparison of IRT vs SFM

Polymer chemists debate the cause of rate retardation in RAFT, with three main theories: Intermediate radical termination (IRT; see 1.11) proposed by Monteiro and DeBrouwer et al.;[55,56] where cross-termination occurs forming a 3-armed chain species shown by species (3). Secondly, slow fragmentation method (SFM) proposed by Barner-Kowolik et al.[57,58] operates on the assumption that fragmentation is slow and cross termination does not occur. In Figure 1.11, the RAFT equilibrium constant (K_{RAFT}) is shown to favour the radical adduct (2'). Furthermore, SFM has been supported by calculations *ab initio* looking at the effect of Z and R groups on the stabilisation energies of the radical adduct intermediate species.[59] Since this debate, a third theory has also been postulated by Buback and Vana et al.[58,60] who have used time-resolved electron paramagnetic resonance spectroscopy (EPR) to identify a missing reaction step in the IRT mechanism. It was initially assumed that rate retardation was only present for noncompatible monomers with dithiobenzoates; however, recent work suggests that it is ubiquitous in varying amounts for most combinations of the RAFT agent and the monomer.[61]

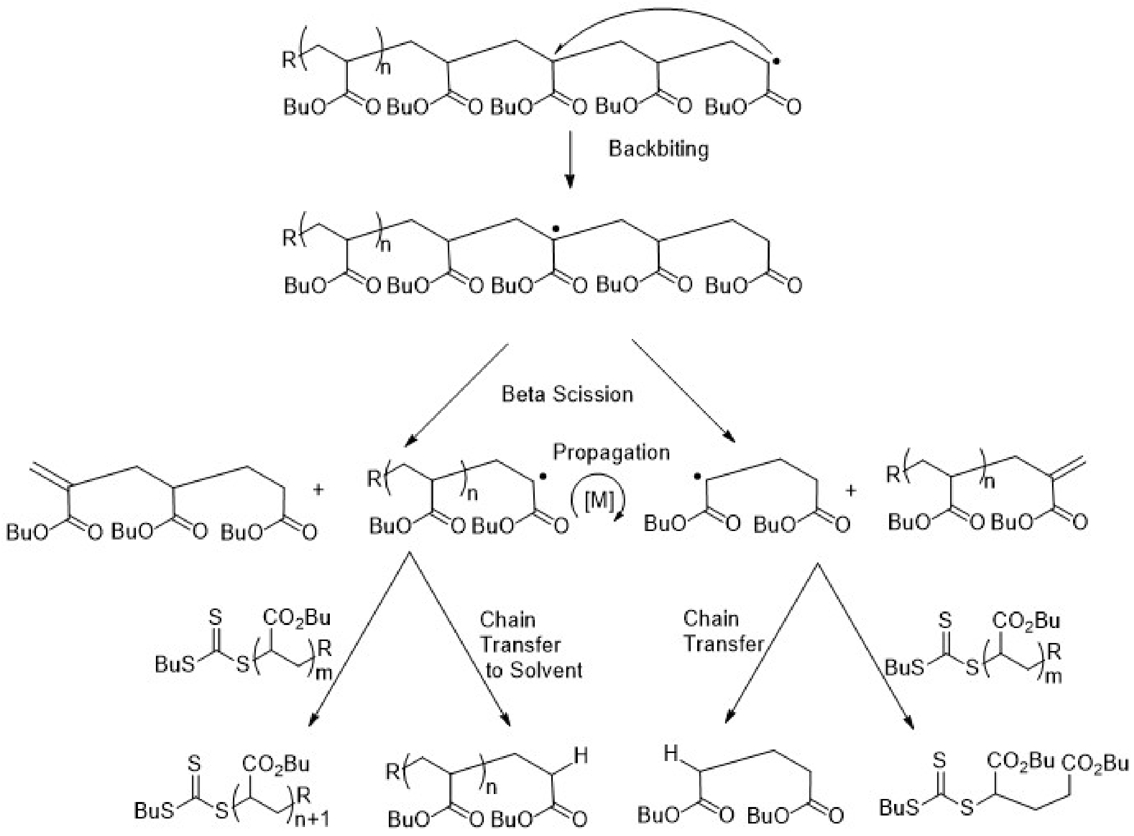

Figure 1.12: The formation of mid-chain radicals and the side reactions such as beta scission, chain transfers and reactions with the raft agent in the RAFT polymerisation of butyl acrylate.

For bulkier, more active monomers, the likelihood of side reactions is high. The formation of mid-chain radicals (MCRs) has been shown to undergo β-scission and macromonomer formation at temperatures greater than 120 $°C$. Mass spectrometry has shown that the formation of macromonomers and short-chain radicals reduces the overall rate of polymerisation and explained the formation of shorter average molecular weights at such temperatures.[62,63] As mentioned previously, oxygen is a carbon radical scavenger,**[bh]** which can cause rate retardation. Oxygen-tolerant RAFT has been demonstrated by exciting ^3O to ^1O using photocatalysts; this is called photoinduced energy transfer RAFT (PET-RAFT). The energy from the energy transfer from the excited photo-redox catalyst and reaction of singlet oxygen with solvent or reducing agent affords oxygen tolerance. In efforts to improve industrial and economic viability, the Fenton reaction initially used to produce hydroxyl radicals in the FRP of vinyl monomers was coupled with RAFT by Qiao and co-workers in minutes. They showed that a degree of oxygen tolerance was accessed; however, the MWD obtained via SEC were much broader.[64] Other advances in RAFT polymerisation have come in the form of the use of enzymes to improve oxygen tolerance while providing biologically viable conditions. GO$_x$ has been used to remove oxygen in the form of peroxides.[65] An inherent challenge of precision radical polymerisation is increasing the rate of polymerisation without losing control over the molecular weight. Significant improvements have been made in increasing the rate of polymerisation. Perrier and coworkers managed to reduce the time taken for the one-pot sequence controlled synthesis of an icosablock copolymer from 24 h per block to 2 h per block with a dispersity of <1.4.[66] RAFT operates on the proportionality between the rate of polymerisation and the k_p of the monomer and the concentration of propagating radicals. k_p is temperature dependent, so an increase in temperature will increase k_p. If rapidly decomposing initiators are used at higher temperature, the concentration of propagating radicals will increase; this, combined with the temperature dependence of k_p, will increase the rate of polymerisation. The concentration of the initiator must be regulated because a high concentration of propagating radicals can lead to an increased termination rate $R_t = 2k_t[P_r]^2$ and a broadening of the MWD. Initiators with a high k_d are typically used because the "livingness" is dictated by the number of radical species throughout the reaction and not the rate of initiation, therefore therefore by using relatively lower [I]:[CTA]. Subsequently, the same group reduced this to 3 minutes by using 2,2-azobis[2-(2-imidazolin-2-yl)propane]dihydrochloride (VA044) in aqueous conditions at 100 °C and achieve full conversion.[67]

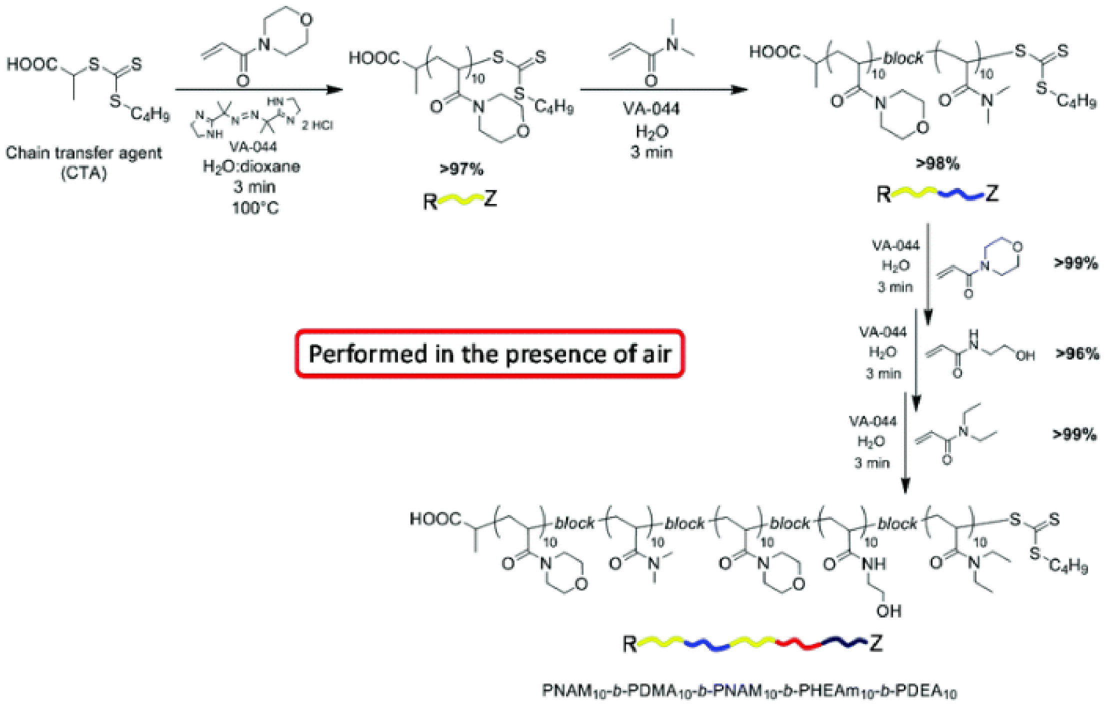

Figure 1.13: Sequential multi-block co-polymerisation reaction under ultra-fast RAFT conditions. Reproduced from Gody *et al*[67] with permission from the Royal Society of Chemistry, Copyright ©2014.

1.1.4 Other Polymerisation Techniques

Ring opening polymerisations (ROP) were introduced in the early 1900s and were initially used for the synthesis of polypeptides.[68] Unlike in the polymerisation techniques considered above, the thermodynamic driving force in ROP is the ring strain and the sterics.[6] Although the propagation rate constants for ROP are of a magnitude similar to that of step growth polymerisation, the kinetics often exhibit more chain-like/ living behaviour. Ring-opening metathesis (ROMP) is another type of ring-opening polymerisation in which unsaturated cycloalkene can undergo polymerisation due to the cyclic strain in the presence of a Ruthenium Grubbs catalyst or a Molybdenum Schrock catalyst.[69,70]

1.1.5 Modelling Polymerisation

Conversion and molecular weight are the most reported objectives that are modelled in the literature. The modelling of radical polymerisation requires sufficient knowledge of the rate constants corresponding to each step. Propagation (k_p), termination (k_t) and initiation (k_d) rate constants can be considered the same in RDRP compared to FRP. As mentioned above k_p and k_t are commonly found using PLP coupled with SEC and/or EPR, as shown in Figure 1.5. Whereas, k_d is typically found measuring the gas evolution following thermal or photo-chemical decomposition.[23,71,72] Numerical methods are a popular choice in polymer chemistry to model the reaction kinetics; there are two main types, stochastic and deterministic. Stochastic techniques are probabilistic and random. Reaction events are discretised and the rates are treated as probabilistic with temporal resolution. Since the first application of kinetic Monte Carlo (*kMC*) to chemical reactions in the 1970s by Gillespie,[73] *kMC* has emerged as the most popular stochastic techniques for modelling complex polymerisation due to its ability to obtain topological and microstuctural information. MC has been applied to ATRP,[74,75] NMP,[76,77] RAFT[78–80] and FRP.[81,82]Nevertheless, MC is considered a computationally expensive modelling technique. *kMC* can be divided into 6 steps: (1) initialisation, (2) reaction selection, (3) calculation of the time step, (4) reaction simulation, (5) model updates, and (6) iteration. Firstly, initialisation where the total number of molecules is set, (N) in a certain volume at time 0, followed by setting the value for the reaction rates, R_i, see Equation 1.7.

$$R_i = k_i X^c \tag{1.7}$$

where the reaction number, $i = 1, 2, \ldots, N_R$. The total number of reaction steps is given by N_R, so k_i is therefore the rate coefficient of the i^{th} reaction and X^c is the number of combinations of molecules in the i^{th} reaction. The experimental rate constants, k^{exp},found by the above methods are converted into microscopic rate coefficients for each reaction being considered. For a first-order reaction, this is the same as the experimental; however, for bimolecular reactions k^{exp} is divided by Avogadro's number (N_A) multiplied by the control volume, as seen in Equation 1.8.

$$k = \frac{Xk^{exp}}{N_A V} \tag{1.8}$$

If the two molecules in the step are the same $X = 1$, if they are different $X = 2$. R_i can then be identified by multiplying the microscopic rate coefficient by the number of species, i or j.

$$R_i = k_i n_i Y \tag{1.9}$$

If the reaction is first-order Y = 0, if it is bimolecular with different species $Y = n_j$, if the species are identical $Y = \frac{(n_i - 1)}{2}$, seen in Equation 1.9. In Step 2, the probability of the i^{th} reaction occurring P_i is given by the ratio of R_i to the sum of all R for all reactions (see Equation 1.10.

$$P_i = \frac{R_i}{\sum_{i=1}^{N_R} R_i} \tag{1.10}$$

The computational expense originates from the number of iterations required to evaluate the values of R_i and P_i, since R_i does not change in some iterations. Upon satisfaction of the inequality described by 1.11, reaction μ will be selected.

$$\sum_{i=1}^{\mu-1} P_i < r_1 < \sum_{i=1}^{\mu} P_i \tag{1.11}$$

Modified MC algorithms have been reported to address the redundancy of some iterations, such as the use of dependency graphs[83] and the use of the binary tree data structure.[84] Thirdly, the elapsed time step is typically found by t=t+Δt, given by Equation 1.12

$$\Delta t = e_{Rt} = \frac{e_1}{R_t} \tag{1.12}$$

Here e_{R_t} is a randomly generated number obtained from an exponential distribution.The fourth step is where the simulation occurs, and random selection of the molecules reacting from the control volume is required. This is already computationally expensive for non-polymeric samples, and this expense is increased upon inclusion of different chain lengths of the same species having different behaviour. Consequently, the way data are stored is important in *kMC*. The penultimate step requires updating the rates calculated in Equation 1.9 as the numbers of each molecule are now different. The final step is to iterate from the reaction selection step until a maximum conversion or time is achieved. Drache *et al.* demonstrated the use of kMC, which they subsequently experimentally validated for the bulk RAFT polymerisation of methyl acrylate. They obtained conversion, molecular weight, and concentration of RAFT species using FTIR, SEC, and ESR and the data were consistent with the model.[7879,85] Deterministic techniques treat concentration as a dependent variable and time as an independent variable. For polymerisation, a simultaneous solution of mass balance equations representing each chain species can be used to collect information about the molecular weight distribution and/or the branching density distribution.[86] The more mass balance equations, the more computationally expensive; to reduce the expense, discretisation of time intervals is usually carried out. The method of moments (MoM) is the most common deterministic technique for chemical reactions and minimises the number of mass balance equations. In this process, the resolution of the achievable data is compromised, so that only average chain properties are available. Moments can be predefined, for example, if we consider two types of polymer chain species, propagating chains ($P_r\cdot$), Y_i(1.13), and terminated chains(P_d), Q_i (1.14), where i represents the moment.

$$Y_i = \sum_{r=0}^{\infty} r^i [P_r \cdot] \tag{1.13}$$

$$Q_i = \sum_{r=0}^{\infty} r^i [P_d] \tag{1.14}$$

The zeroth order moment (i=0) represents the concentration of polymer chains in the system, and the first order moment (i=1) represents the number of monomeric units in the polymer chain. Ultimately, this allows one to find the number fraction and weight fractions. The dispersity can then be related to moments of the zeroth, first, and second order.[86] The method of moments has been applied to ATRP,[87–89] FRP,[90,91] NMP[92–94] and RAFT.[95,96]

$$Đ = \frac{Q_2 Q_0}{Q_1^2} \tag{1.15}$$

The mass dispersity can be identified by taking the ratio of the zeroth (Q_0) and second order (Q_2) moment to the square of the first order number moment (Q_1).

Alternatively, the commercially available user-friendly PREDICI software by Wulkow[97,98] is another deterministic technique. Through the implementation of the discrete Galerkin h-p method in the C++ programming language, PREDICI enables the modelling of polymerisations with: arbitrary numbers of species and CLD, arbitrary numbers of reaction steps and complex MWDs.[97] RAFT was one of the preliminary examples of PREDICI simulations where MWDs were simulated with respect to time by Vana *et al.*.[99] Furthermore, they reported the ability to find optimum conditions for "livingness" in RAFT and reported that the rate of addition of propagating radical species to the polyRAFT species was crucial to the control of the polymerisation.[99] PREDICI has since been used to simulate the kinetics of more sophisticated RAFT reactions. Zetterlund *et al.*[100] reported the use of PREDICI for the modelling of sequence-defined block copolymers comprising 10 blocks. Here, they find that the number of dead chains is indicated by the number of chains generated from the initiator and that they can achieve a "livingness" of approximately 7 %.[100] The use of PREDICI has also been shown to effectively model the synthesis of star polymers by Chaffney-Millar *et al.* where they use the RAFT R group approach. Their findings include the dependence of termination on the concentration of linear chains that can lead to nonstar MWDs and, in turn, the broad MWDs observed using the R-group approach.[84] Recently, Corrigan and Boyer[101] proposed a mathematical predictive model to blend molecular weight distributions using moments to obtain statistical parameters that describe the shape. In addition, they proposed a data storage method to encode and decode polymer blends using the American Standard Code for Information Interchange (ASCII).[101]

Mathematical Equations Mechanistic knowledge of what happens in polymerisations can enable the development of mathematical models to predict the outcomes in reaction kinetics. Assumptions based on ideality can enable mass balance Equations to be simplified; removing computational cost and providing a synthetic chemist without any coding experience with a means to predict chemical outcomes. Monomer conversion is often given as the change in monomer concentration over time if we assume that all monomers are converted to polymeric species. Wang *et al.*[102] implemented the steady-state hypothesis to solve the equations for chain species analytically, assuming that all chains behave in the same way regardless of their size. Here, they compared the analytical equation with the equivalent numerically solved moments and found good concordance between the two models as shown in Figure 1.14.[102]

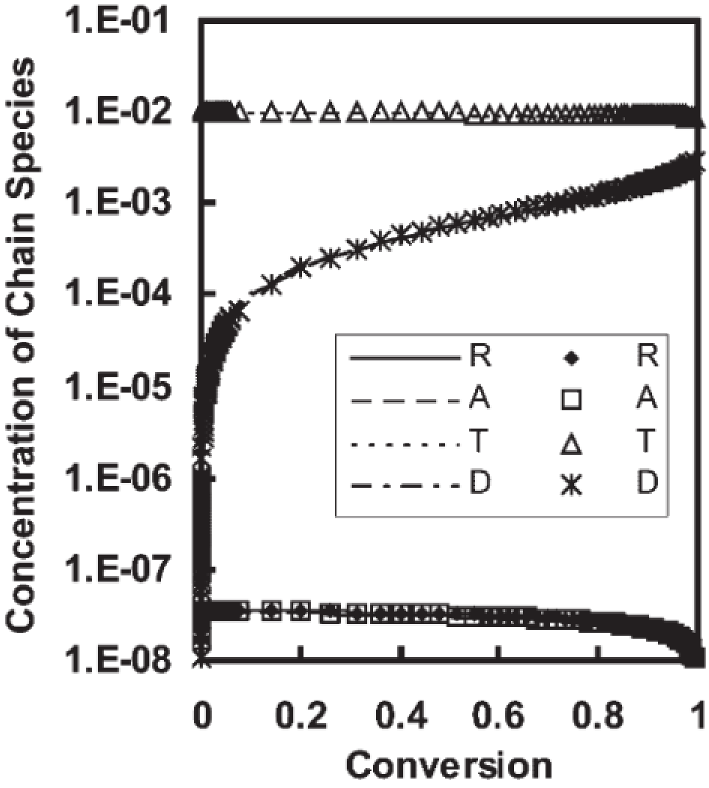

Figure 1.14: Comparison of chain species concentration with increasing concentration solved analytically (lines) and numerically (symbols). Here 4 chain species are modelled, propagating chains (R), radical adduct intermediate (A), chain transfer species (T) and dead chains (D).[102] Reproduced from Wang *et al.*[102] with permission from Wiley and Sons. Copyright ©2003

Table 1.1: Existing models for mass dispersity for ATRP and NMP. Here, k_{act}, k_{deact}, k_p and k_t are the rate constants for activation, deactivation (ATRP and NMP), propagation and termination Initial concentrations of the radical generating species ($[P_nX]_0$) , monomer ($[M]_0$) and catalyst species ($[C]_0$ and $[XC]_0$). Conversion is denoted as (α)

RDRP	**Quantitative Equation**	
ATRP[103]	$Đ = 1 + \frac{[P_nX]_0}{[M]_0\alpha} + \frac{k_{act}[P_nX]}{k_{deact}[XC]}\left(\frac{2}{\alpha} - 1\right) + \frac{k_t k_{act}[C]_0}{4k_p k_{deact}[XC]_0}\alpha$	$[XC]_0 \neq 0$
NMP[104]	$Đ = 1 + \frac{[P_nX]_0}{[M]_0\alpha} + \frac{k_{act}[P_nX]}{k_{deact}[X\bullet]}\left(\frac{2}{\alpha} - 1\right) + \frac{k_t k_{act}}{4k_p k_{deact}[X\bullet]}\alpha$	$[X\bullet] \neq 0$

Equilibria in many types of controlled polymerisations, where the rate of exchange as a function of conversion causes broadening of the MWD, a phenomenon theoretically explained by Figini[105,106] and Coleman *et al.*.[107] Explicit quantitative models for dispersity are attractive due to the ease of use and redundancy of expensive software or high-performance PCs. Zhu and co-workers, derived dispersity as a composite equation for RDRP comprising a living step, transfer steps and terminative steps[108] Currently, only complete equations have been derived for normal ATRP[103] and NMP[104] have been derived (Table. 1.1) by employing blend and block theory. Blend and block theory is a strategy in which chain growth and termination is discretised by time interval. For ATRP and NMP, activation/deactivation effects dominate during the initial stages of polymerisation, where chains are relatively short, but it is commonly speculated that terminative events become more significant during the later stages, where polymer chains are much longer.[109–111] Work simulating molecular weight distributions for living anionic,[112] ATRP,[103] RAFT[113] and cationic polymerisations[109] based on the first 3 terms of the dispersity equation that exist in the literature have been fitted to the experimental data to provide information about the control.[110] Terminative events are quantified in the final term of both equations for ATRP and NMP and manifest in an increase in $Đ$.[114]

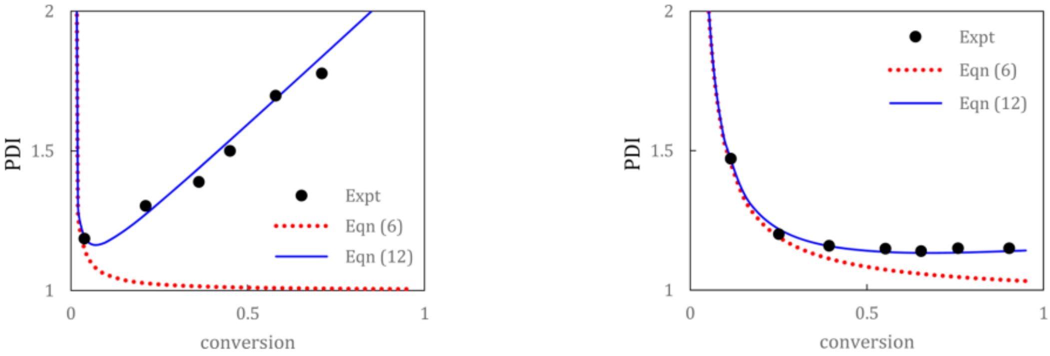

Figure 1.15: (left) validation of the dispersity Equation for the ATRP by Mastan *et al.*[103] of HEMA in DMF at room temperature using experimental data from Beers *et al.*[115] and (right) MMA in anisole at 90 ° C with validation using experimental data from Gromada.[116] Reproduced from Mastan *et al.*[103] with permission from Americal Chemical Society, Copyright ©2015.

Mastan *et al.*[103] have validated their quantitative equation for dispersity using experimental data from the literature and showed that the equation predicts the minima and accounts for the terminative events well for the polymerisation of HEMA and MMA by ATRP, shown in Figure 1.15.[103]

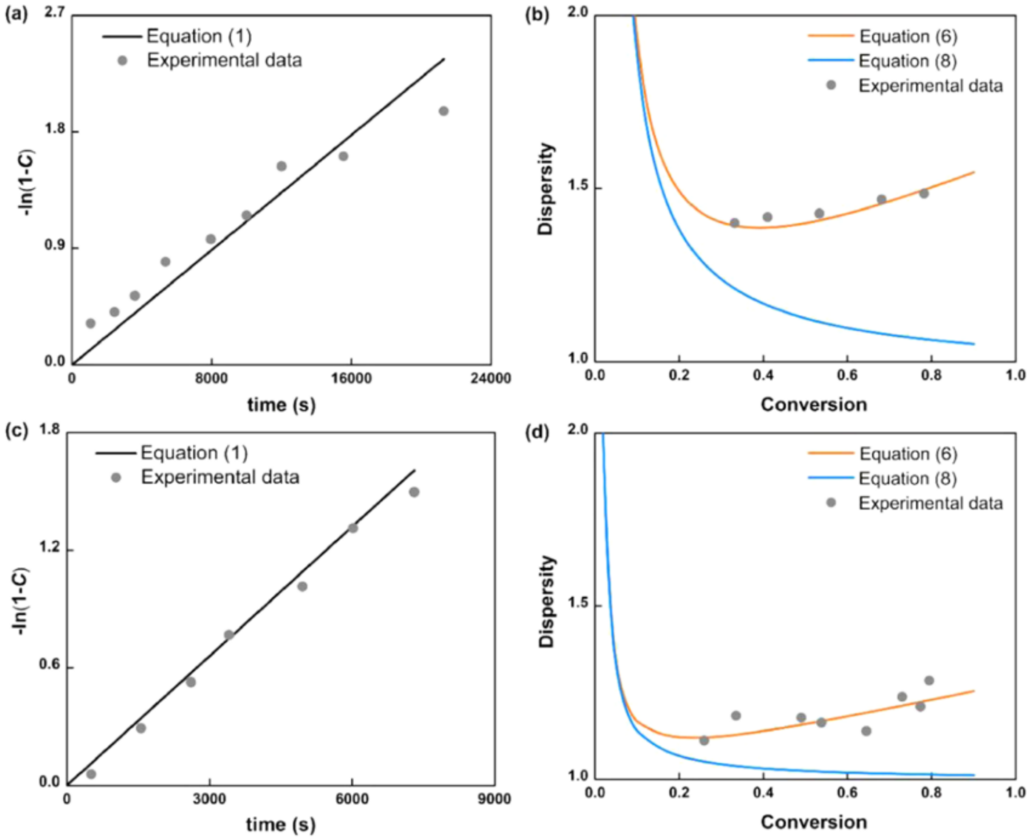

Figure 1.16: (a,b) validation of the dispersity Equation for the NMP by Wang *et al.*[104] of DEAmin and (c,d) HEA. Reproduced from Wang *et al.*[104] with permission by the Americal Chemical Society, Copyright ©2020.

Wang *et al.*[104] demonstrated that for first-order NMP, their model was also validated, as shown in Figure 1.16. Here, they proposed 2 models: (1) a first-order kinetic approach - as in Mastan *et al.* and (2) a power law approach. They also provided an Excel spreadsheet to calculate the molecular weight distribution using this dispersity value.[104]

In this section, a variety of polymerisation techniques, process conditions, and modelling techniques have been discussed. In the context of this thesis, RAFT polymerisation has been used due to the plethora of monomers that could be accessed through compatible chain-transfer agents. In addition, a place in the literature for an equation of dispersity as a function of conversion accounting for terminative events has been identified.

1.2 Flow Chemistry

1.2.1 Reactors

Traditionally, chemical synthesis is conducted in round bottom quick-fit flasks, and an ideal batch reactor model can be applied to characterise performance on a small scale. Reactor geometries that use continuous flow have piqued interest in the last century, offering better control over reaction conditions. Continuous flow can afford a plethora of advantages: the high surface area-to-volume ratio provides efficient heat transfer/light absorption and mixing, and the reduced volume can improve safety.[117] Typically, tubular reactors constructed from stainless steel or polymeric materials (PFA or PEEK) are used; which is often the least expensive option. Alternatively, continuous stirred tank reactors (CSTR) provide a hybrid of continuous-flow and batch-type platforms.[117] Tubular flow reactors are categorised according to channel size mesofluidic (0.5-5mm) or microfluidic (0.01-0.5 mm).[118] Unlike batch production where the reaction composition changes over time, C_t, continuous flow reactors must reach a steady state where the composition does not change; this may take several reactor volumes to stabilise, schematics of reactors and their compositional changes is shown in Figure 1.17. In flow, residence time is used to describe the time a molecule experiences in the reactor; this depends on the flow rate, viscosity, vessel dimensions, and whether the stream is homogeneous in phase.[117,119]

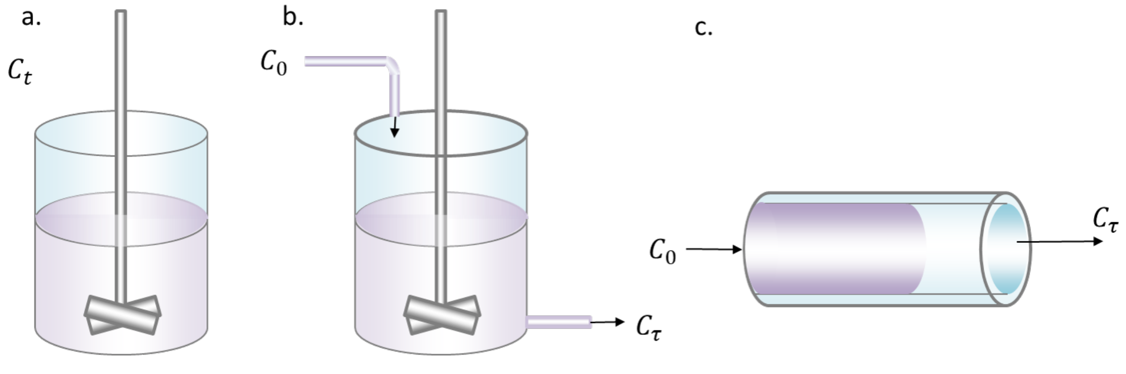

Figure 1.17: Comparison of the compositional change of a reaction in (a) a batch reactor, (b) continuous stirrer tank reactor (CSTR) and (c) a tubular flow reactor.

The velocity profile of a fluid passing through a tubular reactor can be perturbed due to molecular and turbulent diffusion - this is called dispersion and leads to a distribution in the residence times. The effect of dispersion can be characterised by the dimensionless Bodenstein number,

B_O which is calculated by Equation 1.16.[120]

$$B_O = \frac{uL}{D_{ax}} \tag{1.16}$$

Here, u is the flowrate, L is the length of the channel and D_{ax} is the axial dispersion coefficient. A B_O value greater than 100 suggests dispersion is low and if it is greater 1000, ideal plug flow is achieved. B_O less than 100 indicated deviation from the dispersion model and the convective model may be more appropriate.[120,121] Residence time distributions can be used to characterise the performance of a flow reactor (e.g. dead zones), relevant flow regime and mixing information. Typical experiments involve pulsed injection of a tracer into the reactor and timing how long it takes to be detected. The C-curve is a term used to describe change in concentration of the effluent tracer. The residence time distribution function, E(t), describes how long molecules have spent in a reactor in a certain time interval, which can be found by dividing the concentration of each discrete time from the C-curve by the area under the curve and is given by 1.17.[122]

$$E(t) = \frac{C(t)}{\int_0^\infty C(t)dt} \tag{1.17}$$

The first moment gives the mean residence time (τ) or 1.18

$$\tau = \int_0^\infty tE(t)dt \tag{1.18}$$

The second moment is used to describe the variance about E(t) described by 1.18

$$\sigma^2 = \int_0^\infty (t - t_m)^2 E(t)dt \tag{1.19}$$

To compare reactors of different sizes, a dimensionless RTD is required, these are typically described by 1.20 and 1.21.

$$\theta = \frac{t}{\tau} \tag{1.20}$$

$$E(\theta) = \tau E(t) \tag{1.21}$$

The residence time distribution has been shown to be largely affected by the internal diameter, the mean residence time, and the use of static mixing. Gobert *et al.* conducted extensive reactor characterisation, demonstrating the effect of these variables on RTD using dispersion and convective models.

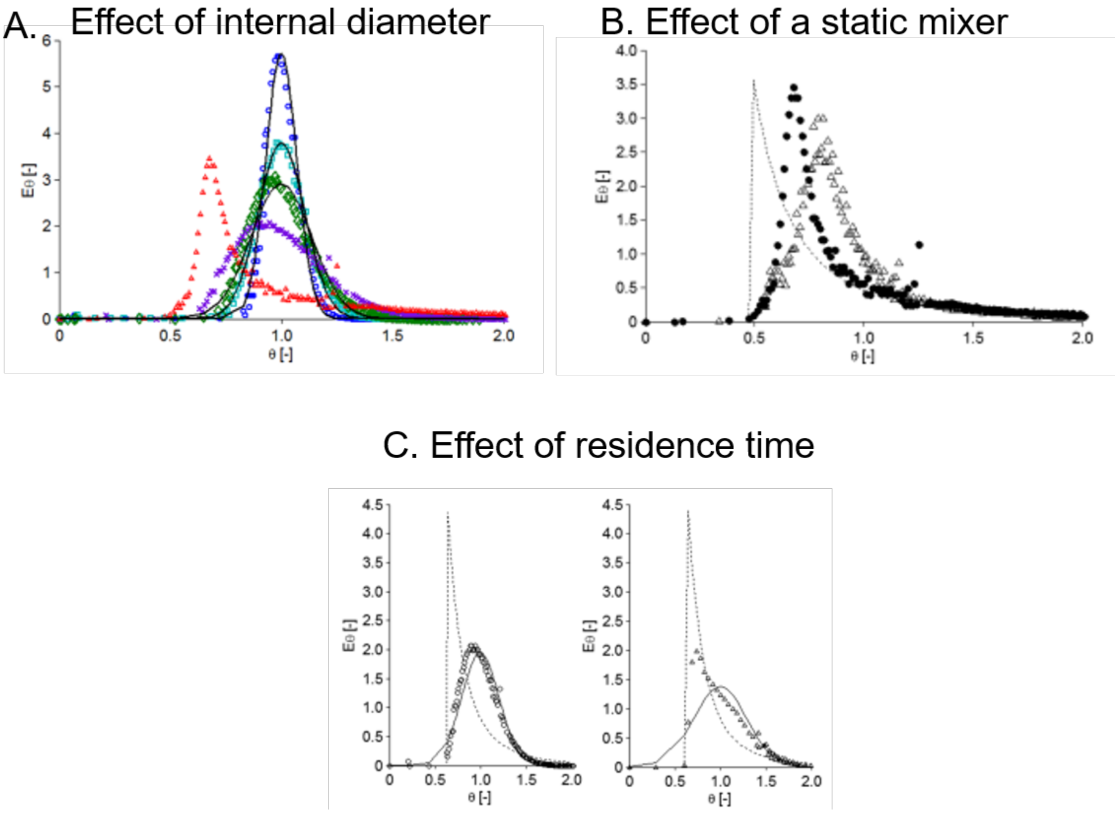

Figure 1.18: Demonstration by Gobert *et al.* of the effect of (A) tubing diameter using tubing diameters of 0.4 circle, 0.7 (square), 1.6 (diamond), 2.4 (cross) and 4.8 (triangles) mm on the RTD modelled using dispersion (line). (B) the effect of static mixing (triangles) on RTD compared to without static mixing (filled circle) using the convective model(dashed line) and (C) The effect of mean residence time 56 s (circle) and 14 s (triangle) on RTD using both dispersion (solid line) and convective models (dashed line).[123] Adapted from Gobert *et al.*[121] with permission from the American Chemical Society, copyright ©2017.

Gobert *et al.*[121] showed that the RTD broadens and asymmetry increases as the diameter increases. They also reported the invalidity of the dispersion model for tubing diameters greater than 2.4 mm - this can be observed in Figure 1.18 by the asymmetry in the triangle and cross data. In addition, the larger diameter tubing was also investigated to see the effect of a commercially available static mixer placed directly after a y mixer where they reported a slight shift in the peak towards 1 and a slight narrowing. Furthermore, they reported that shorter residence times lead to more convective behaviour whereas longer residence times are more consistent with the dispersion model.[121]

1.2.2 Flow Regimes

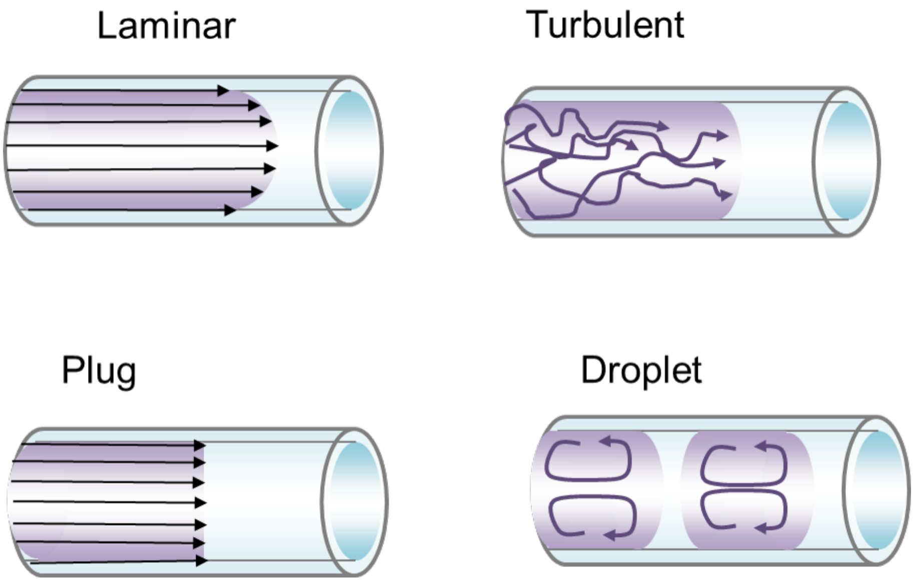

Figure 1.19: Schematic of flow patterns for laminar, turbulent, plug and droplet flow

Flow regime is highly dependent on the phase of the components in the channel. A single velocity is unachievable for many reactions. For liquid-liquid mixtures there are several possible flow regimes that can occur - laminar and turbulent are the most common and can be predicted based upon the Reynolds Number. Reynolds' number is dependent on flow-rate, viscosity, channel diameter, Laminar flow regimes occur when the longitudinal flow is not obstructed by parallel phases. Low flow-rates, viscous liquids and large diameter channels can facilitate laminar flow ($R_e < 2040$). In gas-liquid systems the gas phase can form bubbles, plugs or annular flow as the flow-rate of the gas is increased, in larger diameter reactors slug flow is more likely due to the increase in pressure behind the liquid phase causing a droplet to form from the liquid phase. Inert gases may be introduced into liquid phase reactions, to induce droplet flow and improve mixing.[117] A schematic representation of the flow regimes is observed in Figure 1.19.

1.2.3 Mixing

Mixing is considered a diffusion process. Segregation of flow regimes is typically seen in batch reactors with the extent of segregation being reduced with decreased vessel size. However, the flow regime is never uniform. Turbulent flow exists closer to the stirrer bar whereas laminar flow may be experienced closer to the walls of the vessels.[117] Due to the high surface area to volume ratio, in a tubular reactors the diffusion path is reduced which can increase mixing. Damkohlers number, (Da) can be used to approximate the ratio of reaction rate to the rate of mass transport. For an n^{th} order reaction: reaction rate (k), initial concentration (C_0^{n-1}), diameter of tubing (d_t) and diffusion coefficient (D) the value for Da can be given by Equation 1.22. For rapid reactions where the rate of diffusion is less than the rate of reaction; additional pre-mixing may be required.[120,124]

$$Da = \frac{kC_0^{n-1}d_t^2}{4D} \tag{1.22}$$

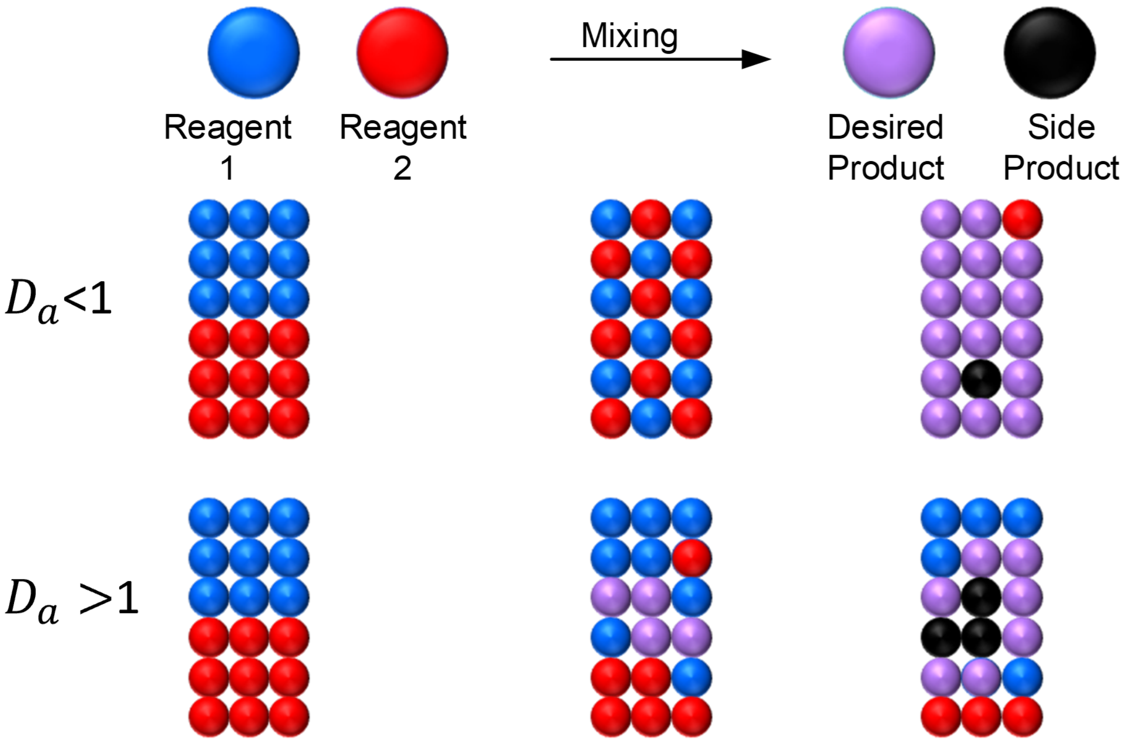

Figure 1.20: Schematic depiction of uniform mixing compared to non-uniform mixing in flow where the Da value is less than 1 and greater than 1, respectively. For the case of non-uniform mixing, localised variation in concentration of each reagent can lead to increased concentration of side-product

If the rate of diffusion is greater than the rate of reaction leading to more of the desired product, then the Da number will be less than 1, shown in Figure 1.20. If the rate of diffusion is less than the rate of reaction then the reaction mixture will have localised variation of reagents so Da will be greater than 1.

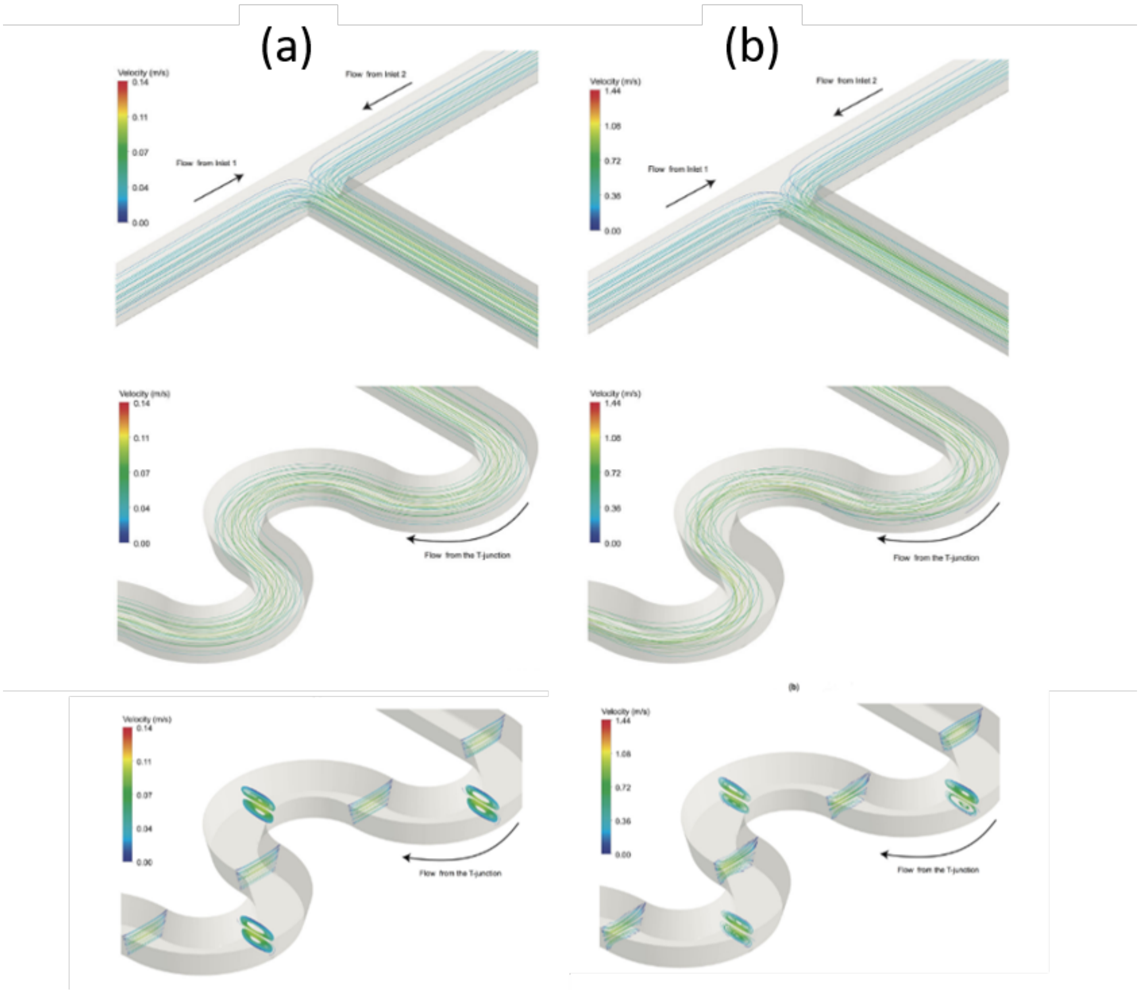

Figure 1.21: CFD simulated data showing the effect of velocity at (a) 25 and (b)250 μL/min on the mixing immediately after the T junction (top), in the curved mixing sections (middle) and secondary flow in the curved mixing section (bottom). Adapted from Peres *et al.*[125] with permission from Wiley and Sons, copyright ©2019.

Computational fluid dynamics can enable visualisation of what is happening inside the tube or channel - this is especially useful for visualising the mixing within the reactor. Peres *et al.*[125] demonstrated the mixing efficiency in a serpentine microfluidic device for the synthesis of nanocrystals using CFD and experimental data. Parallel flow is shown immediately after the two streams interaction in Figure 1.21.a at the lower velocity stream even at points in the tube which may experience more centrifugal forces such as at curved regions. A more disordered flow is shown in Figure 1.21.b. at higher flow-rates. For the secondary flow CFDs, the fluid flows are effected by the inertial effect causing fluid to flow towards the wall. Dean Vortices are also reported to be experienced in the tube as a result of the combination of centripetal and centrifugal forces as shown in the bottom section of Figure 1.21.[125]

1.2.4 Heat Transfer

Heat transfer describes the transfer of thermal energy in a system. In traditional batch glassware the heat has to travel through the glass and reaction solution, where it has dissipated significantly by the time it reaches the centre. Flow reactors afford improved heat transfer leading to precise thermal control; due to the large surface area to volume ratio. Enhanced control over temperature in tubular flow reactors can provide a safer reactor geometry for exothermic reactions, and offer better selectivity..[117,124] Heat transfer for exothermic reactions is dependent on a range of factors: rate of heat generated from the reaction($-r\Delta H_{rxn}$), rate of heat removed from the reactor wall to surroundings, the heat of reaction(ΔH_{rxn}), adiabatic temperature rise ($\Delta \mathrm{T}_{ad}$), dimensions (d_f) and thermal conductivity of the reaction mixture (κ). This can be simplified to the ratio of heat generated to the heat removed. Furthermore, the ratio can given as, β_B.[126]

$$\beta_B = \frac{-r\Delta H_{rxn} d_F^2}{4\Delta T_{ad}\kappa} \tag{1.23}$$

1.2.5 Safety and Scale-up

Risk is often written as a function of the hazard, exposure and vulnerability.[127] Performing chemical reactions in laboratory-scale flow reactors has become of high interest to industry due to inherent safety aspects.[128] Improved knowledge of chemical interactions and hazards has allowed a range of tailored reaction vessels (such as thin walls) compared to early examples. As mentioned above, flow reactors can facilitate the dissipation of heat arising from exothermic reactions, providing better control than in batch. Continuous flow operation can reduce the amounts of hazardous reagents (e.g., explosives) used because of the low inventory. In some cases, hazardous intermediates generated in a reaction are consumed in the reactor. Kappe and co-workers have successfully demonstrated a reactor that can produce diazomethane, a highly sensitive and explosive gas - ($CH_2\mathrm{N}_2$) in-situ which then undergoes downstream methylations..[129,130] Extreme temperatures and pressures can be used to accelerate reactions; high temperature and pressure are difficult to achieve safely in standard glassware. Back pressure regulators are often used in flow to exceed the boiling points of solvents, such as in the synthesis of a 1,2,3-triazole precursor of Rufinamide where a Huisgen cycloaddition was carried out at 210 °C and 69 bar. From the HPLC yields they identified an optimal temperature of 210 °C after a 10 min residence time. Here, reactor fouling was successfully avoided by operating at temperatures higher than

Rufinamide's melting point.[131]

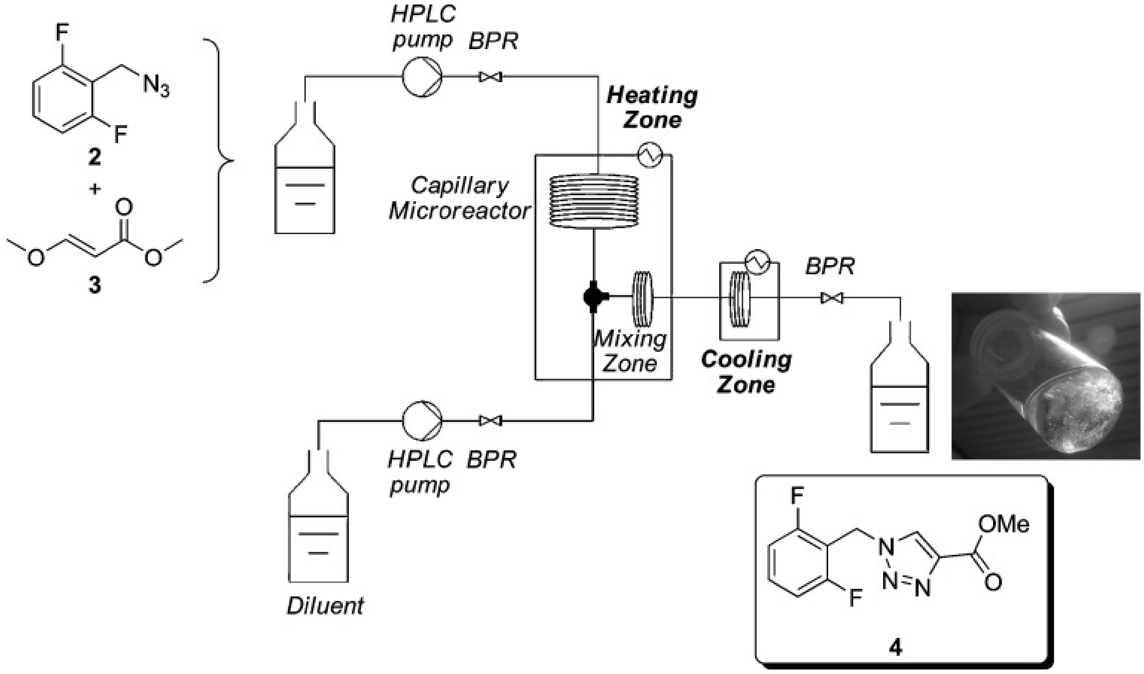

Figure 1.22: Example of the use of backpressure regulators to enable extreme temperatures to produce a precursor of Rufinamide Reproduced from Borukhova *et al.*[131] with permission from Wiley and Sons, copyright ©2013.

Scale-up enables increased productivity which is desirable in industry. For batch synthesis, scaling up can be challenging due to mixing, heat transfer, and safety considerations. Flow has its own scale-up issues; however, the chemistry may not permit scale-up as a result of RTD. Competitive productivity is hard to achieve in microscale flow reactors, even when the system is scaled out. Typically, to scale up microscale flow, the internal volume of the reactor is increased to milliscale while maintaining the diameter of the channels..[132] Numbering up reactors can often be the viable option for reactions that require narrow channels (e.g. photochemical reactions). Noel and co-workers developed a single chip reactor (Figure. 1.23) that divides the reaction stream into 8 channels enabling parallel synthesis. This chip was used for the photooxidation of 9,10-diphenyl anthracene, and they reported superior flow partitioning even in chips with up to 32 channels. In addition, they reported that the photochemically driven reaction conversion consistent with a single-channel chip was also observed.[133]

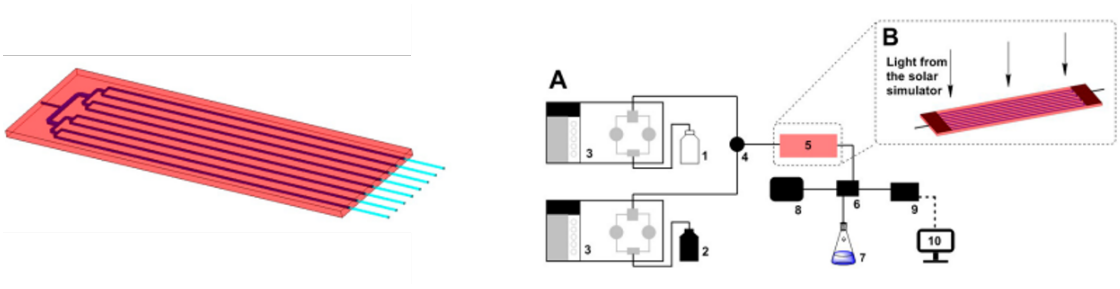

Figure 1.23: Numbered up chip reactor for photochemical flow reactions. Adapted from Zhao *et al.*[133] with permission from The American chemical society, under Creative Commons, copyright ©2017

1.2.6 Automation and Online-Monitoring

The first automated reactor can be traced back to 1966, where the stepwise synthesis of peptides was performed autonomously.[134] Advances in computation have afforded sophisticated platforms controlled by desktop PCs whereby pumps, thermal controllers/light sources, analytical equipment and data management are controlled in programmes such as LabVIEW,[135–137] MATLAB[138,139] or Python.[140,141] Where custom software may be inaccessible, Vaportec offers a commercially available flow reactor that allows for the precision scale-up of flow systems with condition monitoring (e.g., pressure) which has been used for many reactions.[142,143] Gilmore *et al.*[142] reported the use of a Vapourtec R-2 + model to continuously synthesise artemisinin-derived drug molecules using a modular approach. Their findings report 4 antimalarial APIs autonomously synthesised with modular transformation and continuous purification. Through incorporation of specialised flow cells and sampling, inline analytical techniques have enabled chemists to monitor conversion, yields, selectivity, impurity, pressure, and temperatures without the error related to taking samples for offline analysis. A plethora of in-line/on-line analytical techniques have been developed. Jensen and co-workers implemented a commercially available HPLC to analyse the yield from a Heck-type coupling.[144] Subsequently, they used optimised reaction conditions to scale up the reactor 50-fold. Process analytical techniques can be categorised into: offline, at-line and, online. Offline is traditional analytical techniques where the user will prepare the sample and then take it to the analytical equipment, At-line is similar except that the person is replaced with a sampling valve which takes a sample and sends it to the equipment. Online monitoring occurs when the sensor is placed in or on the reaction solution without user intervention. On-line FTIR was used to monitor conversion in a condensation synthesis of pyrazole, allylation and reduction-crotonation synthesised in flow by Ley and co-workers;[145] later Jensen and co-workers demonstrated the use of FTIR to monitor reaction yields of a Paal-Knorr reaction.[146] Online UV-Vis has been used to monitor nucleophilic substitutions and Aza-Diels Alder.[147,148] Benchtop NMR has been integrated into flow platforms for monitoring of oxidation and cyclopropanation.[149]

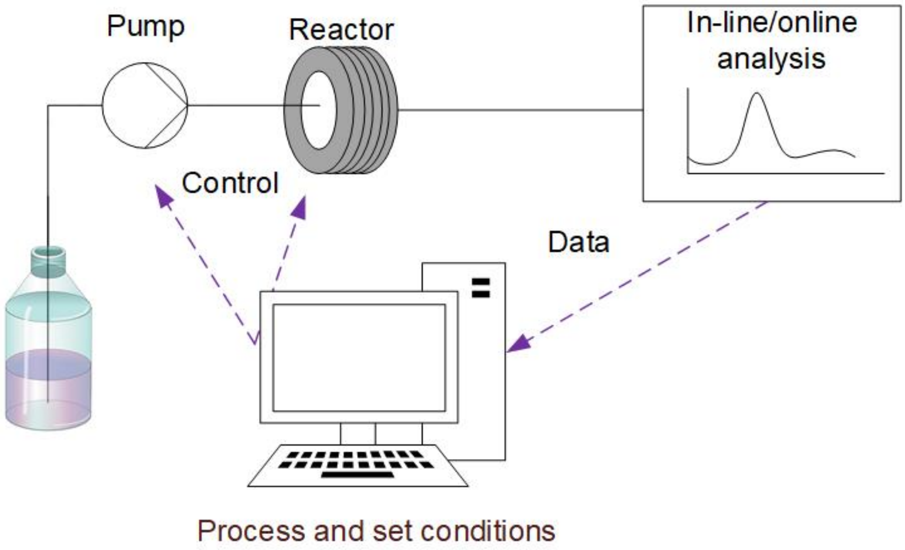

Figure 1.24: Schematic of an autonomous flow reactor with in-line/online analysis.

In this section, the challenges and benefits of conducting reactions in flow have been discussed. The high surface area-to-volume ratio leads to improved heat transfer, which can lead to faster kinetics. Mixing is typically improved for flow if the reaction kinetics are slower than the rate of mixing by diffusion; however, for rapid reactions, this is reduced. In this thesis, mixing is an important consideration due to the rapid nature of radical polymerisations which was investigated in Chapter 3. Challenges associated with the change in viscosity were investigated in the context of this thesis, and this knowledge was subsequently used to account for flow effects in the development of the RAFT model.

1.3 Optimisation of Chemical Systems

Traditional optimisation uses the one-variable at a time (OVAT) approach, which involves the systematic changing of a reaction condition, conducting analysis, and then deciding where to try next. OVAT is often time consuming, inefficient, and the likelihood of getting to the optima is low as it is unable to separate experimental noise (variation between repeats of the same experiment).[150]

1.3.1 Local Optimisation

Design of experiments (DoE) is a model-based statistical approach to optimisation that can allow multiple variables to be changed at a time and also gives the operator an idea of the direction the objective is moving in reaction parameter space. The objective(outputs), each variable, and the boundaries need to be defined. For example, a 3 variable (factor) DoE with 2 values (high and low limits) for each factor will have 8 trial experiments(at each vertice of reaction parameter space). The data from these experiments can have a response surface model that can be fitted[150,151] Some mechanistic knowledge is required for weighting variables.

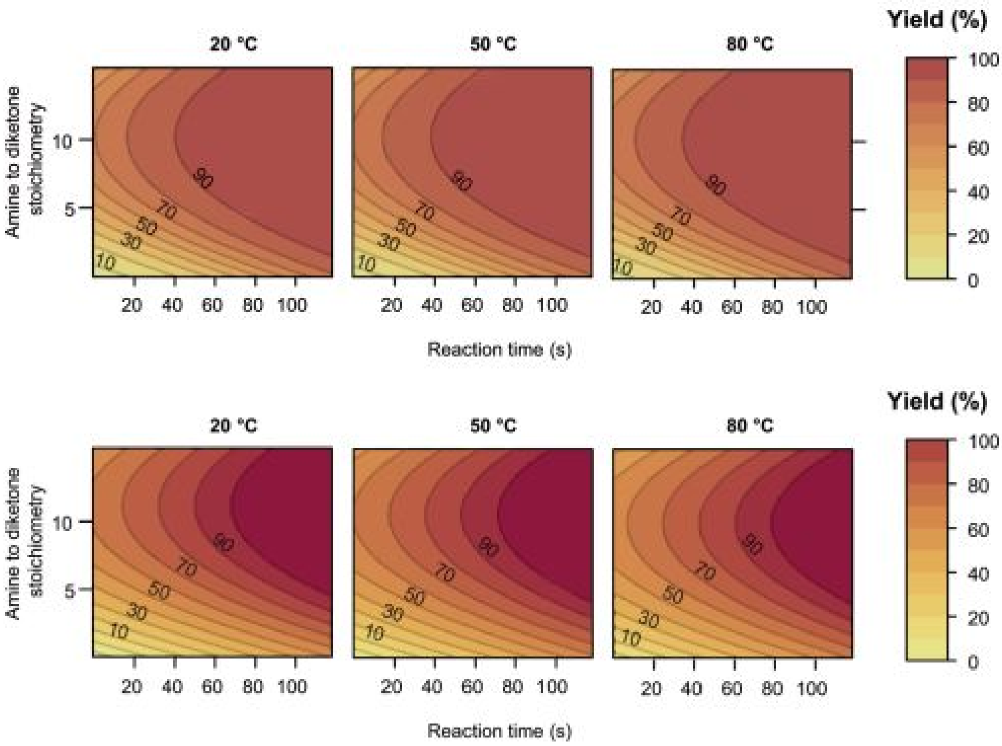

Figure 1.25: Optimisation of yield by DoE demonstrated by Rutjes and co-workers for a Paal-Knorr cyclocondensation of 2 ethanoamine 2 (top) and ethylamine 3 (bottom) reaction. Reproduced from Nieuwland *et al.*[152] with permission from the American Chemical Society, Copyright ©2011

Rutjes and co-workers optimised a Paal-Knorr cyclocondensation for yield via GCFID varying the stoichiometry of the amine to diketone, residence time, and temperature in a microreactor. The resultant surface plots are shown in Figure 1.25 They conducted this for 2 amines. A polynomial was fit to the data. The findings identify optimal conditions for the ethanolamine substrate as 20 ° C after 100 s with an amine:diketone ratio of 5; whereas, if an ethylamine is used the amine:diketone ratio must be doubled.[152]

Simplex algorithms such as Nelder Mead Simplex (NMSIM), where n is the number of variables a convex polyhedron can be made of n+1 vertices. The worst vertex is removed, and a geometric transformation selects the next conditions. The transformations can include; multiple contractions, inside and outside contractions, reflection and expansion. There are many examples of simplex being used in the literature. Cronin and co-workers used a modified NMSIM coupled to a fitting function to optimise 2 variables (composition and residence time) and 1H in-line NMR to obtain yield for an imine synthesis.[153] Another example of local optimisation is the steepest decent method, this is a gradient based method where a 2^k orthogonal design or central composite design (DoE) is initialised. A response surface is mapped, which then allows for the calculation of a gradient. Conditions along the gradient are conducted until a poor response is observed, indicating that the optimum has been surpassed.

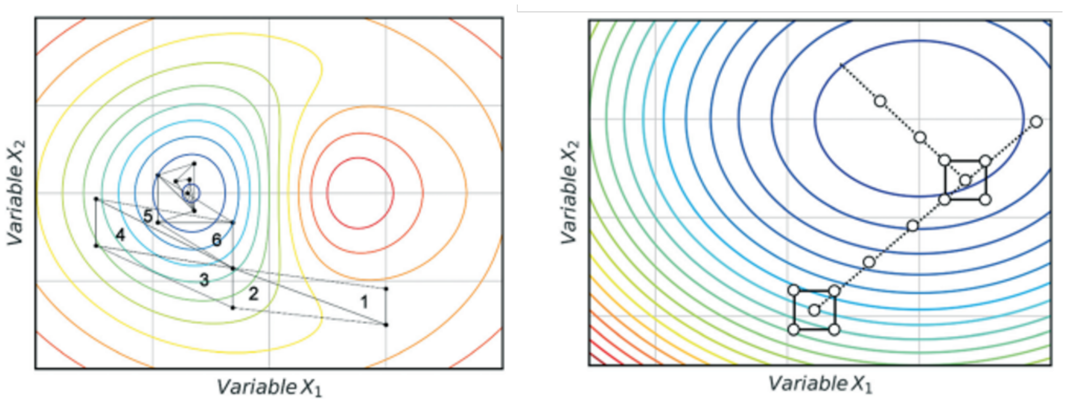

Figure 1.26: (left) Demonstration of convergence in a simplex algorithm overlayed onto a response surface showing maxima (red) and minima (blue) where the simplex algorithm converges to a minimum. (right) Steepest descent method with an initial point and 2^k orthogonal design. Reproduced from Clayton *et al.*[154] with permission from the Royal Society of Chemistry. Copyright ©2019.

The advantages of local optimisation is rapid convergence to an optima; however, it operates on the assumption that there is only a single optimum. Local optimisation algorithms also neglect the effect of experimental noise, which can delay the algorithm's evaluation.

1.3.2 Global Optimisation

Stable Noisy Optimisation by Branch and Fit (SNOBFIT) is a popular local single-objective optimisation algorithm that can effectively tackle the problem of noise. The algorithm takes the input data and generates a surrogate model.[154] Unlike the gradient-based simplex approaches, SNOBFIT does not require explicit gradients to be defined; rather, they are approximated by the surrogate model. SNOBFIT searches different subregions in parallel through identifying local points. Cheaper models are fit to the function, which allows the quality of the model to be quantified and the noise to be reduced. An initial space filling design may be incorporated to ensure that the surrogate model is representative. SNOBFIT classifies into: (1) a point that minimises the local quadratic about (x_{best}), (2) estimated local minimising points, (3) estimated global minimisers, (4) possible points of interest and (5) random points.

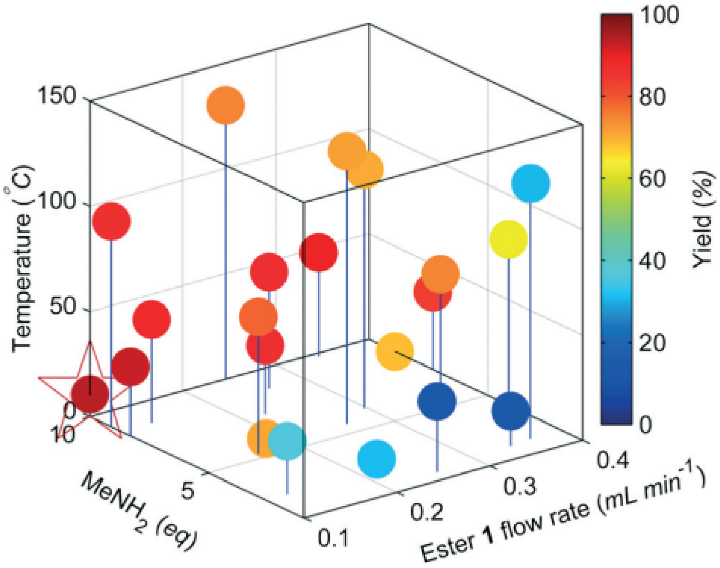

Figure 1.27: SNOBFIT optimisation of N-methyl nicotinamide with the highest conversion being the darkest red circle highlighted with a star. Reproduced from Holmes *et al.*[155] with permission from Royal Society of Chemistry. Copyright ©2015.

SNOBFIT[138,155,156] has been used in a variety of reactions; an example is its use in closed-loop optimisation of the synthesis of N-methyl nicotinamide, where the optimisation objective is yield (obtained by mass spectrometry). Here, the authors varied relative concentrations of the reagent and the temperature of reaction and reported higher yields were obtained at higher concentrations of amine, low temperatures, and slow flow rates. The optimum is identified at an ester flow rate of 0.1 mL/min using 10 eq of $MeNH_2$ at 10.6 °C, which is shown in Figure 1.27[155]

When two or more conflicting objectives are being considered; a more suitable optimisation algorithm considers both objectives at the same time. A set of solutions is typically identified for a multiobjective optimisation algorithm. This set of solutions is defined as the Pareto front, where there can be no effect of one objective without having a detrimental effect on the other. Bayesian optimisation is a popular type of multiobjective optimisation, these do not require *a* *priori* knowledge to evaluate. Bayesian optimisation works by fitting a Gaussian process (GP) to a set of data. The GP treats variables as having a normal (Gaussian) distribution with a mean and a covariance function. The covariance function enables noise to be considered, whilst the mean function indicates the expected solution. GPs provide a computationally inexpensive and stochastic method of evaluating the objective function, the GP is sampled and further exploration along the GP allows better fitting.[157] An acquisition function is used to find the probability of an optima, which is designed to explore and exploit chemical space.

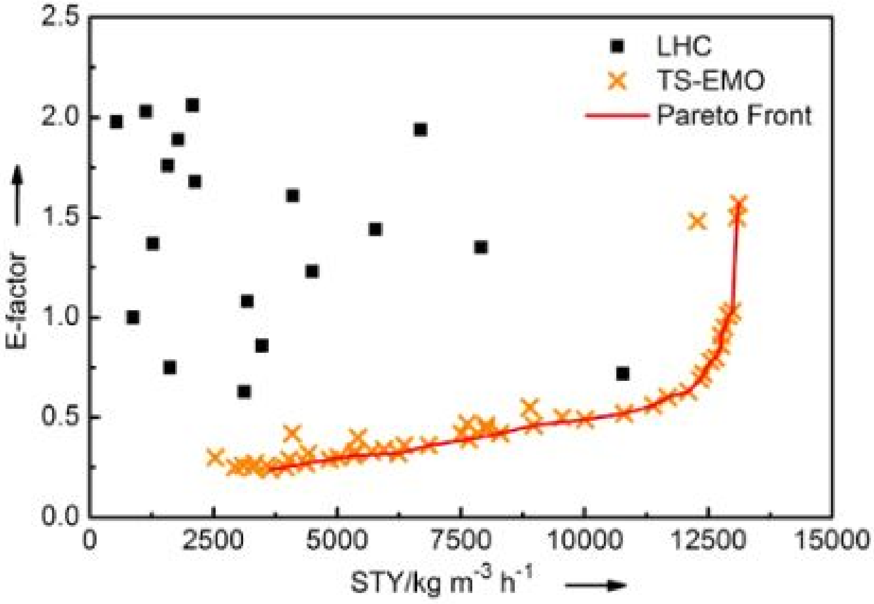

Figure 1.28: Demonstration of the TSEMO algorithm finding the Pareto front for space time yield (STY) and E-Factor. Black squares represent the initial training experiments and the crosses are the solutions to the TSEMO generated conditions Reproduced from Schweidtmann *et. al.*[158] with permission from Elsevier Chemical Engineering under Creative Commons. Copyright ©1969.

Comparisons of different types of Bayesian optimisation have been conducted comparing algorithms such as Thompson sampling efficient multiobjective optimisation (TS-EMO),[158] Pareto efficient global optimisation (ParEGO),[159] expected hypervolume improvement (EHI),[160] non-sorting genetic algorithm II (NSGA-II)[161] with TS-EMO outperforming the latter.[158,162] TS-EMO has been used to optimise three conflicting objectives for a Claisen-Schmidt condensation reaction. Here Clayton *et. al*[163] identify the trade-off in 65 h by automating what would typically take 6 optimisations over weeks, allowing high-throughput optimisation[163] Another example where a multi-objective optimisation algorithm was used is a multi-objective active learner (MOAL) was applied to a complex, expensive-to-evaluate nanoparticle platform optimising 14 variables for 2 objectives.[135] Prior to the work addressed in this thesis, TS-EMO has not been applied to polymerisation. Multi-objective optimisation algorithms have also been applied to discrete variable systems. Mixed-variable multi-objective optimisation (MVMOO),[164] was demonstrated for a nucleophilic aromatic substitution reaction changing the solvent, the selection of the ligand on the regioselectivity of the product. Here, the polarity of the solvent was identified as a significant variable in the reaction of amines and 2,4-nitrobenzene. The phosphine ligand that experienced the least steric hindrance was also found to perform best despite a contrasting understanding.[165]

As previously discussed in the polymerisation section, dispersity is a quantitative measurement of the control over the polymerisation that can often increase as the monomer is converted into polymer chains. This results in a trade-off in dispersity and conversion; therefore, this is an ideal candidate for Bayesian optimisation therefore these were selected as optimisation objectives in this thesis.

1.4 Polymerisation in Flow

Seminal work on flow polymerisation can be traced back to the 1950s. In 1953 Melville and co-workers demonstrated the use of glass flow reactors for photoinitiated block copolymer synthesis.[166] Flow chemistry also enabled M. Swarc *et al.*[167] to investigate the kinetics of a rapid "living" anionic polymerisation of styrene in THF. Meira *et al.*[168] suggested that the varied addition of monomer and initiator in a living anionic polymerisation using continuous flow can enable control over MWDs. Over the past century, the benefits provided to polymerisation by flow chemistry have been appreciated. Safety improvements attributed to flow have enabled polymerisations in which stringent conditions (i.e., in living anionic polymerisation) are required to be performed in flow.[169,170]

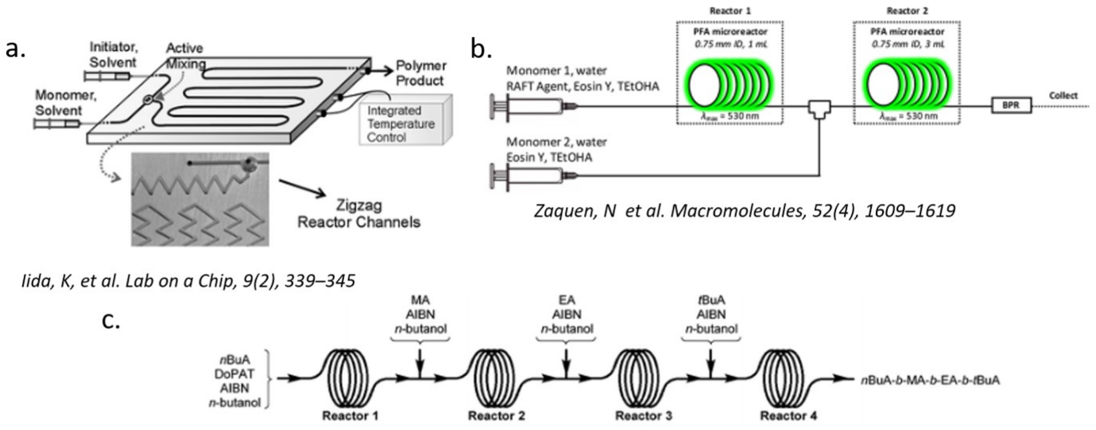

Iida, K, et al. Lab on a Chip, 9(2), 339–345

Zaquen, N et al. Macromolecules, 52(4), 1609–1619

Baeten, E, et al. Polymer Chemistry, 8(25), 3815–3824

Figure 1.29: (a) Living anionic polymerisation flow platform using microfluidics with different geometry channels to polymerise styrene.[170] Adapted from by Iida *et al.* with permission from The Royal Society of Chemistry, copyright ©2009. (b) Oxygen-tolerant PET-RAFT platform for (homo)polymers and blockcopolymer synthesis Adapted from Zaquen *et al.*[171] with permission by American Chemical Society, copyright ©2019. (c) Telescoped multi-block copolymerisation platform demonstrated Adapted from Baeten *et al.*[172] with permission from The Royal Society of Chemistry, copyright ©2017

.

Iida *et al.* used microfluidic devices to conduct anionic polymerisation of styrene in cyclohexane at elevated temperatures and monomer concentration; otherwise, this would lead to dangerous pressure buildup in batches (shown in Figure 1.29).[170] The thermal transfer advantages of flow make it a great tool for thermally initiated polymerisation. Radical polymerisations are typically exothermic, which can cause loss of control; here, flow chemistry can enable efficient dissipation of this exotherm. In the 00s/early 10s ATRP,[173–176] NMP,[177,178] FRP[179,180] and anionic[14] and cationic polymerisations.[181] The functional group tolerance of RAFT makes it attractive for polymer discovery platforms. Diehl *et al.* compared the effect of different diameters of tubing to batch on the RAFT polymerisation of NIPAM,[182] while Hornung and co-workers expanded on this by looking at other combinations of monomer / RAFT agent / initiator, as well as comparing PFA and stainless steel tubular reactors and the synthesis of block copolymers. They found that conversions obtained using batch, a microwave reactor and stainless steel tubing were similar; whilst PFA tubing under-performed significantly. For RAFT there was no monomer conversion, which they attribute to the permeability of the PFA tubing.[183,184] Building on the work of Meira *et al.*[168] Fors and co-workers have enabled the fine-tuning of the broadness, shape, and asymmetry of MWDs by altering the flow rate of the initiator in a living anionic polymerisation.[185] Sophisticated telescoped cascade platforms have been developed that allow for tetrablock and quarterpolymer[172] (shown in Figure 1.29), as well as droplet flow reactors for co-polymer libraries.[186] Inherently short path lengths (Beer-Lambert law) in flow reactors also offer efficient absorption of light in photomediated polymerisations. PET-RAFT has been demonstrated in flow to provide an oxygen-tolerant way of producing (homo)polymers and block copolymers in PFA tubing.[171,187] (shown in Figure 1.29) Photoiniferter RAFT was successfully reported to achieve high conversion and high molecular weight polymers in continuous flow.[39,188,189] Furthermore, photo-redox mediated controlled polymerisation of MMA using $Ir(ppy)_3$ has also been carried out in a flow reactor; here, they optimised the type of tubing the reactor was made of and found that Halar tubing afforded a higher conversion than PFA, FEP and Tefzel.[190] As O-ATRP relies on UV/Vis radiation, it is suitable for flow and has been carried out in PFA tubing[191,192] In recent years, polymeric nano-objects have been able to be synthesised in flow. Parkinson *et al.* used dispersion UF-RAFT Polymerisation to synthesise PDMAm-PDAAm nano-objects using PISA.[193,194]

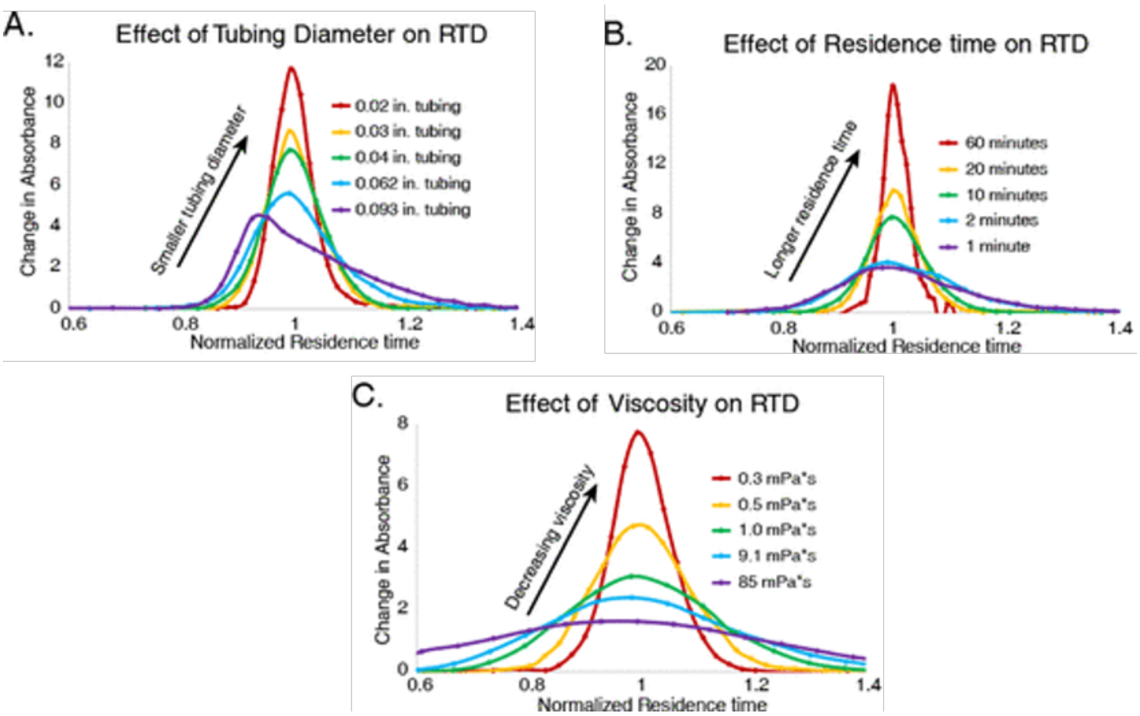

Figure 1.30: The effect of (A) tubing diameter, (B) mean residence time and (C) viscosity on the RTD modelled using the dispersion model reported by Reis *et al.*.[123] Adapted from Reis *et al.* with permission from The American Chemical Society, Copyright ©2019.

Continuous stirred tank reactors have also been used to synthesise polymers using FRP,[195] RAFT,[196] ATRP[197] and NMP[198] which have shown conversions comparable to batch data; however, showed a broadening of the MWD. Fluid dynamics provides a fundamental challenge for conducting polymerisation in flow; interactions between the channel wall and the outer reaction solution can broaden the velocity profile, affecting the molar mass distribution.[123,187] Interactions between the channel wall and the polymer solution can lead to a pressure drop, there is a balance between viscosity, flow rates, channel diameter and tube length to minimise pressure drops. Plug flow has been shown to improve the polymer properties; through, circular mixing as a result of the gas-liquid interface. Leibfarth and co-workers demonstrated the effect of viscosity and tubing diameter on the dispersity and conversion of polymerisation in continuous and plug flow.[123] Deviations from the dispersion model are reported at large tubing diameters, which was also previously reported in.[121] Here, the viscosity is also investigated, showing a significant increase in the broadness of the RTD at high viscosity.

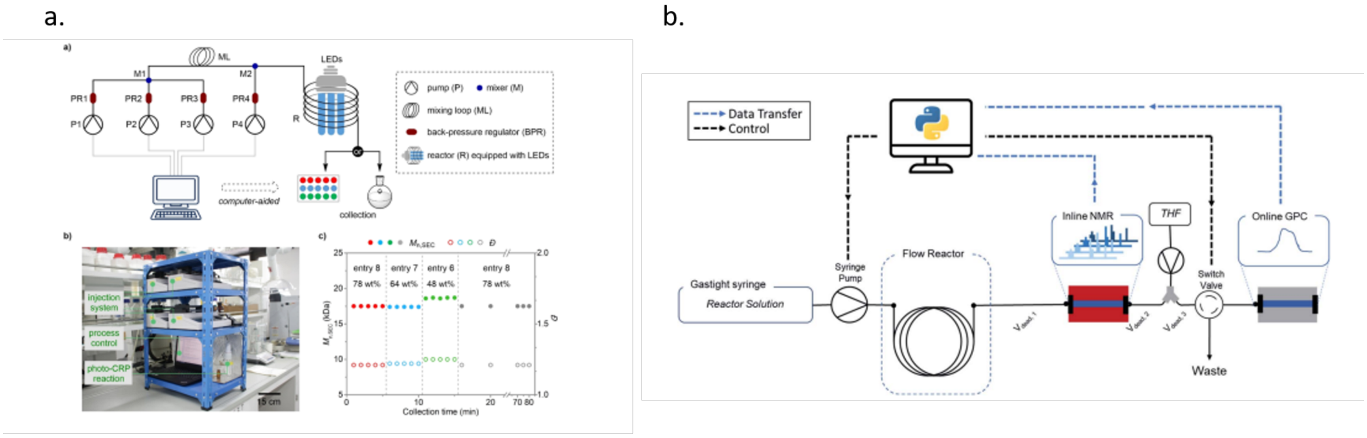

Zhou, Y. et al. Macromolecules, 52(15), 5611–5617

Herck, J. van, et al. Digital Discovery (2022).

Figure 1.31: (a) computer controlled droplet flow platform by Zhou *et al.* using RAFT photo-induced RAFT. Adapted from Zhou *et al.*[186] with permission from the American Chemical Society. Copyright ©2019 American Chemical Society. (b) Operator independent platform reported by Van-Herck *et al.* for the thermal transient kinetic screening of RAFT polymerisation in continuous flow.Adapted from Van-Herck *et al.*[141] with permission from the Royal Society of Chemistry under Creative Commons. Copyright ©2022.

Computer-aided platforms for high-throughput screening of co-polymer libraries have since been reported by Zhou *et al*,[186] shown in Figure 1.31. a. In this paper, the authors take advantage of plug flow with an immiscible solvent carrier for high-viscosity RAFT polymerisations. More recently, Junkers and co-workers[141] have developed a closed-loop automated screening platform for big data collection in continuous flow, successfully elucidating the transient kinetics collected by bench-top NMR and online SEC. The workflow is seen in Figure 1.31.b.[141,199]

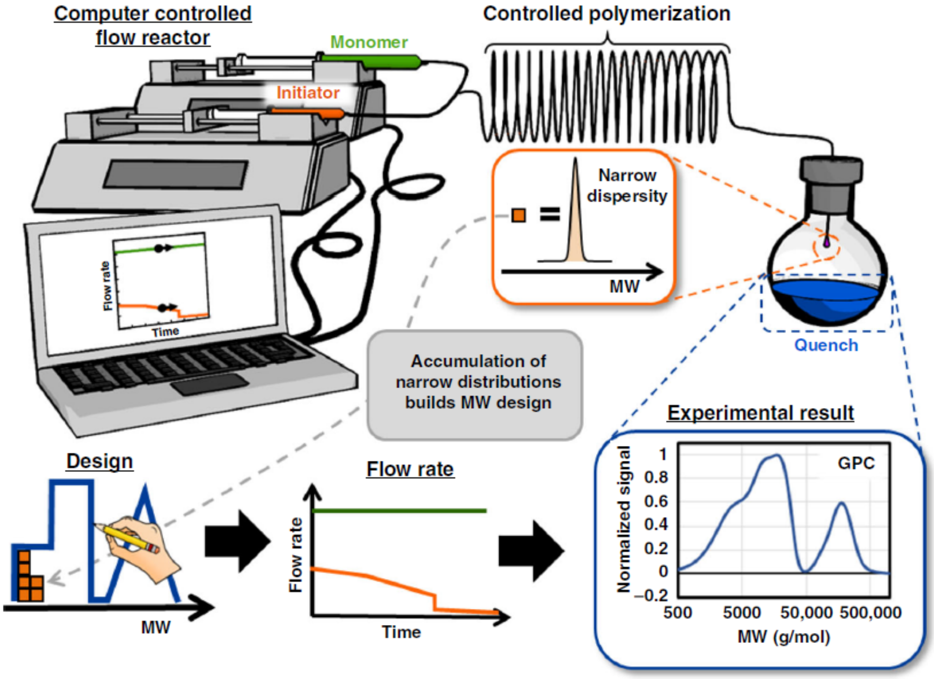

Figure 1.32: Molecular weight distribution design and synthesis platform using computer controlled platforms. Reproduced with permission from Springer Nature under Creative Commons. Copyright ©2020.

Through extensive characterisation of a plug flow reactor and the effect of flow profile on the molecular weight distribution, Guironnet and co-workers have developed a flow reactor capable of synthesising a predicted molecular weight distribution. The authors applied mathematical models to ROP, ROMP, and anionic polymerisation and obtained square, triangular, and complex MWDs that are consistent with the empirical data of the plug flow, this is shown in Figure 1.32.

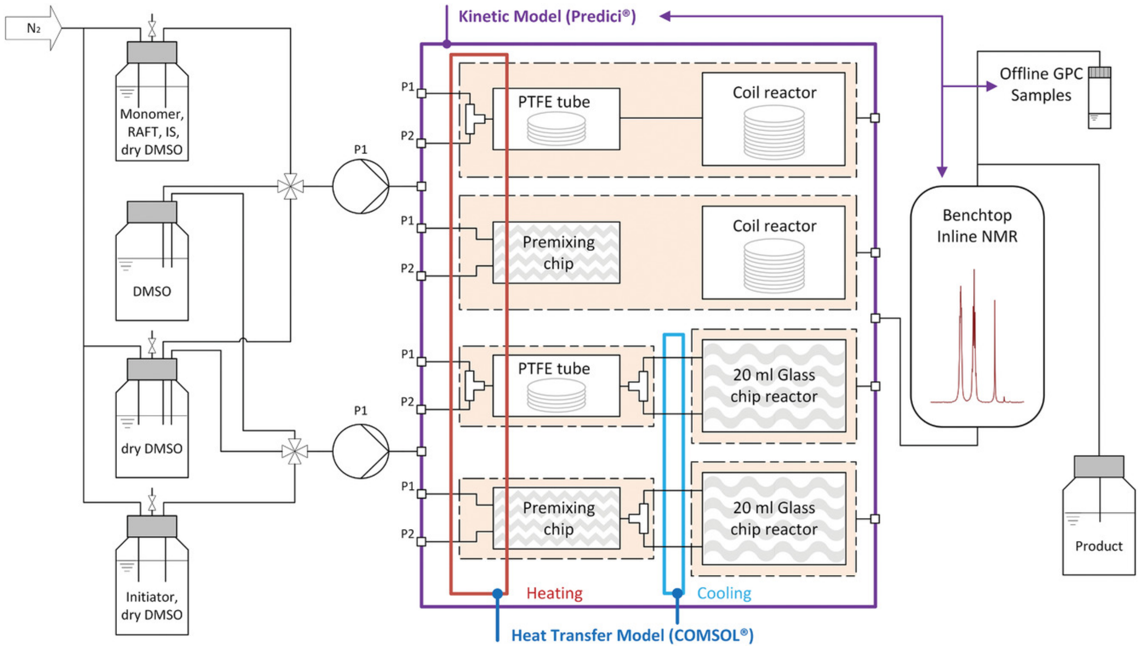

Figure 1.33: Rig used by Eckhert *et al.*[151] to optimise RAFT polymerisation in multiple reactor combinations. Reproduced from Eckhert *et al.* with permission by MDPI. Copyright: ©2021. Creative Commons.

Eckhert *et al.* have used commercially available multiphysics analysis software (COMSOL) to develop the CFD and thermal properties of the reactors (this is shown in Figure 1.33). The kinetics of the reaction was then simulated using PREDICI, which was optimised for high conversion, low *Đ* and molecular weight. The reactions were conducted experimentally in the reactors; followed by optimisation with respect to the COMSOL model. The authors found that using a premixing chip and a 20 mL glass reactor chip provided the lowest *Đ* with the highest conversion.[200]

1.5 Online monitoring of polymerisation

Typically, when polymer kinetics are monitored, monomer conversion (α), M_n, M_w, and *Đ* are of interest as they provide information on the degree of control and macromolecular structure. Online monitoring can provide uniform real-time detection of changes in a chemical system.

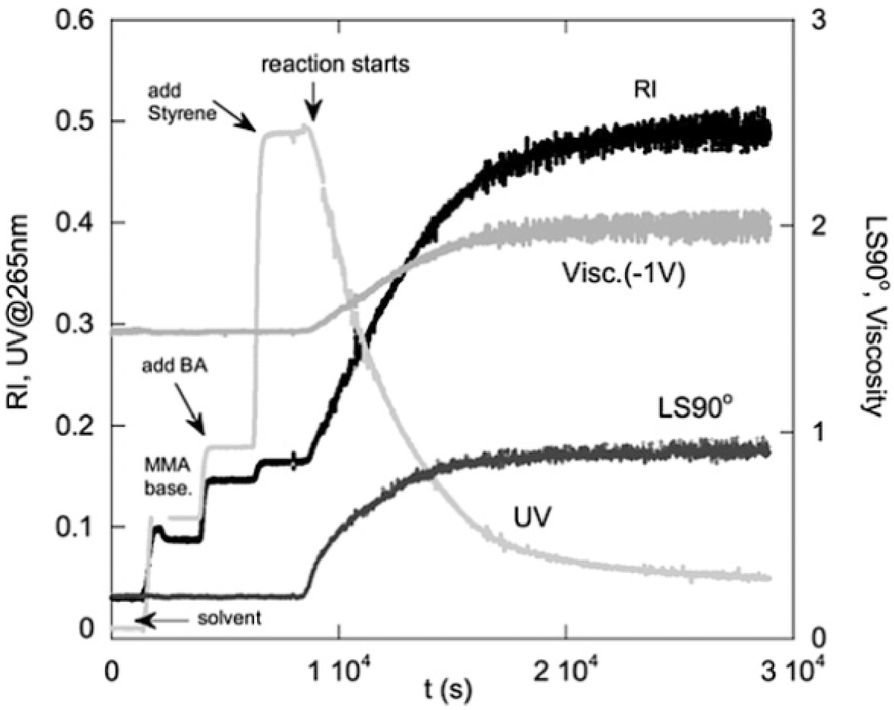

Figure 1.34: Response traces from ACOMP using UV, RI and viscometric analysis. Reproduced with permission by Wiley and Sons. Society of Chemical Industry, Copyright ©2007

Automatic continuous online monitoring of polymerisation (ACOMP) is a term coined to describe a platform that uses non-chromatographic/non-model techniques. A sample is taken from the reaction and diluted in stream and taken to a detector (light scattering, spectroscopic, viscometric) for conversion, composition, weight average molar mass, and intrinsic viscosity (seen in Figure 1.34) can be monitored without the need for models.[201]

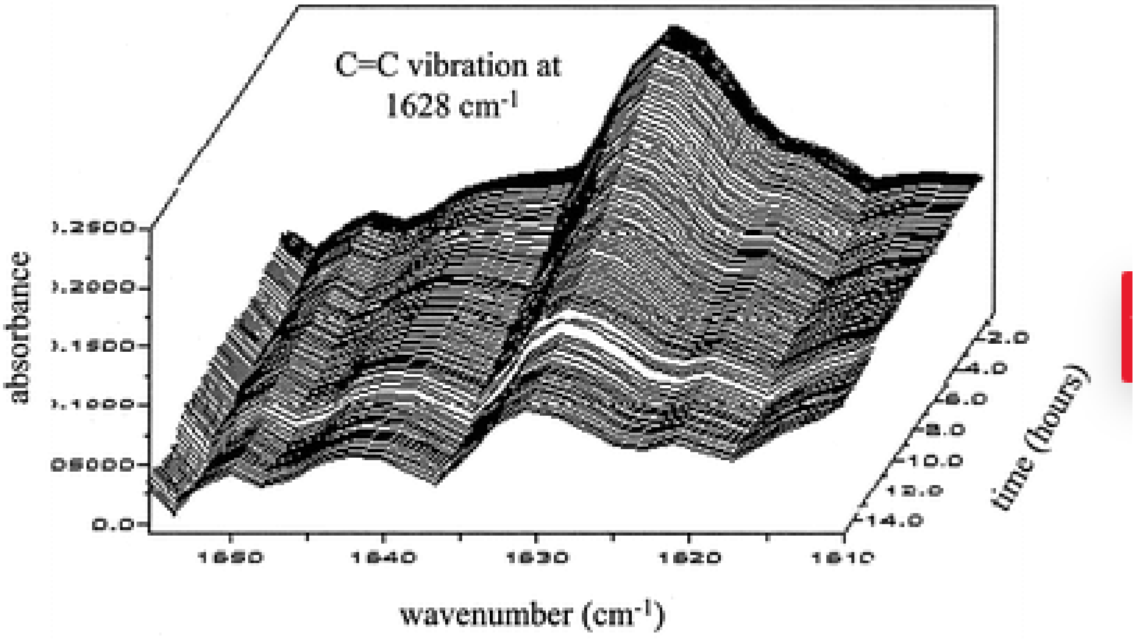

Figure 1.35: A demonstration of the use of real-time IR for online monitoring of radical polymerisations. Reproduced with permission from American Chemical Society ©1999.

Spectroscopy operates on the principles of energy transitions in the atomic and molecular energy levels (i.e. rotational, vibrational, and electronic transitions). In FT-IR the bonds in the molecule absorb a certain frequency of IR radiation that causes certain vibrational modes. FT-IR is a popular technique for monitoring the depletion of the C=C absorbance, which can then be related to concentration via the Beer-Lambert law. Long and coworkers (1999) demonstrated the use of React IR probe to monitor living cationic polymerisation via the C=C stretch at 1628 cm^{-1}.[202] Raman is a type of vibrational spectroscopy that measures the amount of inelastic scattered light - some photons are absorbed, but the rest are emitted at a different frequency. Reiss *et al*[203] have compared NIR with Raman spectroscopy for emulsion polymerisations where they identified that Raman exhibited the least signal/noise ratio that could be overcome with a filter. Both methods allowed a sufficient quality of mononomer concentration to be monitored; but Raman also offered water tolerance.[203]

UV/Vis is a technique similar to IR except that the molecule absorbs photons of energy that caused electronic transitions. The amount of light absorbed is monitored. In RAFT, UV/Vis is popular for monitoring degradation of the chain end groups with respect to time.[204] The ACOMP UV/Vis methods have been used to monitor RAFT homopolymerisation for conversion, M_w and

η_r.[205] A novel calculation for the conversion of monomers was proposed by Lauterbach *et al.*,[206] where they used the reduction in the molar free volumes of the monomer ($V_{m,M}$) when it is converted to polymer ($V_{m,P}$). The total volume (V$_{all}$) decreases while the overall composition is constant. This can be related to the concentration in the Beer-Lambert law and to the change in absorbance (A), as shown in 1.24

$$A(\lambda, \alpha) = \epsilon(\lambda) \cdot l \cdot c(\alpha) = \epsilon(\lambda) \cdot d \cdot \frac{n}{V_{all}\alpha)} \tag{1.24}$$

In a flow reactor, the diameter of the channel, d is the optical path length. V_{all} can be assumed to be the sum of the volume of monomer, polymer, control agent, solvent and an excess volume. A further set of calculations allows for the derived equation for conversion (α) shown in Equation 1.25.

$$\alpha = \frac{V_{all}(0)}{\Delta V_{max}} - \frac{\epsilon(\lambda) \cdot d \cdot n}{\Delta V_{max}} \cdot \frac{1}{A(\lambda, \alpha)} \tag{1.25}$$

where ΔV_{max} is the maximum volume of contraction, For inline conversion, a calibration is required to obtain the extinction coefficient.

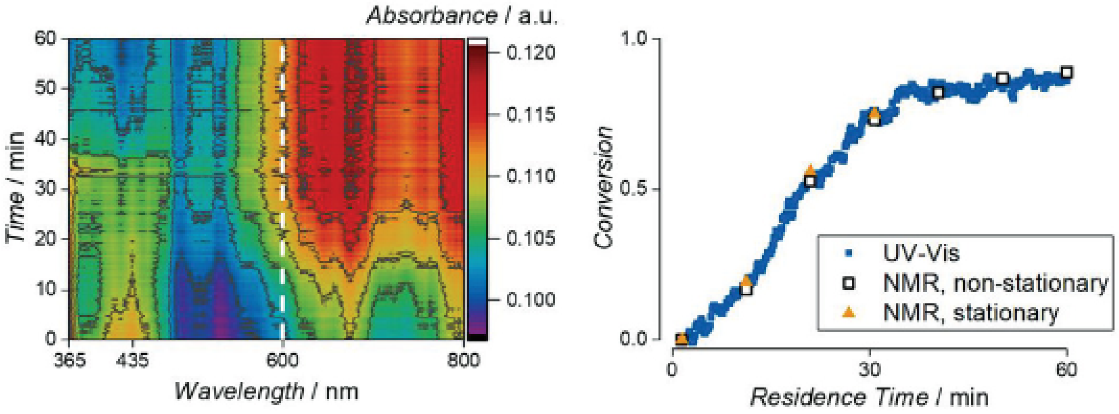

Figure 1.36: Comparison of the UV/Vis conversion monitoring used by Abetz *et al.* to continuous and stationary NMR measurements demonstrating concordant results. Reproduced from Lauterbach *et al.*[206] with permission from Wiley and Sons. Copyright ©2020.

Subsequently, the results of this were compared to those of continuous and stationary NMR and showed comparable results as demonstrated in Figure 1.36 where the kinetic traces of UV/Vis and NMR overlap. Mass spectrometry (MS) is a technique that involves measuring the mass-charge ratio by ionising the sample. Ionisation is usually categorised into hard and soft.

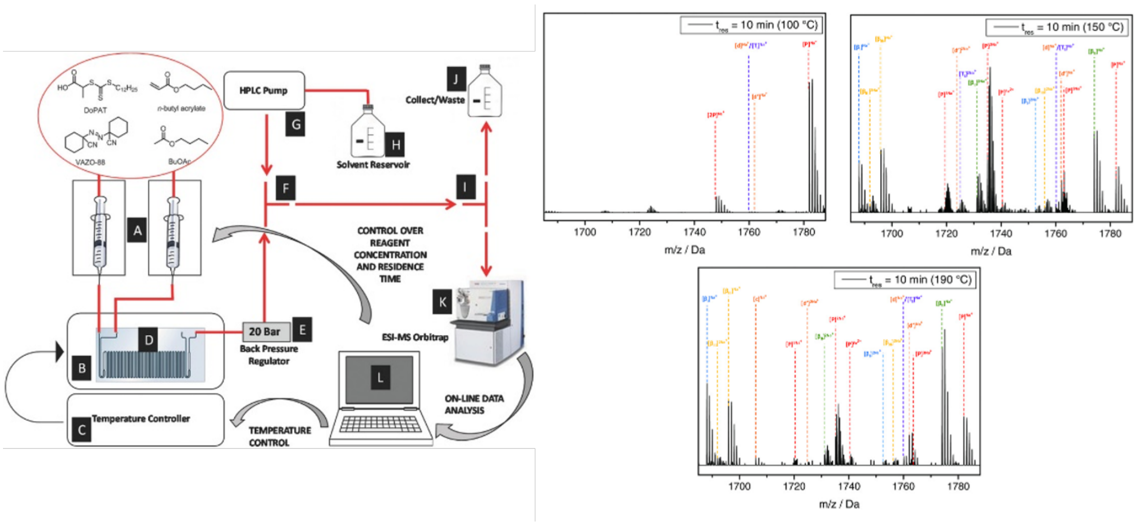

Figure 1.37: Demonstration of ESI-MS being used for the monitoring of side reactions at temperatures greater than 100 deg C. Reproduced from Haven *et al.*[207] with permission from Wiley and Sons, copyright ©2017

Online-MS was first reported for radical polymerisation by Junkers and co-workers[207] where an electron-spray ionisation setup was used to track side reactions at high temperatures for the polymerisation of nBuA by RAFT. This set up is shown in Figure 1.37.

Nuclear magnetic resonance spectroscopy operates on the nuclei having spin angular momentum. Spin leads to a magnetic field, and thus a magnetic moment. When an external magnetic field is applied, the nuclei align with or against the magnetic field. If a radio frequency proportional to the energy gap between spin states is applied, the relaxation of the spin from higher to lower energy corresponds to certain nuclei (i.e. ^{1}H). Different electronic environments (i.e., electron withdrawing groups) within a molecule will have their own local magnetic field that opposes the applied field, which provides structural information. Interactions of neighbouring non-equivalent atoms can lead to spin-spin coupling, enabling fine structural information to be obtained.[208,209] Traditional NMR requires large cryogenically cooled superconducting magnets, and a technician is usually employed to manage these multimillion GBP instruments. Advances in the miniaturisation of traditional NMR have enabled the online monitoring of reactions. Bench-top NMR utilises smaller permanent magnets positioned in a way to achieve optimised spectra. Field frequency locking allows homogeneity of the magnetic field that would otherwise drift, while external locking allows non-deuterated solvents to be used.[210] Bench-top instruments have been incorporated into polymer synthesis platforms to analyse monomer conversion from depletion of the vinyl group and growth of the polymer backbone.[200,211,212] High-field flow diffusion order

(DOSY) NMR adds another dimension to traditional NMR by adding a diffusion coefficient for polymerisation, which has been shown to permit elucidation of the molecular weight.[213]

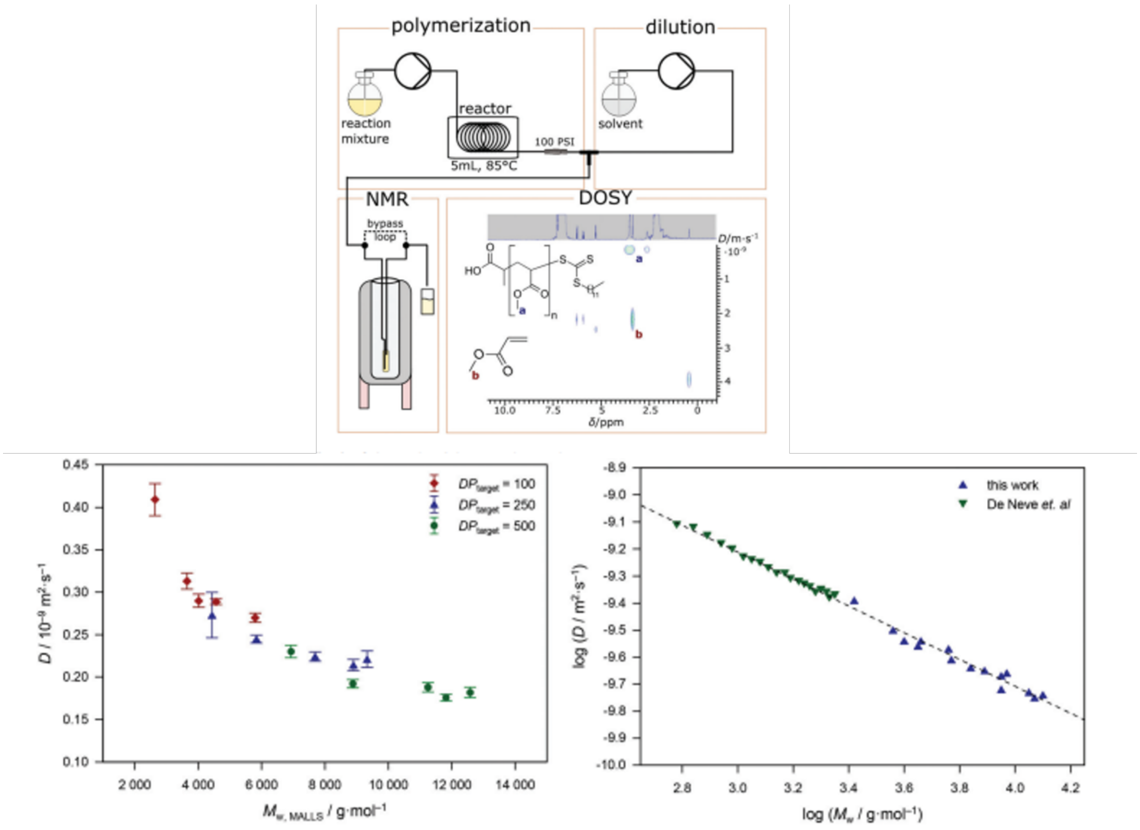

Figure 1.38: The monitoring of molecular weight by DOSY and the linearisation of the data to enable the radius of gyration of the polymer particle to be found. Adapted from Vrijsen *et al.*[214] with permission from the Royal Society of Chemistry under Creative Commons. Copyright ©2020.

High-resolution flow DOSY was coupled to a flow reactor, which is shown in Figure 1.38 to enable online monitoring of a RAFT polymerisation and to elucidate the conversion and MWDs of poly(methylacrylate).[214] A linear relationship was found between the logarithm of both the diffusion coefficient and the average weight molecular weight of a dilute solution that allowed the gyration radius of the polymer to be evaluated.[214]

Commonly, polymer molecular weights and MWD are determined by size exclusion chromatography/gel permeation chromatography (SEC/GPC). A diluted sample is injected into columns containing porous beads, and the coiled polymer chains are separated depending on size. Larger chains will elute sooner than shorter chains, which will penetrate the porous beads. The columns are attached to multiple detectors; frequently, viscometers, UV/Vis and light scattering. To analyse a sample, the instrument must be calibrated against standards with a known molecular weight and concentration.[6] Typical SEC samples take 30 min to analyse; for online monitoring this needs to be faster. Haddleton and co-workers developed online monitoring of SEC where they diluted a batch SET-LRP reaction of methylacrylate with eluent by varying the flow rate of HPLC pumps, which could then be injected into a rapid column, bringing the data collection time to 3 min.[215] Subsequently, automated sampling valves have been used to take injections every 12 min for the NMP and copolymerisation of nBuA and stryene synthesised in flow; SEC was coupled to multiple detectors so that linear and branched polymers could be evaluated. This was named continuous online rapid size exclusion chromatography (CORSEMP).[**BallyAA**] SEC has also been coupled to high-field and bench-top NMR as a detector for online analysis of copolymer MWDs.[216,217]

1.6 Self-Optimisation platforms for polymer synthesis

Flow polymerisation offers high throughput polymer discovery and optimisation and is a growing area within polymer chemistry. Many online polymerisation platforms look at optimising the collection of molecular weight information - i.e precise M_n and/or shape. A degree of automation is required for online analysis, and several examples using computer-controlled equipment are mentioned above.[218]

Machine learning (ML) algorithms have been shown to be effective in reaction self-optimisation by reducing the number of experiments compared to traditional techniques by Design of Experiments (DoE). Complex multivariate, multiobjective, multistep self-optimising platforms have been developed for small molecules.[140,144,162,165]

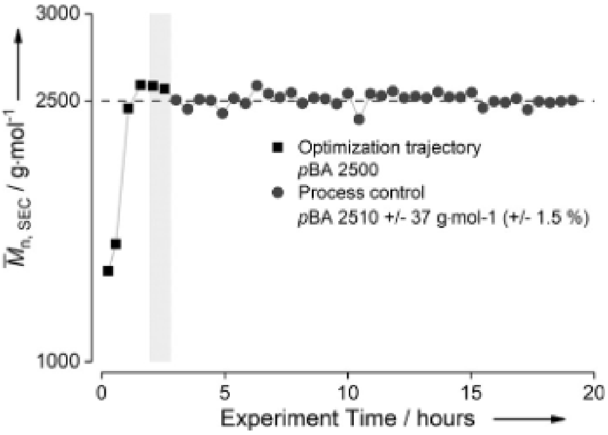

Figure 1.39: Optimisation of molecular weight showing little deviation from the target DP after 5 hours reported. Reproduced from Rubens *et al.*[219] with permission by Wiley and Sons. Copyright ©2019

A Lab-View based autonomous platform consisting of three syringe pumps was used by Rubens *et al.*[219] in conjunction with a microfluidic reactor to target a defined molecular weight (monitored by SEC) using an algorithm. A screening set of data was conducted to explore different target degree of polymerisation and the kinetics evolving the M_n. An algorithm was then used to identify the optimised reaction conditions corresponding to the target DP; such that the accuracy of the M_n value is directly related to the accuracy of the equipment.[219]

Houben et al.[135] reported the use of a multiobjective active learner (MOAL) algorithm to optimise particle size and conversion in an emulsion polymerisation varying 14 input variables. Initially, they ran an *in-silico* optimisation of an emulsion copolymerisation and conducted the experiment on a semi-automated closed-loop reactor platform, seen in Figure 1.40.[135] Frequently, optimisation objectives contradict each other, meaning that one cannot be improved on without having a detrimental effect on the other - also known as the pareto front – in this circumstance Bayesian optimisation algorithms are better suited. Their successful optimisation led to the identification of a series of conditions with 14 input variables that led to a particle size of 100 nm and full conversion[135]

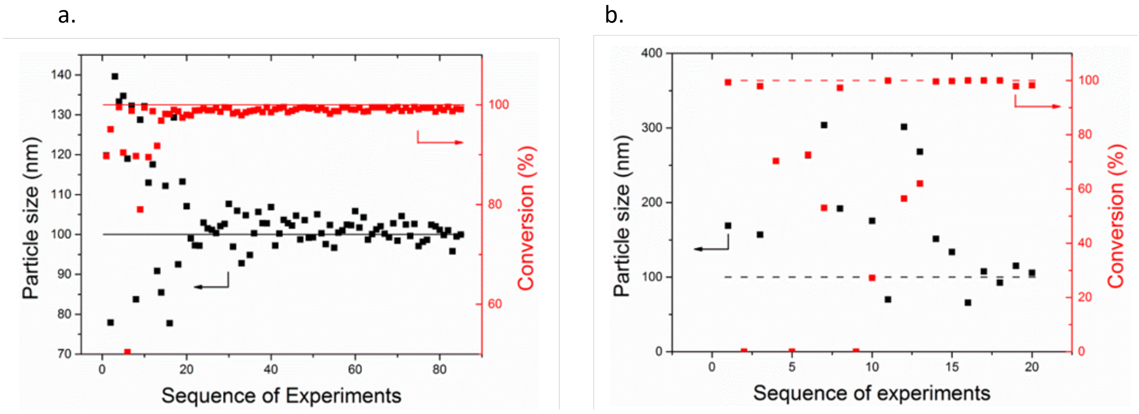

Figure 1.40: Data from the MOAL optimisation by Houben *et al.* targeting high conversion and particle size of 100 nm for an emulsion copolymerisation, where the dashed lines are the target objectives (a) *in-silico* model looking at potential recipes where the target is reached after 27 experiments and (b) closed-loop experimental data where the target was reached in 17 exeriments. Reproduced from Houben *et al.*[135] with permission from American Chemical Society under Creative Commons. Copyright ©2015.

ML has been applied to polymer synthesis by Gu *et al.*[220] where they used experimental data and setting inputs and outputs (feedstock concentration and M_w), the data sets were analysed for relationships between conditions and objectives using various ML algorithms to predict conditions leading to tailored polymers. The non-linear nature of the data meant that the Random Forest algorithm outperformed all of the others. Through multivariate analysis, they identified complex interactions between covariables - M_w decreases when [CTA] $<$ 33 x smaller than [M] and then increases for PET-RAFT. Their findings report that at high [CTA]/[M] and lower [PC]/[CTA] they obtain the lowest propagating groups % and lowest Đ, as demonstrated in Figure 1.41. They called this platform the ML-assisted systematic polymerisation planning platform (SPP).[220]

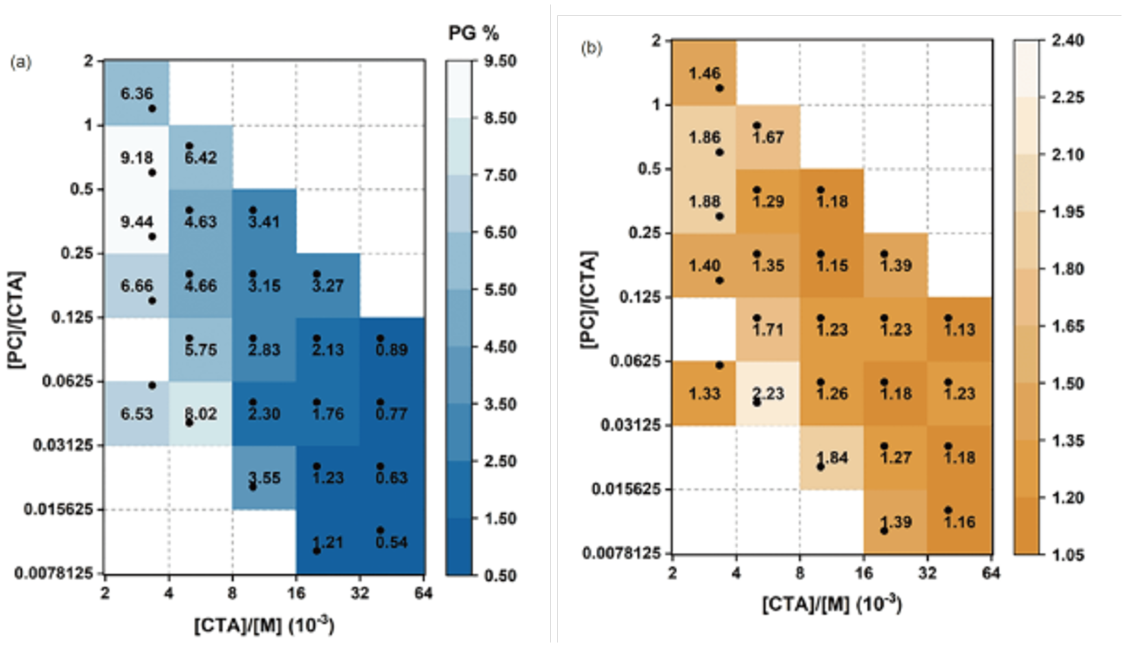

Figure 1.41: Heat maps produced by Gu *et al.*[220] where the input variables are CTA/monomer ratio and photocatalyst/CTA ratio.the colour corresponds to (a) propagating group percent and (b) Đ. Reproduced from Gu *et al.* with permission from Science China Press and Springer-Verlag GmbH Germany, part of Springer Nature. Copyright ©2021

Alternatively, a DOE algorithm using a face-centred central composite design has also been used for thermally initiated RAFT. Eckhert *et al.*[151] have successfully shown the power of DoE in exploration of reaction space, this allowed them to fit surfaces and equations that enabled generations of accurate predictive models. Using the predictive models, they found that the experimental data fall within the 95 % prediction limits of the models, therefore, it is validated.[151] Reis *et al.*[221] have developed a Bayesian-based optimisation platform capable of optimising the synthesis of ^{19}F MRI agents. Using plug flow, they optimised a series of copolymers with varying composition of fluorinated acrylate monomers in 2 min per copolymer. Here they overcame the solubility issue owing to the fluorine substituent by forming statistical copolymers while optimising the ^{19}F MRI activity of the copolymer. This trade-off in solubility and activity makes this an ideal candidate for Bayesian optimisation. They identified a number of copolymers with sensitivity greater than previously reported and found that the signal-to-noise ratio is not directly related to the composition of fluorine in the co-polymer. In general, this work will allow for further discovery of ^{19} MRI agents.[221]

1.7 Project Aims and Objectives

Advanced polymeric nanoobjects used in the pharmaceutical, agrichemical and electronics industries typically require sequence-controlled. RAFT is an attractive type of polymerisation because of its functional group tolerance and ability to produce sequence-defined block copolymers; for sequence-defined block copolymers, defined homopolymers with low molar mass dispersity are required. Formation of homopolymers with narrow MWDs is not a trivial process for RAFT because of the presence of side reactions, chain-transfer, and termination, which can cause a trade-off in conversion and dispersity. The overall aim of this thesis was to reduce the number of experiments required to identify the Pareto front; subsequently, decreasing the amount of reagents required and increase the throughput of optimisation while exploring a large amount of experimental reaction space. This main aim has been compartmentalised into 4 chapters.

In Chapter 2, the main aim is to introduce the use of a state-of-the-art Bayesian optimisation algorithm that can efficiently explore and exploit 2D reaction parameter space. In a simple flow platform consisting of a single pump and a tubular flow reactor, the 2D reaction parameter space (temperature and residence time) will be explored. Affording first-instance Bayesian optimisation for the exploration of solution RAFT polymerisation in continuous flow.

The aim of Chapter 3 is reactor optimisation; which is important when carrying out continuous flow of rapid reactions such as radical polymerisation. The mixing has been optimised to ensure uniform mixing before the solution enters the reactor. Several variables have been changed to investigate their effect on the residence time distribution, which is useful later in Chapter 4.

Chapter 4 addresses a gap in the literature by providing a quantitative Equation for dispersity as a function of conversion, accounting for chain growth, transfer, and terminative events. This has been coupled with an existing kinetic model to obtain conversion and written into a *MATLAB* application. Experimental validation in both batch and flow has been carried out from the literature and from data obtained in this work.

Finally, in Chapter 5 the model developed in Chapter 4 and the experimental platform optimised in chapter 3 has been used to investigate the effects of initiator concentration, temperature, and residence time on the trade-off in conversion and dispersity.

Chapter 2

Multi-objective Self-Optimisation of RAFT Polymerisation in a One Pump Continuous Flow Reactor Platform

2.1 Introduction

Self-optimising reactors can enable chemists to visualise rapidly what is happening with green metrics, selectivity, yield, conversion, wavelength, or other objectives when exploring the reaction space. Examples of self-optimising reactors have been reported in abundance for small molecules, with the fine chemical industry showing great interest in the area. In some cases, if a combination of objectives is looked at, the effect of certain reaction conditions may improve one objective but severely impact the other objective. These reactions can be considered expensive-to-evaluate problems. Bayesian optimisation can offer a way to overcome these issues. A surrogate model can be used to build an approximate objective function based on experimental or modelled data. An acquisition function is then applied to sample from this surrogate model. These functions typically aim to exploit and explore the reaction space in the case of chemical systems. This allows identification of the Pareto front, which can be described as the set of experiments that lead to the optimal trade-off in objectives. Bayesian optimisation algorithms can be considered a "black-box" where no *a priori* knowledge is required, which means that they can be considered ideal for discovery platforms. Bayesian optimisation applied to polymerisations has been reported a handful of times in the literature. As shown in Chapter 1. Reis *et al.*[221] have described the use of Bayesian optimisation for the synthesis of copolymer-based ^{19}F MRI agents. Whilst Houben *et al.*[135] have demonstrated the use of MOAL for the discovery of recipes that lead to full conversion and a specific particle size.

In this chapter, 2D reaction parameter space was optimised for the RAFT polymerisation of dimethylacrylamide, tert-butylacrylamide, n-butylacrylate and the statistical copolymerisation of PDMAm-PFPA. Optimisation objectives were conversion(α) and dispersity (), which were monitored using NMR and GPC, respectively. The effect of oxygen on the continuity of the surface was also investigated using an inline degasser. The platform in this chapter uses Latin-Hyper Cube (LHC) to select screening experiments to conduct as the initial exploration of experimental space. The output data from these experiments were fed into the main ML algorithm based on Bayesian optimisation. A surrogate Gaussian process (GP) model was generated from training data, the GP was sampled from, and the hyperparameters identified; the point that has the largest hypervolume improvement was carried out as the next real-time experiment. The algorithm does not require *a priori* knowledge of the chemical system, its computationally inexpensive, and finds the global optima.

2.2 Experimental

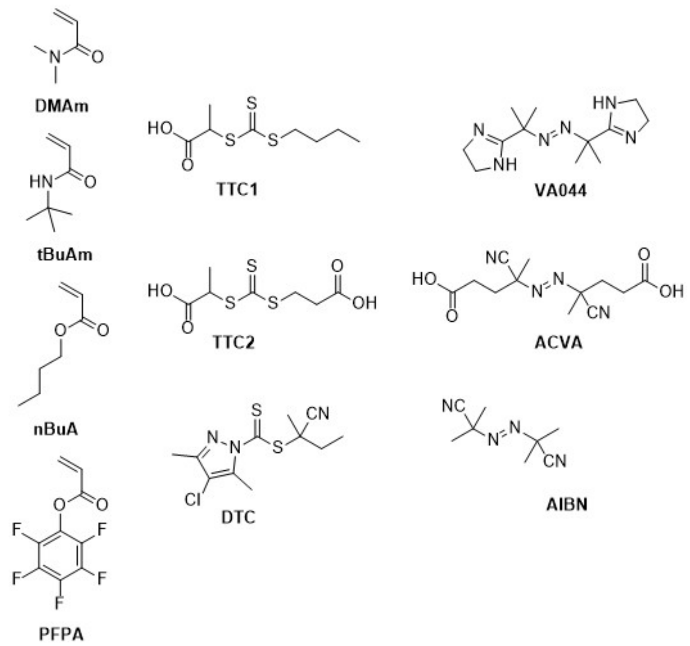

Figure 2.1: Reagents used in the experimental work of this thesis

Monomers used in this thesis:

N,N-dimethylacrylamide ((DMAm) 99 %, contains 500 ppm monomethyl ether hydroquinone as inhibitor, CAS 2680-03-7) purchased from Sigma Aldrich, tert-butylacrylamide ((tBuAm), 97 %, CAS 107-58-4) purchased from Alfa Aesar and butyl acrylate ((nBuA), 99 %, contains 10-60 ppm monomethyl ether hydroquinone as inhibitor, CAS 141-32-2) purchased from Sigma Aldrich. Pentafluorophenyl acrylate was synthesised by A.G (CAS-71195-85-2)

RAFT agents were all purchased from Boron Molecular:

2-(Butylthiocarbonothioylthio)propanoic acid ((TTC1) 95 %, CAS 480436-46-2),

3-((((1-carboxyethyl)thio)carbonothioyl)thio)propanoic acid ((TTC2) 95 %, CAS 870451-09-5) and 2-cyanobutan-2-yl 4-chloro-3,5-dimethyl-1H-pyrazole-1-carbodithioate((DTC) 95 %, CAS 2052159-02-9).

Initiators used:

2,2'-Azobis[2-(2-imidazolin-2-yl)propane]dihydrochloride ((VA044), CAS 27776-21-2), 4,4'-Azobis(4-cyanovaleric acid) ((ACVA), CAS 2638-94-0) and 2,2'-Azobis(isobutyronitrile) ((AIBN), CAS 78-67-1)

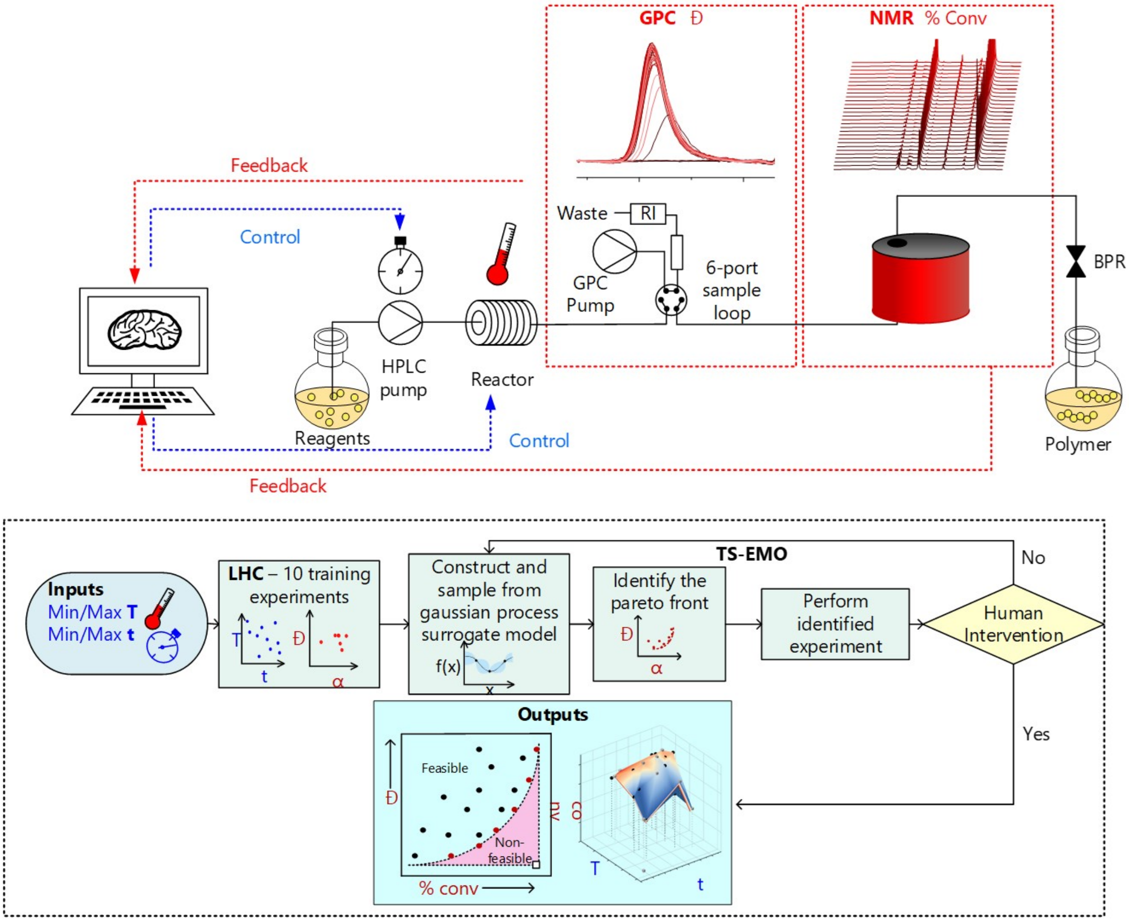

Figure 2.2: (top) Schematic depiction of the autonomous self-optimising platform used in this chapter for 2D reaction space optimisation.(bottom) Flow diagram showing how the computer decides on experiments

A premixed solution of reagents was supplied, using a computer-controlled HPLC pump (JASCO PU980), into a 2 mL tubular flow reactor coiled around a cylindrical heating block. Temporal resolution was achieved by varying the flow rate. After 3 reactor volumes, the flow rate was reduced to around 0.1 mL/min, where an at-line GPC was used to analyse a sample. The at-line GPC consists of a VICI EHMA 6 port switching valve and a 2 position actuator that enables a 100 μL sample to be injected into the online GPC setup mentioned in the analytical techniques section below. The reacted solution continues through a length of perfluoroalkyl alkane (PFA) tubing threaded through the hole in the NMR. A 7 bar (100 psi) IDEX cartridge back pressure regulator (BPR) was used to mediate flow throughout the tube. The GPC analyses the M_n, M_p and the $Đ$ from the resultant chromatogram after 6 min. In tandem, xml commands were called, which trigger the NMR, conduct a quick shim on the reaction mixture, and then run a PRESAT scan as mentioned in the analytical techniques section. Mestrenova then opens the script, and a template that allows signal processing is called. The integrals were then analysed and substituted in the equations in Table 2.7. Subsequently, the collected data form an objective function that was fed into the TS-EMO algorithm along with the corresponding conditions. The suggested residence time was converted into a flow rate; where this and the new temperature were then supplied to the pump and the Eurotherm temperature controller, respectively, forming a feedback loop.

a. DMAm: TTC1: ACVA in water

Table 2.1: Limits used in the implementation of the TS-EMO algorithm for the RAFT polymerisation of DMAm in the presence of TTC1 using ACVA in water, with a reagent ratio of 200: 1: 0.1, respectively, at a mass content of 30 w/w%. Each TS-EMO iteration suggested a single experiment.

Input	Lower limit	Upper limit	Variance limit
Temperature (°C)	70	100	2
Residence time (min)	5	20	1

DMAm (80 g, 0.81 mol), TTC1 (0.96 g, 4.04 mmol) and ACVA (0.11 g, 0.403 mmol) were dissolved in water (189.17 g). The reagent reservoir was not degassed under an atmosphere of nitrogen. Ten training experiments were suggested by the Latin hypercube sampling algorithm, then the TS-EMO suggested one experiment per iteration. The optimisation limits are shown in Table 2.1.

b. i. tBuAm:TTC1:AIBN in methanol

Table 2.2: Limits used in the implementation of the TS-EMO algorithm for the RAFT polymerisation of tBuAm in the presence of TTC1 using AIBN in methanol, in a reagent ratio of 200:1:0.1, respectively, with a mass content of 30 w/w %. Each TS-EMO iteration suggested four experiments.

Input	Lower limit	Upper limit	Variance limit
Temperature (°C)	80	120	2
Residence time (min)	4	20	1

tBuAm (80 g, 0.62 mol), TTC1 (0.75 g, 3.1 mmol) and AIBN (0.052 g, 0.31 mmol) were dissolved in methanol (188.5 g). The reagent reservoir was not degassed under an atmosphere of nitrogen. Ten training experiments were suggested by the Latin hypercube sampling algorithm; then, the TS-EMO suggested four experiments per iteration so that the waiting time for GPC would be reduced. The optimisation limits are shown in Table 2.2.

b. ii. tBuAm: TTC2: AIBN in methanol

Table 2.3: Limits used in the implementation of the TS-EMO algorithm for the RAFT polymerisation of tBuAm in the presence of TTC2 using AIBN in methanol, in a reagent ratio of 200:1:0.1, respectively, with a mass content of 30 w/w %. Each TS-EMO iteration suggested four experiments.

Input	Lower limit	Upper limit	Variance limit
Temperature (°C)	80	120	2
Residence time (min)	4	20	1

tBuAm (80 g, 0.62 mol), TTC2 (0.79 g, 3.1 mmol) and AIBN (0.052 g, 0.31 mmol) were dissolved in methanol (188.5 g). The reagent reservoir was not degassed under an atmosphere of nitrogen. Ten training experiments were suggested by the Latin hypercube sampling algorithm; then, the TS-EMO suggested four experiments per iteration so that the waiting time for GPC would be reduced. The optimisation limits are shown in Table 2.2.

b. iii. tBuAm: DTC: AIBN in methanol

tBuAm (80 g, 0.62 mol), TTC1 (0.91g, 3.1 mmol) and AIBN (0.052 g, 0.31 mmol) were dissolved in methanol (188.9 g). The reagent reservoir was not degassed under an atmosphere of nitrogen. Ten training experiments were suggested by the Latin hypercube sampling algorithm; then, the TS-EMO suggested four experiments per iteration so that the waiting time for GPC would be reduced. The optimisation limits are shown in Table 2.4.

Table 2.4: Limits used in the implementation of the TS-EMO algorithm for the polymerisation of tBuAm in the presence of DTC using AIBN in methanol, in a reagent ratio of 200:1:0.1, respectively, with a mass content of 30 w/w %. Each TS-EMO iteration suggested four experiments.

Input	Lower limit	Upper limit	Variance limit
Temperature (°C)	80	120	2
Residence time (min)	4	20	1

b. iv. tBuAm: TTC2: AIBN in methanol with inline degassing

For degassed experiments, a JASCO DG-2080-53 was used to remove oxygen from the reaction. The optimisation limits and procedure were the same as in the equivalent nondegassed experiment (ii).

c. nBuA: TTC1: AIBN in 1,4-dioxane

nBuA(80 g, 0.62 mol), TTC1 (0.74g, 3.1 mmol) and AIBN (0.051 g, 0.31 mmol) were dissolved in 1,4-dioxane (188.5 g). The reagent reservoir was not degassed under an atmosphere of nitrogen. Ten training experiments were suggested by the Latin hypercube sampling algorithm; then, the TS-EMO suggested four experiments per iteration so that the waiting time for GPC would be reduced. The optimisation limits are shown in Table 2.4

Table 2.5: Limits used in the implementation of the TS-EMO algorithm for the polymerisation of nBuA in the presence of TTC1 using AIBN in 1,4-dioxane, in a reagent ratio of 200:1:0.1, respectively, with a mass content of 30 w/w %/. Each TS-EMO iteration suggested four experiments.

Input	Lower limit	Upper limit	Variance limit
Temperature (°C)	80	120	2
Residence time (min)	3	30	1

d. Statistical co-polymerisation of DMAm: PFPA: TTC1: ACVA in acetonitrile

Table 2.6: Limits used in the implementation of the TS-EMO algorithm for the statistical copolymerisation of PDMAm and PFPA in the presence of TTC1 using ACVA in acetonitrile, in a reagent ratio of 90:10:1:0.1, respectively, with a mass content of 30 w/w %/. Each TS-EMO iteration suggested four experiments.

Input	Lower limit	Upper limit	Variance limit
Temperature (°C)	70	120	2
Residence time (min)	10	60	1

DMAm (44 g, 0.45 mol), PFPA (10.8 g, 0.045 mol), TTC1 (1.19 g, 5.0 mmol) and AIBN (0.14 g, 0.5 mmol) were dissolved in acetonitrile (107.7 g). The reagent reservoir was not degassed under an atmosphere of nitrogen. Ten training experiments were suggested by the Latin hypercube sampling algorithm; then, the TS-EMO suggested one experiment per iteration. The optimisation limits are shown in Table 2.6.

2.2.1 Heating vessel

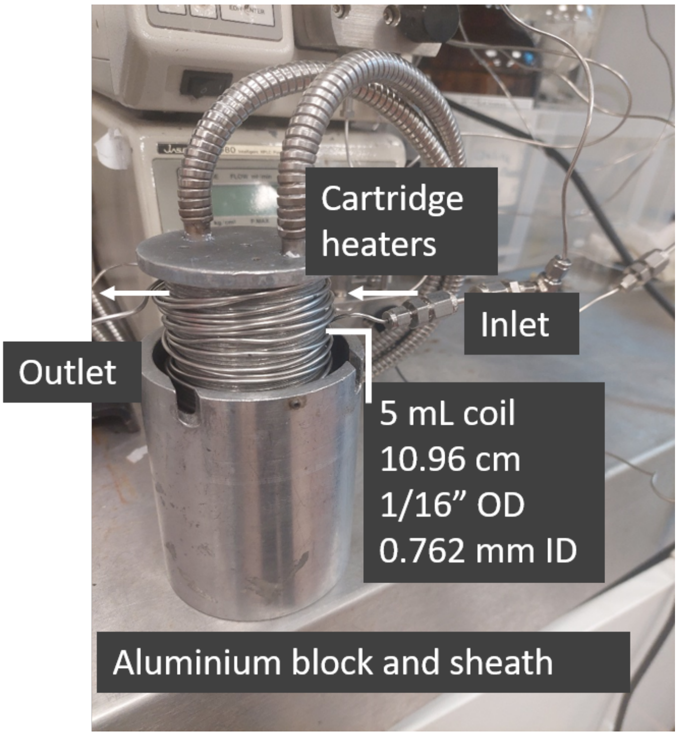

Figure 2.3: Diagram of the heating block used in this Chapter and Chapters 3, 4 and 5.

The heating block consisted of an aluminium cylinder with 2 holes to fit 2 cartridge heaters and an aluminium sheath. A 2 mL reactor stainless steel tube with an internal diameter of 0.762 mm was used as the reactor vessel for all experiments in this chapter, except for the DMAm experiment, where a 5 mL coil was used. The setup can be seen in Figure 2.3.

2.2.2 Analytical techniques

Bench-top-Nuclear Magnetic Resonance

A Magritek Spinsolve Ultra benchtop NMR (60 MHz) was used to characterise homopolymers. Online measurements were taken by flowing the solution through at 0.1 mL/min. The PRESAT setting conducted two scans, at a saturation frequency set to 4.79 for water, 3.53 for dioxane, 3.31 for methanol and 1.94 for acetonitrile, at a sat power of -65 dB For these experiments, the PFA tubing was clamped at the top and bottom of the NMR using a standard laboratory clamp, stand and boss. The conversions for DMAm/water, nBuA/1,4-dioxane and tBuAm/methanol were calculated by comparing the vinyl integral with the polymer backbone integral, as seen in Table 2.7. For the optimisation of the statistical copolymer PDMAm-PFPA, only relative vinyl integrals were used for the conversion.

$$\alpha = 1 - \frac{[M]}{([M] + [P])} \tag{2.1}$$

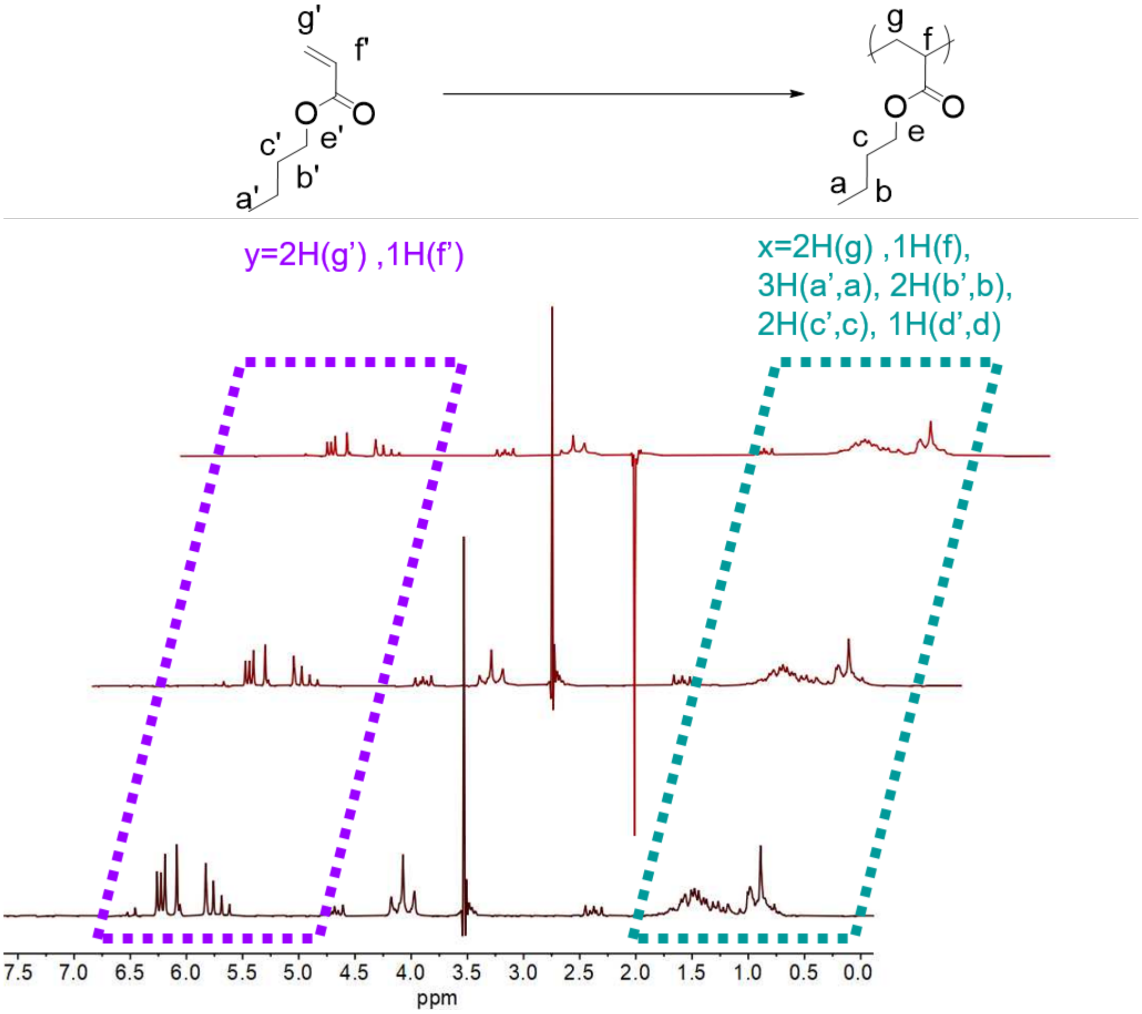

Figure 2.4: NMR assignments used to identify the equation for conversion of nBuA in 1,4-dioxane.

The NMR conversion protocol requires the assignment of the vinyl and polymer backbone regions and the number of protons in those environments[211] For nBuA the vinyl region exists at chemical shifts between 5.5 and 6.5 ppm, there were only 3 protons in this environment. Due to benchtop NMR operating at a lower resonance frequency, the backbone and the pendant group were difficult to discern; thus, the region from 0 to 2.1 ppm required normalisation. Qualitatively, in Figure 2.4 the depletion of monomer vinyl peaks can be observed from bottom to top corresponding to the increase in monomer conversion.

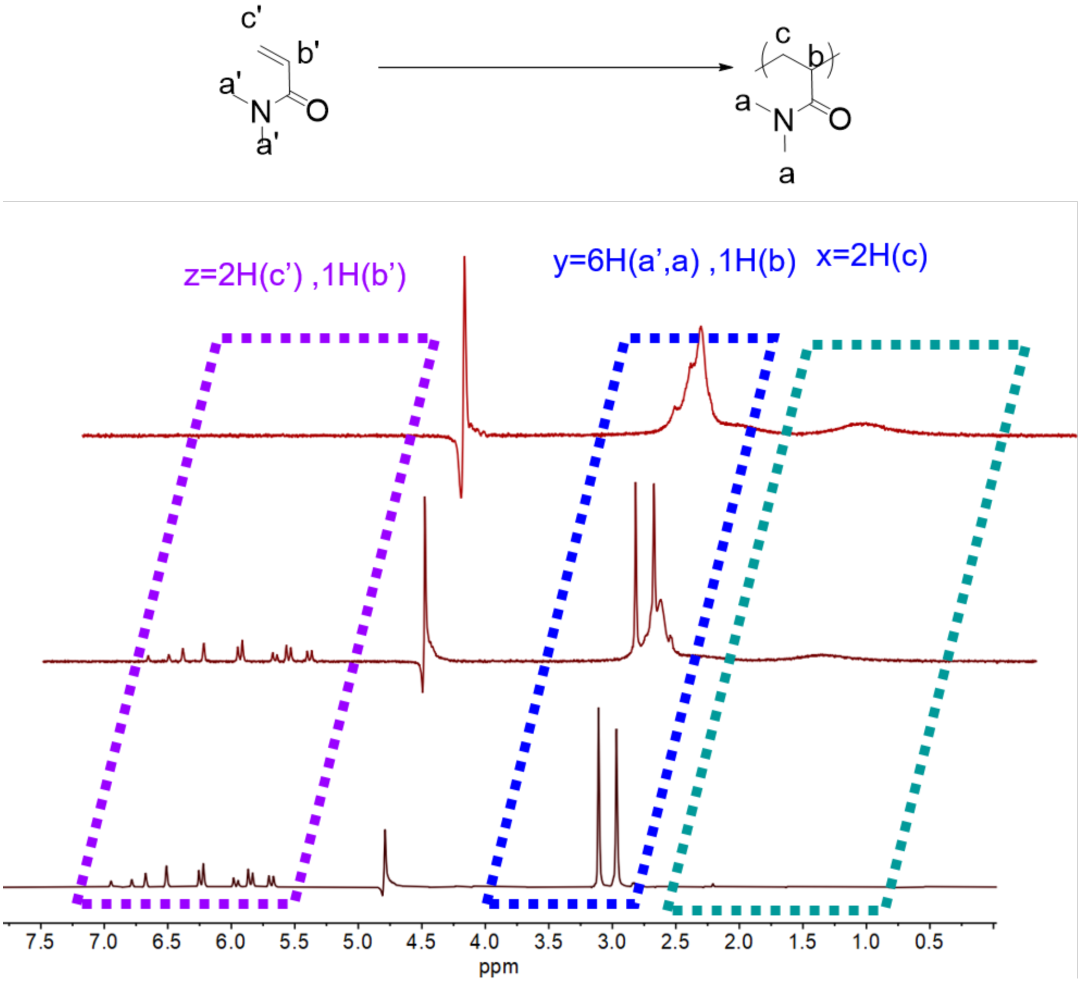

Figure 2.5: NMR assignments were used to identify the equation for the conversion of DMAm in water.

For DMAm, the chemical shift for the 2 protons associated with the polymer backbone can be seen to grow in spectra between 1.0 and 2.5 ppm, as seen in the Figure 2.5. Seven protons were present in integral y; however, these protons were shared between the pendant group in the monomer and the polymer, as well as proton b in the polymer. The increased conversion of the monomer is demonstrated in Figure 2.5 in the integral region z, where the peak disappears from the bottom to the top spectra. Using Equation 2.1, an equation for conversion can be identified following normalisation of shared protons, which are shown in Table 2.7.

Table 2.7: Equations for the quantification of the monomers used

Entry number	Monomer	Equation
1	DMAm	$\alpha = 1 - \frac{2z}{y - \frac{x}{2}}$
2	tBuAm	$\alpha = 1 - \frac{10x}{3(x+y)}$
3	nBuA	$\alpha = 1 - \frac{10x}{3(x+y)}$

Gel-Permeation Chromatography

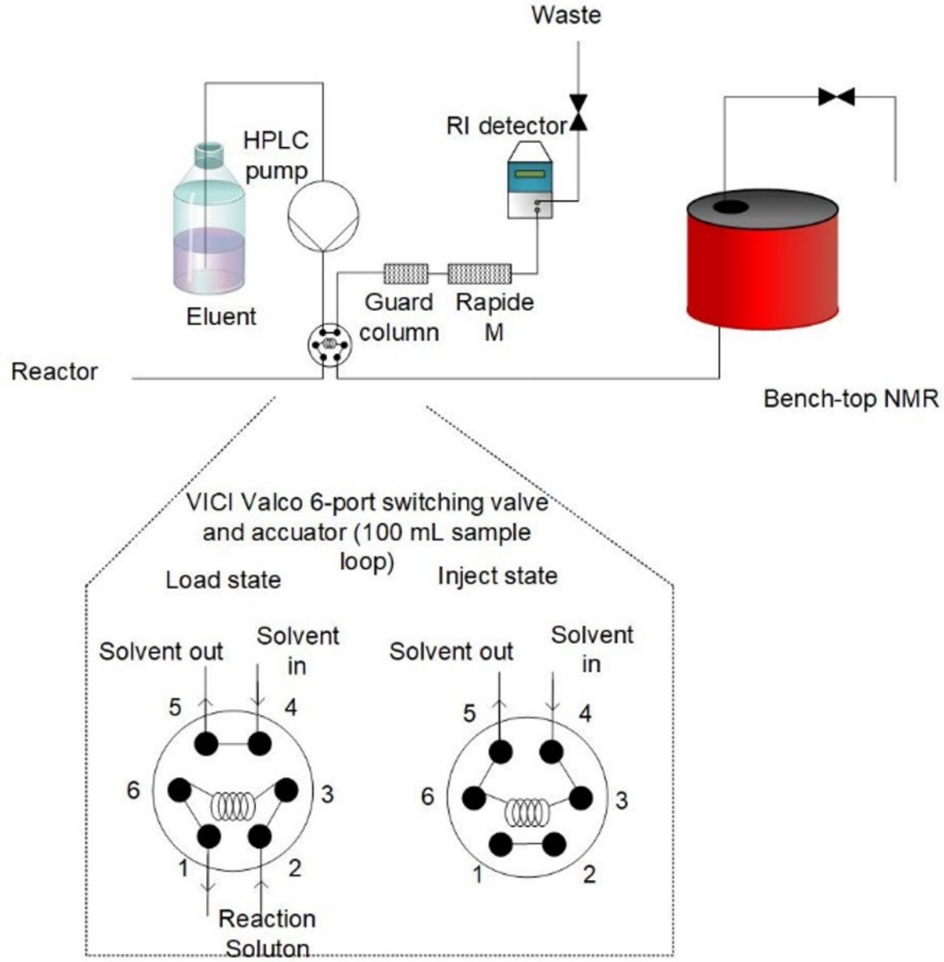

Figure 2.6: Schematic of the online GPC set up used in this Chapter and Chapter 5 showing the switching valve sampling

The at-line GPC used in this chapter was a home-made setup consisting of a JASCO PU-980 HPLC pump connected to a 6-port VICI EHMA switching valve with a 2 position actuator. This allows injection into an Agilent 5 μm guard column adjacent to an Agilent Rapide M column. A Knauer K2301 RI detector was used to monitor the refractive index response, pressure was regulated with an IDEX P767 7 BPR. In this chapter, THF treated with BHT / TEA (0.05/1 w/w %) was used for experiments in which tBuAm or nBuAm was used, while LiBr treated DMF (0.1 w/w %) was used in the cases of DMAm and DMAm-PFPA.

2.3 Results and Discussion

A large challenge in data analysis where there are 2 objectives and multiple variables is presenting the data clearly. In this chapter, 3D plots are used, where the x and y axes represent the two reaction conditions (temperature and residence time), and the z axis is objective 1 (monomer conversion). A colour map surface is fitted to the data to make the change in objective 2 ($Đ$) clear. A high point corresponds to high conversion and where the surface is blue corresponds to low $Đ$. The objective plots are also provided in tandem, demonstrating the training data set and the data where the Bayesian algorithm takes over. The circles in both the surfaces and the objective plots correspond to the training data sets (LHC), whereas a square corresponds to the data obtained by TS-EMO predicted conditions. On the surfaces, a black data point corresponds to points that lie on the Pareto front, whereas on the objective plots these data points are filled. Firstly, the optimisation of dimethylacrylamide was carried out. DMAm is a well-studied monomer with predictable behaviour in flow.[67] The experimental procedure can be found in the experimental section of this chapter, as well as the NMR and GPC procedure.

2.3.1 a. DMAm:TTC1:ACVA in water

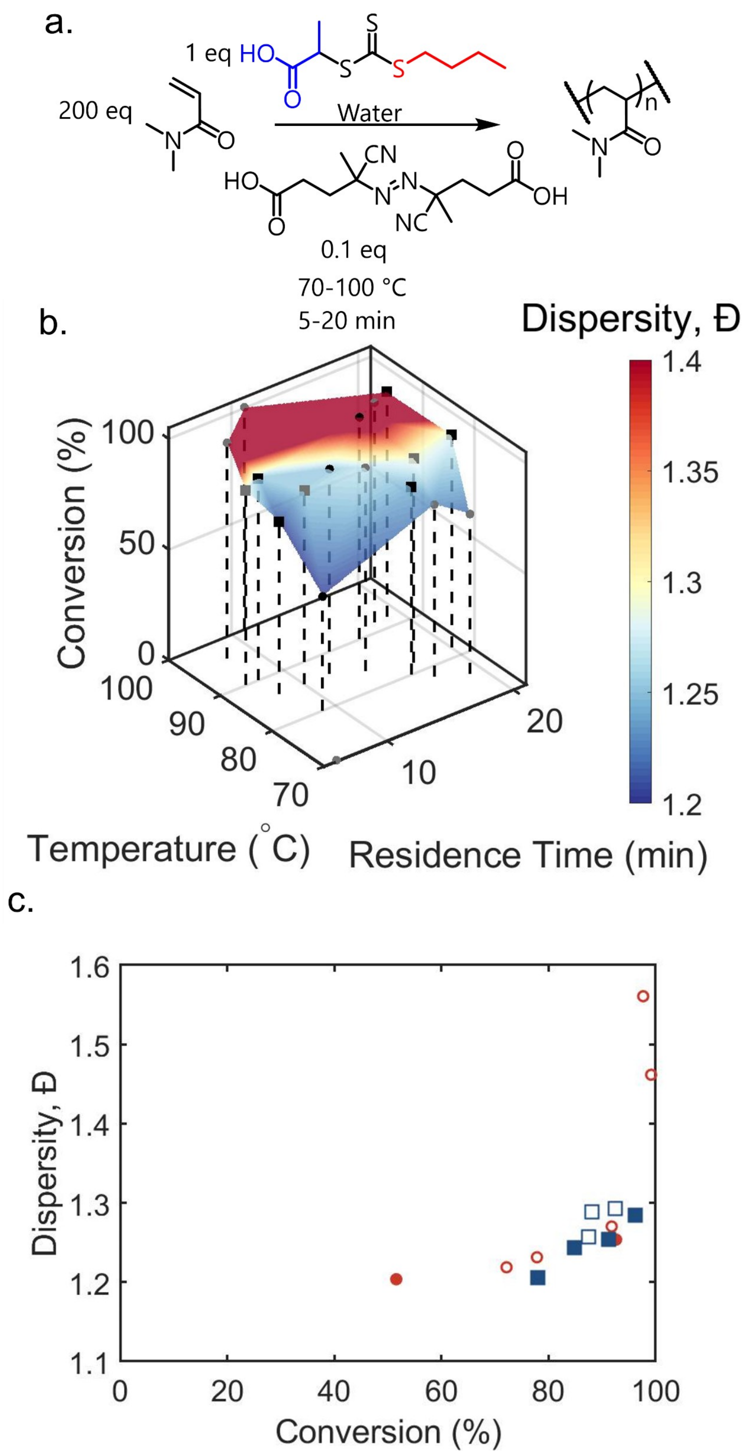

Figure 2.7: (a) The reaction scheme for the aqueous polymerisation of DMAm using TTC1 and ACVA. (b) 3D surface for the black-box optimisation demonstrating the effect of temperature and residence time on the molar mass dispersity (red =high *Đ*, blue = low *Đ*) and monomer conversion. Here, 10 LHC training data points (circles) were conducted then the TS-EMO (squares) in batches of 4 were suggested. Black data points represent the solutions that lie on the Pareto front. (c) Objective plot showing the trade off in conversion and dispersity (LHC - red circles TS-EMO -blue squares) and the points that lie on the Pareto front (filled data points)

As expected, at higher temperatures, higher conversions were achieved due to an increase in the initiation rate and higher k_d values. An increase in dispersity was observed at higher temperatures; which is typically observed when the rate of termination increases, This can be due to increased viscosity leading to increased rate of termination by disproportionation at higher temperatures which can broaden the MWD. The highest bluest point is the most desirable for most precision polymer applications; the nondominated solution with the lowest dispersity and the highest conversion can be identified at 82 °C after 20 min with a conversion of 96 % and a $Đ$ of 1.28. If high conversion was most desirable; the nondominated solution with the highest conversion and the lowest dispersity was observed at 90 °C and 16 min where full conversion and a $Đ$ of 1.45 were achieved. The Pareto front lies between temperatures of 76 and 92 °C; producing the most precise polymers between 4 and 15 min. The lowest $Đ$ of 1.20 was obtained after 9 min at 80 °C; however, only 51 % conversion was achieved. Here, a defined Pareto front can be observed in Figure 2.7.c which the TS-EMO successfully maps in 8 additional experiments. For the points where complete conversion was achieved, temperature has a large effect on dispersity with a $Đ$ of 1.64 and 1.72 at 92 and 100 °C, respectively; this was indicative of increased termination.

2.3.2 b. i. tBuAm:TTC1:AIBN in methanol

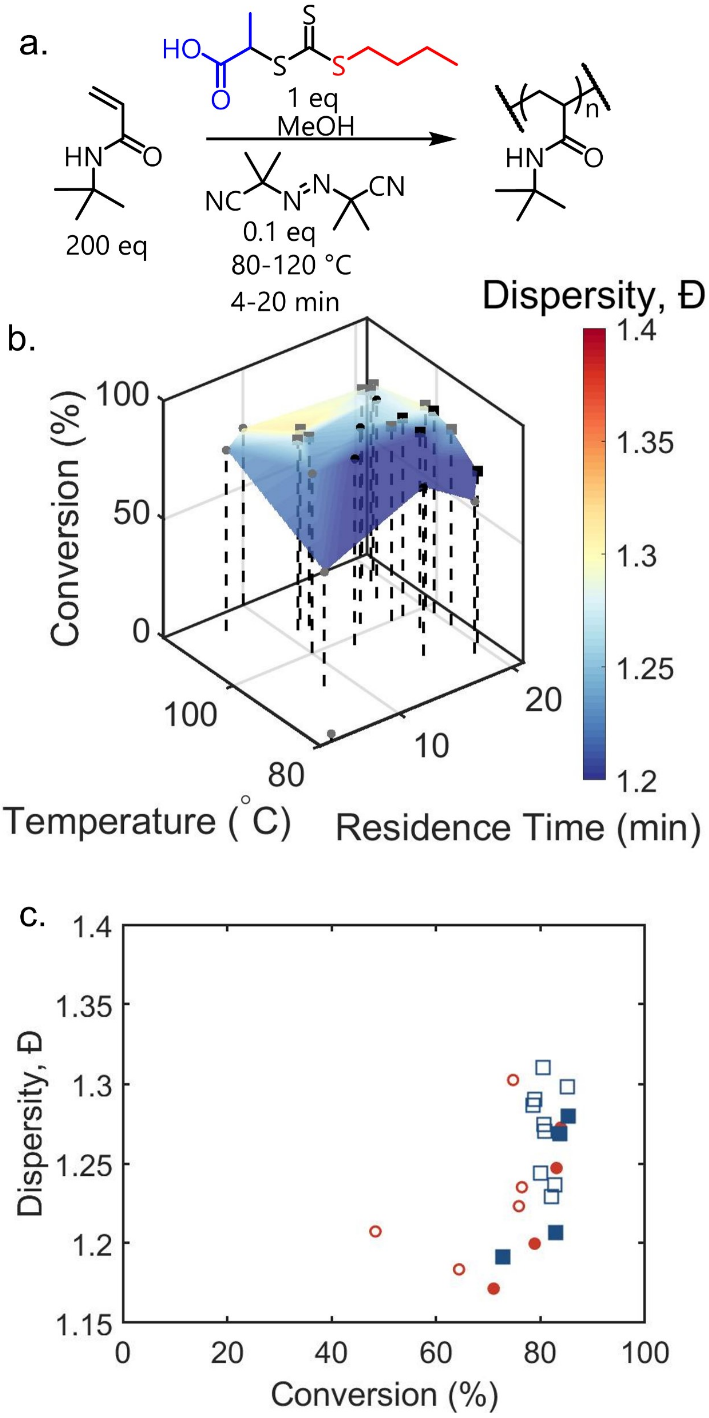

Figure 2.8: (a) The reaction scheme for the polymerisation of tBuAm using TTC1 and AIBN in methanol. (b) 3D surface for the black-box optimisation demonstrating the effect of temperature and residence time on the molar mass dispersity (red =high *Đ*, blue = low *Đ*) and monomer conversion. Here, 10 LHC training data points (circles) were conducted then the TS-EMO (squares) in batches of 4 were suggested. Black data points represent the solutions that lie on the Pareto front. (c) Objective plot showing the trade off in conversion and dispersity (LHC - red circles TS-EMO -blue squares) and the points that lie on the Pareto front (filled data points)

tBuAm is a less ideal monomer than DMAm due to its bulky pendant group. Here, a maximum conversion of 84 % was reached; to our knowledge, the literature shows that tBuAm conversion in alcoholic media never reaches a full conversion.[222] This has been thought to be due to backbiting in the same way that it affects AAm and MA as studied through pulsed laser polymerisation(PLP). Agboluaje *et al.*[222] have supported this idea by reducing the w/w % of the monomer in solution, reporting a broadening of the MWD and rate-retardation that can be attributed to backbiting through the formation of dead chains.

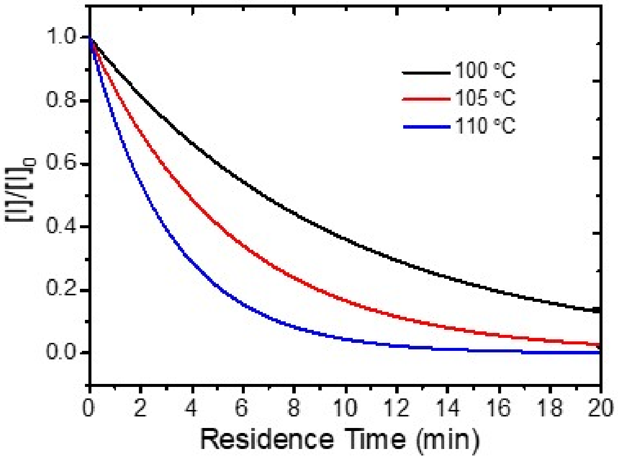

Figure 2.9: Simulated initiator fraction left if $E_a = 132.4\ kJ/mol$ and $\ln A = 36.6$ from the literature were inserted into the first order rate law.[223]

Conversion increases with temperature; however, at higher temperatures >100 °C a decrease in conversion can be seen. This can likely be explained by the low fraction of the initiator left; see Figure 2.9. The reaction will slow down if the concentration of radicals becomes 0 because the overall rate of polymerisation depends on the supply of radicals. Dispersity also increased at this point, probably as a result of an increase in the termination of the propagating radicals. The nondominated solution with the highest conversion and the lowest dispersity can be observed at 98 °C after 20 min, with a conversion of 85 % and a Đ of 1.28. The nondominated solution with the lowest dispersity and the highest conversion was identified at 90 °C after 16 min, which corresponds to a Đ of 1.17 at 71 %.

2.3.3 b. ii. tBuAm:TTC2:AIBN in methanol

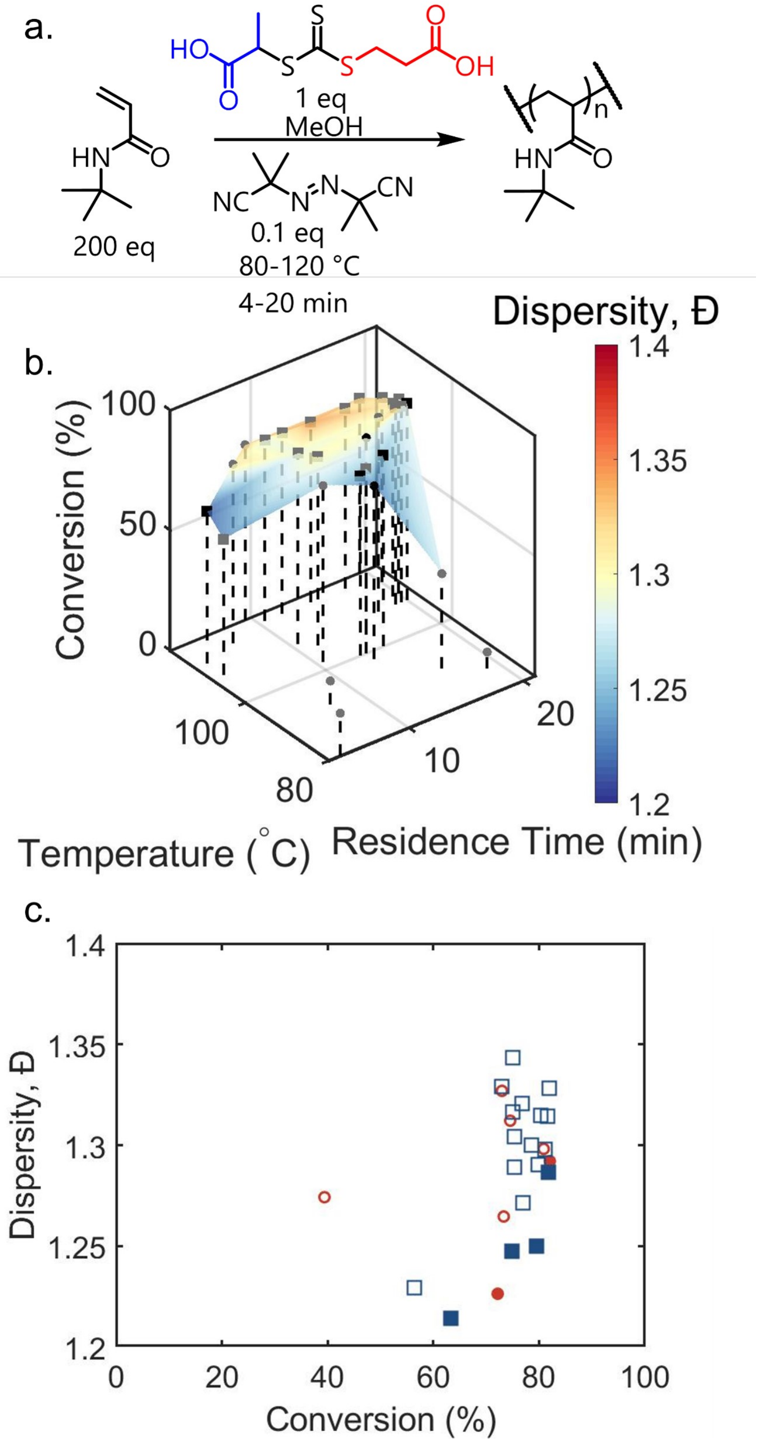

Figure 2.10: (a) The reaction scheme for the polymerisation of tBuAm using TTC2 and AIBN in methanol. (b) 3D surface for the black-box optimisation demonstrating the effect of temperature and residence time on the molar mass dispersity (red =high *Đ*, blue = low *Đ*) and monomer conversion. Here, 10 LHC training data points (circles) were conducted then the TS-EMO (squares) in batches of 4 were suggested. Black data points represent the solutions that lie on the Pareto front. (c) Objective plot showing the trade off in conversion and dispersity (LHC - red circles TS-EMO -blue squares) and the points that lie on the Pareto front (filled data points)

The highest conversion nondominated solution with the lowest dispersity can be observed at 104 °C after 15 min, where a conversion of 82 % and a *Đ* of 1.29. The nondominated solution with the lowest dispersity and the highest conversion was identified at 112 °C after 4 min, which corresponds to a *Đ* of 1.21 at 64 %. The overall dispersity observed for the polymerisation of tBuAm in the presence of TTC2 is higher, indicated by the lighter blue surface shown in Figure 2.10. b. The RAFT agent only differs depending on the Z group, TTC2 has a carboxylic acid at the end, which appears to lead to slightly lower conversion and higher values, these are evident by the 3 points in the LHC at low temperature that are outside of the colourmap limits. Lower conversions may be a result of increased rate of addition, whereas the presence of the more activated tBuAm chains on the radical adduct intermediate may affect the ability of the radical adduct intermediate from reforming the RAFT species and decrease the rate of fragmentation, increasing side reactions and dispersity.

2.3.4 b. iii. tBuAm: DTC: AIBN in methanol

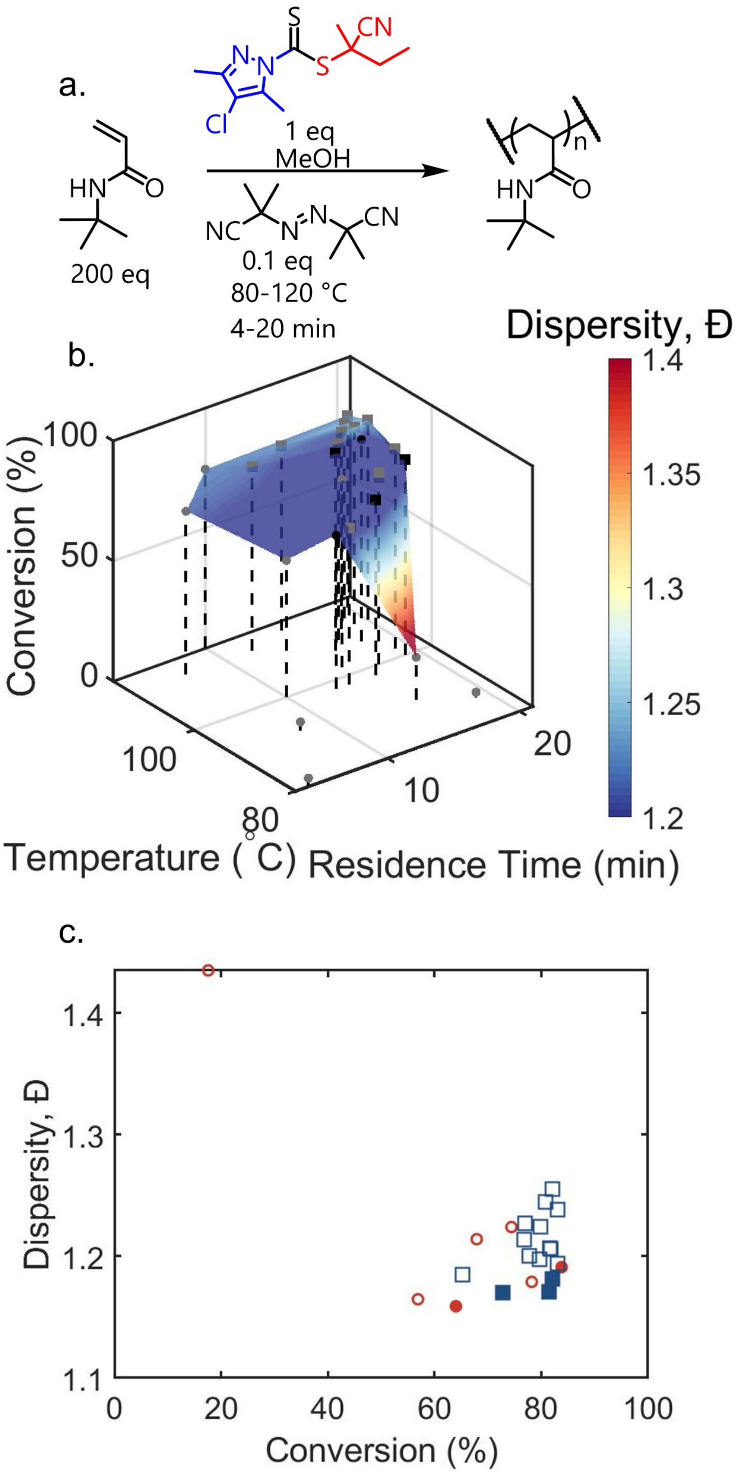

Figure 2.11: (a) The reaction scheme for the polymerisation of tBuAm using DTC and AIBN in methanol. (b) 3D surface for the black-box optimisation demonstrating the effect of temperature and residence time on the molar mass dispersity (red =high *Đ*, blue = low *Đ*) and monomer conversion. Here, 10 LHC training data points (circles) were conducted then the TS-EMO (squares) in batches of 4 were suggested. Black data points represent the solutions that lie on the Pareto front. (c) Objective plot showing the trade off in conversion and dispersity (LHC - red circles TS-EMO -blue squares) and the points that lie on the Pareto front (filled data points)

Here, the nondominated solution with the highest conversion and the lowest dispersity can be observed at 100 °C after 17 min, where a conversion of 80 % and a *Đ* of 1.19. The lowest dispersity nondominated solution with the highest conversion was identified at 98 °C after 13 min, which corresponds to a *Đ* of 1.16 at 64 %. Figure 2.11. b. has more blue on the surface compared to the surface in Figure 2.10. b., suggesting that the DTC species offers more control over the polymerisation of tBuAm. The black data points for the more controlled reactions shown in Figures 2.8. b and 2.11. b. are more clustered between 80 and 100 °C and 10 to 20 min, suggesting a more ideal reaction system where the trade-off was more defined.

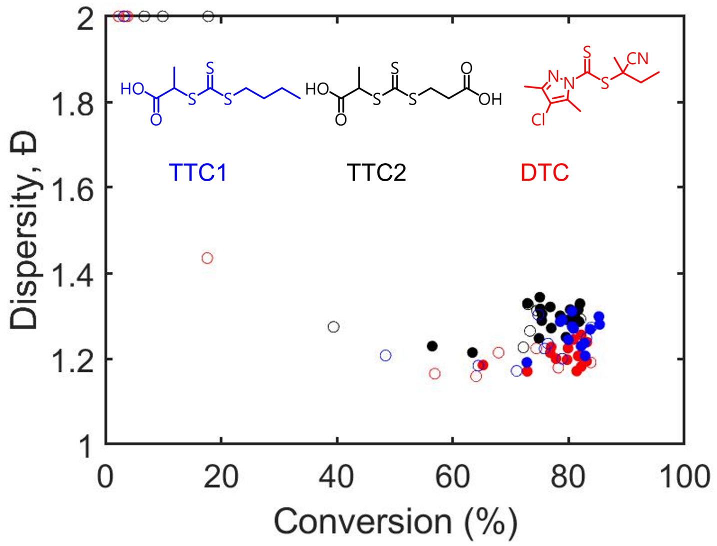

Figure 2.12: Objective comparison for tBuAm using RAFT agents TTC1(blue), TTC2(black) and DTC(red)

The objective plot in Figure 2.12 demonstrates the huge effect the Z group can have on the control of polymerisation. The monomer tBuAm is a more active monomer due to the presence of the electron-withdrawing amide group, TTC1 and TTC2 differ with respect to the Z group. Both TTC1 and TTC2 have identical R groups; which, in theory would mean the radical leaving groups have the same stability. However, the carboxylic acid on the Z group on TTC2 may offer some stability to the radical adduct intermediate, increasing k_f.[48] DTC provides a higher level of control indicated by the low *Đ*, computational studies have shown the halogen on the pyrazole ring could decrease the electron density of the ring increasing the availability of the lone pair on the N to be delocalised activating the C=S bond, increasing the addition rate constant. Low *Đ* obtained using DTC could be due to the improved homolytic leaving group capabilities of the 2-cyano-butyl radical compared to the propagating radicals, increasing fragmentation.[224]

2.3.5 b. iv. tBuAm:TTC2:AIBN in methanol with inline degassing

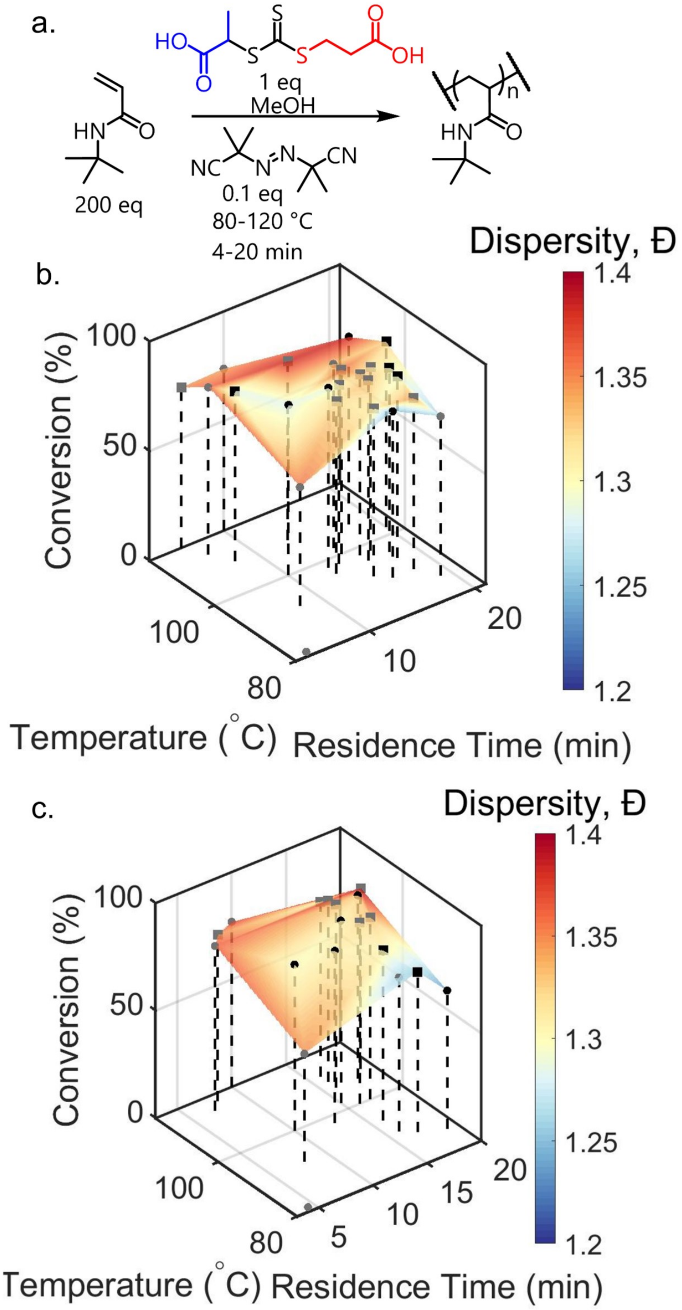

Figure 2.13: (a) The reaction scheme for the polymerisation of tBuAm using TTC2 and AIBN in methanol for the experiments using inline degasser. (b) 3D surface for the black-box optimisation using one degassing channel demonstrating the effect of temperature and residence time on the molar mass dispersity (red =high *Đ*, blue = low *Đ*) and monomer conversion. Here, 10 LHC training data points (circles) were conducted then the TS-EMO (squares) in batches of 4 were suggested. Black data points represent the solutions that lie on the Pareto front. (c) 3D surface for the black-box optimisation using three degassing channels demonstrating the effect of temperature and residence time on the molar mass dispersity (red =high *Đ*, blue = low *Đ*) and monomer conversion. Here, 10 LHC training data points (circles) were conducted then the TS-EMO (squares) in batches of 4 were suggested. Black data points represent the solutions that lie on the Pareto front.

To address the issue of oxygen quenching, an inline degasser was implemented into the platform prior to the reagent pump and an optimisation was performed using 1 and 3 channels overnight. A fairly discontinuous surface was observed using 1 degassing channel shown in Figure2.13. b. compared to the non-degassed platform shown in Figure 2.8. b, suggesting that the dissolved oxygen concentration was irregular. Following this experiment, the number of degassing channels was increased to 3 to see if the degassing efficiency would increase. The surface using 3 channels shown in Figure 2.13.c. is more continuous than that shown in Figure 2.13. b. From this it can be assumed that the longer the solution has to degass, the lower the oxygen concentration. This suggests that a steady state of degassing is required to efficiently use the inline degasser.

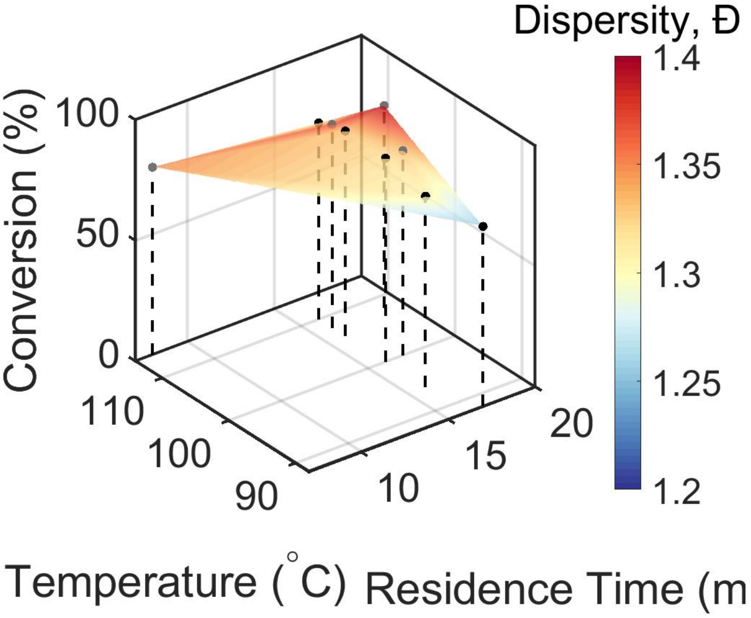

Figure 2.14: Surface for the optimisation of tBuAm:TTC2:AIBN using 3 degassing channels with the first 10 LHC experiments removed.

Subsequently, this effect that relates time to degassing efficiency was further investigated by removing the LHC from the surface. The surface becomes continuous after the first 60 mL of reaction solution. Each channel in the degasser is 10 mL; thus a 30 mL excess in reagents is required. A rapid priming rate was used to get the solution through the pump head to start optimisation. This 30 mL of solution would be degassed less than that at lower flow rates, as used in the optimisation. The level of degassing will vary depending on the flow rate; therefore, the inline degasser is not the best choice for removing oxygen.

2.3.6 c. nBuA:TTC1:AIBN in 1,4-dioxane

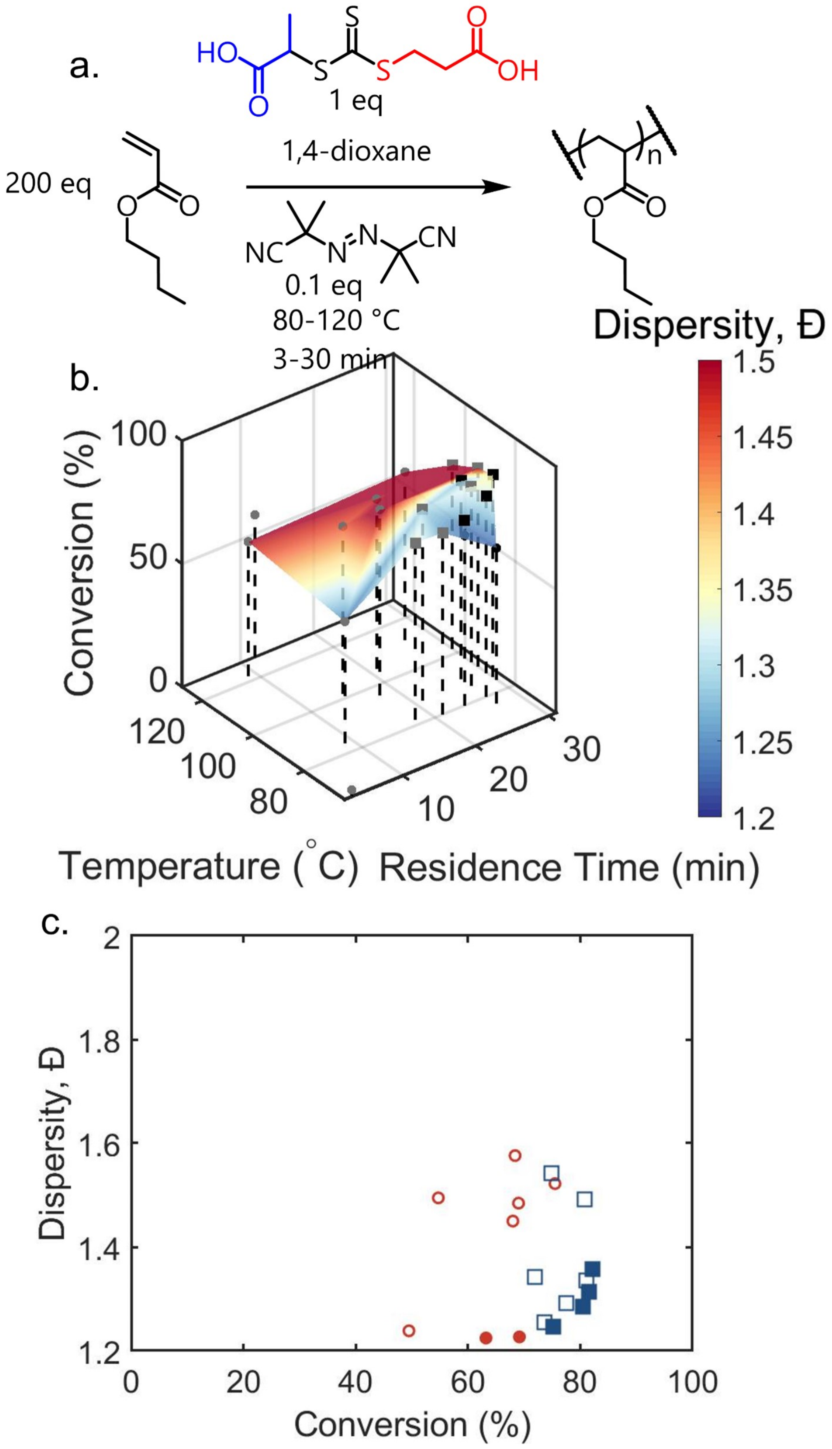

Figure 2.15: (a) The reaction scheme for the polymerisation of nBuA using TTC2 and AIBN in 1,4-dioxane. (b) 3D surface for the black-box optimisation demonstrating the effect of temperature and residence time on the molar mass dispersity (red =high *Đ*, blue = low *Đ*) and monomer conversion. Here, 10 LHC training data points (circles) were conducted then the TS-EMO (squares) in batches of 4 were suggested. Black data points represent the solutions that lie on the Pareto front. (c) Objective plot showing the trade off in conversion and dispersity (LHC - red circles TS-EMO -blue squares) and the points that lie on the Pareto front (filled data points)

Acrylates are another challenging monomer. The surface in Figure 2.15 shows a general increase in conversion between 80 and 100 °C with increasing $Đ$ at higher temperatures. At temperatures greater than 100 °C, the conversion begins to decrease significantly. This retardation in the rate of monomer conversion is likely due to side reactions that decrease the rate of propagation associated with the formation of mid-chain radicals(MCRs) and (secondary propagating radicals (SPRs), as mentioned in Chapter 1. It is unlikely that at the temperatures used in this optimisation, a sufficient amount of macromonomer would form due to β-scission that would cause an larger vinyl integrals and a maximum apparent conversion of 80 %. A significant macromonomer concentration has been found at temperatures >140 °C by mass spectrometry.[225] However, it may be possible that other reactions that occur at the same time due to the formation of MCR and SPR lead to the observed rate retardation. In Figure 2.15.b, the lowest $Đ$ nondominated solution with the highest conversion was found to be 1.22 with a conversion of 63 % after 27 mins at 76 °C. However, the nondominated solution with the highest conversion and the lowest dispersity was found to be 82 % with a $Đ$ of 1.31 after 27 min at 80 °C which is only 4 degrees higher than the lowest $Đ$ data; showing a strong temperature dependence.

A statistical block copolymerisation was also performed using DMAm and pentafluorophenyl acrylate in a 5 mL tubular flow reactor. The GUI was also adapted to obtain ^{19}F NMR spectra to allow the conversion of the fluorinated monomer to be analysed; however, the usability of this requires further development of data processing due to the low resolution ^{19}F NMR spectra.

2.3.7 d. Statistical co-polymerisation of DMAm:PFPA:TTC2:ACVA in acetonitrile

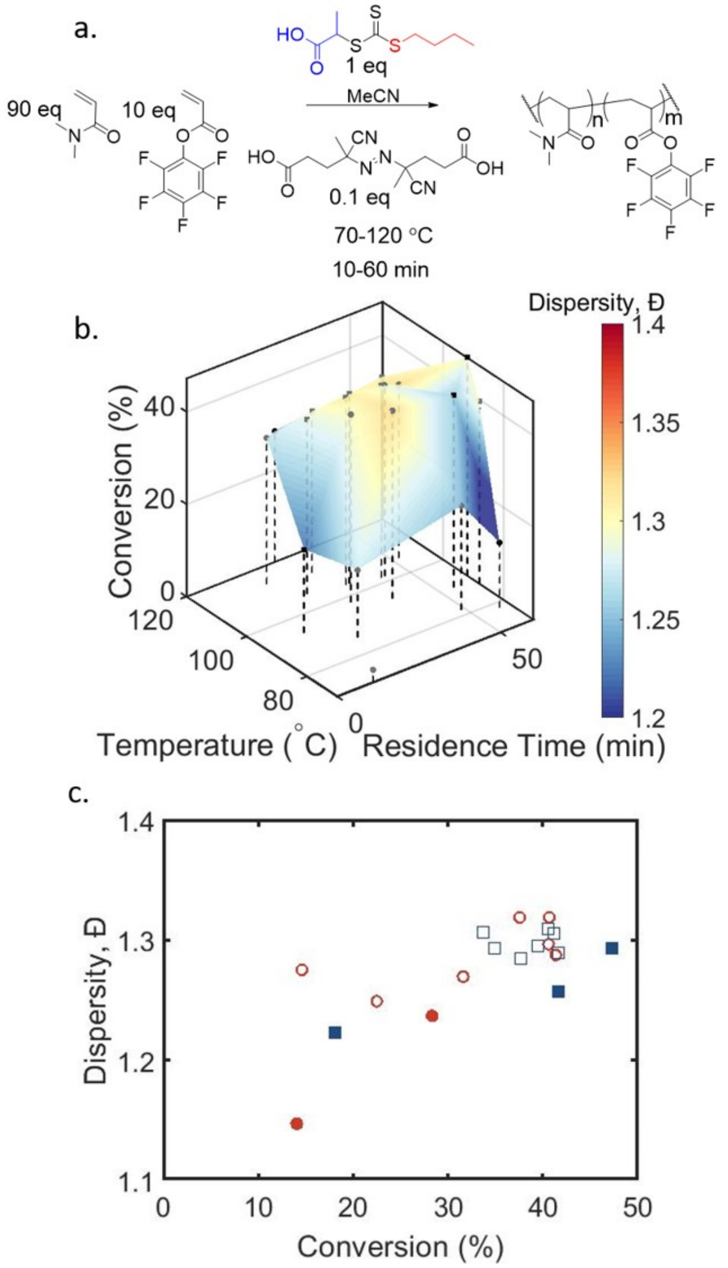

Figure 2.16: (a) The reaction scheme for the statistical co-polymerisation of DMAm and PFPA in the presence of TTC2 using ACVA as the initiator at a 90:10:1:0.1 reagent ratio in aceto nitrile. (b) 3D surface for the black-box optimisation demonstrating the effect of temperature and residence time on the molar mass dispersity (red =high *Đ*, blue = low *Đ*) and monomer conversion. Here, 10 LHC training data points (circles) were conducted then the TS-EMO (squares) in batches of 4 were suggested. Black data points represent the solutions that lie on the Pareto front. (c) Objective plot showing the trade off in conversion and dispersity (LHC - red circles TS-EMO -blue squares) and the points that lie on the Pareto front (filled data points)

The lowest Đ nondominated solution with the highest conversion is observed after 57 min at 78 °C, where a Đ of 1.15 and a conversion of 14 %. However, the non-dominated solution with the highest conversion and the lowest Đ is identified after 60 min at 90 °C , obtaining a conversion of 47 % and a of 1.29. The data shown in Figure 2.16.b show low conversion with a maximum conversion of 47 % achieved. This may be explained by the fact that the polarity of the solvent has been shown to be critical to the polymerisation rate. Polar protic solvents such as water have been shown to stabilise the transition states of propagating radicals, lowering activation energies by hydrogen bonding to the amide bond.[226] In acetonitrile, the rate of polymerisation is slower as there is no opportunity for hydrogen bonds to increase the reactivity of the C=C bond. It is important to note that the presence of PFPA can also cause slower kinetics, due to the fact that acrylates exhibit slower propagation rates, as studied using PLP by Lacik *et al.*.[227] Higher temperatures are shown to lead to a decrease in the polymerisation rate here, which could be due to the activation energy of the PFPA being overcome, causing it to consume some of the radicals.

2.4 Conclusions

To conclude this section, a series of operator-independent optimisations have been performed for challenging RAFT polymerisations. A series of RAFT agents for polymerisations of tBuAm have been compared, which have shown that a Cl-substituted DTC offers superior control. For TTCs, reduction of the electron-withdrawing capability of the Z group offers improved control. The use of an in-line degasser proved inefficient and the internal volume was shown to be too large to be a feasible way of degassing the system. Rate retardation has also been shown to be largely affected at temperatures >80 °C owing to the presence of secondary and mid-chain radicals that subsequently increase the dispersity of polymers. The optimisation platform has also been used to optimise a statistical copolymerisation, where the data demonstrated a rate retardation at high temperatures that led to a maximum conversion of 47 %. ^{19}F NMR was collected to see if PFPA conversion could be monitored; however, resolution limited the usability of these data. Further experimentation may require repeating this experiment by using a higher initiator concentration and optimising data processing of the fluorine NMR. This series of reactions provided proof of concept for the self-optimisation of RAFT in an operator independent reactor. The data obtained provides valuable information on RAFT agent suitability which is used in the rest of this thesis, directly or implied. The limitation of this chapter was that the initiator concentration, which also effects the kinetics, was fixed. In the next chapter, the engineering challenges and solutions associated with changing initiator concentration inline will be addressed.

Chapter 3

Reactor Design and Characterisation of a Three-Pump Reactor Platform for Multi-objective RAFT Polymerisation

3.1 Introduction

Having explored the 2D reaction space in Chapter 2 focussing on the effect of temperature and residence on kinetics and $Đ$ the aim of this Chapter was to develop the platform by addressing and characterising potential challenges. As discussed in Chapter 1, both Gobert *et al.*[121] and Reis *et al.*[123] have investigated the effects of certain parameters on RTD, such as mean residence time,[121,123] channel diameter,[121,123] static mixing[121] and viscosity.[123] Reis *et al.*[123] reported a great effect on MWD and therefore molar mass dispersity. Here, we conduct RTDs on two different tubing diameters, using a UV/Vis-responsive dye tracer on a 2 pump platform. An RI detector was used to replace the UV/Vis detector, the RI signal for a DMAm and $PDMAm_{200}$ tracer was conducted in the narrowest diameter, and the dispersion model for RTD was applied. This enabled the viscosity, mean residence time, and temperature effects to be investigated. Mixing is important when considering fast reactions. Zhong *et al.*[228] demonstrated the effect of a Y mixer compared with that for a packed-bed plug mixer on the dispersity for photochemically driven RAFT. The packed bed was shown to lead to narrower MWDs and lower dispersity than the Y-mixer.[228] Here, the mixing ability of 3 commercially available mixers was compared to a homemade packed bed by investigating the effect of dispersity. In tandem, the effect of different reactor sizes and viscosity on RTD was compared for a 2 pump and a 3 pump platform to minimise the effect of RTD on the MWDs.

3.2 Mixing

3.2.1 Experimental

The monomer used for the mixing study was N,N-dimethyl acrylamide ((DMAm) 99 %, contains 500 ppm monomethyl ether hydroquinone as inhibitor, CAS 2680-03-7) purchased from Sigma Aldrich. 3-((((1-carboxyethyl)thio)carbonothioyl)thio)propanoic acid ((TTC2) 95 %, CAS 870451-09-5) and 2,2'-Azobis[2-(2-imidazolin-2-yl)propane]dihydrochloride ((VA044), CAS 27776-21-2)

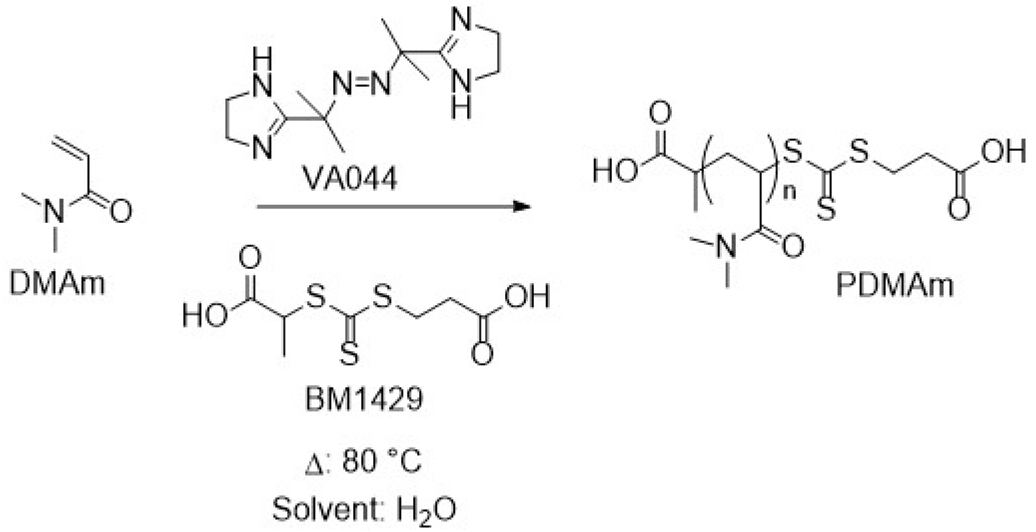

Figure 3.1: Reaction scheme for the the all-aqueous solution RAFT polymerisation of DMAm using TTC1 and VA044 under an atmosphere of nitrogen, using the ratio 100:1:0.02 at 50 w/w %

Batch

A solution of BM1429 (0.25 g, 0.097 M) and VA-044 (6.20 mg, 0.0019 M) was prepared in water (10 g) using sodium bicarbonate (1 M) as a solubility agent for the carboxylic acid groups of CTA. To this solution, neat DMAm (9.62 g, 9.7 M) was added. This was stirred under an atmosphere of nitrogen for 20 min before heating to 80 °C.

Continuous Flow Set-up

Neat DMA (20 g, 0.20 mol) was degassed under nitrogen for 20 min together with a separate solution of CCTP (0.51 g, 0.002 mol) and VA044 (13 mg, 0.04 mmol) in H2O (20.0 g) using sodium bicarbonate (1 M) dropwise as solubilising agent. The two solutions were pumped through a 5 mL 1/8" reactor at 2 separate flow rates, maintaining residence times of 10 min and 20 min, respectively. Static samples were taken by GPC and low-field NMR was used to characterise mixing.

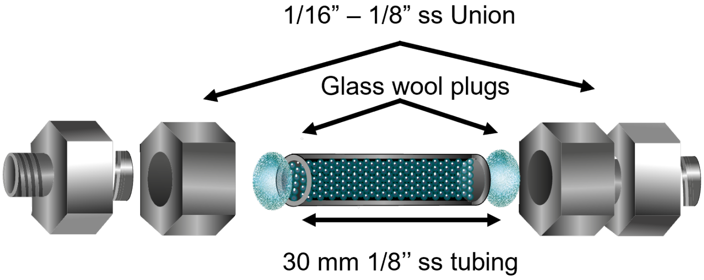

Figure 3.2: Home-made packed bed mixer, consisting of a 30 mm piece of stainless steel tubing filled with 40 mesh glass beads and glass plugs at each side to stop to beads from getting into the reactor

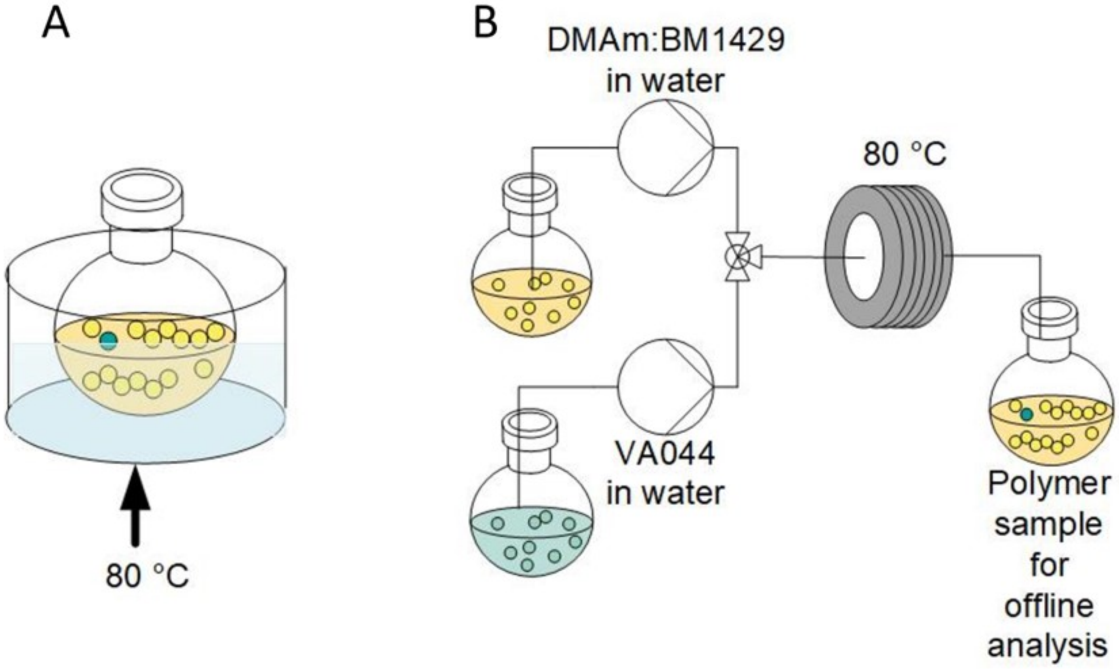

Figure 3.3: (A) Schematic of the batch set up where samples were taken after 20 mins (B) schematic of the initial flow setup

3.2.2 Results and Discussion

The ultra-fast RAFT polymerisation of dimethylacrylamide was selected as a model system due to its predictable and rapid kinetics in water.[229] Rapid kinetics associated with RAFT polymerisation require additional mixing. Efficient mixing by diffusion is often regarded an inherent feature of flow reactors because of the large surface area to volume ratio. The Damkohler number, Da, mentioned in Chapter 1 can give us an idea of the chemical reaction rate to the rate of mass transfer by diffusion ratio; if Da $>$ 1 then mixing is slower than the reaction rate and vice versa.[117] I

Table 3.1: Table comparing mixing in flow relying on diffusion compared to batch after 10 minutes. Conversion (α) was found using bench-top NMR and off-line GPC was used to obtain molecular M_w *(g/mol)*and M_n *(g/mol)*

Mixer	M_n *(g/mol)*	M_w *(g/mol)*	Đ	α (%)
T-piece	27300	50100	1.84	51
Batch	8600	10500	1.22	96

It is very evident from Table 3.1 that relying solely on diffusion causes a huge effect on conversion and dispersity. For the Swagelok t-piece the conversion is reduced by 46 %; this combined with the high M_w in dictated that there is localised variation in the the reactor and that mixing by diffusion is slower than the rate of the reaction.[117]From these findings a series of RAFT polymerisations were conducted in continuous flow using 3 micromixers: (1) a packed bed, (2) a high-pressure t-piece(Idex High-Pressure micro-static mixing tee) and (3) an inversion tee(Idex PEEK High-Pressure Mixing Tee Body) these were then compared to each other and a standard Swagelok t-piece.

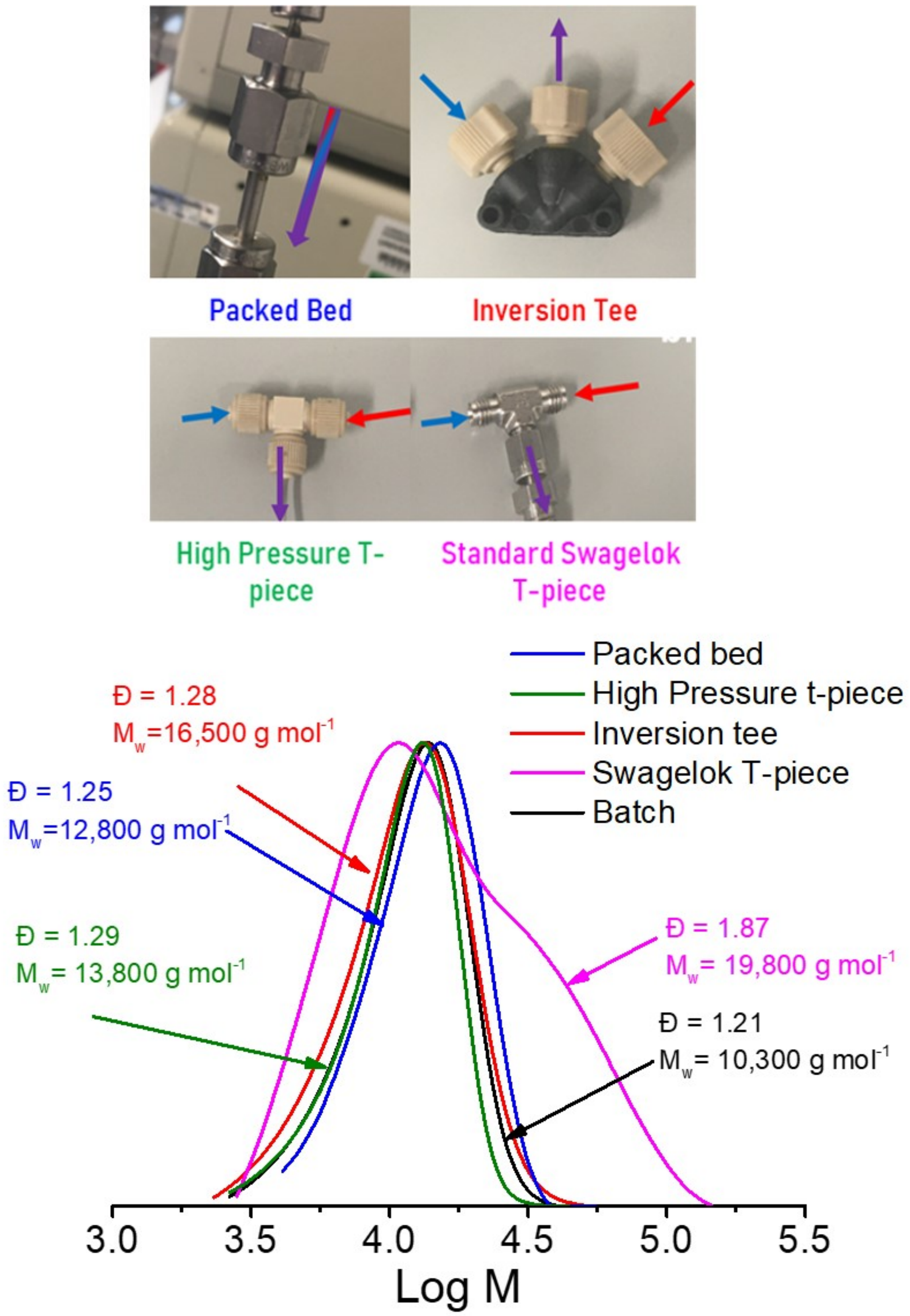

Figure 3.4: Molecular weight distributions comparing batch (black), the packed bed (blue), inversion tee (red), High-pressure t-piece (green) and the swagelok t-piece (magenta).

The MWD for the control Swagelok t-piece in Figure 3.4 demonstrates very poor mixing. A shoulder in the distribution was indicative of local variation in the concentration of the reagents. This was not unexpected because mass transport by diffusion takes longer than the rate of the reaction; consequently, it can be assumed that the reaction solution has not reached homogeneity as it enters the heated reactor. The packed bed outperformed both commercially available micromixers; which showed slight narrowing of the MWD compared to the swagelok t-piece with the inversion tee being the best commercial option. The presence of glass beads in the packed bed potentially increases the surface area to volume ratio whilst also providing disruption in the fluid flow. The mixing effects on the dispersity were further investigated for the 2 superior mixers. in this case, the packed bed and the inversion tee.

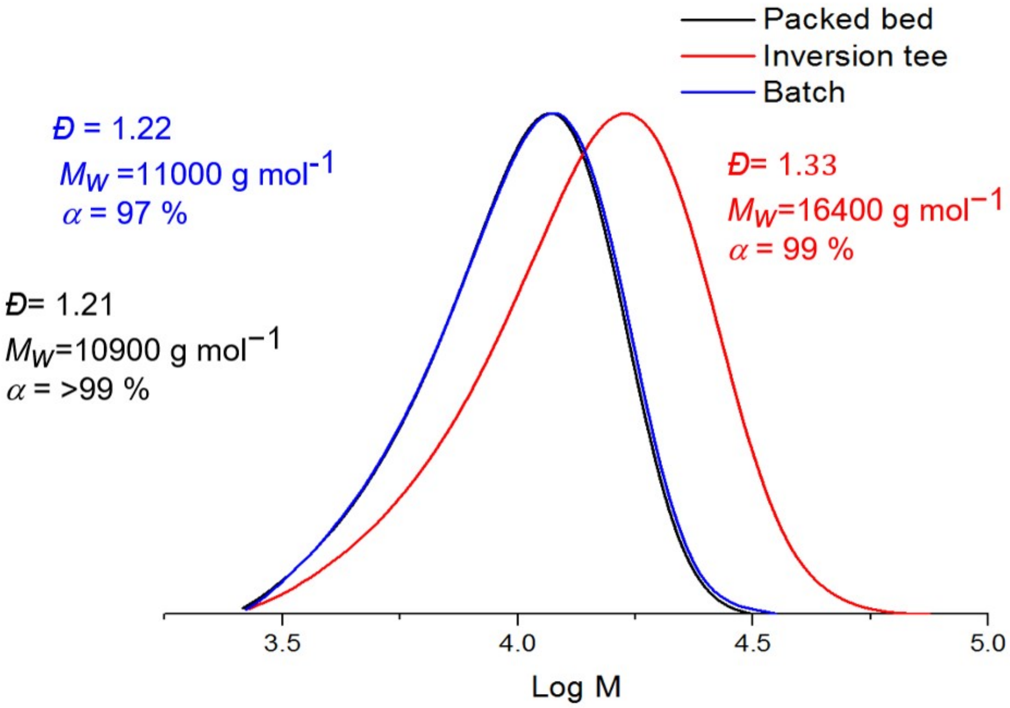

Figure 3.5: Molecular weight distributions for the black (blue), inversion tee (red) and batch (black) taken after 20 minutes.

The data in Figure 3.5 show an improved conversion for the packed bed and the inversion tee compared to the batch experiment after 20 min. This is indicative of improved heat transfer, which is a well-studied benefit of flow as a result of increased surface area to volume ratios.[117] The lower $Đ$ observed for the packed bed compared to the inversion tee can be attributed to increased surface area-to-volume ratio and the alteration of flow patterns. The higher M_w for the inversion tee is due to the localised variation in reagent concentrations and inefficient mixing leading to higher molecular weights. This is because the degree of polymerisation is proportional to the ratio of monomer to RAFT agent multiplied by the conversion, so a variation in the concentration of RAFT agent can lead to a variation in molecular weight. Additionally, conversion depends on the concentration of propagating radicals generated, so variation in initiator concentration can lead to variations in conversion and, in turn, molecular weight.

3.3 Residence time distributions

3.3.1 Experimental

The reagents used in this section, were: N,N-dimethylacrylamide ((DMAm) 99 %, contains 500 ppm monomethyl ether hydroquinone as inhibitor, CAS 2680-03-7) purchased from Sigma Aldrich, 2-(Butylthiocarbonothioylthio)propanoic acid ((TTC1) 95 %, CAS 480436-46-2) purchased from Boron Molecular. The polymer was synthesised using 2,2'-Azobis[2-(2-imidazolin-2-yl)propane]dihydrochloride ((VA044), CAS 27776-21-2) purchased from Wako.

The PDMAm tracer was synthesised in flow:

DMAm (20 g, 200 eq) and TTC1 (0.28 g, 1 eq) and VA044 (32 mg, 0.1 eq) were dissolved in water (47.5 g) and the solution was pumped through a 5 mL reactor at 92 °C for 3 reactor volumes. A conversion monitored by benchtop NMR of $>$99% was reached with an offline GPC $Đ$ of 1.18.

For the DMAm:TTC1 tracer:

DMAm (10 g, 200 eq) and TTC1 (0.07 g, 1 eq) were dissolved in water (11.8 g). Offline bench-top NMR was used for characterisation in the mixing study, using the same PRESAT configuration as in Chapter 2. Offline GPC was used to characterise the molecular weight distributions, for the offline measurements in this Chapter and Chapter 4 an Agilent 1260 infinity GPC was used with refractive index (RI) and UV/Vis detectors (309 nm). Fitted with two 5 μm Mixed-C columns and guard column, the eluent used was LiBr treated DMF (0.1 w/w %). The GPC was calibrated with methyl methacrylate standards with M_p values between 833-2,200,000 g/mol.

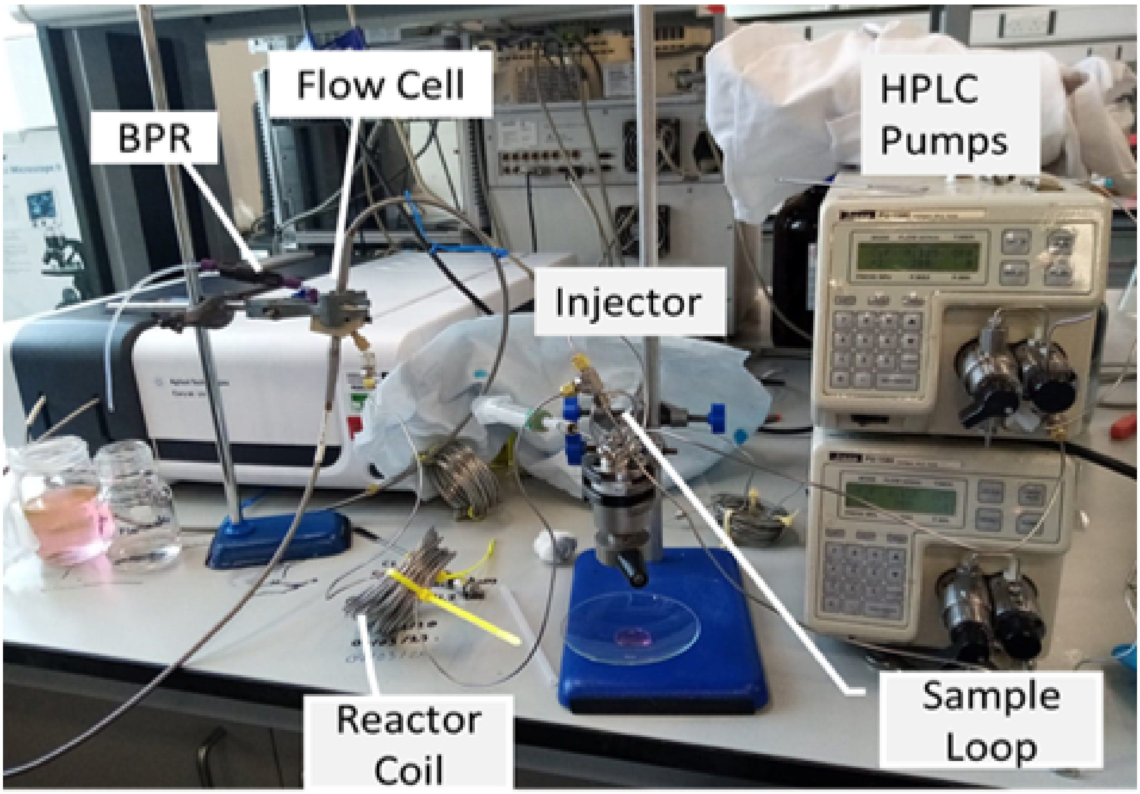

Figure 3.6: Image of how the UV RTDs seen in this section were collected using a manual switching valve to inject eosin Y into the coils

As the RTD has been shown to have an impact on the dispersity of polymers[123] Here, two RTD set-ups were used to characterise the behaviour of a set of tubular flow reactors operating in a series of configurations. Firstly, the diameter of the tubing and effect of a single packed bed was compared using set-up 1 (two pumps, Eosin Y tracer in water detected with UV/Vis). Subsequently, a third pump was added and the monomer and polymer were used as tracers to observe the effect of viscosity, residence time, temperature, and reactor volume using RI detection. Then, a program was integrated into the platform for autonomous RTD elucidation.

3.3.2 Results and Discussion

UV/Vis Detection

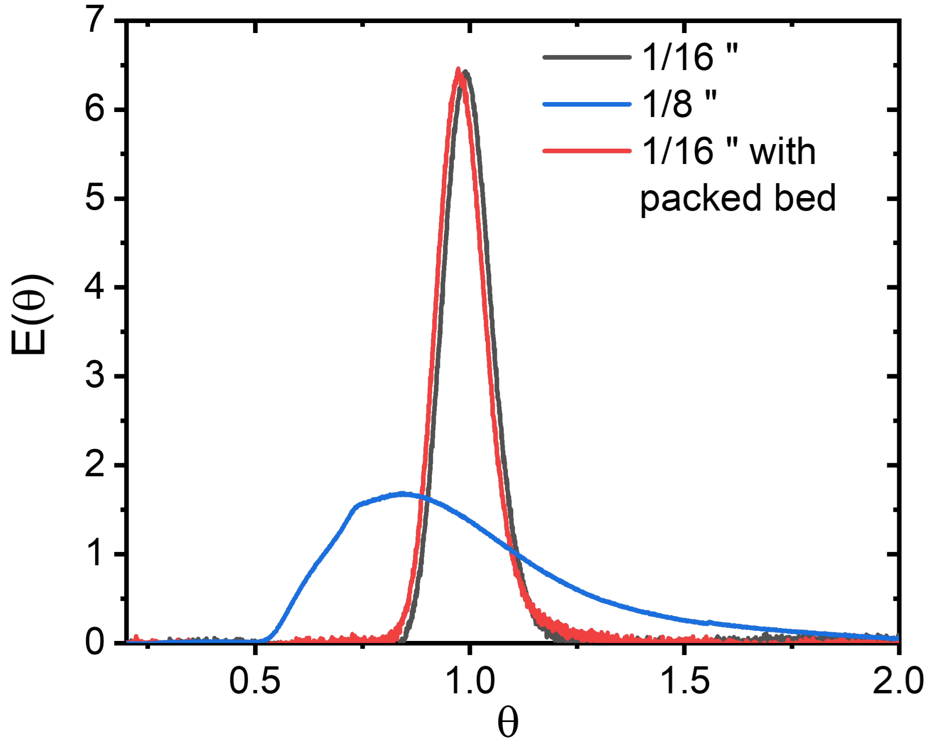

Figure 3.7: Comparison of the dimensionless RTDs investigating the effect of tubing diameters of 1/8" stainless steel(blue line), 1/16" stainless steel(black line) and the effect of the packed bed(redline)

Figure 3.7 was in agreement with the trends observed in Reis *et al.*.[123] The RTD for the 1/8" outer diameter (OD) reactor was much broader than the 1/16" OD reactor, and the tracer takes much longer to leave the reactor. Dimensionless θ represents the number of reactor volumes taken for the tracer to be expelled from the reactor. For the 1/8" OD tubing, this was around 2 reactor volumes compared to around 1.1 for both 1/16" OD with and without the packed bed. A known drawback of packed-bed reactors/mixers is the pressure drop associated with the plug, to limit this effect 425-600 μm (30-40 sieve) SiO_2 beads were used and the mixer length was kept short. The packed bed was shown to have minimal impact on the RTD which could be attributed to the short-length and relatively large-diameter beads. The 1/8" OD reactor also shows an asymmetric RTD suggesting that the dispersion model has fallen apart, which occurs when increasing the diameter of the tubing; thus, the convective model is more appropriate.[120]

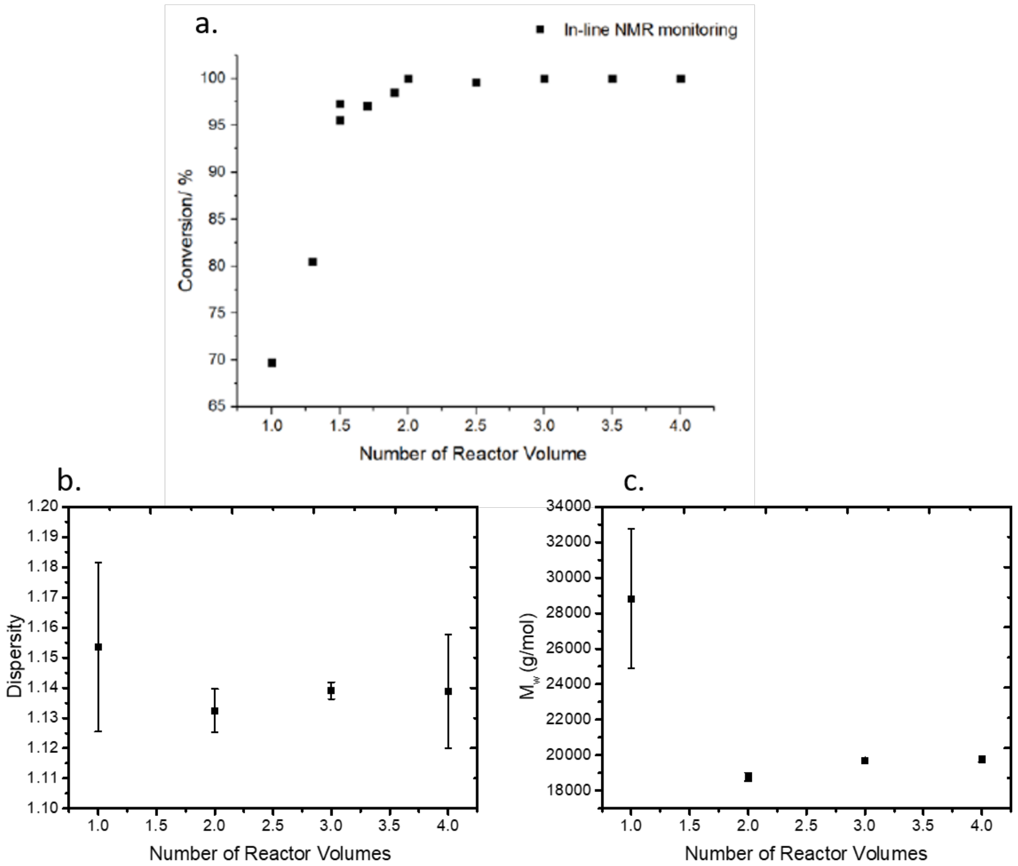

Figure 3.8: (a) Conversion monitored by online NMR, (b) offline GPC calculated dispersity and (c) weight average molecular weight for the polymerisation of DMAm (100:1:0.02 DMAm:TTC1:VA044 as a function of reactor volume for a residence time of 20 mins in the 3 pump reactor.

The number of reactor volumes could then be validated by monitoring the conversion change with respect to the number of reactor volumes. The monitored reaction conversion shows a steep incline between 0 and 2 reactor volumes, as seen in Figure 3.8.a. The NMR conversion reaches a steady state after 2.5 reactor volumes, conversion by NMR was concordant with *Đ* andM_n reaching a relatively constant value after 2 reactor volumes. Higher dispersity was shown after 1 reactor volume which was likely a result of localised variation of reagent concentrations leading to broader molecular weight distributions, this was also corroborated by the higher M_w. Therefore, all kinetic experiments were conducted after 3 reactor volumes to ensure that the system had reached steady state prior to analysis.

RI detection

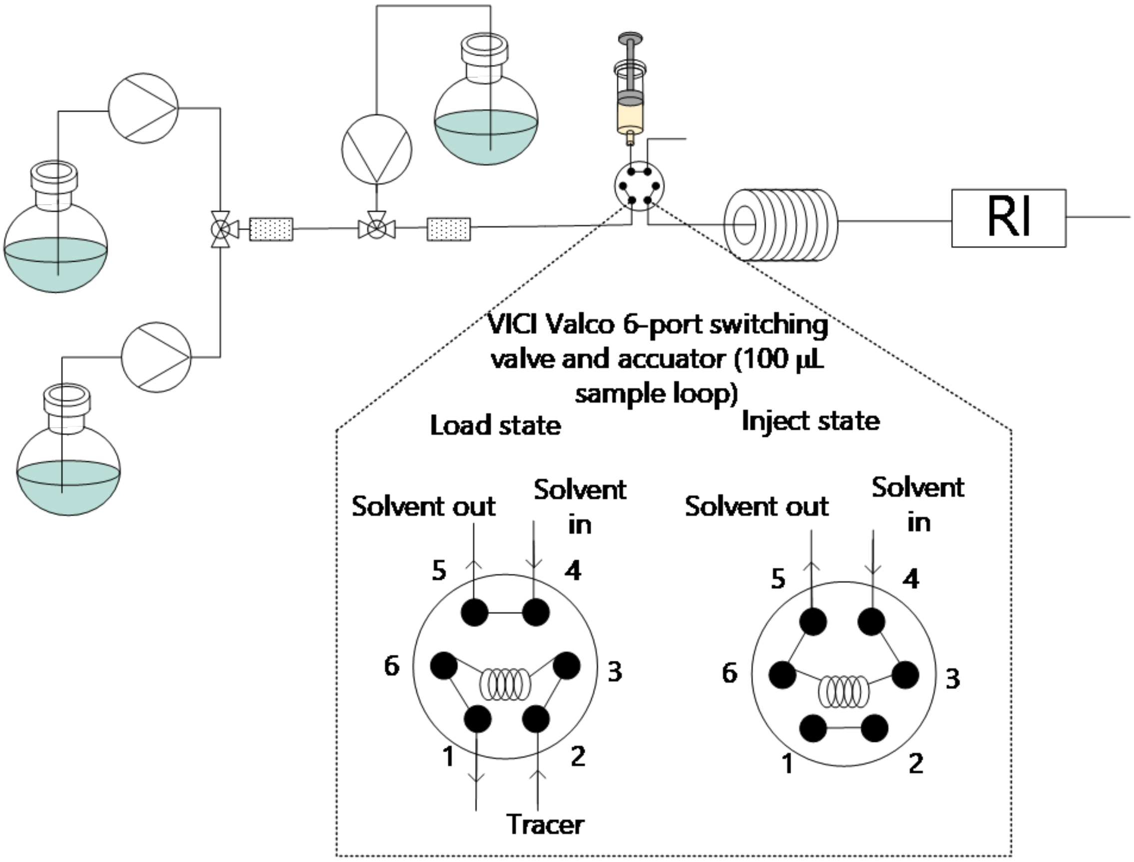

Figure 3.9: The reactor set-up used to obtain RTDs autonomously

An automated residence time distribution platform was developed based on the RI response of the monomer and polymer seen in Figure 3.9. Here, the monomer solution and the polymer solution were injected into a 100 (μL) sample loop, a 2 position VICI Valco 6 port switching valve and actuator were used to autonomously inject the polymer into the reactor coil and/or mixer. The RI signal was then detected by a Knauer RI detector. First, the RTD of a 5 mL and a 2 mL coil with an OD of 1/16" were compared.

The Effect of Residence Time

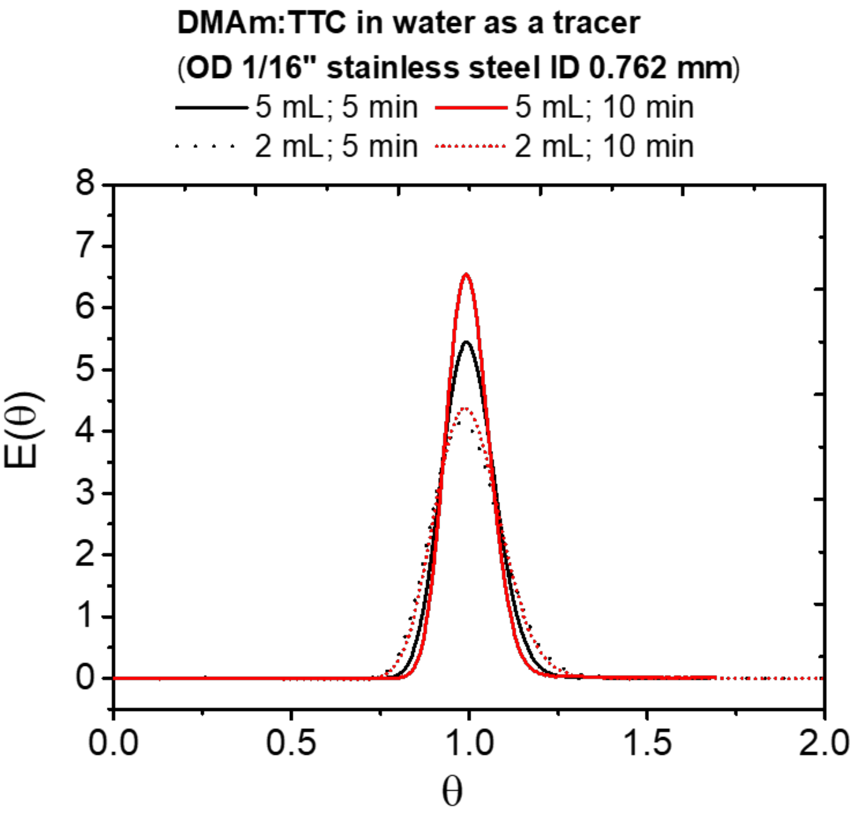

Figure 3.10: Dimensionless RTDs for a 2 mL coil (dotted line) and 5 mL coil (solid line) at a target residence time of 5 min (black) and 10 mins(red)

The residence time distributions obtained using the set-up in Figure 3.9 with two reactors of different sizes (2 mL and 5 mL) were compared with the two different target residence times. The larger volume coil produced the narrowest RTD, which was likely due to having a larger Reynolds number. Furthermore, longer residence times (slower flow rates) have a narrower RTD, which is consistent with studies by Reis *et al.*[123] and Gobert *et al.*[121]

The Effect of The Tracer Viscosity

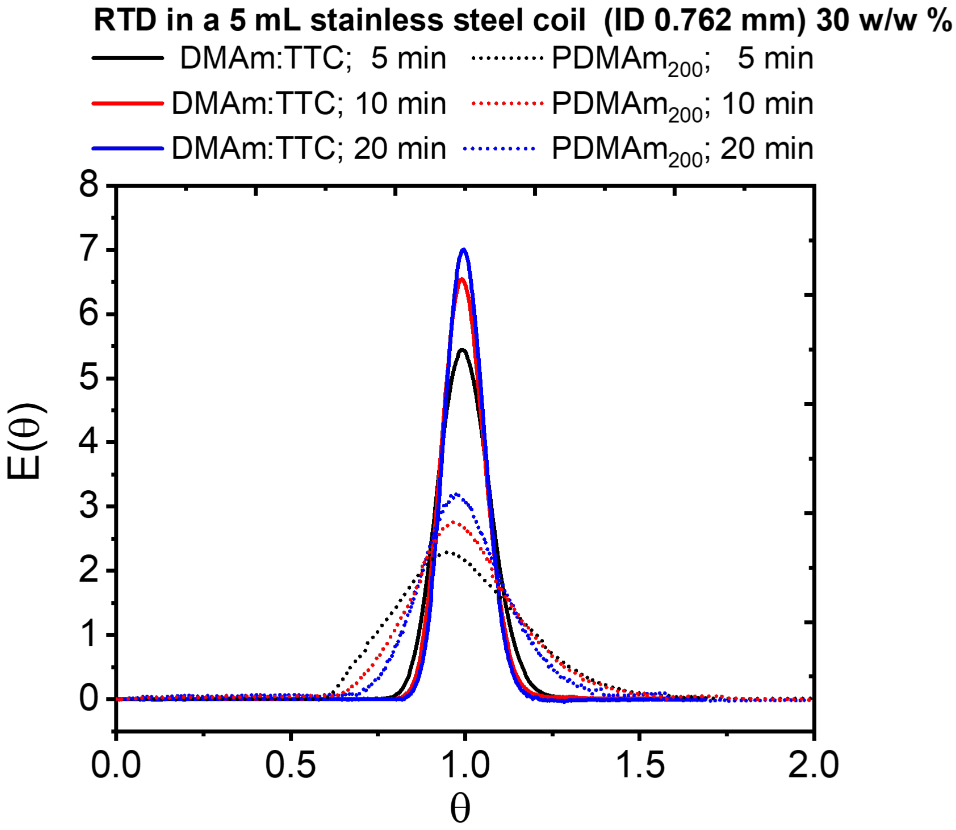

Figure 3.11: Dimensionless RTDs for a 5 mL coil at a target residence time of 5 min (black), 10 mins (red) and 20 mins (blue) using DMAm:TTC(solid line) and $PDMAm_200$/TTC(dotted line) as a tracer

Polymers typically have a viscosity higher than that of the monomer even in solution. Here, a solution of DMAm/TTC and $PDMAm_{200}$/TTC both at at 30 w/w % in water was injected as a pulse into a stream of solvent. The RTDs where the PDMA tracer was injected were broader and shorter than those of the DMAm; this is a result of the forces between the tube wall and the outer solution, causing a broader velocity profile, and the effect of residence time is evident here, with longer average residence times having narrower distributions. For the polymer tracer, the distributions were asymmetric, indicating that the dispersion model was no longer in effect because of the slow molecular diffusion and viscosity associated with polymer chains. This was previously predicted by Reis *et al.*[123] As viscosity can be affected by temperature, the polymer tracer was injected into the reactor at 2 temperatures, 70 ° C and room temperature to account for this.

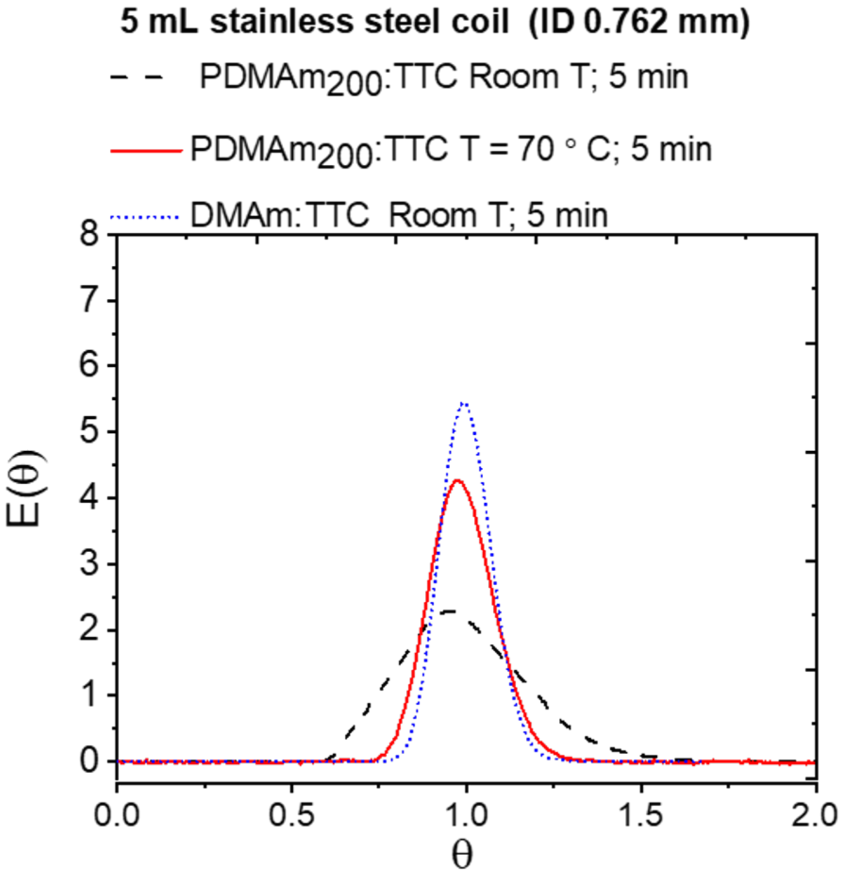

Figure 3.12: Dimensionless RTDs for a 5 mL coil heated to 70 °C (red solid line) and at room temperature(black dashed) using PDMAm as the tracer.

At room temperature, the polymer RTD was broader and slightly asymmetric; explained by the dispersion model falling apart. However, in a heated reactor, this becomes more symmetric. This is likely due to the reduction in viscosity at higher temperature and the increased free movement of the polymer chains. However, even at 70 ° C the RTD of the PDMAm tracer is still broader than that of the monomer tracer.

Table 3.2: Table of average residence time(τ), calculated using equation 1.18 in Chapter 1. † Conducted at 70 °C

Tracer	V	t_{target}	τ
DMAm	2	5	5.57
DMAm	2	10	11.79
DMAm	5	5	4.75
DMAm	5	10	9.99
PDMAm	2	5	5.52
PDMAm	2	10	9.94
PDMAm	5	5	4.91
PDMAm	5	10	10.45
PDMAm†	5	5	4.39
PDMAm†	5	10	8.33

The average residence time calculated using equation 1.18 is shown in Table 3.2 for each experiment. For the monomer tracer with the same target residence time in different reactor volumes, the value τ is shorter for the longer reactor coil. The value of a 2 mL coil with a t_{target} of 5 min is 0.57 min larger; whereas, the 5 mL coil is only 0.25 min smaller than the target. This could be due to the accuracy of the pump at low flow rates. This effect is also seen for the longer residence time of 10 mins, which would require lower flow rates; here τ is much closer (0.01 mins) less than t_{target} for the 5 mL coil compared to the 2 mL coil. For PDMAm, the residence time of 10 minutes does not show this trend and τ is further away from t_{target} which is likely a result of a greater pressure drop in the more viscous system that will affect flow rate. For the heated tracers significantly lower τ values are obtained; this is possibly the result of the decrease in viscosity and increase in velocity caused by elevated temperatures.

3.4 Modifications to the analysis in flow

A low cost oven was constructed to enable GPC using DMF as the eluent at a controlled temperature of 30°C. An Asynth hotplate and thermocouple and an aluminium block covered in aluminium foil was constructed. Figure 3.13 where DMF enter through the guard column then through the Rapide M column and out to the RI detector. This set up enables a more temperature controlled environment for the columns to improve elution and signal quality.

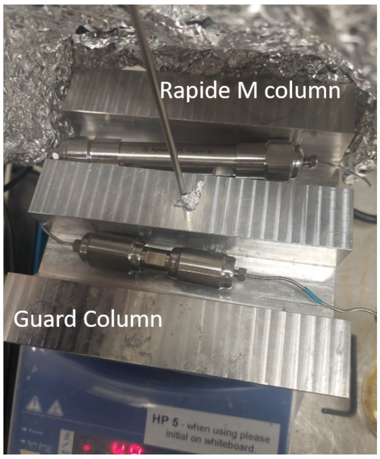

Figure 3.13: DMF GPC set up set to 30 °C

Furthermore, a zaiput BPR (shown in 3.14.a) has been implemented and pressurised with nitrogen at 7 bar to replace the IDEX cartridges that had the propensity to foul. A 55 cm glass tube (shown in Figure 3.14.b.) that can accommodate 1/8" PFA tubing has been included in the flow NMR protocol to provide a more reproducible environment to improve the quality of the spectrum.

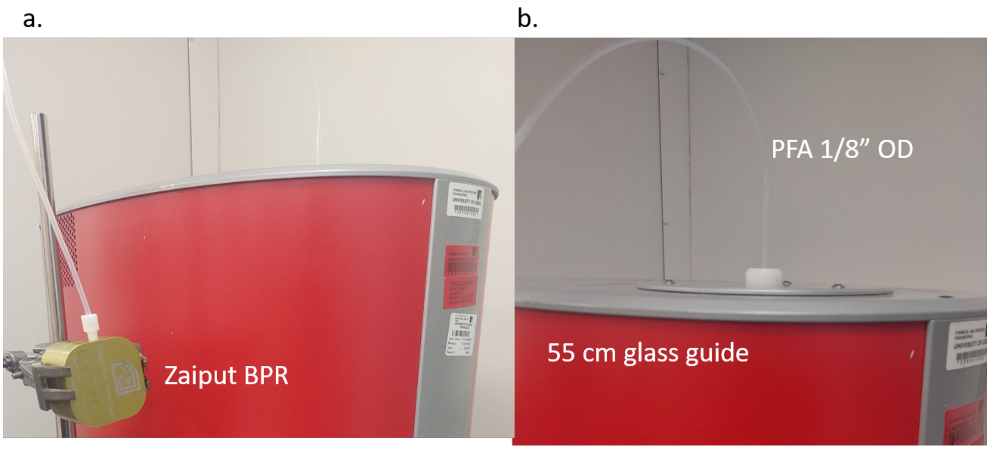

Figure 3.14: (a) Zaiput BPR used in Chapters 4 and 5 instead of the IDEX cartridge as used in Chapter 2. (b) NMR set up using a hollow glass rod with the PFA tubing through the middle.

3.4.1 Conclusions

To conclude this Chapter, a low-cost home-made mixer provided superior mixing with respect to commercially available options. A short path length and relatively large glass beads circumvent the pressure drop associated with packed beds and showed a minimal effect on the RTD. This type of mixer is therefore selected for multi-pump flow experiments in the subsequent Chapters. The 1/16 " OD tubing afforded the narrowest RTD compared to 1/8". Thus, 1/16" OD tubing was selected for the flow platform. Characterisation of the RTD has been conducted to look at the effect of viscosity, volume, and temperature; showing that 5 mL tubing and longer residence times produce the narrowest dimensionless RTDs. It has also been concluded that measurements need to be conducted after at least 3 reactor volumes for steady state to be established. Further modifications have been made to the platform to ensure homogeneity in data collection, such as a self-constructed heated GPC unit. In addition, a glass guide has been implemented to ensure that the PFA tube is taut through the NMR. Optimisation of the reactor platform was important for the subsequent chapters in order to reduce the effects of poor mixing and asymmetrical flow regimes. The RTDs obtained in this chapter came in useful in the next chapter where they were super-imposed onto the batch MWD data and used to account for the flow regimes observed in flow in the model developed in Chapter 4.

Chapter 4

Development and Validation of a Kinetic and Dispersity Model for *in-silico* RAFT Polymerisation

4.1 Introduction

In Chapter 1, current modelling techniques have been discussed in detail. Commercially available PREDICI is the most popular technique due to its user interface and ability to model full chain-length distributions with temporal resolution, as reported in the seminal work by Vana *et al.*[99] Improved performance in the software in recent upgrades has enabled sophisticated systems to be modelled, such as the work by Zetterlund,[100] and the formation of sequence defined multi-block co-polymers. Improvements in computation has enabled this to become a rapid prediction platform for kinetics; however, cross platform incorporation and the pay-wall make it less accessible. Non-commercially available alternatives for RAFT kinetics, such as the method of moments (MoM) have been shown to be powerful contenders to PREDICI with tunable computational expense by simplification. Introduction of the pseudo steady state approximation has enabled Zapata-Gonzales *et al.*[230] to model the full molecular weight distributions whilst accounting for intermediate radical termination (IRT), slow fragmentation (SF) and intermediate radical termination with oligomers (IRTO). Improvements of *kMC* have been reported across multiple programming language with the most efficient being.[79] Drache and co-workers reported a modular user interface named "mcPolymer" for the use of *kMC*, which they compared to PREDICI. Here they found "mcPolymer" capable of modelling concentration time profiles and CLDs with comparable precision to PREDICI.[85] Explicit analytical models have been reported for obtaining the conversion from RAFT assuming steady state approximation, Wang *et al.* successfully simulated conversion from manual analytical solvation of a set of ODEs,[102] with comparable data to the numerical MoM method.[95] Thus, providing a simple mathematical equation for relative chain species concentrations and conversions. The same method for analytically deriving an equation for dispersity as a function of conversion has also been used to derive the final termination step for RAFT polymerisation. Prior work deriving predictive equations for dispersity as a function of conversion are discussed in depth in Chapter 1. Mastan *et al.*, successfully derived an equation accounting for terminative events for normal ATRP validating this against the method of moments and experimental work for the polymerisations of 2-hydroxyethyl methacrylate, methyl methacrylate, and N-isopropylacrylamide..[103] In a similar vein, Wang *et al.* successfully derived a similar equation using both pseudo-first order kinetics and power law kinetics and validated it for DMAm, MA, BuA and MMA.[104] Previously, only the first 3 terms of this equation have been derived for RAFT polymerisation,[113] this was then used to model the MWDs using a Poisson distribution fitting to experimental data by Kearns *et al.*[110] where there os no termination to gain information about propagation to transfer. Here, we expand on the equation derived for the ideal chain transfer example and account for termination and re-initiation. With the intention to use a model to augment the Bayesian Optimisation platform, the analytical pseudo-first order model proposed by Wang *et al.*[102] was adapted to include CLD-T proposed by Heuts *et al.*[111]which account for the change in termination rate from short to long chain polymers and successfully validate conversion for flow and batch. Subsequently, this was then coupled to a dispersity equation derived in this chapter to simulate and validate against experimental data. The conversion and dispersity was validated for DMAm(this work) and literature data for AAm, AA and MA.

4.2 Experimental

Monomer used in the validation in this chapter were N,N-dimethyl acrylamide ((DMAm) 99 %, contains 500 ppm monomethyl ether hydroquinone as inhibitor, CAS 2680-03-7) purchased from Sigma Aldrich, RAFT agents used were both purchased from Boron Molecular: 2-(Butylthiocarbonothioylthio)propanoic acid ((TTC1) 95 %, CAS 480436-46-2), 3-((((1-carboxyethyl)thio)carbonothioyl)thio)propanoic acid ((TTC2) 95 %, CAS 870451-09-5) Initiators used were 2,2'-Azobis[2-(2-imidazolin-2-yl)propane]dihydrochloride ((VA044), CAS 27776-21-2), 4,4'-Azobis(4-cyanovaleric acid) ((ACVA), CAS 2638-94-0)

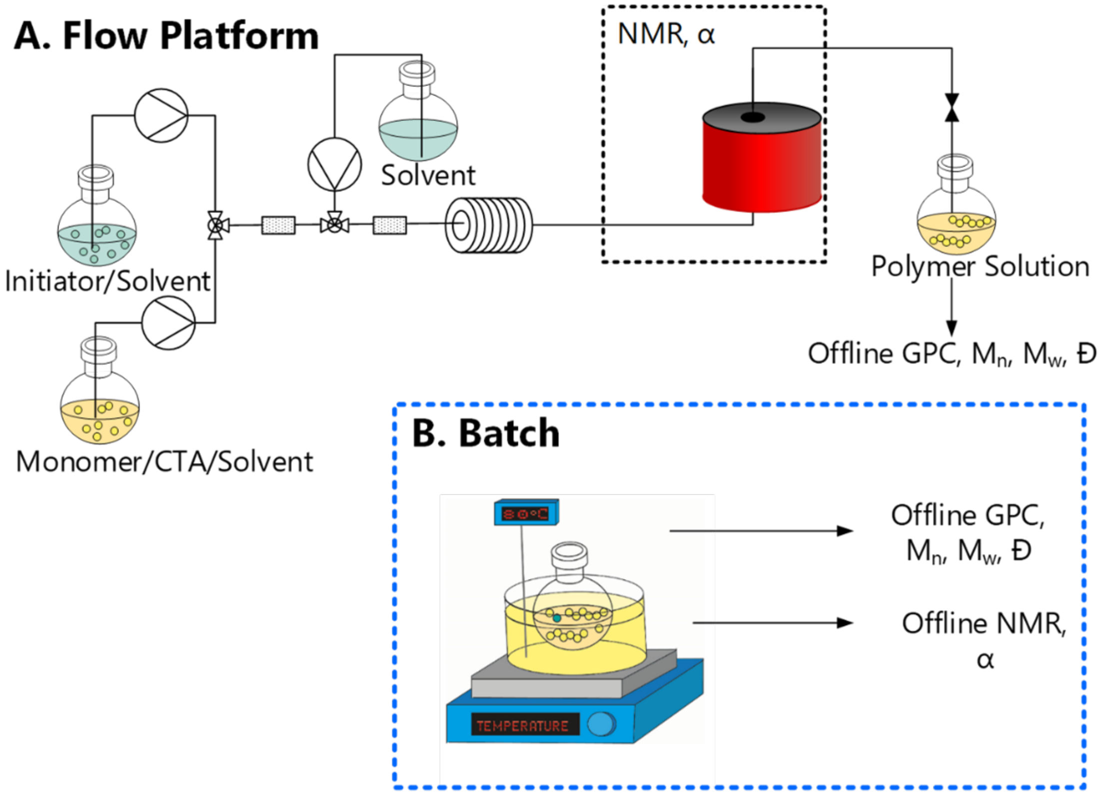

Figure 4.1: (A) Autonomous flow set-up used for model validation in chapter 4 using online NMR and offline GPC

The validation platform comprises of 3 computer controlled pumps using 2 inline packed bed mixers (See Figure 3.2 in Chapter 3). These facilitate mixing before the reaction solution enters the flow reactor coiled around a cylindrical heating block. Temporal resolution was achieved by varying the flow-rate. An At-line GPC comprising of a VICI EHMA 6-port switching valve and 2 position actuator enables a 100 μL sample to be injected into the online GPC mentioned above - this was done by switching positions for 4 ms. The reacted solution continues into length of

PFA threaded though a glass guide in the NMR. A 7 bar (100 psi) Zaiput BPR was used to mediate the flow within the tube, as shown in Chapter 3.

4.2.1 DMAm:TTC2:VA044 (100:1:0.02)

DMAm (60 g, 100 eq) and TTC2 (1.54 g, 1 eq) were dissolved in deionised water (67.6 g). To a separate flask VA044 (0.49 g, 0.1 eq) was dissolved in 102.9 g of deionised water. A third flask was dosed with deionised water only. The 3 vessels were degassed under an atmosphere of nitrogen for 20 mins prior to reaction then kept under nitrogen for the rest of the experimental time. Off-line NMR and offline GPC was used in this case. For the batch experiments a Deep Matter digital glassware probe was used. A 3 necked RBF was dosed with DMAm (15.0 g, 0.15 mol, 100 eq), TTC2 (0.385 g, 1.51 mmol, 1 eq) and VA044 (9.7 mg, 0.030 mmol, 0.02 eq) was dissolved in water (35.9 g). The solution was degassed under nitrogen for 20 mins and submerged into a preheated oil bath set to 80 °C. Samples were analysed by offline NMR and offline GPC.

4.2.2 DMAm: TTC1: ACVA (200:1:0.02)

DMAm (60 g, 200 eq) and TTC1 (0.72 g, 1 eq) was dissolved in deionised water (40.5 g). To a separate flask ACVA (0.21 g, 0.1 eq) was dissolved in 101.3 g of deionised water. A third flask was dosed with deionised water only. The 3 vessels were degassed under an atmosphere of nitrogen for 20 mins prior to reaction then kept under nitrogen for the rest of the experimental time. The reagents were then diluted in stream to 30 w/w %

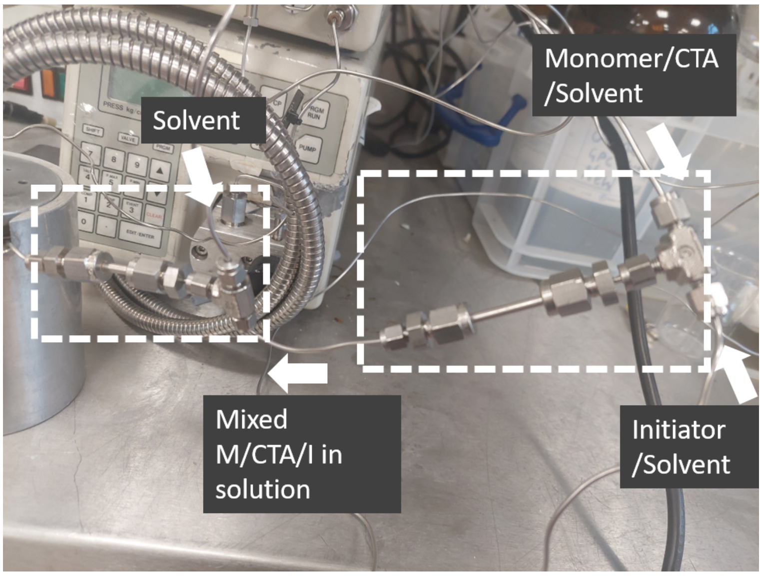

Figure 4.2: Two adjacent packed bed mixers used to mix each stream. The first mixes the Monomer and CTA solution with the Initiator solution and the second is used to dilute the streams. This configuration is also used in Chapter 5

4.3 Results and Discussion

4.3.1 Kinetic Model

To model monomer consumption, a series of ordinary differential equations (ODE) were constructed to describe the kinetic parameters for the reaction (4.1 and solved for monomer conversion (α). Arrhenius equation was used to account for the temperature in the rate constants. The concentration of chain species: propagating radicals (P_r), chain transfer agent species (CTA), and radical adduct intermediates (CTA_a) was assumed to be independent of chain length. $[CTA]$ described in (4.1.iv) is a summation of chain transfer species including the initial $[CTA]$ at time 0. R seen in the pre-equilibrium represents the leaving group of the RAFT agent whilst P_i and P_j represent any length of propagating chain. It is important to note that the r in P_r does not refer to the chain-length. Steady state hypothesis was applied to enable simplification of the equations to an ODE for $\frac{d[CTA]}{dt}$ and then solved using the symbolic solution toolbox in MATLAB. This was then used to find $[P_r]$ at steady state enabling solution of (ii) for monomer concentration, $[M]_t$ at a given time and thus conversion.

$$\alpha = 1 - \frac{[M]_t}{[M]_0} \tag{4.1}$$

Table 4.1: Steps describing the general RAFT mechanism and rate equations for each species. Species included are: the initiator (I_2), initiator radicals (I), monomer (M), propagating radicals (P_r), chain-transfer agents (CTA), radical adduct intermediate (CTA_a), polymer (P) and the 3-armed polymer (P').

Step		**Rate Equation**	**#**
Initiation	$\mathrm{I_2} \xrightarrow{\mathrm{fk_d}} \mathrm{2I}$	$\frac{d[I]}{dt} = -2fk_d[I]$	i
Propagation	$\mathrm{M} + \mathrm{P_r} \xrightarrow{\mathrm{k_p}} \mathrm{P_r}$	$\frac{d[M]}{dt} = -k_p[M][P_r]$	ii
Pre-equilibrium	$\mathrm{P_r} + \mathrm{CTA} \underset{\mathrm{k_{-a}}}{\overset{\mathrm{k_a}}{\rightleftharpoons}} \mathrm{CTA_a} \underset{\mathrm{k_{-\beta}}}{\overset{\mathrm{k_\beta}}{\rightleftharpoons}} \mathrm{CTA} + \mathrm{R}$	$\frac{d[P_r]}{dt} = r_1 + k_\beta[CTA_a] - k_a\,[P_r][CTA] - 2k_t[P_r]^2 - k_{ct}[P_r][CTA_a]$	iii
Re-initiation	$\mathrm{R} + \mathrm{M} \xrightarrow{\mathrm{k_i}} \mathrm{P_r}$	$\frac{d[CTA_a]}{dt} = k_a[P_r][CTA] - k_\beta[CTA_a] - k_{ct}[P_r][CTA_a]$	iv
Main equilibrium	$\mathrm{P_r} + \mathrm{CTA} \underset{\mathrm{k_{-a}}}{\overset{\mathrm{k_a}}{\rightleftharpoons}} \mathrm{CTA_a} \underset{\mathrm{k_{-\beta}}}{\overset{\mathrm{k_\beta}}{\rightleftharpoons}} \mathrm{CTA} + \mathrm{P_r}$	$\frac{d[CTA]}{dt} = k_\beta[CTA_a] - k_a[P_r][CTA]$	v
Termination by disproportionation	$\mathrm{P_r} + \mathrm{P_r} \xrightarrow{\mathrm{k_{td}}} \mathrm{P} + \mathrm{P}$		
Termination by coupling	$\mathrm{P_r} + \mathrm{P_r} \xrightarrow{\mathrm{k_{tc}}} \mathrm{P}$	$\frac{d[P]}{dt} = k_{td}[\mathrm{P_r}]^2 + \frac{1}{2}k_{tc}[\mathrm{P_r}]^2$	vi
Cross-termination	$\mathrm{P_r} + \mathrm{CTA_a} \xrightarrow{\mathrm{k_{ct}}} \mathrm{P'}$	$\frac{d[P\prime]}{dt} = k_{ct}[\mathrm{P_r}][CTA_a]$	vii
Chain Species Summations		$[P_r] = \sum_{i=1}^{\infty}[P_i\,\cdot]$ $[CTA] = \sum_{i=1}^{\infty}[CTA - P_i]$ $[CTA_a] = \sum_{j>1}^{\infty}\sum_{i=1}^{\infty}[P_j - CTA_a \cdot - P_i]$ $[P'] = \sum_{i=1}^{\infty}[P_\mathrm{i}']$ $[P] = \sum_{i=1}^{\infty}[P_\mathrm{i}]$	

Assuming steady state hypothesis, $\frac{d[CTA_a]}{dt} = 0$, so the concentration of the Dormant species was constant. Consequently, ODE iv in Table 4.1 can be simplified down to equation 4.2

$$0 = k_a [P_r] [CTA] - k_\beta [CTA_a] - k_{ct} [P_r] [CTA_a] \tag{4.2}$$

If the concentration of radical adducts does not change there has to be a constant rate of cross termination that allows equation 4.2 to be simplified down to equation4.3.

$$[CTA_a] = \frac{k_a}{k_\beta} [P_r] [CTA] \tag{4.3}$$

The rate of radical transfer from the CTA adduct species to form a branched polymer species was assumed to be constant at steady state so that, $\frac{d[CTA_{adduct}]+d[P_r]}{dt}$, ODE iv and ODE ii in Table 4.1 can be combined and simplified down. This allows an equation for [P$_r$] at steady state to be formulated from 4.3 to 4.4.

$$\begin{aligned}\frac{d[CTA_a] + d[P_r]}{dt} &= k_a [P_r] [CTA] - k_\beta [CTA_a] - k_{ct} [P_r] [CTA_a] + \\ &(r_1 + k_\beta [CTA_a] - k_a [P_r] [CTA] - 2k_t [P_r]^2 - k_{ct} [P_r] [CTA_a])\end{aligned} \tag{4.4}$$

where r$_I$ is the initiation rate. As steady state was assumed $\frac{d[P_r]+d[CTA_a]}{dt} = 0$ Equation 4.4 can be simplified to equation 4.5

$$[P_r] = \sqrt{\frac{r_I}{k_t + 2 [CTA] \frac{k_a k_{ct}}{k_\beta}}} \tag{4.5}$$

Combining ODE v with ODE iv in Table 4.1 when $\frac{d[CTA_a]}{dt} = 0$, can be used to find the rate of change of [CTA], while accounting for the equilibrium, equation 4.6 was obtained.

$$\begin{aligned}\frac{d[CTA]}{dt} + \frac{d[CTA_a]}{dt} &= k_\beta [CTA_a] - k_a [P_r] [CTA] + (k_a [P_r] [CTA] - k_\beta [CTA_a] - \\ &k_{ct} [P_r] [CTA_a])\end{aligned} \tag{4.6}$$

Equation 4.6 can be simplified to a single value for $\frac{d[CTA]}{dt}$, if it is assumed that the concentration of the radical adduct intermediate does not change over time. The algebraic values for $[P_r]$ and $[CTA_a]$ can be substituted in to equation 4.6 to form equation 4.7.

$$\frac{d[CTA]}{dt} = -\sqrt{\frac{r_I}{\frac{k_t k_\beta}{k_a k_{ct} [CTA]} + 2}} \tag{4.7}$$

The rate equation of $[CTA]$ can then be solved symbolically in $MATLAB$ and then substituted into the equation 4.5. To account for chain-length dependence the power law equations proposed by Heuts *et al.*[111] were used. Once $[M]_t$ was determined for the non-chain-length dependent reaction, a second iteration was performed accounting for chain-length dependent termination (CLD-T).[111] This involves a cross-over chain length where the termination rate operates using 2 separate equations for calculating k_t: short chain ($L<L_c$) and long chain ($L>L_c$). The cross-over chain length is typically identified experimentally by single-pulse pulsed laser polymerisation (SPPLP) coupled to electroparamagnetic resonance spectroscopy (EPR).[231] A log plot of the radical concentration (c_R) at t =0 and after the pulse against time enables the power law and cross over chain length to be identified. The kinetic model was used to obtain the kinetic data in the simulation for the dispersity model..[232]

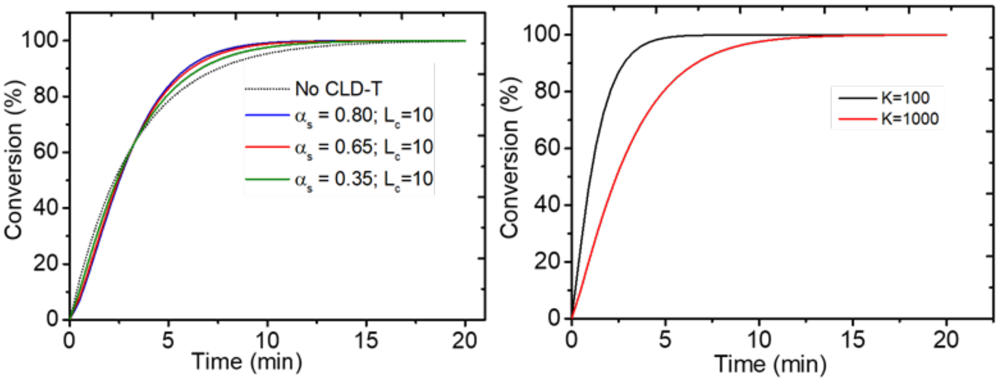

Figure 4.3: (left) Simulated conversion plot comparing the effect of different α_s against no CLD-T (dotted line), where $\alpha_s = 0.80$ (blue solid line), 0.65 (red solid line) and 0.35 (green solid line). (right) simulated conversion plot comparing the effect of the equilibrium, K, (right) on the monomer conversion

The inaccessibility of rate constants in the literature is often stated as the primary issue when modelling RAFT;[233] thus, it is important to note the dependence of the model on explicit rate constants. The model relies on 5 rate constants: k_p, k_d, k_t, k_a and k_β, where k_p and k_t are the most experimentally studied by Pulsed-Laser polymerisation (PLP) combined with SEC and electron spin resonance spectroscopy (ESR).[234–236] k_d values are also abundant in the literature; and are typically found by measuring gas evolution with respect to time.[237] Less commonly studied are k_a, k_{-a}, k_β and, $k_{-\beta}$ which are uniquely associated with RAFT polymerisation. k_a is typically calculated from the chain transfer coefficient obtained experimentally by a Mayo plot or by comparing monomer conversion with RAFT agent conversion; this is described in more detail in Chapter 1. Efforts to quantify k_β via the RAFT equilibrium constant have been limited to retarded RAFT polymerisation, by comparing polymerisation rates at different concentrations of the RAFT agent[56] and through *ab initio* studies.[238]

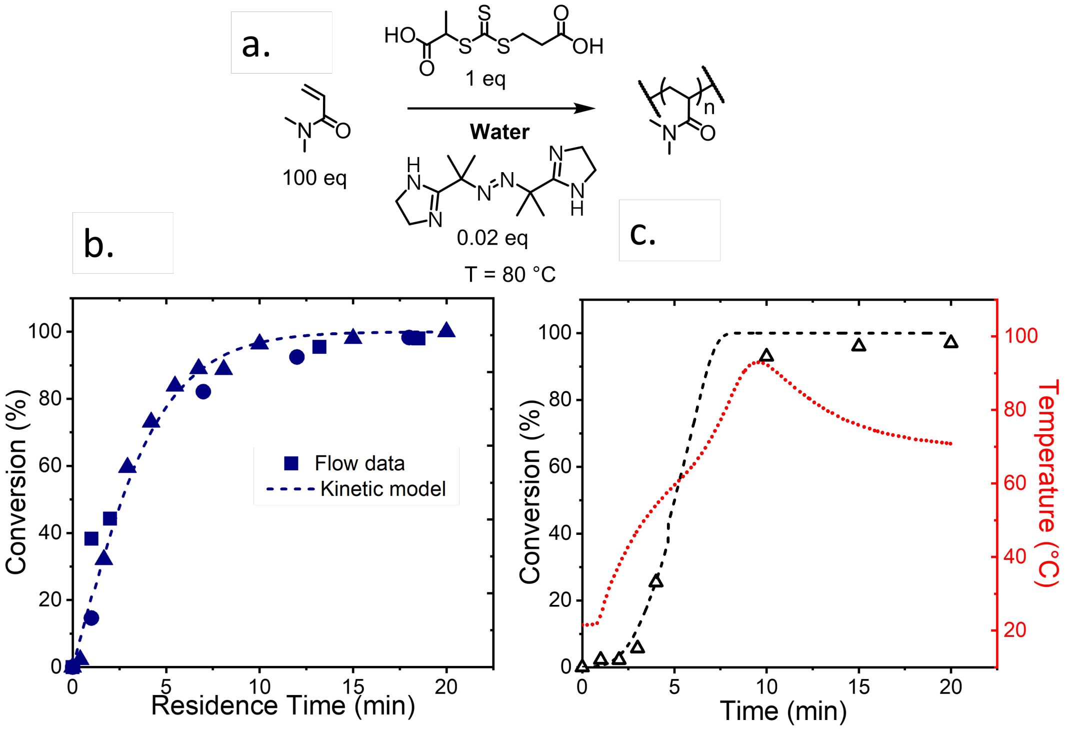

Figure 4.4: Kinetic model validation experiments for the ultrafast RAFT polymerization of DMAm:TTC1:VA044 (100:1:0.02) in H_2O 30 w/w % at 80 °C. (a) The simulated kinetics (dashed line) are compared to experimental results for the flow reactor (data points) where squares, circles and triangles represent separate runs of the same reaction (b) In batch, the non-isothermal kinetics (black) were simulated using the temperature measured in-situ (red line). The temperature profile illustrates the poor heat transfer leading to an initial induction period and subsequent polymerization exotherm.

An initial simulation was performed for the RAFT polymerization of dimethylacrylamide (DMAm) under ideal "isothermal" conditions in water and compared to data obtained experimentally in batch (Figure 4.4.b) and flow (Figure 4.4.a). This system was chosen because it is widely studied[193,239] and the propagation constants are widely available.[227,240] To best reproduce isothermal conditions (Figure 4.4.a), the polymerisation was carried out in a flow reactor, where the higher surface area to volume ratio facilitated superior heat transfer, which has the benefits of rapid heating and dissipation of exotherms. In this case, the experimental data was in good agreement with the model (dashed line), exhibiting the expected pseudo-first order kinetics. An equivalent batch reaction was also performed, whereby the reaction solution at ambient temperature was immersed in an oil bath at 80 °C. Experimental data indicated a delayed onset of polymerisation followed by a large increase in conversion over a short time interval. This did not align with the isothermal kinetic model due to the poor heat transfer resulting in an initially slow polymerisation that auto-accelerates due to the poor dissipation of the exotherm, resulting in a temperature peak > 90 °C. During the process, the reaction temperature was also recorded, resulting in the ability to build a semi-empirical model which considers the varying temperature. When this was plotted, it fit well with the batch data, demonstrating the wide applicability of this kinetic model. Subsequently, the temperature dependence was then investigated in flow for a different RAFT agent and initiator combination using a higher monomer concentration to ensure a dynamic model for simulating ideal systems.

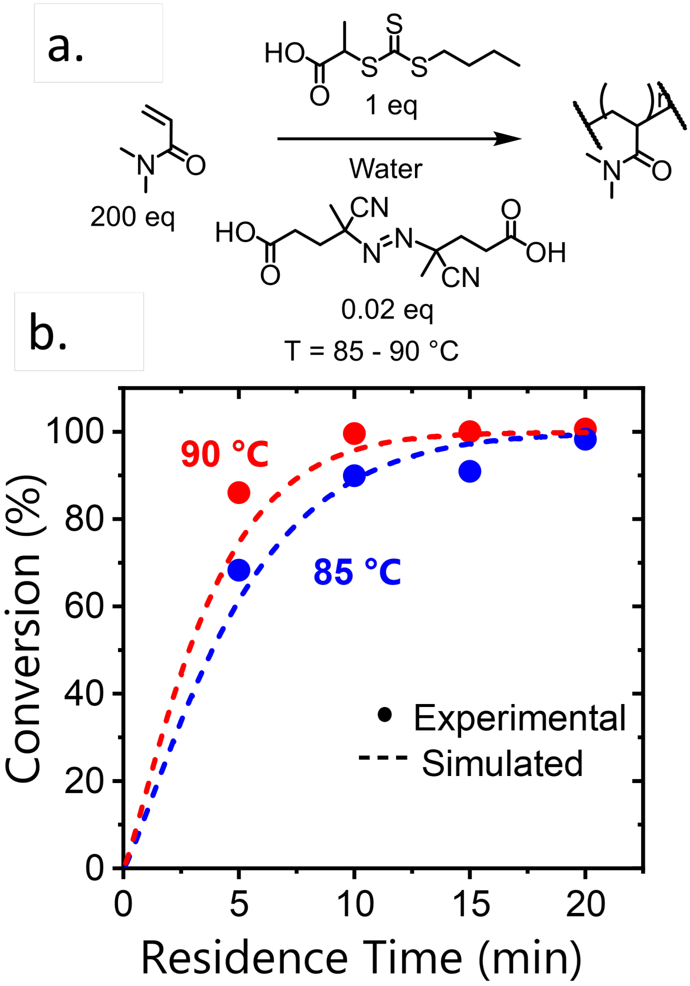

Figure 4.5: Comparison of kinetic conversion data obtained for DMAm : TTC2: ACVA 200:1:0.02 at 30 w/w% in flow (filled circles) at different temperatures. Here, the colour of the symbol and dashed line corresponds to a different temperature, 85 °C (blue) and 90 °C (red) and simulation at the corresponding temperature.

The simulated conversion traces again show good concordance with the experimental flow data even when an initiator with a slower rate of decomposition was used. It is increasingly important to consider temperature dependence for radical polymerisations; highlighted in Figure 4.5 by the change in rate observed when the temperature was elevated by 5 °C. The expected increase in rate was observed for the simulation suggesting that the Arrhenius equation used to account for temperature was satisfactory for this reaction system. For bulky acrylate polymerisations where high temperature can lead to increased rate of side reactions (e.g. formation of mid-chain radicals) a reduced polymerisation rate can be observed – in which case the model would fall apart.

4.3.2 Molar Mass Dispersity

For "living" radical polymerization (no terminative or reversible transfer steps), dispersity decreases exponentially asymptotically as a function of conversion (equation 4.8 - where $\frac{[CTA]_0}{[M]_0\alpha} = \frac{1}{DP}$ and the MWD is typically a Poisson distribution). Following block theory, which assumes that there is no termination or chain transfer after each time step, equation 4.8 has been defined for completely living polymerization.

$$Đ = T_1 + T_2 = 1 + \frac{[CTA]_0}{[M]_0\alpha} \tag{4.8}$$

Where $[CTA]_0$ and $[M]_0$ are the initial concentrations of CTA and monomer, respectively. For simplicity, here each term derived was abbreviated as T_n where T_1 is the first term, T_2 is the second term etc. Due to the reversible activation/transfer steps involved in RDRP, the term previously derived by Harrisson et al.[113,114] can be added, resulting in an equation for dispersity as a function of conversion:

$$Đ = T_1 + T_2 + T_3 = 1 + \frac{[CTA]_0}{[M]_0\alpha} + \frac{k_p}{k_{tr}}(\frac{2}{\alpha} - 1) \tag{4.9}$$

Where $[CTA]_t$ is the concentration of CTA at time, t. k_p and k_{tr} are the rate constants for propagation of radicals and transfer of monomer to CTA, respectively. This step broadens the MWD leading to slightly higher Đ. Harrison et al.[113]further simplify the formula by assuming that the ratio of $\frac{[CTA]_0}{[CTA]_t} = 1$ for the ideal case. To provide a further improvement in dispersity prediction, a fourth term, T_4, is necessary to account for terminative events leading to dead polymer chains. To derive T_4, it is important to propose assumptions required to achieve an explicit value, which can be achieved using blend and block theory[103] (Figure 4.7), where chain growth and terminative subpopulations were discretised per time interval to quantify Đ as a function of time and, in turn, conversion. The model assumes a thermally initiated polymerization will begin instantaneously on introduction of radicals, i.e. as soon as the reaction medium is heated. A further major assumption is that radical concentration was at steady state in each time interval; thus, if all the initiator radicals have been consumed (i.e., at high temperature at long reaction times) then the model will break down. Realistically, all radicals may be consumed under intense conditions, thus leading to rate retardation and reduced conversion as the concentration of dead polymer increases.

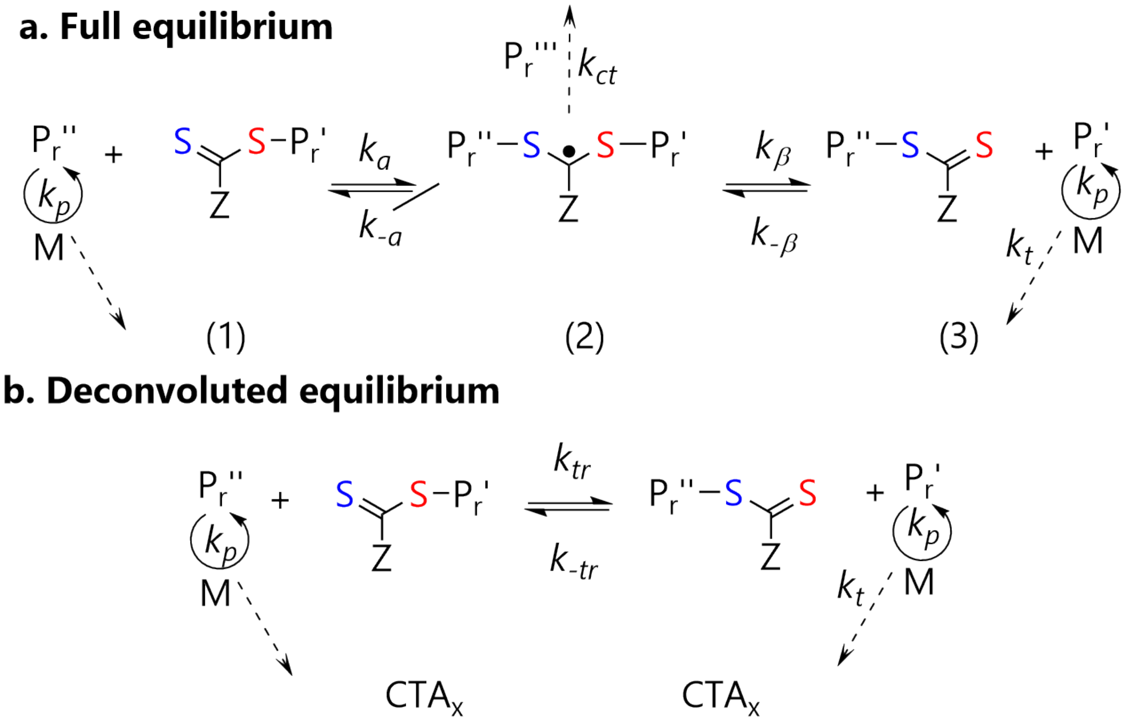

Figure 4.6: (a) Complete RAFT equilibrium following, highlighting the mechanism of chain transfer. Addition (k_a) of P_r to CTA (1), then beta scission (k_β) of radical adduct intermediate (2) to form CTA (3). Intermediate (2) can also undergo cross termination (k_{ct}) to form branched polymer species. In RAFT, termination (k_t) and propagation (k_p) are also happening at the same time. (b) A simplified equation for the RAFT equilibrium where k_{tr} and k_{-tr} account for $k_a, k_{-a}, k_{-\beta}$ and k_β and the partitioning of species (2).[241]

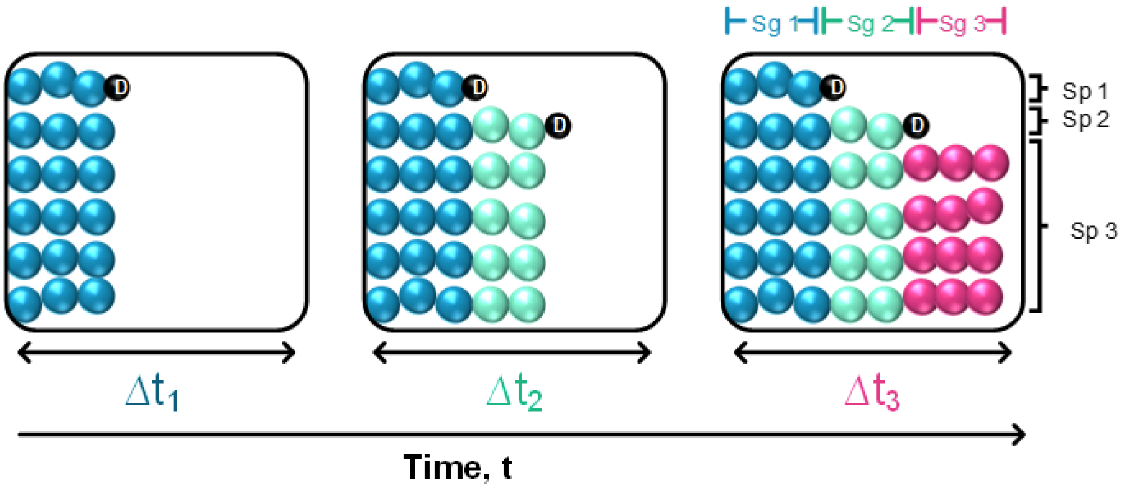

Figure 4.7: Schematic of how the model describes chain-growth in CRP based on the blend and block strategy demonstrated by E.Mastan et al.[86] Sg # = Segment and Sp # = Subpopulation. The black spheres labelled "D" represent dead polymer in the reaction. The model assumes that after each time step,Δt_i , there is a degree of "livingness" and termination. Such that, in Δt_1 Sg 1 terminates to form Sp 1 but Sg 2 grows and in Δt_2 Sg 2 terminates forming Sp 2 and Sg 3 grows etc.

In this model, the simplified RAFT equilibrium is used which accounts for the degree of partitioning of the radical adduct intermediate, this is given by equations 1.5 and 1.6 in Chapter 1. Firstly, a term to describe the probability of propagation in each RAFT equilibrium cycle is defined as, ρ_p which is found by finding the ratio of propagation of active polymer chains to all steps using propagating radicals, given by equation 4.10

$$\rho_p = \frac{k_p\,[M]}{k_p\,[M] + k_{tr}\,[CTA] + k_t\,[P_r]} \tag{4.10}$$

Where the overall rate constants for the equilibrium are described by equations 1.5 and 1.6. Approximate k_a, and partition coefficient, ϕ, can be found in the literature. Next, the number of transfer cycles $\Delta\tau_i$ for each segment, i, can be defined as equation 4.11.

$$\Delta\tau_i = k_{-tr}\frac{[P_r][CTA]}{[CTA]} = k_{-tr}[P_r]\Delta t_i \tag{4.11}$$

The number of monomer units added in each equilibrium cycle, x, can be given by equation 4.12, when $k_{tr}\,[CTA] \gg k_t\,[P_r]$

$$x = \frac{\rho_p}{1-\rho_p} = \frac{k_p\,[M]}{k_{tr}\,[CTA] + k_t\,[P_r]} = \frac{k_p\,[M]}{k_{tr}\,[CTA]} \tag{4.12}$$

Subsequently, the degree of polymerisation of each block can then be given as the number of monomeric units added per cycle multiplied by the number of transfer cycles to give equation 4.13.

$$r_{n,i} = \frac{k_p\,[M]_i\,k_{-tr}[P_r]}{k_{tr}\,[CTA]_i}\Delta t_i \tag{4.13}$$

$$Đ = 1 + \frac{1}{r_{n,i}} + \frac{2}{k_{-tr}\Delta t_i} \tag{4.14}$$

where $[M]_0$ is the monomer concentration at $t = 0$, α is the conversion and $[CTA]_0$ is the concentration of CTA at time = 0. The dispersity of a segment can be given by equation 4.14, $Đ$, previously derived by Mastan et al.[242] The discretised total degree of polymerisation can then be solved as the sum of all chains in each Δt_i, as Δt_i approaches 0 is shown in equation 4.16 which can then be integrated to find the DP of all chains. This can then be converted to a function of conversion using the rate of polymerisation as a function of conversion.

$$\frac{d\alpha}{dt} = k_p(1-\alpha)[P_r] \rightarrow dt = \frac{d\alpha}{k_p(1-\alpha)[P_r]} \tag{4.15}$$

$$\begin{aligned} r_n^{block} = \sum_{i=1}^{N} r_{n,i} &= \lim_{\Delta t_i \to 0} \sum\nolimits_{i=1}^{N} \frac{k_p\,[M]_i\,k_{-tr}[P_r]}{k_{tr}\,[CTA]_i}\Delta t_i \\ &= \int_0^t \frac{k_p\,[M]\,k_{-tr}[P_r]}{k_{tr}\,[CTA]}dt \\ &= \frac{[M]_0\alpha}{[CTA]_0} \end{aligned} \tag{4.16}$$

by substituting equation 4.1 from the kinetics section into equation 4.15, equation 4.16 can be simplified down as shown. The total dispersity of the all segments can be given as equation4.17

$$Đ^{block} = 1 + \frac{1}{(r_n^{block})^2}\sum_{i=1}^{N} r_{n,i}^2(Đ_i - 1) \tag{4.17}$$

In RAFT, termination is unavoidable and leads to dead polymers, as seen in Figure 4.7. Here, the fraction of dead polymer as a subpopulation is considered. Propagating chains terminated in each Δt_i were discretized into their sub populations as shown in Figure 4.8. Blend strategy which assumes that there is termination of every chain in each interval so the total polymer will be a blend of each subpopulation, was applied to account for this.

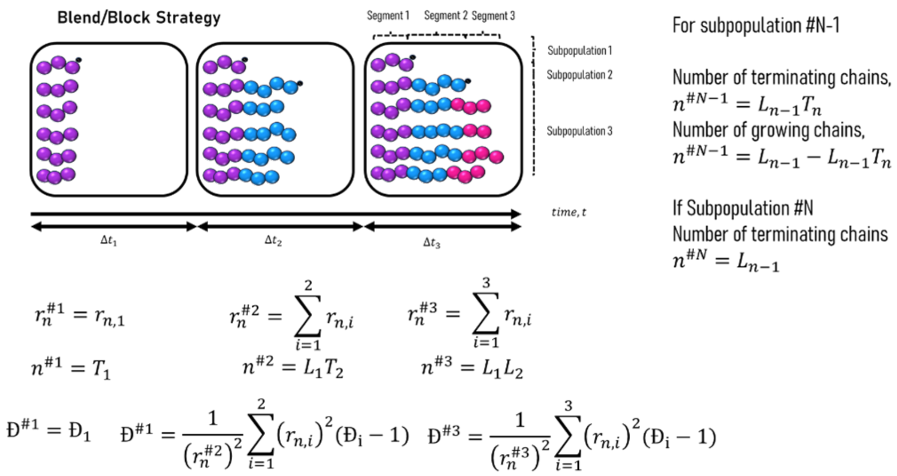

Figure 4.8: Contributions of termination and "livingness" in blend and block theory.

For example, in subpopulation 1 there is 1 terminating chain so $n^{\#1} = T_1$, in subpopulation 2 segments 1 and 2 grow so $n^{\#2} = L_1T_2$ and in subpopulation 3, the number of growing chains is 2 so $n^{\#3} = L_1L_2$. T is the number fraction of dead chains whereas L is the number fraction of Living chains. The "livingness" can described by the ratio of $\frac{[CTA]_t}{[CTA]_0}$ based off the equation for "livingness" given in Perrier *et al.*[29] In this Chapter, the number fraction of dead chains can be described by the ratio of $\frac{[P]}{[CTA]}$. Consequently, the overall DP and $Đ$ for a polymerisation exhibiting both terminative and chain transfer, r_n^{blend} and $Đ^{blend}$ can be obtained, respectively.

$$r_n^{blend} = \sum_{i=1}^{N} n_i r_{n,i}^{block} = \frac{[M]_0}{[CTA]_0}\alpha \tag{4.18}$$

$$Đ^{blend} = 1 + \frac{1}{(r_n^{block})^2}\sum_{i=1}^{N} r_{n,i}^2(Đ_i - 1)Đ_i^{block} \tag{4.19}$$

by substituting $Đ_i$ and $r_{n,i}$ from equation 4.14 and 4.13 and $r_{n,i}^{block}$ from equation 4.17 into 4.19, an equation accounting for livingness and terminative events can be formed.

$$Đ = 1 + \frac{1}{r_n^2}\lim_{\Delta t \to 0}\sum_{i=1}^{N} L_{i-1}^{o}(r_{n,i}^2)(Đ_i - 1) + \frac{2}{r_n^2}\lim_{\Delta t \to 0}\sum_{i=1}^{N} L_{i-j} r_{n,i}\sum_{j=1}^{i} T_{j-1}^{o} r_{n,j} \tag{4.20}$$

subsequently, L, T, $r_{n,i}$ (equation 4.13) and $Đ_i$ (equation 4.14) can be substituted into equation

4.20 and simplified down to a 3 term summation.

$$
\begin{aligned}
Đ = 1+ & \\
& \frac{[CTA]_0[CTA]}{[M]_0^2\alpha^2}\lim_{\Delta t_i\to 0}\sum_{i=1}^{N}\left(\frac{k_p[M]_i k_{-tr}[P_r]}{k_{tr}[CTA]_i}\Delta t_i\right)+ \\
& \frac{[CTA]_0[CTA]}{[M]_0^2\alpha^2}\lim_{\Delta t_i\to 0}\sum_{i=1}^{N}\frac{2k_p[M]_i}{k_{tr}[CTA]_i}\frac{k_p[M]_i k_{-tr}[P_r]}{k_{tr}[CTA]_i}\Delta t_i+ \\
& \frac{[CTA]_0^2}{[M]_0^2\alpha^2}\lim_{\Delta t_i\to 0}\sum_{i=1}^{N}\frac{2[CTA]_i}{[CTA]_0}\left(\frac{k_p[M]_i k_{-tr}[P_r]}{k_{tr}[CTA]_i}\Delta t_i\right)\sum_{j=1}^{i}\frac{[P]}{[CTA]_i}\left(\frac{k_p[M]_i k_{-tr}[P_r]}{k_{tr}[CTA]_i}\Delta t_i\right)
\end{aligned}
\tag{4.21}
$$

As Δt_i approaches 0, equation 4.21 can be written as an integral in terms of time, t.

$$
\begin{aligned}
Đ = 1+ & \\
& \frac{[CTA]_0[CTA]}{[M]_0^2\alpha^2}\int_0^t \frac{k_p[M]k_{-tr}[P_r]}{k_{tr}[CTA]}dt+ \\
& \frac{[CTA]_0[CTA]}{[M]_0^2\alpha^2}\int_0^t \frac{2k_p[M]}{k_{tr}[CTA]}\frac{k_p[M]k_{-tr}[P_r]}{k_{tr}[CTA]}dt+ \\
& \frac{2[CTA]_0[CTA]}{[M]_0^2\alpha^2}\int_0^t \frac{k_p[M]k_{-tr}[P_r]}{k_{tr}[CTA]}dt\int_0^t \frac{[P]}{[CTA]}\frac{k_p[M]k_{-tr}[P_r]}{k_{tr}[CTA]}dt
\end{aligned}
\tag{4.22}
$$

Using equation 4.1 substituted into equation 4.15, An equation in terms of conversion can be identified, shown in equation 4.23. Furthermore this can then be simplified down to form equation 4.24.

$$
\begin{aligned}
Đ = 1+ & \\
& \frac{[CTA]_0}{[M]_0\alpha}+ \\
& \frac{[CTA]_0[CTA]}{[M]_0^2\alpha^2}\int_0^\alpha \frac{2k_p[M]_0(1-a)}{k_{tr}[CTA]}\frac{[M]_0}{[CTA]}da \\
& \frac{2[CTA]_0[CTA]}{[M]_0^2\alpha^2}\int_0^\alpha \frac{[M]_0}{[CTA]_0}da\int_0^\alpha \frac{[P]}{[CTA]}\frac{[M]_0}{[CTA]_0}da
\end{aligned}
\tag{4.23}
$$

$$
Đ = 1+\frac{[CTA]_0}{[M]_0\alpha}+\frac{2k_p[CTA]_0}{k_{tr}\alpha^2}\int_0^\alpha \frac{(1-a)}{[CTA]}da+\frac{2}{\alpha^2}\int_0^\alpha\left(\int_0^a \frac{[P]}{[CTA]}da\right)d\alpha \tag{4.24}
$$

Here on in, the equation is separated out into T_{1-3} and T_4 for simplicity. Integration via equation 4.25 and If degeneracy is assumed for the equilibrium, such that $[CTA] = [CTA]_0$ equation 4.9

was derived.

$$T_3 = \frac{2}{\alpha^2}\frac{k_p}{k_{tr}}\frac{[CTA]_0}{[CTA]}\left[a - \frac{1}{2}a^2\right]_0^\alpha \tag{4.25}$$

In order to solve the fourth term, T_4, an expression for the change in concentration of polymer chains $[P]$ with respect to time, was required. The ODE $\frac{d[P]}{dt}$ - shown by equation 4.26 - was rearranged and integrated to give an expression for $[P]$ in terms of k_t and the concentration of propagating radicals, $[P_r]$ (see equation 4.27)

$$\frac{d\,[P]}{dt} = k_t\,[P_r]^2 \tag{4.26}$$

$$[P] = k_t\,[P_r]^2\,t \tag{4.27}$$

Equation 4.27 can be substituted back into equation 4.24 then written as a function of conversion using the integrated version of equation 4.15 into t and the the non-integrated form into dt.

$$T_4 = \int_0^\alpha \left(\int_0^\alpha -\frac{k_t[P_r]}{k_p[CTA]}\ln(1-a)da\right)d\alpha \tag{4.28}$$

The rate of initiation can be given as, $r_{ini} = 2k_d f\,[I]_0\,e^{-k_d t}$, which produces the initiating radicals instantaneously. At time = 0 this was given by $r_{ini} = 2k_d f\,[I]_0$. Here, regeneration of radicals is loosely accounted for by using the rate of formation of single monomeric radicals as the radical forming step, which can be seen in equation 4.29 . $-\frac{d[M]}{dt} = \frac{d[M\bullet]}{dt} = k_p[M][M\bullet]$. Where $[M\bullet]$ is given by $\sqrt{\frac{r_{ini}}{k_t}}$

$$r_R = k_p\,[M]\sqrt{\frac{r_{ini}}{2k_t}} \tag{4.29}$$

$$\frac{d\,[P_r]}{dt} = r_R - k_{tr}\,[CTA]_x\,[P_r] + k_{-tr}\,[CTA]_y\,[P_r] - k_t\,[P_r]^2 = 0 \rightarrow \frac{d\,[P_r]}{dt} = r_R - k_t\,[P_r]^2 = 0 \tag{4.30}$$

If the steady state hypothesis is applied to the equation for change in $[P_r]$ with respect to time, the resultant quadratic equation 4.30 can be solved analytically for $[P_r]$, 2 solutions are returned, a positive and a negative. However, only a positive solution can be used, as the concentration cannot be negative. Consecutively, the new expression for T_4 can be given as follows.

$$T_4 = -\frac{k_t}{k_p[CTA]_0}\frac{2}{\alpha^2}\sqrt{\frac{r_R}{k_t}}\int_0^\alpha\left(\int_0^\alpha \ln(1-a)da\right)da \tag{4.31}$$

For ATRP Mastan *et al.*[103] first used Gaussian quadrature with 1 node twice followed by a single term Taylor expansion to solve the double integral. Through truncation of the infinite Taylor series a simple formula can be obtained; however this is only an approximation and the true value of T_4 would require computational intervention. Here, two methods of solving this are demonstrated (1) Gaussian quadrature with a single Taylor term (2) an analytical method using the *symbolic math toolbox* in *MATLAB*.

Gaussian Quadrature The result of 2 iterations of Gaussian quadrature using one node gives equation 4.32

$$T_4 = \frac{k_t}{k_p[CTA]_0}\sqrt{\frac{r_R}{k_t}}\Big[-\ln\left(1-\frac{\alpha}{4}\right)\Big]_0^{\alpha} \tag{4.32}$$

Writing the integral solution 4.32 in its Taylor form gives equation 4.33

$$T_4 = -\frac{k_t}{k_p[CTA]_0}\sqrt{\frac{r_R}{k_t}}\Big\{-\frac{\alpha}{4}-\frac{\alpha^2}{32}-\frac{\alpha^3}{192}+...\Big\} \tag{4.33}$$

Taking a single Taylor term gives a simplified formula for dispersity as a function of conversion.

$$T_4 \approx \frac{k_t}{k_p[CTA]_0}\sqrt{\frac{r_R}{k_t}}\frac{\alpha}{4} \tag{4.34}$$

A more accurate mathematical treatment is possible, whereby the integral is solved analytically and expressed as a Taylor expansion with one and two terms.

Analytical Integrating T_4 analytically twice and simplifying down gives equation 4.35. Subsequently, the log value can be written as a Taylor series to give equation 4.37.

$$T_4 = -\frac{2}{\alpha^2}\frac{k_t}{k_p[CTA]_0}\sqrt{\frac{r_R}{k_t}}\frac{2(\ln(1-\alpha)(\alpha^2-1)-(2-3\alpha)\alpha}{4} \tag{4.35}$$

$$T_4 = -\frac{k_t}{k_p[CTA]_0}\sqrt{\frac{r_R}{k_t}}\Big\{\frac{(2-3\alpha)}{2\alpha}+\frac{(\alpha^2-1)}{\alpha^2}\left(-\alpha-\frac{\alpha^2}{2}-\frac{\alpha^3}{3}+...\right)\Big\} \tag{4.36}$$

Taking a single Taylor term from the analytically derived T_4 in this case is more accurate than the Gaussian quadrature method.

$$T_4 \approx \frac{k_t}{k_p[CTA]_0}\sqrt{\frac{r_R}{k_t}}\left(\frac{\alpha}{3}+\frac{\alpha^2}{12}\right) \tag{4.37}$$

Accounting for RTD

It has been demonstrated in Chapter 3 that the volume of the reactor affects the RTD. The 2 mL coil required much slower flow-rates, which reduced the accuracy of the pump. The residence time distributions obtained for the PDMAm tracer were broader than the DMAm equivalent; viscosity has been shown by Reis *et al.*[123] has shown viscosity to affect the residence time distributions. Using the RTD for a polymer sample in Chapter 3.

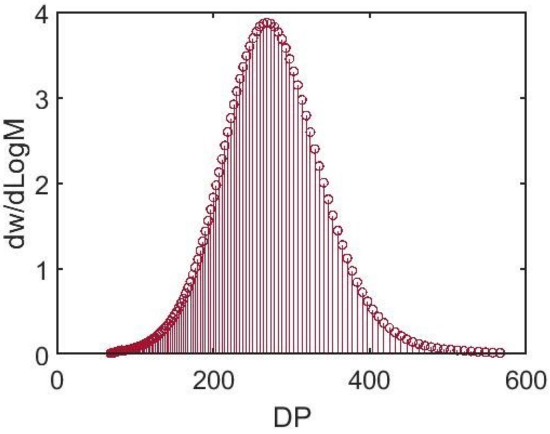

Figure 4.9: Distribution of molecular weights as obtained by GPC for PDMAm$_{200}$ at 98 % conversion.

$$E(MW) = E(\theta)\frac{dw}{dLogM} \tag{4.38}$$

$$MW = \theta M \tag{4.39}$$

Here, it was assumed that each degree of polymerisation eluted in the GPC experiences its own RTD due to laminar flow. Firstly, each chain in the MWD from batch assuming ideal mixing was multiplied through by the residence time distribution function.

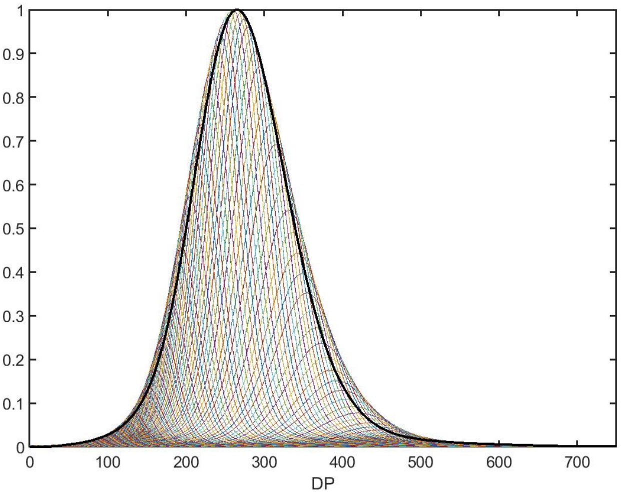

Figure 4.10: RTD (coloured line superimposed onto each of the stems seen in the MW with the batch molecular weight distribution overlayed

A Gaussian fitting function *gmfitdist MATLAB* was used to fit coefficients, μ,σ and c as seen in equation 4.40.

$$G(x) = \frac{1}{\sigma\sqrt{2\pi}} e^{-\frac{1}{2}(\frac{x-\mu}{\sigma})} + c \tag{4.40}$$

The individual Gaussians were then simulated on a known linearly spaced X scale between a DP 0 and 900 and convoluted to give Figure 4.11. Using equations 1.2,1.3 and 1.1 in Chapter 1. The contribution of RTD to the dispersity for the flow platform can be accounted for, seen in Table 4.2.

Table 4.2: Simulated RTD contribution calculations compared to GPC chromatograms from flow

	Experimental^{GPC}	With RTD	Contributuion
Batch	1.0725		
Flow	1.1351	1.1022	0.0277

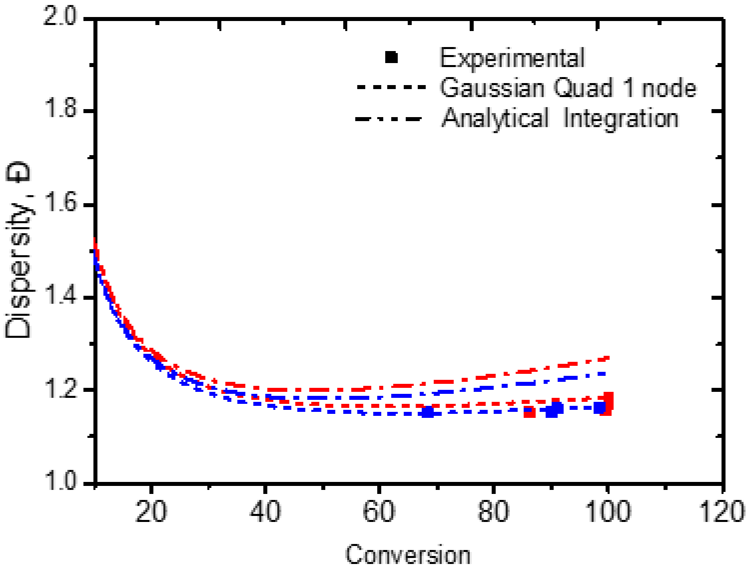

Figure 4.11: Comparison of the model using analytical integration (dotted and dashed) and Gaussian quadrature (short dashed)

If the conversion vs dispersity plots using the Gaussian quadrature method with one node are compared to an analytical integration, the truncated Gaussian quadrature method fits better. A more accurate integration increases Đ, but the experimental data are more closely in agreement with the simpler treatment. This indicates that the assumptions in the mathematical model are insufficient to account for the complexity of the polymerisation system. This includes neglecting the effects of chain transfer to solvent, which could lead to an overestimation of T_4. The final dispersity expression used can be given by the following.

$$Đ = 1 + \frac{[CTA]_0}{[M]_0\alpha} + \frac{k_p}{k_{tr}}\left(\frac{2}{\alpha} - 1\right) + \frac{k_t}{4[CTA]_0 k_p}\left(\sqrt{\frac{r_R}{k_t}}\right)\alpha \tag{4.41}$$

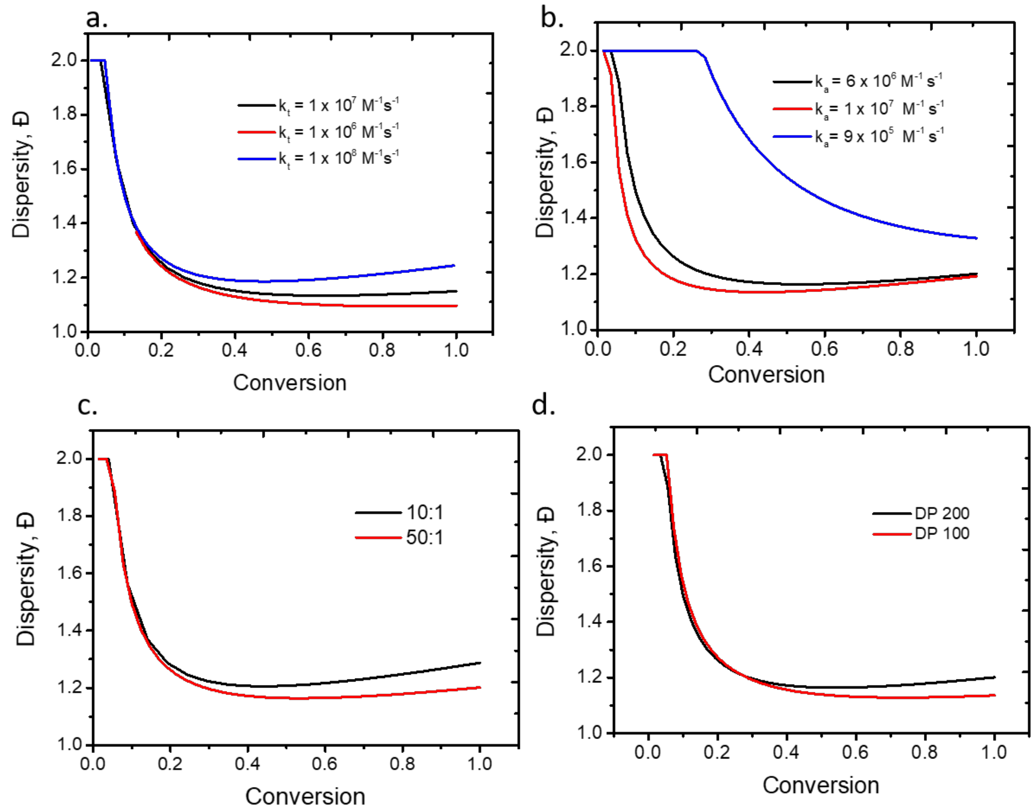

Figure 4.12: simulated dispersity vs conversion plots using the rate constants for DMAm:BM1640:VA044 (200:1:0.02) unless otherwise changed in the simulation, investigating the effect of the magnitude of (a) k_t, (b) k_a, (c) $[CTA]_0 : [I]_0$ and (d) DP are changed.

When changing the termination rate constant, as shown in figure 4.12.a. If k_t was increased, an increase in the Đ was observed. Higher Đ were seen for a larger k_t, this corresponds to a faster rate of termination which would cause broadening of the MWD. As shown in Figure 4.12 the minimum of the Đ was lower for the higher k_a; which was expected as increased transfer will increase control and afford a higher transfer coefficient. A higher initiator concentration and higher DPs as shown in Figure 4.12. c and d. lead to higher Đ. The higher initiator concentrations cause an increase in rate of initiation, which leads to increased termination due to a higher concentration of propagating radicals. Higher target DPs mean there was a higher concentration of monomer, this will lead to increased rate of re-initiation, as accounted for by the model. This would have led to increased propagation and chain growth, leading to a wider MWD and higher dispersity. Following simulation and looking at the effect of each rate constant, the model was further validated using experimental literature data and experiments conducted in this chapter.

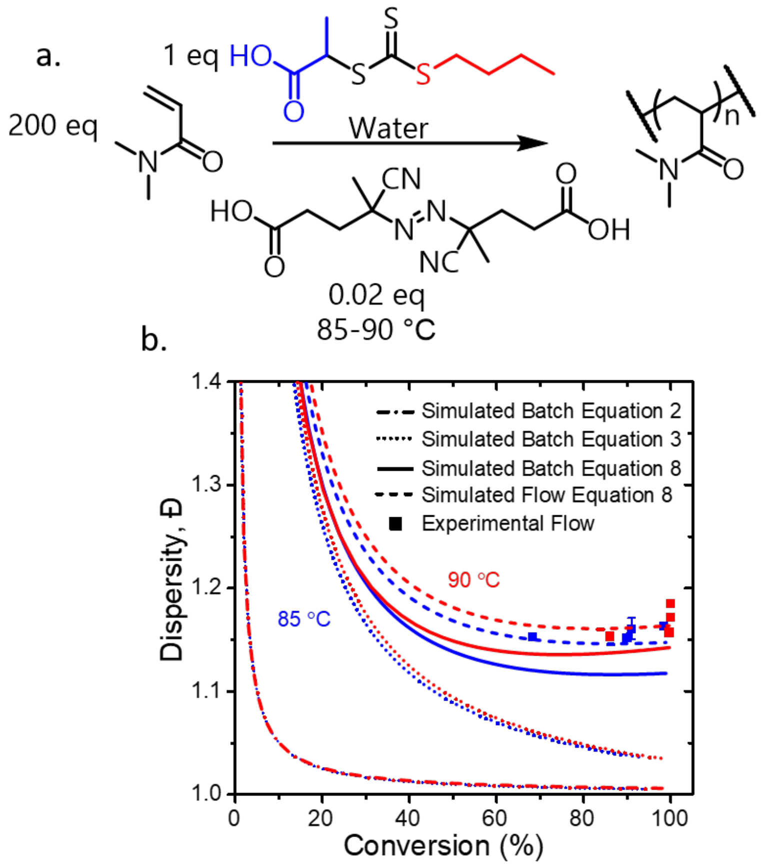

Figure 4.13: (a) Reaction scheme for DMAm : TTC2: ACVA 200:1:0.1 at 30 w/w % (b) Comparison of experimental dispersity and conversion (squares) obtained for DMAm : TTC2: ACVA 200:1:0.1 at 30 w/w % in flow versus the simulated batch(solid line)and flow (dashed line) reaction using equation 4.41. Monomer conversion was obtained via online flow-NMR, molecular weight distributions were obtained using an offline GPC calibrated with PMMA standards. The data shown here was subsequently corrected to consider the residence time distribution within the reactor. The simulated dispersity using equations 4.8 and 4.9 where no termination was accounted for.

Comparing the simulated data generated from Equation 4.41 at two temperatures to the experimental data, the data at 85 ° lies on the simulated trace suggesting the model works well for this system. Equation 4.41 fits the experimental data better than the existing literature equations 4.9 or 4.8. Although the use of flow chemistry has advantages in the context of efficient heat transfer, the fluid dynamics mean an inherent feature was a residence time distribution (RTD), which causes higher dispersity[123] even in narrow tubing (1/16”) – consequently the model needs an additional term to account for this. Assuming, that residence time of each polymer chain at a set flow rate can lie anywhere on the RTD, the RTD function (E(θ) was superimposed onto each molecular weight in the MWD forming a distribution of distributions. A fitting function was used in MATLAB to obtain the Gaussian fitting parameters. Using the fitting parameters, the Gaussians were simulated and merged. The dispersity can then be calculated and the RTD contribution determined through subtraction. It is important to note the effect of viscosity on the RTD seen in the SI, as the viscosity increases with the degree of polymerization the dispersity will also increase.[123]

Following successful validation for DMAm, literature values for the solution RAFT polymerization of acrylamide (AAm),[243] acrylic acid (AA),[244] and methylacrylate (MA)[245] were compared to the model. Firstly, the reported experimental conversion was entered into Equation 4.41 then the conditions were simulated using the kinetic model coupled to Equation 4.41. The resultant data can be seen in Table 4.3. The rate parameters can be found in the appendix for this section. For acrylic acids, the presence of the acid group can cause issues so often rate parameters for kp account for the pH.[240] Rate parameter tables for each system can be found in the Appendix C.

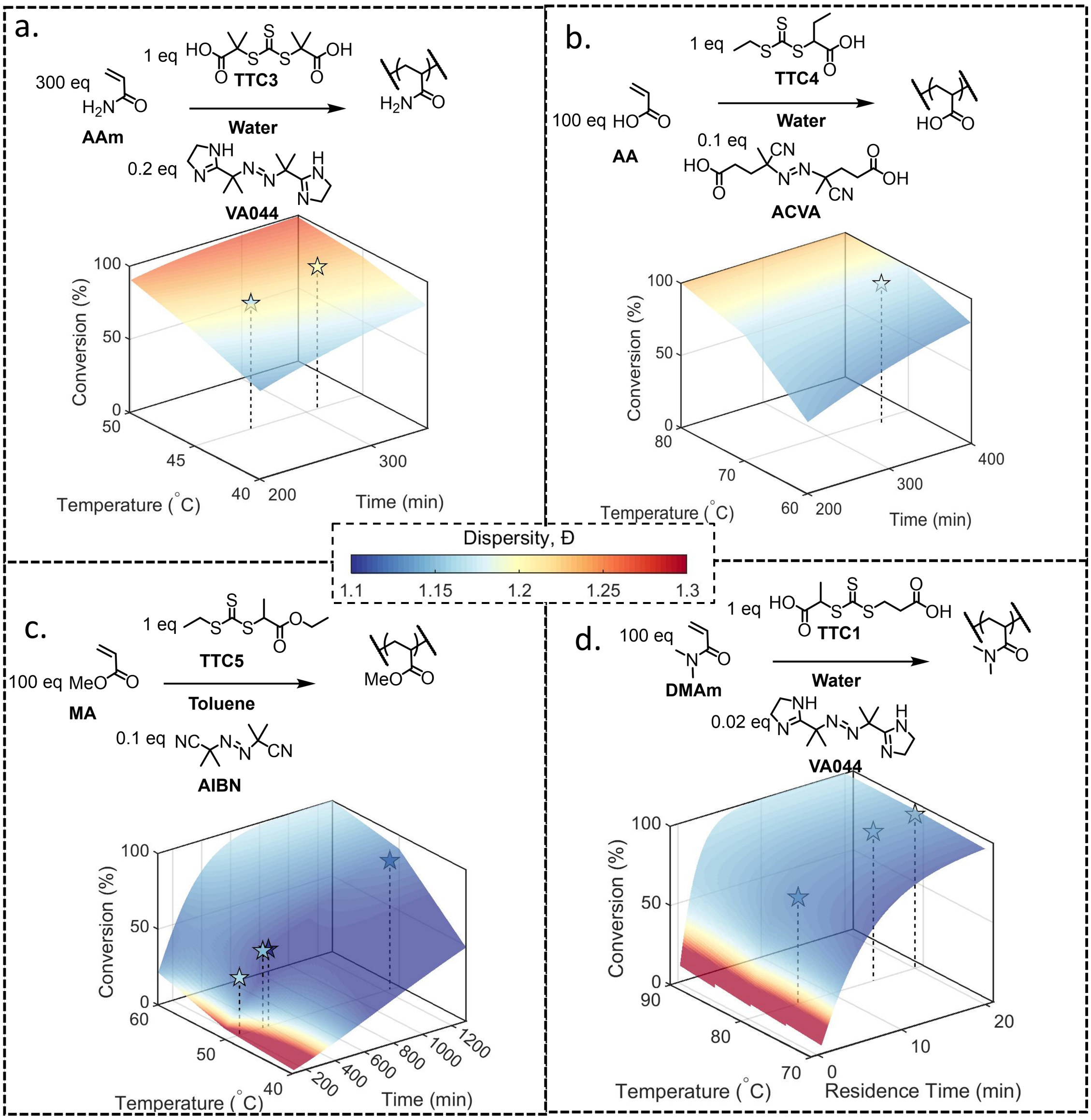

Figure 4.14: *in-silico* kinetic surfaces with literature data (stars) imposed for the polymerization of (a) AAm,[243] (b) AA,[244] (c) MA,[245] and (d) DMAm (this work). The colour of the star and surface corresponds to dispersity and the colourbar (blue = low $Đ$, red = high$Đ$.) The literature values for AAM was reproduced from Liang *et al.*[243] with permission from Springer ©2016, AA was reproduced from Ji *et al.*[244] with permission from Taylor and Francis ©2010, MA was reproduced from Wood *et al.*[245] with permission from CSIRO publishing ©2007.

Broad agreement between the literature data and simulation was observed (Figure 4.14). Deviations for both conversion and dispersity were limited (Table 4.3) for AAm and AA. For AAm the effect of initiator can be observed; as the initiator concentration was increased the reaction takes less time to reach high conversion. This was also reflected in the simulated dispersity, the increased radical concentration increases the rate of termination leading to broader MWDs A systematic underestimation of conversion was observed for MA, which could be attributed to a lower concentration of solids (10 w/w %)[246] used for the rate constant measurement compared to the experimental data (30 w/w %),[245] or the neglection of side reactions that increase the concentration of propagating species. For monomers such as acrylamides and acrylic acid and less bulky acrylates the equation and model work well; however due to the absence of backbiting and cross termination effects, the model fails for bulky acrylates.

4.4 Conclusions

A combined model has been designed to enable computational simulation of the RAFT polymerisation process to guide an automated platform. This combines an effective model for conversion, which could be implemented under isothermal conditions or under polythermal conditions, where the simulation can take into account a varying temperature. These were both validated by conducting the RAFT polymerisation of DMAm in a flow-reactor (operating near isothermally due to efficient heat transfer) or a batch reactor, where a previously recorded temperature profile was used in the simulation. The model for predicting dispersity as a function of the conversion was derived based on block-and-blend theory, with the addition of a novel fourth term quantifying the contribution of the terminative events at higher conversion. This results in an up-turn in the dispersity at high conversion which is typically seen in RAFT polymerisation. This could enable the user to predict the transfer constants of their reaction, through fitting, which are less abundant in the literature. Current methods of identifying propagation and termination rate constants are often given as a range and can vary between groups, the model developed in this thesis could provide a way of bench-marking these rate constants. Finally, to simulate the outcome of reactions in a flow reactor, it was necessary to add a term to account for the contribution of the RTD to the molar mass dispersity. The conversion and dispersity models, and the option for an RTD correction (for flow reactors) were programmed into a computational package which enabled prediction of the outcome of RAFT polymerization using trithiocarbonate RAFT agents for monomers with known k_p. Validation of the model was performed in flow, where the experimental values for conversion and dispersity were in good agreement. Furthermore, the model was also in good agreement with several examples from the literature. Although it is recognised that models may not always reflect the exact polymerization process, it provides an opportunity to better predict the outcome of a RAFT polymerisation reaction which can be used to guide an automated reactor, potentially streamlining closed-loop self-optimization systems which previously had no prior knowledge of the chemistry. With the aim to develop 2nd

Table 4.3: Comparison of literature experimental data conducted in batch (conversion, α, and dispersity, $Đ^{GPC}$) to the dispersity obtained by substituting the experimental conversion into Equation 4.41 $Đ^{th}$) and fully simulated conversion, α^{si} and dispersity,$Đ^{si}$). T = temperature, t =reaction time.

	Monomer	Solvent	CTA	Initiator	[CTA]:[I]	w/w (%)	Temp (∘C)	Time(min)	α (%)	$Đ^{GPC}$	$Đ^{th}$	α^{si}(%)	$Đ^{si}$	Ref
1	Acrylamide	H2O	TTC3	VA044	10:01	15	45	427	87	1.2	1.17	92	1.18	[243]
2	Acrylamide	H2O	TTC3	VA044	05:01	15	45	310	97	1.2	1.22	93	1.22	[243]
3	Acrylamide	H2O	TTC3	VA044	05:01	15	45	250	86	1.17	1.2	86	1.20	[243]
4	Acrylic acid	H2O	TTC4	ACVA	10:01	13	65	360	97	1.18	1.17	99	1.17	[244]
5	Methyl acrylate	Toluene	TTC5	AIBN	10:01	30	50	199	38	1.16	1.11	16	1.14	[245]
6	Methyl acrylate	Toluene	TTC5	AIBN	10:01	30	50	360	51	1.15	1.12	31	1.11	[245]
7	Methyl acrylate	Toluene	TTC5	AIBN	10:01	30	50	399	56	1.13	1.12	35	1.11	[245]
8	Methyl acrylate	Toluene	TTC5	AIBN	10:01	30	50	1236	85	1.12	1.17	87	1.17	[245]
9	Dimethyl Acrylamide	Water	TTC1	VA044	50:01:00	30	80	6	67	1.15	1.15	81	1.15	
10	Dimethyl Acrylamide	Water	TTC1	VA044	50:01:00	30	80	15	94	1.17	1.16	99	1.16	
11	Dimethyl Acrylamide	Water	TTC1	VA044	50:01:00	30	80	20	97	1.19	1.16	99	1.16	

generation reactor that reduces time, cost and environmental impact of optimisation further, the next chapter reports the use of a digitally directed platform. In the next chapter, the model that accounts for RTD from this chapter could be embedded into the graphical user interface, to enable *in-silico* prediction of the objectives obtained from the LHC.

Chapter 5

Digitally Augmented Self-Optimisation of RAFT polymerisation

5.1 Introduction

Self-optimisation of 2D reaction parameter space has already been covered in this thesis in Chapter 2 for the RAFT polymerisation of several monomers. Kinetic understanding can help polymer chemists to direct OVAT approaches to optimise their polymerisations. Houben *et al.*[135] have demonstrated a fully *in-silico* self-optimisation using their MOAL algorithm - in which, out of 84 simulated conditions, only 18 were at the desired 100 nm particle size and full conversion. Overall, it was at experiment 27, when the algorithm found the optimum conditions to make the emulsion polymer. Validation of some of these data points were not concordant with the the model, which led them to run the optimisation experimentally and found the optimum in 17 experiments.[135] More recently, Kandelhard *et al.*[200]have shown the power of multiphysics analysis and kinetic modelling, using commercially available COMSOL and PREDICI software, respectively. Here, they compared the simulations for a series of reactors for their conversion by changing initiator concentration, temperature and residence time. Where they found a 20 mL glass chip with a 2 mL premixing chip were the superior both *in-silico* and experimentally.[200] This is a good example of the use of theoretical knowledge using existing software that can enable computer aided optimisation. In this Chapter, a closed-loop operator independent polymer synthesis platform that used in built knowledge of RAFT kinetics to direct optimisation has been developed. The affect of temperature, residence time and relative initiator concentration

([I]:[CTA]) was investigates. As reported by Gody *et al.*[67] the degree of "livingness" is related to the number of dead chains and not the rate of polymerisation. So initiators with high k_d can be used to increase reaction rates without decreasing the "livingness" too significantly. Experimental Validation showed that the model proposed in Chapter 4 was relatively good at predicting conversion and dispersity for DMAm. Computationally inexpensive models will always have some conditions where they fall apart; however, the ideality can be used to direct an experiment. In precision polymer synthesis, low $Đ$ is desired to synthesise nano-objects, high conversion is also desirable to reduce the work-up and improve the sustainability. Although, ML algorithms have reduced the optimisation time involved; hypothetically, the number of number of experiments required to find the trade-off could be reduced further. Thus, it was proposed that the model would be a valid enough to train a first iteration of the TS-EMO algorithm to reduce the number of experiments that correspond to dispersity > 1.3, which are typically undesirable for high value polymeric materials, discussed in Chapter 1.

5.2 Experimental

Monomers used in this chapter were N,N-dimethylacrylamide ((DMAm) 99 %, contains 500 ppm monomethyl ether hydroquinone as inhibitor, CAS 2680-03-7) purchased from Sigma Aldrich, tert-butyl acrylamide ((tBuAm), 97 %, CAS 107-58-4) purchased from Alfa Aesar and butyl acrylate ((nBuA) 99 %, contains 10-60 ppm monomethyl ether hydroquinone as inhibitor, CAS 141-32-2) purchased from Sigma Aldrich.
RAFT agents were all purchased from Boron Molecular: 2-(Butylthiocarbonothioylthio)propanoic acid ((TTC1) 95 %, CAS 480436-46-2)
Initiators used were 2,2'-Azobis[2-(2-imidazolin-2-yl)propane]dihydrochloride ((VA044), CAS 27776-21-2), 2,2'-Azobis(isobutyronitrile) ((AIBN), CAS 78-67-1)

The platform in this chapter (shown in Figure 5.1 was comprised of 3 pumps (JASCO PU980 or 1580 HPLC). Here, the reservoirs that were of higher concentration to the target were pumped and diluted in stream. Pump 1 delivers a premixed solution of monomer and CTA with a fixed molar ratio, pump 2 delivers a fixed concentration of initiator and pump 3 delivers solvent to dilute the concentration of initiator and total w/w % of the the reaction mixture. As in Chapter 3 the orthogonal analyses were the same except for the use of DMF/LiBr GPC. Two graphical user interfaces were used in this chapter: (1) a black box fully experimental GUI and (2) a model assisted version. Both platforms were closed-loop and require a set of inputs for defining the reaction parameter space, a target total w/w %, number of training experiments and a set number of experiments predicted by the TS-EMO algorithm.

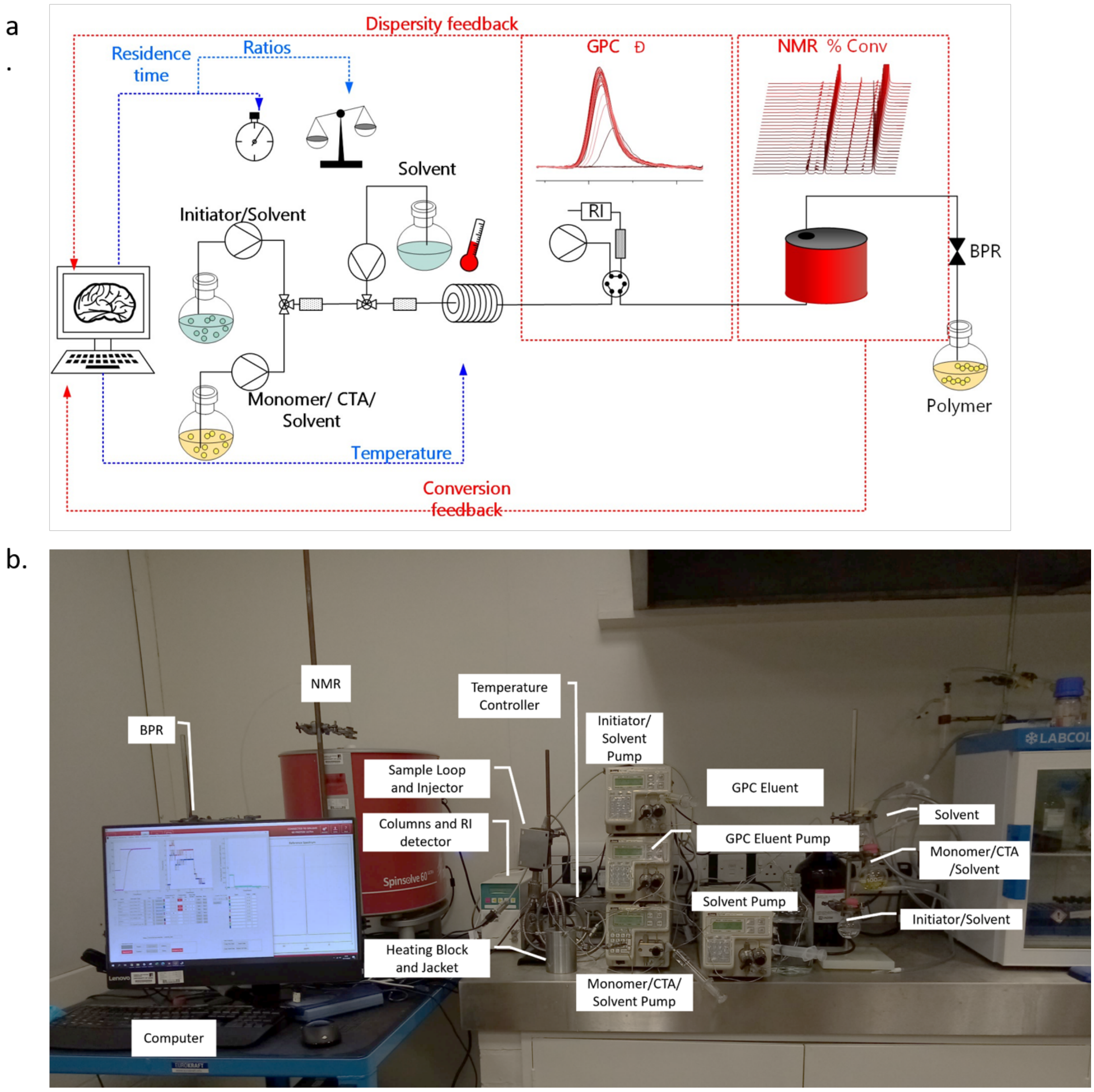

Figure 5.1: (a) Schematic for the 3D reaction parameter space self-optimising platform used here for closed-loop model optimisation of RAFT polymerisation (b) Photograph of the platform showing the pumps, temperature controller, home-built GPC and bench top NMR,

The algorithm for the black-box optimisation involves defining the reaction space by entering the upper and lower bounds of [I]/[CTA], temperature, and residence times. In addition, a rounding limit is required that describes the space limit between each variable of the reaction space. For the black-box platform, a Latin hypercube sampling algorithm finds pseudo-random conditions for the reactor to conduct experimentally. These data form an objective function that was returned to TS-EMO. The algorithm was stopped when sufficient reaction space was evaluated.

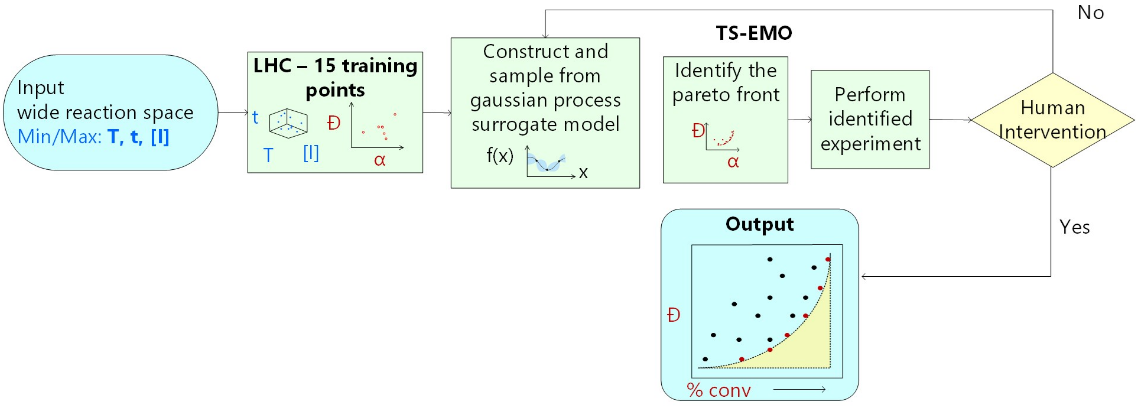

Figure 5.2: Implementation of the TS-EMO algorithm into the multi-pump platform for black-box optimisation

5.2.1 Black-box self optimisation of 3D reaction parameter space for DMAm

Firstly, concentrated reservoirs were prepared; these were diluted in the stream to 30 w/w %. To a solution of DMAm (250 g, 2.52 mol) in water (169.1 g), TTC1 (3.00 g, 0.013 mol) was added. A separate flask was charged with VA044 (0.73g , 2.27 mmol) dissolved in water(202.9 g). A third flask was charged with water. These were kept at room temperature, and the solutions were not degassed under an atmosphere of nitrogen. 15 training experiments were suggested by a Latin hypercube algorithm; the limits of these inputs can be seen in Table 5.1

Table 5.1: The limits used in the implementation of the algorithms for DMAm in the presence of TTC1 in a 200: 1 ratio using VA044 as the initiator in water with a regent content of (30 w/w% 200:1:x) each TS-EMO iteration suggested a single experiment.

Input	Lower limit	Upper limit	Variance limit
Temperature (°C)	50	80	2
[I][CTA] (1:x)	0.09	0.04	0.005
Residence time (min)	5	20	1

5.2.2 Black-box self optimisation of 3D reaction parameter space for nBuA

Firstly, concentrated reservoirs were prepared - these were diluted in stream to 30 w/w %. In a solution of nBuA (200 g, 1.56 mol) in 1,4-dioxane (134.7 g), TTC1 (1.86 g, 70 mmol) was added. A separate flask was charged with AIBN (0.289g , 1.76 mmol) dissolved in 1,4-dioxane (202.1 g). A third flask was charged with water. These were kept at room temperature, and the solutions were not degassed under an atmosphere of nitrogen. 15 training experiments selected using a Latin Hyper Cube algorithm were conducted, the limits for these inputs can be seen in Table 5.2

Table 5.2: Limits used in the implementation of the algorithms for nBuA in the presence of TTC1 in a ratio of 200:1 using AIBN as the initiator in 1,4-dioxane with a reagent content of 30 w/w %. Each TS-EMO iteration suggested a single experiment.

Input	Lower limit	Upper limit	Variance limit
Temperature (°C)	70	100	2
[I][CTA] (1:x)	0.09	0.04	0.005
Residence time (min)	5	20	1

The model-assisted platform uses the validated model from Chapter 2 to conduct the LHC experiment with 15 training points. This was then fed into the first iteration of TS-EMO (TS-EMO1), suggesting experiments with greater spread to avoid clustering. These were conducted, and the TS-EMO proceeded identically to the completely experimental platform using only the experimental points (TS-EMO2).

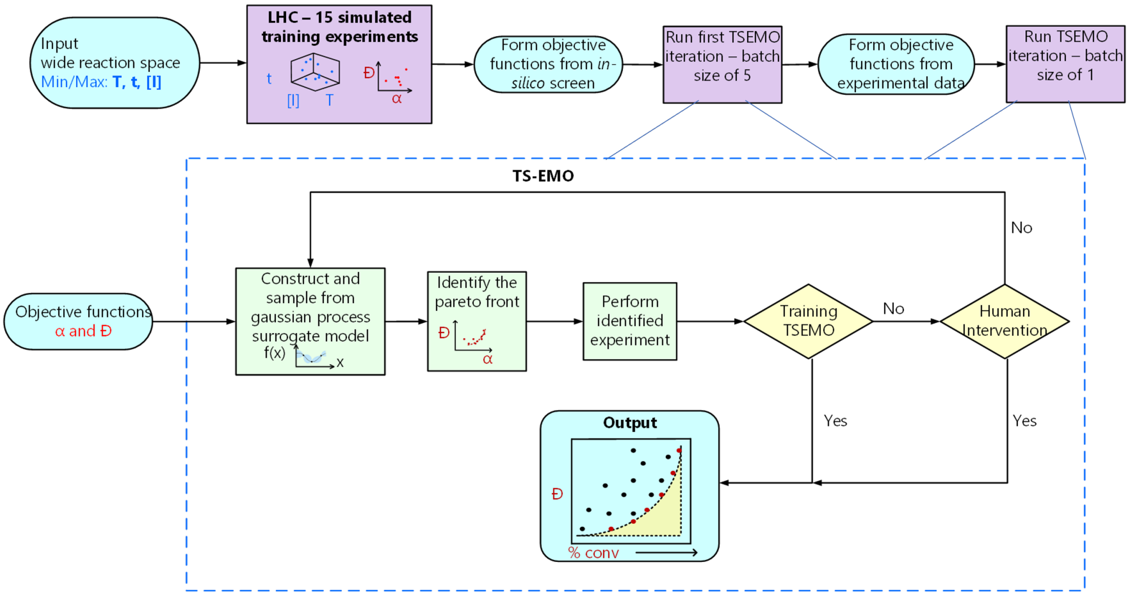

Figure 5.3: Flow diagram for the digitally augmented platform showing where the model and TS-EMO was implemented

5.2.3 Model assisted self optimisation of 3D reaction parameter space for DMAm

Firstly, concentrated reservoirs were prepared- these were diluted in stream to 30 w/w %. To a solution of DMAm (150 g, 2.52 mol) in water (101.4 g) and TTC1 (1.80 g, 7.56 mmol) was added. A separate flask was charged with VA044 (0.73g , 2.27 mmol) dissolved in water(202.9

g). A third flask was charged with water. These were kept at room temperature, and the solutions were not degassed under an atmosphere of nitrogen. 15 training experiments selected by a Latin Hyper Cube algorithm were conducted *in-silico*. The objective function from the training simulation was then fed into the first TS-EMO[a] iteration and a batch size of 5 was set. The 5 suggested experiments were conducted and the results were fed into TS-EMO[b]; From this the experiments were suggested in batches of one. The limits for these inputs can be seen in Table 5.3

Table 5.3: [a]Limits used in the implementation of the first TS-EMO iteration for the RAFT polymerisation of DMAm in the presence of TTC1 using VA044 as the initiator in water at a reagent content of 30 w/w %. The objective data from the first iteration suggested five potential conditions to ensure a large directed exploration. [b]Limits used in the implementation of all other iterations of the TS-EMO

Input	Lower limit	Upper limit	Variance limit
Temperature (°C)[a]	50	80	6
Temperature(°C)[b]	50	80	2
[I]:[CTA] (1:x)[a]	0.09	0.04	0.015
[I]:[CTA] (1:x) [b]	0.09	0.04	0.005
Residence time(min) [a]	5	20	3
Residence time (min)[b]	5	20	1

5.2.4 Model assisted self optimisation of 3D reaction parameter space nBuA

Firstly, concentrated reservoirs were prepared - these were diluted in stream to 30 w/w %. To a solution of nBuA (200 g, 1.56 mol) in 1,4-dioxane (134.7 g), TTC1 (1.86 g, 70 mmol) was added. A separate flask was charged with AIBN (0.289g , 1.76 mmol) dissolved in 1,4-dioxane (202.1 g). A third flask was charged with water. These were kept at room temperature, and the solutions were not degassed under an atmosphere of nitrogen. 15 training experiments were conducted using a Latin Hyper Cube algorithm were conducted *in-silico*. The objective function from the training simulation was then fed into the first TS-EMO[a] iteration and a batch size of 5 was set. The 5 suggested experiments were conducted and the results were fed into TS-EMO[b]; From this the experiments were suggested in batches of one. The limits of these inputs can be seen in Table 5.5.

Table 5.4: [a]Limits used in the implementation of the first TS-EMO iteration for the RAFT polymerisation of nBuA in the presence of TTC1 using AIBN as the initiator in 1,4-dioxane with a reagent content of 30 w/w %. The objective data from the first iteration suggested five potential conditions to ensure a large directed exploration. [b]Limits used in the implementation of all other iterations of the TS-EMO

Input	Lower limit	Upper limit	Variance limit
Temperature (°C)[a]	70	100	6
Temperature(°C)[b]	70	100	2
[I][CTA] (1:x)[a]	0.09	0.04	0.015
[I][CTA] (1:x) [b]	0.09	0.04	0.005
Residence time(min) [a]	5	20	3
Residence time (min)[b]	5	20	1

5.2.5 Model assisted self optimisation of 3D reaction parameter space for tBuAm

Firstly, concentrated reservoirs were prepared - these were diluted in stream to 20 w/w %. To a solution of tBuAm (164.7 g, 1.30 mol) in methanol (199.3 g), TTC1 (1.54 g, 6.48 mmol) was added. A separate flask was charged with AIBN (0.19 g , 1.18 mmol) dissolved in methanol (242.0 g). A third flask was charged with water. These were kept at room temperature, and the solutions were not degassed under an atmosphere of nitrogen. 15 training experiments selected using a Latin Hyper Cube algorithm *in-silico.* The objective function of the training simulation was then fed into the first TS-EMO[a] iteration and a batch size of 5 was set. The 5 suggested experiments were conducted and the results were fed into TS-EMO[b]; From this the experiments were suggested in batches of one. The limits for these inputs can be seen in Table 5.5.

Table 5.5: [a]Limits used in the implementation of the first TS-EMO iteration for tBuAm in the presence of TTC1 using AIBN in methanol, at a reagent content of 20 w/w %. The objective data from the first iteration suggested five potential conditions to ensure large directed exploration. [b]Limits used in the implementation of all other iterations of the TS-EMO

Input	Lower limit	Upper limit	Variance limit
Temperature (°C)[a]	70	100	6
Temperature(°C)[b]	70	100	2
[I]:[CTA] (1:x)[a]	0.09	0.04	0.015
[I]:[CTA] (1:x) [b]	0.09	0.04	0.005
Residence time(min) [a]	5	20	3
Residence time (min)[b]	5	20	1

5.3 Results and Discussion

Displaying data with increasing numbers of variables and objectives is even more of a challenge in this chapter. Here, bubble plots are used, the x axis in all plots is temperature, the y axis is [I]:[CTA] and the z axis is the residence time. The size of the circle is the conversion where increasing circle diameter corresponds to increasing conversion. The colourmap is kept the same as in Chapter 2 where a darker blue circle corresponds to lower $Đ$. Here, numbers have been provided to indicate which iteration of the TS-EMO they were predicted. The objective plots are kept the same as in Chapter 2 for the fully experimental optimisations. For the model assisted optimisations the *in-silico* LHC is the black diamonds, the first iteration of TS-EMO used for training is the magenta triangles and the subsequent TS-EMO iterations are the blue squares. In this results section, the fully experimental (black-box) optimisation is compared to the model-assisted experiments for the RAFT polymerisations of DMAm and nBuA. The digitally augmented method was subsequently used for the polymerisation of tBuAm.

5.3.1 Black-box self optimisation of 3D reaction parameter space for DMAm

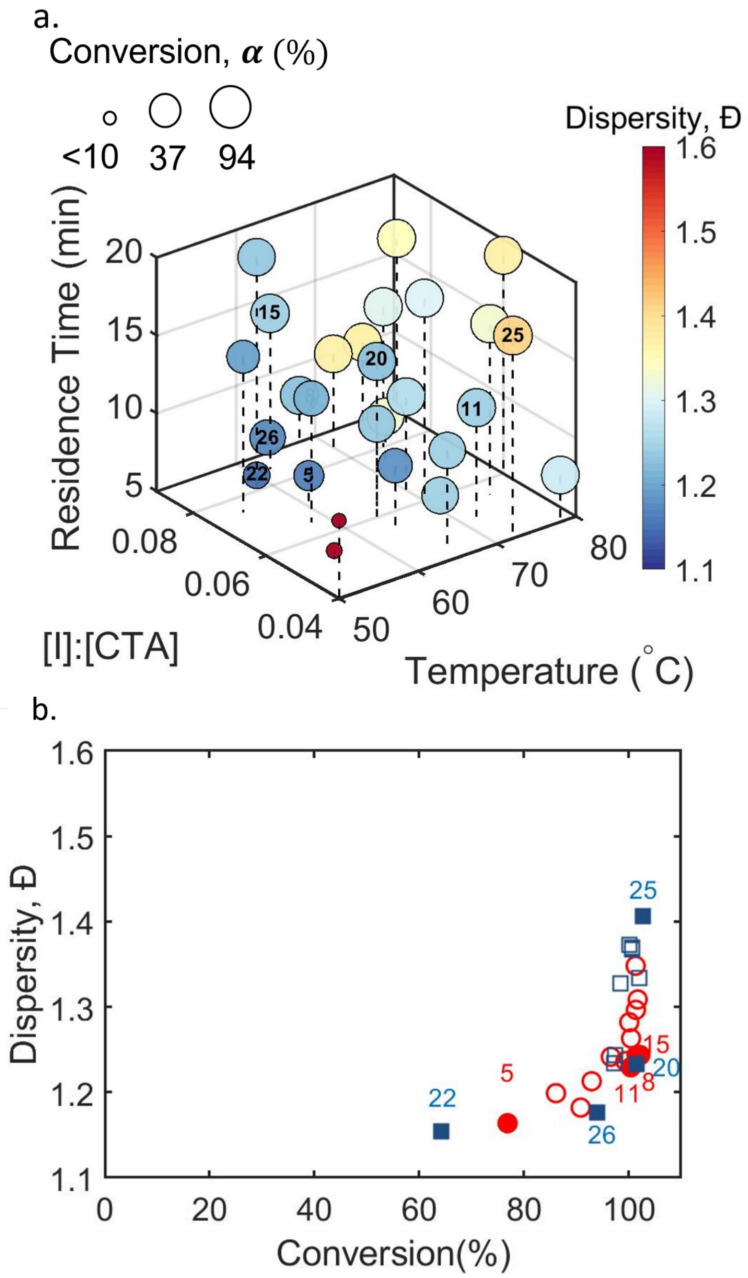

Figure 5.4: (a) 3D Blackbox closed loop optimisation for the RAFT polymerisation of DMAm in the presence of TTC1 using VA044 as the initiator, (200:1:x) where the axes were the reaction conditions used in the optimisation (z = Residence time, y = [I]:[CTA] and x = temperature. The circle size corresponds to monomer conversion. Here, a large circle is indicative of higher conversion and a small circle is indicative of low conversion. The colour of the bubble represents dispersity, where the darker the blue the lower the dispersity and the darker the red the larger dispersity. The number highlighting certain bubbles indicates points that lie on the Pareto front.(b) Objective plot of dispersity vs conversion demonstrating the responses from 15 LHC experiments (red circles) and 13 TS-EMO experiments (blue squares), the filled data points with numbers correspond to the points in the optimisation that lie on the Pareto front

An optimisation was conducted with 15 training experiments for the UF RAFT polymerisation of DMAm, shown in Figure 5.4. The training experiments trained a TS-EMO algorithm that allows exploration of the Pareto front. The continuity in the dispersity colour map in Figure 5.4. a and the defined Pareto front in Figure 5.4. b. was indicative of a well-behaved RAFT polymerisation. Conversions >100 % were obtained; however, this was due to the error associated with the automated NMR baseline. Generally, at low temperatures, lower [I]:[CTA] and shorter residence times were observed with high Đ and low conversion. The data in Figure 5.4 suggests that as long as there are sufficient initiator radicals in the solution and the solution spends enough time in the reactor, high conversion will be achieved. It also shows that for DMAm, too many initiator radicals produced in a given time can lead to increased termination and greater Đ. The effect of CTA:initiator concentration is reflected by the tradeoff in the "livingness" of the reaction and how fast the reaction goes. The degree of formation of dead polymer, leading to higher is not affected by the rate of polymerisation but rather the number of radicals present in the system through-out the polymerisation.[29] In Figure 5.4 the lowest Đ was observed at low temperatures and short times, with the lowest Đ and highest conversion seen at a temperature of 58 °C after 6 minutes with [I]: [CTA] of 0.08. This set of conditions was found using the TS-EMO algorithm after 22 experiments and corresponds to a conversion of 64 % with a Đ of 1.15. Alternatively, at a temperature of 64 °C after 15 minutes with an [I]:[CTA] of 0.06, the highest conversion non-dominated solution, that is within the error of the experiment, with the lowest Đ was also identified by the TS-EMO algorithm after 21 experiments. These conditions correspond to conversion >100 % with a Đ of 1.23. There were two high dispersity and low conversion data points shown in Figure 5.4 that were identified in [I]:[CTA] between 0.04 and 0.05 at low temperatures; suggesting that the initiator concentration severely limited the polymerisation rate in this region of the reaction space; these were not seen in the objective plot in Figure 5.4. b. as the limits of the y axis were between 1.1 and 1.6 for clarity when observing the Pareto front data points. To assess the effect of all independent variables on each of the objectives and whether a linear regression will be suitable to model the reaction further, a multiple linear regression model, using the *Statistics and Machine Learning Toolbox* in *MATLAB*, was fit to each objective set (see the appendix for residuals data).

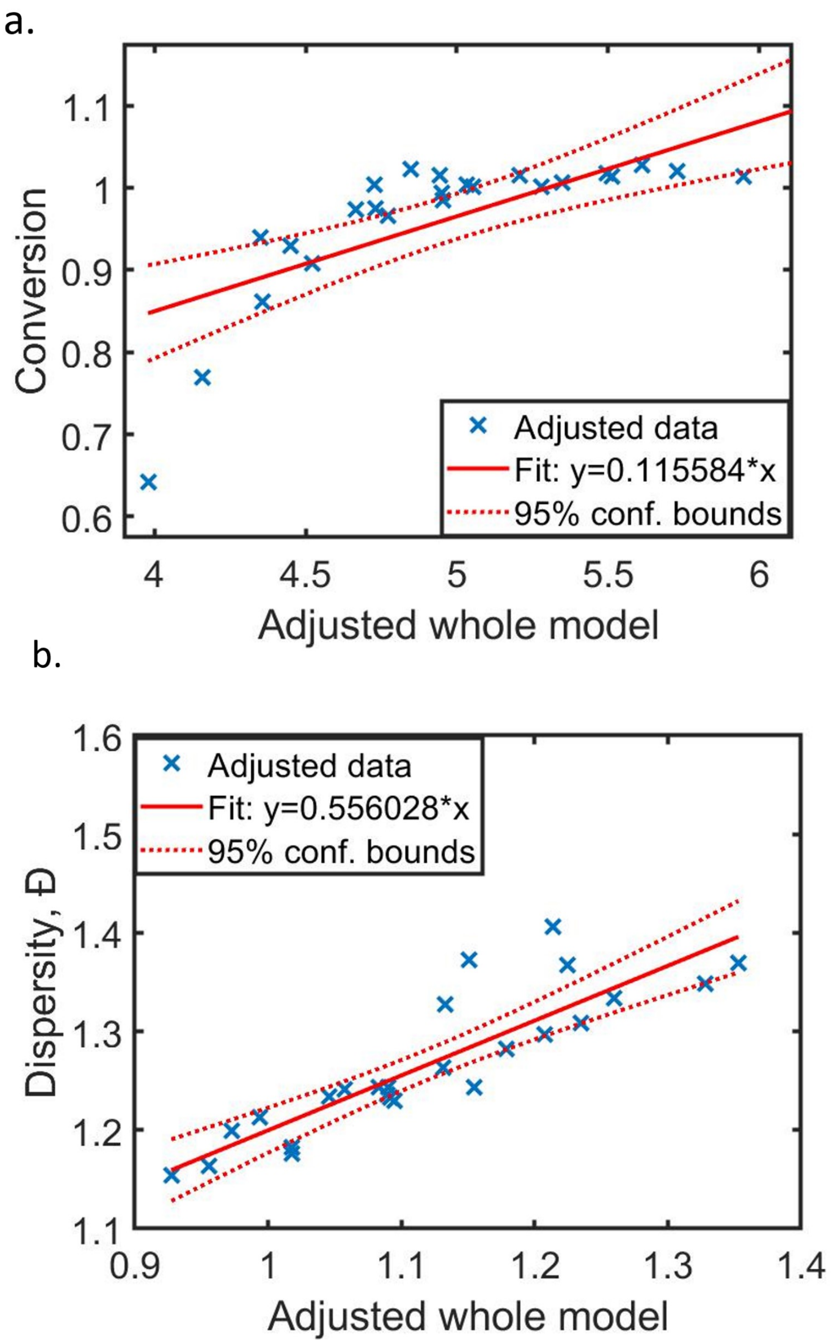

Figure 5.5: Regression analysis plots of (a) conversion and (b) dispersity for the the black box experimental optimisation of DMAm in the presence of TTC1 using VA044 as the initiator at a ratio of 200:1:x(=0.04-0.09), where the x and y axes are the adjusted model and objectives, respectively. The data points represent the real data, the solid red line is the predicted linear regression model and the dotted red lines represent the 95 % confidence limits. The x axis was adjusted due to the presence of 3 independent variables which uses the Frisch-Waugh-Lovell theorem to account for all variables.

There are a series of assumptions that must be met before a multiple linear regression model is implemented. The variables must be continuous, there must be a linear relationship between the independent and dependent variables, there must be no significant outliers, and the residuals exhibit a normal distribution about the regression model. To fit the regression models, data where the conversion was low enough that there was no relevant GPC trace were treated as outliers. The RMSE tells us how well a prediction model fits the data, for the conversion regression model in Figure 5.5. a, the RMSE was 0.067, while the dispersity regression model was 0.037. Low RMSE values were indicative of a good model and increased reliability in predicting objectives. A large proportion of the experimental data points shown in Figure 5.5. a lie above the upper 95 % confidence limit, there were two anomalous points that appeared at low conversions below the 95 % confidence limit, suggesting that the prediction model would fall apart at low conversions. For this instance, a non-linear regression was more appropriate. For the dispersity regression model in Figure 5.5. b, many of the experimental data points lie within the 95 % confidence bounds, suggesting a strong correlation between the independent variables and the dispersity. Four data points exist above the upper 95 % of the linear regression, indicating that these do not fit the prediction as well as the others. These points were identified at longer residence times with a higher initiator concentration; therefore, it was not unusual for MWD to broaden and $Đ$ to increase under these conditions. Multiple regression indicates that the reaction is predictable at low residence times, where the reaction has not yet reached completion.

5.3.2 Model assisted self optimisation of 3D reaction parameter space for DMAm

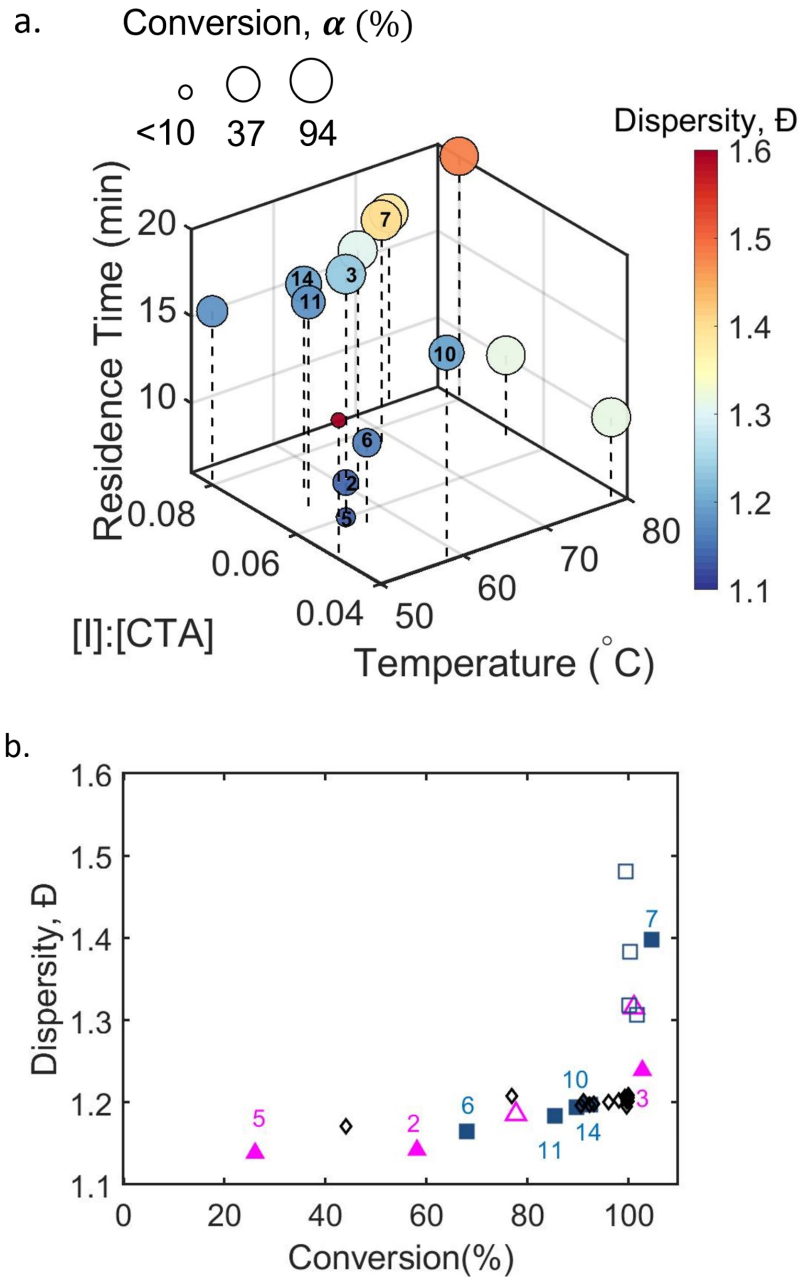

Figure 5.6: (a) 3D Model-Assisted Self Optimisation for the aqueous RAFT polymerisation of DMAm in the presence of TTC1 using VA044 as the initiator at a ratio of 200:1:x(0.04-0.09) Where circle size corresponds to higher conversion and colour represents dispersity. The size of bold circle corresponds to the conversion. (b) Objective plot of dispersity vs conversion where the triangles are the results obtained following the first TS-EMO iteration which utilised an LHC conducted *in-silico* (Black diamonds) to suggest 5 "real" training experiments, TS-EMO1 (magenta triangles) and 2(blue squares)

Firstly, it is worth mentioning that the *in-silico* generated LHC data lie on top of the real experimental data; suggesting the validity of the model for this polymerisation. The model-assisted platform identifies the lowest dispersity at experiment 5 with the highest conversion after 6 min at 56 min using a 0.06 eq of the initiator, where a conversion of 26 % and a Đ of 1.14 which was lower than that found in Figure 5.1. The highest conversion with the lowest Đ can be identified by data point 3 in figures 5.6. a and b. where a Đ of 1.23 was found after 20 min using a 0.06 eq of the initiator at 56 ° C. The difference between experiments 5 and 3 was the residence time; suggesting that a sufficient initiator was still available after 20 min of reaction. The power of the model in finding the Pareto from in the first 5 experiments can be shown by the fact that 4 of 5 of initial TS-EMO generated experiments lie on the Pareto front. A clear reduction in the number of data points required to find the Pareto front was evident in Figure 5.6. a and b by the reduction in the number of data points at low initiator concentrations at high temperatures and the reduction of points at longer residence times. Furthermore, there were significantly fewer data points in conditions leading to conversions >100 %, that were a result of the baselining of the NMR, which reduces the optimisation time. Experimental point 6 was identified after TS-EMO 1 which was similar to the point identified in the black box that took 22 experiments to find, and a higher conversion was found with a Đ only 0.01 higher for the model-assisted platform. This data point here was found using 0.055 initiator eq instead of 0.08, a temperature 2 °C lower and almost twice as long of a reaction time, and this highlights the balance between conversion and control that is crucial in precision polymerisation. Overall, a much clearer Pareto front was observed by training the TS-EMO algorithm with simulated data.

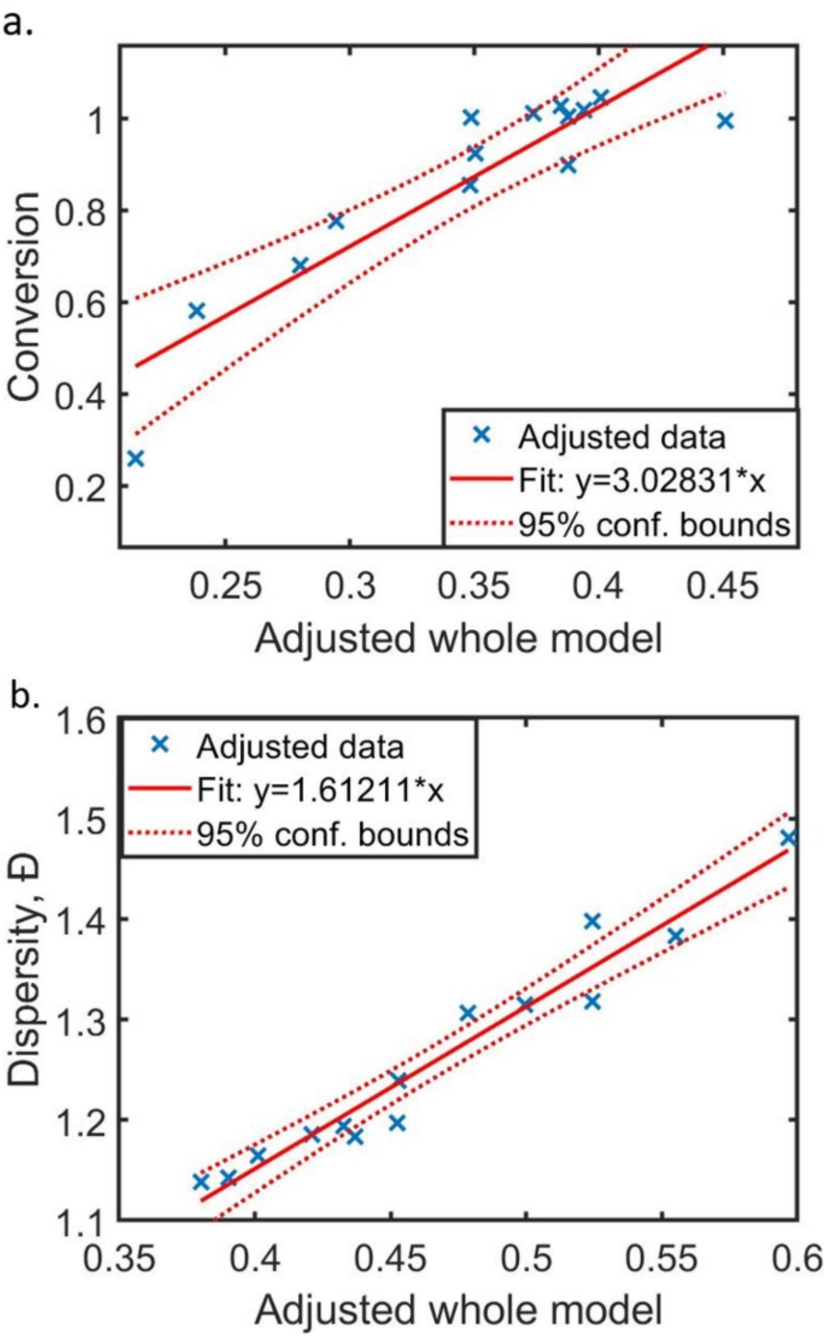

Figure 5.7: Regression analysis plots of (a) conversion and (b) dispersity for the the digitally augmented optimisation for the aqueous RAFT polymerisation of DMAm in the presence of TTC1 using VA044 as the initiator at a ratio of 200:1:x(0.04-0.09). Where the x and y axes were the adjusted model and objectives, respectively. The data points represent the real data, the solid red line is the predicted linear regression model and the dotted red lines represent the 95 % confidence limits. The x axis is adjusted due to the presence of 3 independent variables which uses the Frisch-Waugh-Lovell theorem to account for all variables.

A multiple regression model can also be fitted to the variables and each objective model-assisted platform shown in Figure 5.7 which can be used to further predict the effect of [I]:[CTA], temperature, and residence time on conversion and molar mass dispersity. The effect of all independent variables on the conversion was observed, and here fewer data points can be seen than in the black-box experiment. The abundance of data above 100 % conversion in Figure 5.5. a causes a more significant deviation from linearity with respect to the independent variables model predictions were different compared to Figure 5.7. a. The RMSE of the linear regression for Figure 5.7. a was 0.11 and therefore higher than in Figure 5.5. a; This was probably due to the larger spread in the objective data. The digitally directed optimisation was able to identify lower conversion points, while the completely black-box experiment effectively looked more towards high conversion >100 %. Consequently, the RMSE for directed optimisation was likely to predict lower conversions more accurately than the black box due to fewer experiments conducted at longer residence times. The dispersity regression shown in Figure 5.7. b, has a RMSE of 0.027 which was 0.01 less than the black box. Visually, it can be seen that most of the data points are close to the predicted regression or within the confidence intervals, so it can be concluded that the regression model was reliable. The LHC shown in Figure 5.6. a and b, demonstrate the identification of an approximate minima. It took 30 s to run 15 training experiments *in-silico* on a standard laboratory PC compared to the 560 minutes experimentally shown in Figure 5.4. The initial TS-EMO iteration suggests 5 experiments - 3 out of 5 were identified on the Pareto front. Following TS-EMO 1 the data were then fed into TS-EMO 2 which suggests single condition experiments. Fewer data points in the reaction space region that led to high dispersity and conversions >100 % were observed by the digitally assisted platform. Further points located on the Pareto front were identified in some additional experiments. As a result, there was approximately 40 % reduction in the time taken and the volume of reagents required to optimise the polymerisation of DMAm in flow.

Table 5.6: Table comparing the efficiency of the fully experimental optimisation platform with the model-assisted platform to identify the Pareto front of the RAFT polymerisation of DMAm in the presence of TTC1 using VA044 as the initiator

	Fully Experimental	Digitally Augmented
Number of experiments	28	13
Experimental training points	15	5
Volume of solution (mL)	450	180
Time taken to map Pareto front (h)	17	7

A black-box optimisation of butyl acrylate was carried out as an example of a non-ideal monomer. Several radical species, including secondary propagating radicals and tertiary propagating radicals, are known to exist during polymerisations of nBuA; with the temperature dependence effecting the concentration of these with respect to time. The potential for macromonomer formation is typically seen at temperatures greater than 120 $\circ C$; this is problematic for the bench-top NMR online monitoring as the conversion calculation is dependent on the vinyl integral. To reduce the effect of macromonomer formation, a maximum temperature of 100 °C was selected. Furthermore, a lower temperature bound of 70 °C was selected to challenge to ensure a large reaction space.

5.3.3 Black-box self optimisation of 3D reaction parameter space for nBuA

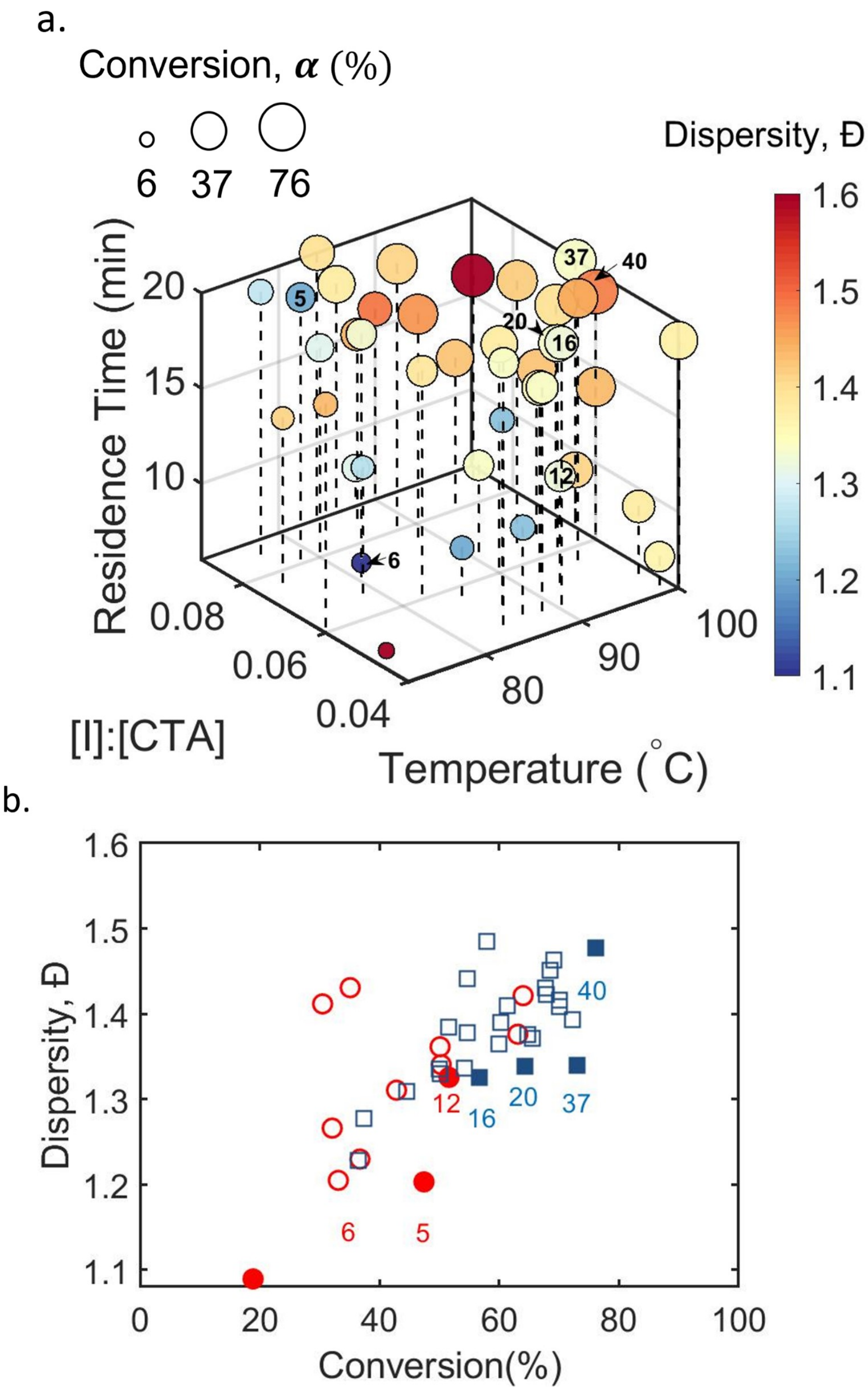

Figure 5.8: 3D black-box closed loop optimisation of (a) conversion and (b) dispersity for the RAFT polymerisation of nBuA in the presence of TTC1 using AIBN as the initiator at a ratio of 200:1:x(0.04-0.09) in dioxane. Where circle size corresponds to higher conversion and colour represents dispersity. (b) objective plot for dispersity vs conversion showing the 15 LHC training experiments(red circles) and the results from the TS-EMO generated example(blue squares), filled circles and squares correspond to data that lies on the Pareto front.

From the black-box optimisation shown in Figure 5.8. a a more discontinuous colour map was observed and a greater variation in conversion; this was indicative of the number of side reactions that occur for acrylates. The condition set corresponding to the lowest *Đ* can be attributed to data point 6 and this was one of the 15 LHC experiments. Here, a conversion of 19 % was obtained with a dispersity of 1.09 after 7 min at 80 ° C using the 0.07 eq of the initiator. Again, more initiators would usually lead to broader MWD and higher *Đ* however, the intermediate temperature and the short residence time indicated that there is relatively good control. The non-dominated solution with the highest conversion and the lowest dispersity can be identified by point 40 where a conversion of 76 % corresponds to a *Đ* of 1.47 which is obtained after 19 min at 100 ° C using a 0.06 eq of the initiator. Under these conditions, the termination rate will be higher and the overall concentration of radicals in solution will be higher, producing broader molecular weight distributions. Of the 42 experiments, only 7 lie on the Pareto front, suggesting that the algorithm struggles to find the Pareto front. In Figure 5.8. b, the LHC data show a good spread in the objective space. The LHC finds the lower conversion part of the trade-off and then finds a further Pareto front at higher conversion by experiment 20. Subsequently, it took until experiments 37 and 40 to identify the Pareto front at 75-80 %. Again, anomalous data points at very low conversion where there was no good GPC trace were treated as outliers and a multiple linear regression analysis was conducted.

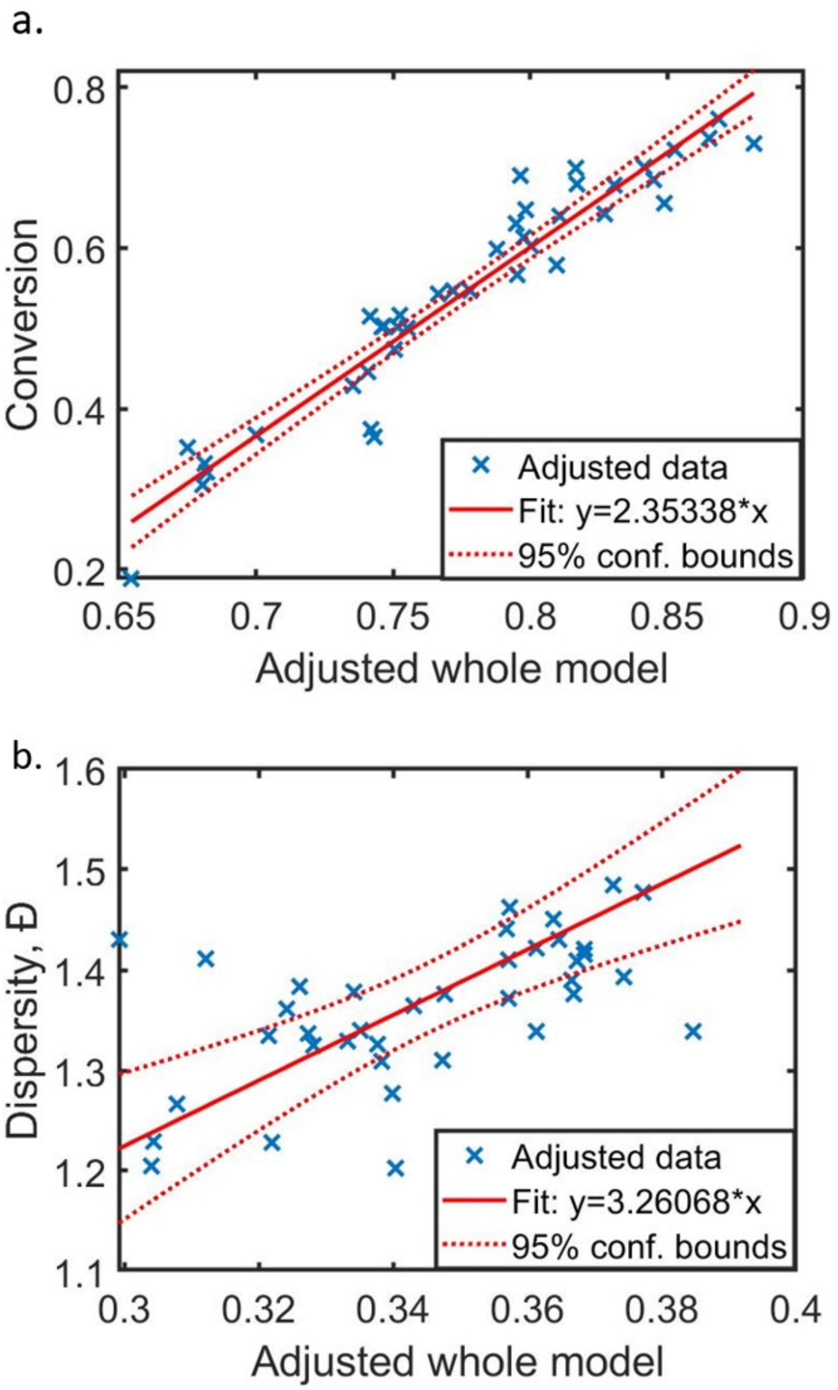

Figure 5.9: Regression analysis plots of (a) conversion and (b) dispersity for the the blackbox experimental optimisation of nBuA in the presence of TTC1 using AIBN as the initiator at a ratio of 200:1:x(=0.04-0.09), where the x and y axes are the adjusted model and objectives, respectively. The data points represent the real data, the solid red line is the predicted linear regression model and the dotted red lines represent the 95 % confidence limits. The x axis was adjusted due to the presence of 3 independent variables which uses the Frisch-Waugh-Lovell theorem to account for all variables

The linear regression showing the effect of all the variables on the conversion shows a good linearity with most of the experimental data points lying within the 95 % confidence limits. The regression analysis for DMAm in Figure 5.5. a shows more spread in the confidence intervals compared to that of nBuA, which was also reflected in the RMSE of nBuA, where an RMSE of 0.042 was achieved. This is likely due to the presence of many data points at full conversion achieved for DMAm which will render poorer predictability by regression analysis. The dispersity data in Figure 5.9. b has much greater 95 % confidence intervals than that seen previously for DMAm in Figure 5.5. b This suggests there is less of a trend between the independent variables and dispersity. Thus the predicted linear regression model is less accurate for nBuA than for DMAm which is typically a result of increased side reactions owing to the formation of secondary propagating radicals.[231] This is reflected in the RMSE of nBuA for $Đ$ where a value of 0.11 was obtained.

5.3.4 Model assisted self optimisation of 3D reaction parameter space for nBuA

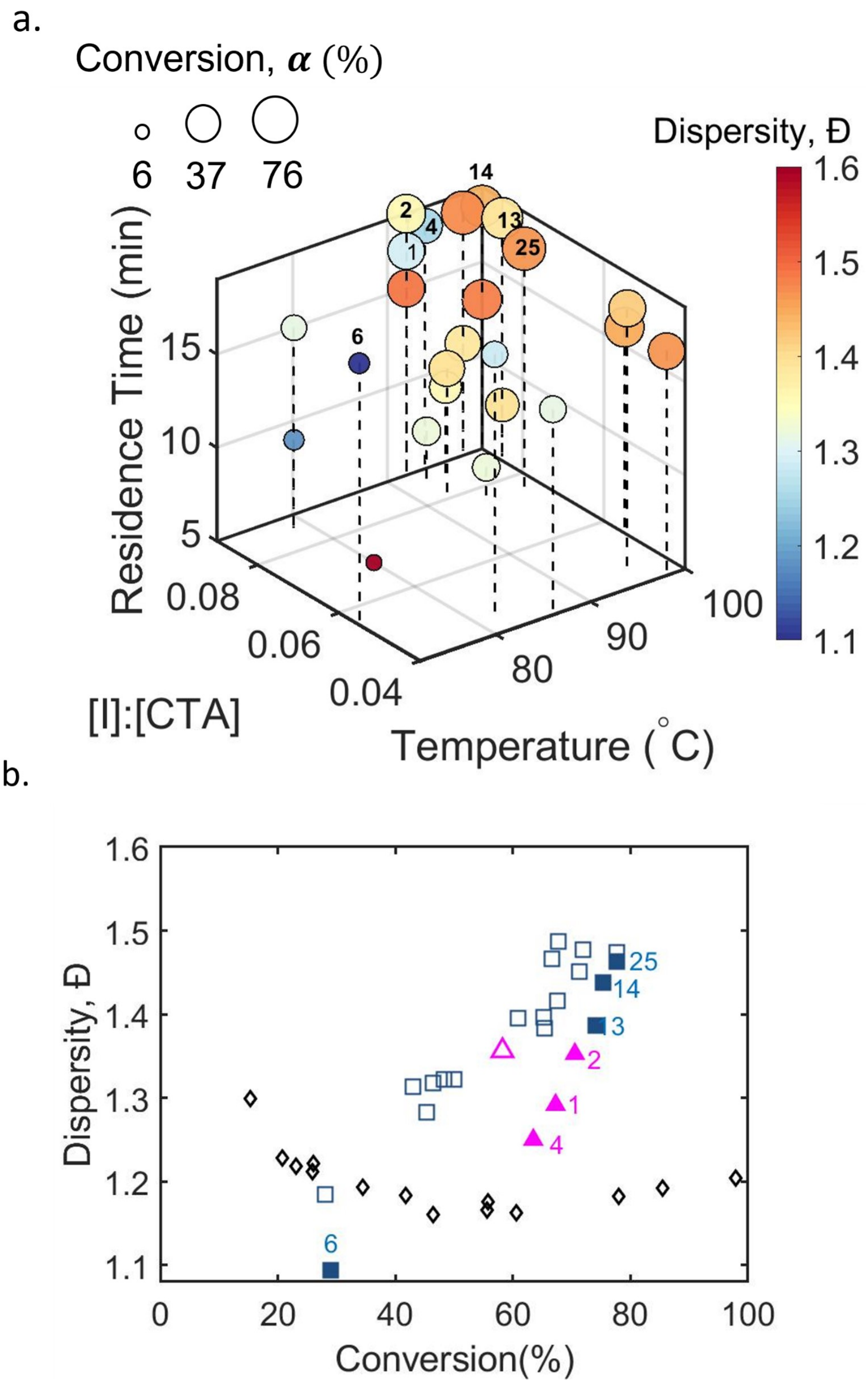

Figure 5.10: (a) 3D model-directed optimisation for the polymerisation of for the RAFT polymerisation of nBuA in the presence of TTC1 using AIBN as the initiator at a ratio of 200:1:x(0.04-0.09) in dioxane. Where circle size corresponds to higher conversion and colour represents dispersity. The size of bold circle corresponds to the conversion. (b) Objective plot of dispersity vs conversion where the triangles are the results obtained following the first TS-EMO iteration which utilised an LHC conducted *in-silico* (Black diamonds) to suggest 5 "real" training experiments, TS-EMO1 (magenta triangles) and 2(blue squares)

The simulated Latin hypercube training experiments shown in Figure 5.10 appear in the centre of the data. The minima of the training data are at a much higher conversion compared to the experimental data. For experimental data, an upturn in dispersity is observed around 20 % compared to 60 % for *in-silico* training data. Similarly, the *in-silico* data reach 100 % conversion, while the experimental data only reach 78 %. Both of these points are indicative of rate retardation, which is not accounted for in the model since the model used is applicable only to RAFT polymerisations that exhibit pseudo-first-order kinetics. Regardless, the model-directed optimisation platform identifies a well-defined Pareto front. Here, the non-dominated solutions with the lowest dispersity and the highest conversion can be identified by point 6 generated by TS-EMO2 in Figure 5.10. b, which corresponds to the dark blue point at 72 °C after 19 min using an initiator ratio of 0.055 obtaining a *Đ* of 1.09. Compared to the fully experimental data, very similar objective data are found in the model-assisted platform, and this point on the Pareto front is found after the same number of experiments. The difference is that the temperature and initiator eq are lower for the digitally trained experiment; this is likely due to the LHC finding the conditions that correspond to a higher level of control. These conditions are low temperatures and low initiator concentrations, since the model operates using rate constants. The non-dominated solution with the highest conversion and the lowest dispersity is identified by the data point at 25 giving a conversion of 78 % and *Đ* of 1.46 corresponding to the data obtained at 98 $°C$ after 17 min using 0.075 eq of the initiator. Compared to the fully experimental nBuA experiment, similar conversion and *Đ* was identified here; however, this is the case lower temperatures and initiator eq are used. It is also important to note the reduction in spread of the data in the model assisted data in Figure 5.10 where is its evident it takes less time to find the Pareto front.

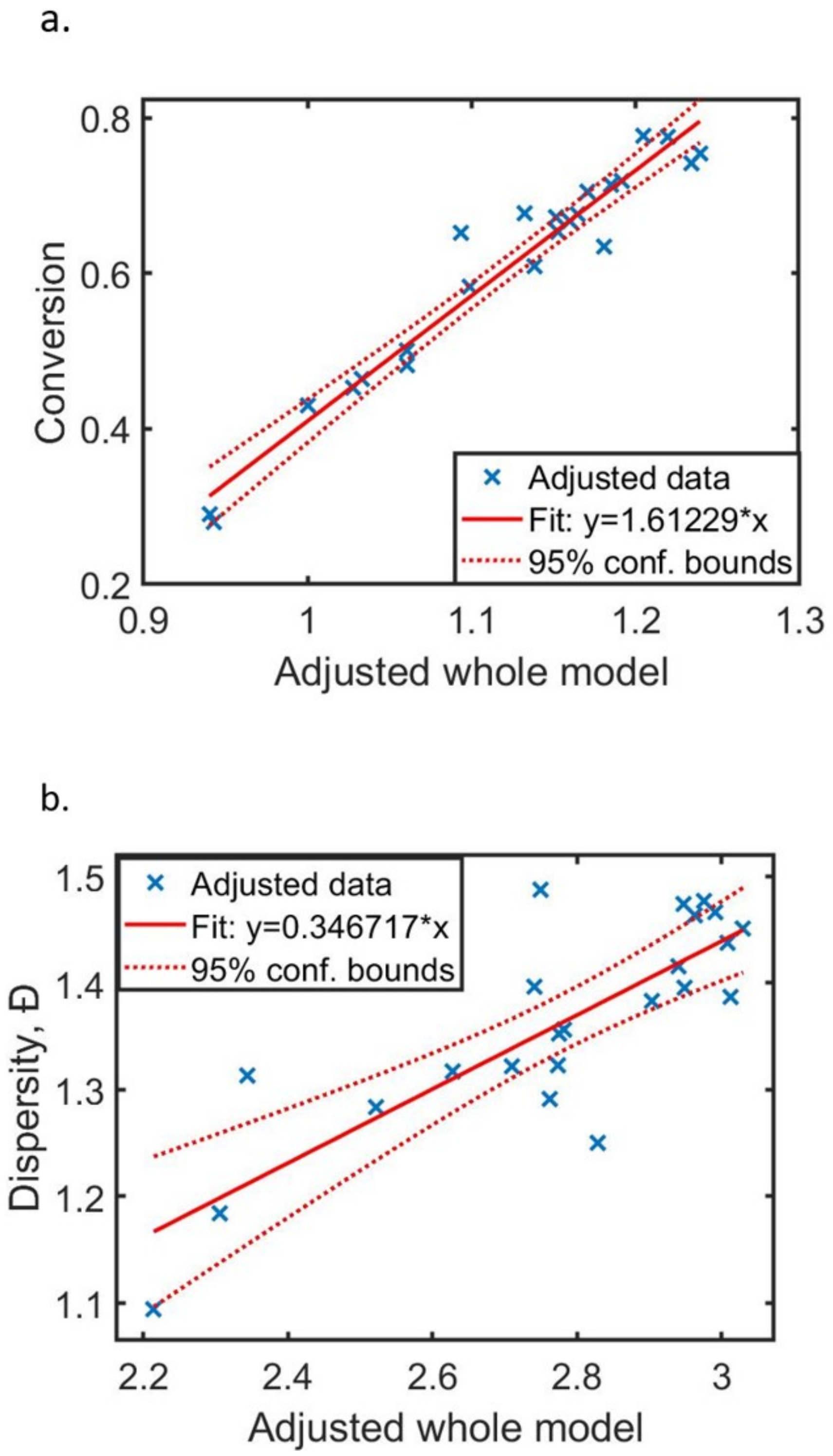

Figure 5.11: Regression analysis plots of (a) conversion and (b) dispersity for the the digitally augmented optimisation for the RAFT polymerisation of nBuA in the presence of TTC1 using AIBN as the initiator at a ratio of 200:1:x(0.04-0.09) in dioxane. Where the x and y axes are the adjusted model and objectives, respectively. The data points represent the real data, the solid red line is the predicted linear regression model and the dotted red lines represent the 95 % confidence limits. The x axis is adjusted due to the presence of 3 independent variables which uses the Frisch-Waugh-Lovell theorem to account for all variables%

Again, like for DMAm, the nBuA linear regressions offer a better fit than the fully experimental runs. In Figure 5.11. a, the conversion shows a good linear fit with fewer anomalous data points compared to the fully experimental-derived model in Figure 5.11. a, which is reflected in a lower RMSE of 0.032. This is not unexpected as many of the data points corresponding to less controlled systems that may experience greater retardation are avoided using the *in-silico* LHC. This is further observed in Figure 5.11. b, where the Đ are much less spread, and an RMSE of 0.061 is achieved, this suggests that the model used for training is good enough to obtain enough experimental data to predict the results of further experiments using a linear regression.

Table 5.7: Table comparing the efficiency of the fully experimental optimisation platform with the model-assisted platform to identify the Pareto front of the RAFT polymerisation of nBuA in the presence of TTC1 using AIBN as the initiator

	Fully Experimental	Digitally Augmented
Number of Experiments	42	26
Number of Training points	15	5
Volume of Solution (mL)	714	442
Time taken to map Pareto front (h)	36	22

Although the model is less suitable for the nBuA system, it showed the ability to identify a similar Pareto front in 38 % less time. This saves 272 mL of reagents and since 1,4-dioxane was used as the solvent, this is a significant reduction in cost. Though the model did not find the Pareto front in as few experiments as DMAm a total reduction was still observed, and a platform capable of learning from theoretical knowledge with little human interaction has been demonstrated.

5.3.5 Model assisted self optimisation of 3D reaction parameter space for tBuAm

Another less ideal bulky monomer was selected and a model-assisted optimisation was conducted on this system. In this case, the solid monomer tBuAm at 60 w/w % was insoluble in methanol; consequently, a reservoir solid content of 45.5 w/w % was used to ensure solubility. To retain a level of accuracy of the pumps, the target solid content of each reaction solution was reduced to 20 w/w %.

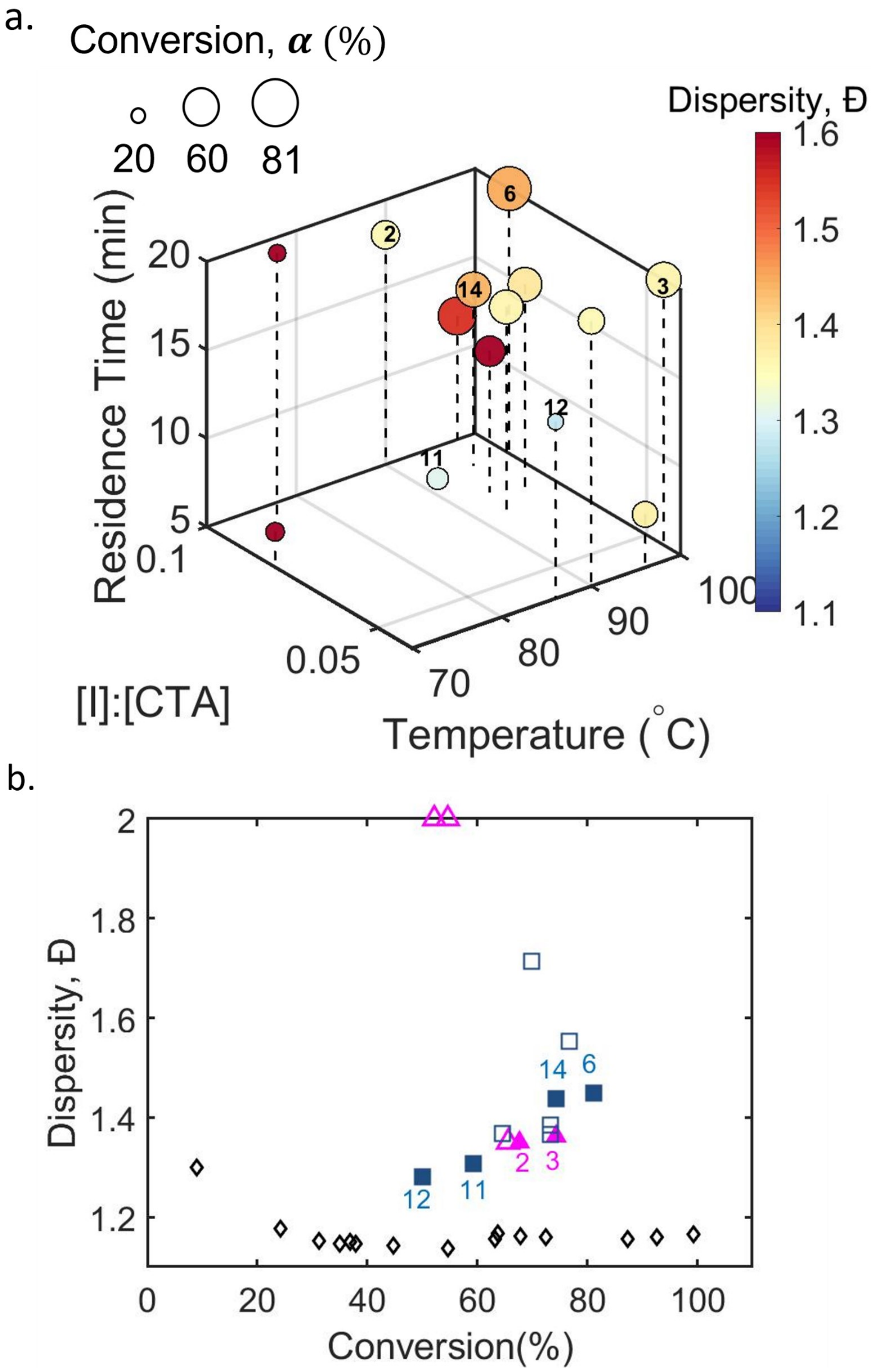

Figure 5.12: (a) 3D model-directed optimisation for the polymerisation of tBuAm in the presence of TTC1 using AIBN as the initiator at a (200:1:x(=0.04-0.09)) at 20 w/w % in methanol.(b) Objective plot of dispersity vs conversion where the triangles are the results obtained following the first TS-EMO iteration which utilised an LHC conducted *in-silico* (Black diamonds) to suggest 5 "real" training experiments, TS-EMO1 (magenta triangles) and 2(blue squares)

The overall Đ was higher for tBuAm even with a low solid content than for DMAm and nBuA. The lowest Đ non-dominated solution achieved was 1.28 with a conversion of 50 % - which was obtained after 15 min at 86 °C with a low initiator ratio of 0.04 eq. This data point was the

17 th to be identified and this was in TS-EMO experiments after TS-EMO 1 which can be seen in the figures 5.12. a and b. On the other hand, the non-dominated solution with the highest conversion and the lowest $Đ$ was identified after 20 min at 100 ° C using a 0.09 eq. Affording a conversion of 81 % and $Đ$ of 1.45 after the 11 th experiment. This suggests that the algorithm tried to identify higher conversions before the lower dispersity, which is the opposite to what was the case for nBuA and DMAm. Compared to previous experiments only 1 of 5 of TS-EMO1 experiments, following the *in-silico* LHC, lies on the Pareto front. It subsequently takes 3 further experiments to identify the next Pareto data point. Here, there are some anomalous data points indicated by the discontinuity of the colour map. The high $Đ$ (deep red) data point at 94 °C using an initiator eq of 0.08 after 13 min gives a $Đ$ greater than points at higher initiator concentrations, longer residence times and higher temperatures. This suggests that there could have been some fouling that enhanced the effects of potential side reactions associated with tBuAm. Data point 2 looks like an anomalous point, as it is lower than its analogous reactions at different initiator concentrations but with the same temperature (° C) and residence times (18 min). The potential rate retardation is evident here, shown by the increase then decrease in conversion, as the initiator is increased from 0.09 to 0.095 to 0.1 eq. It can be can assumed that there were not enough radicals present at 0.09 to react with a high conversion; then at 0.095 there is enough to reach a conversion of 74 %. As there is no indication of fouling in the reactor (i.e. no pressure increase; see the appendix for pressure monitoring), the decrease in conversion at 0.1 eq is possibly caused by an increase in exotherm leading to side reactions; however, further studies and repeats would need to be conducted to determine this. Figure 5.12. b shows that, regardless, the model proposed in Chapter 4 did a relatively good job of finding the Pareto front for this challenging system. To further investigate the effects of these conditions on the conversion and dispersity data, a linear regression analysis was performed.

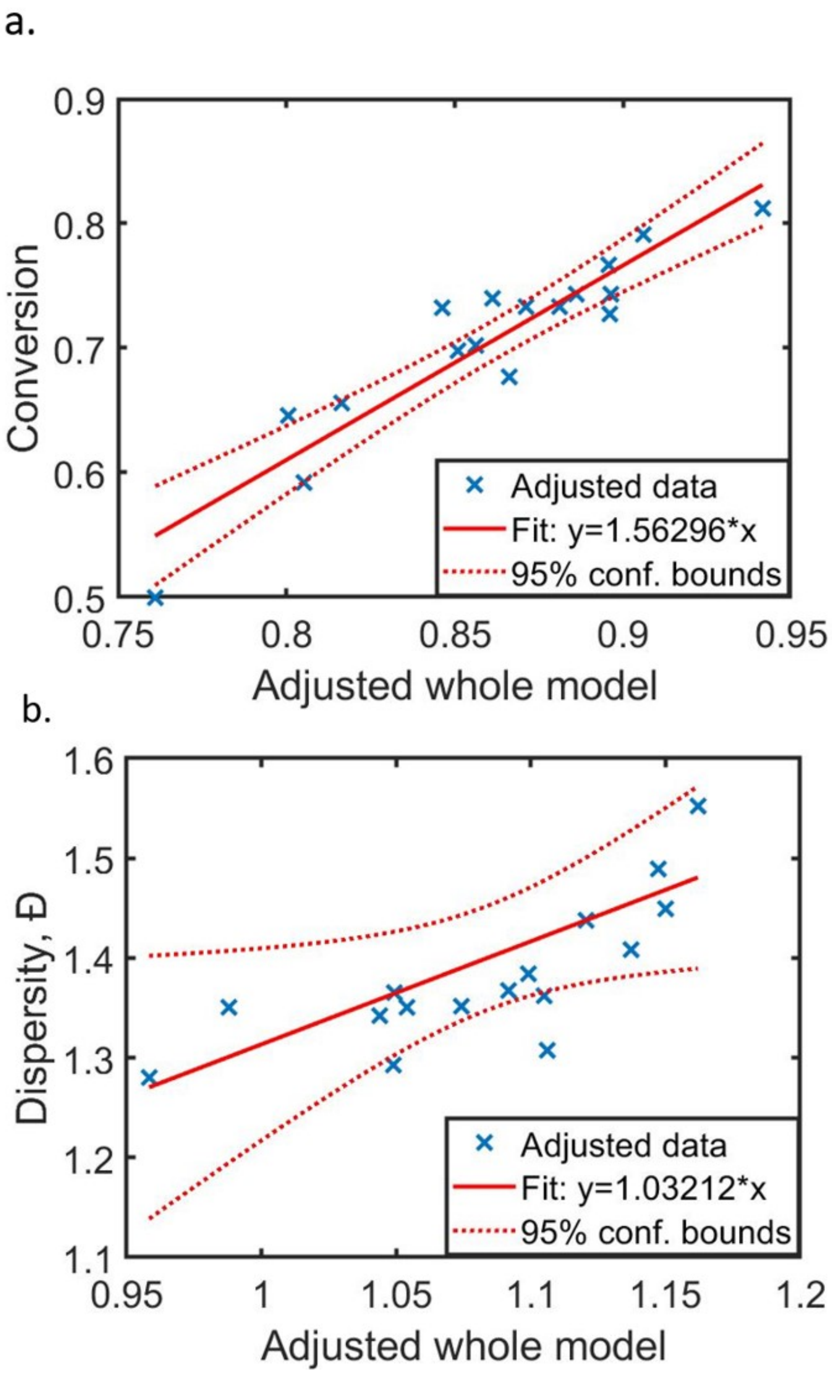

Figure 5.13: Regression analysis plots of (a) conversion and (b) dispersity for the the digitally augmented optimisation for the RAFT polymerisation of tBuAm in the presence of TTC1 using AIBN as the initiator at a ratio of 200:1:x(0.04-0.09) in Methanol. Where the x and y axes are the adjusted model and objectives, respectively. The data points represent the real data, the solid red line is the predicted linear regression model and the dotted red lines represent the 95 % confidence limits. The x axis is adjusted due to the presence of 3 independent variables which uses the Frisch-Waugh-Lovell theorem to account for all variables%

It can be seen from the regression analysis in Figure 5.13 that the conversions have a relatively linear correlation; however, as expected, the data points corresponding to the anomalies in

Figure 5.12. a exist outside of the 95 % confidence intervals. This indicates the presence of other variables, such as side reactions/exotherms/errors, in the analysis. This is even more apparent for the dispersity regressions in Figure 5.13. shown by the large confidence intervals.

5.4 Conclusions

To conclude this section, a platform capable of optimisation of 3 variables and 2 conflicting objectives has been developed requiring no *a priori* knowledge of the reaction. The ultra-fast RAFT polymerisation of DMAm was optimisable in 17 h and the less ideal nBuA was optimisable in 36 h. Linear regression analysis was less appropriate for DMAm conversion data due to the abundance of points at a max conversion of 100 %. More anomalies were observed by the nBuA regressions which is likely due to the presence of side reactions owing to the secondary propagating radicals and chain transfer to solvent. In addition, the ability to pre-program theoretical knowledge of the reactions to improve the efficiency of TS-EMO to find the Pareto front has been demonstrated. For DMAm this was very successful due to the ability of the model to accurately model the conversion and dispersity. For nBuA this was even more of a challenge due to the assumption that there are no other side reactions happening. Regardless, for this system the model was able to find the Pareto front in a shorter time. For tBuAm even less ideality was observed but the algorithm did manage to identify a Pareto front in as few as 19 experiments. The low computational expense of the model enabled rapid training of 15 LHC generated experiments in as little as 30 s. A more complex model such as implementing MoM or *kMC* may improve the ability of the algorithm to find the Pareto front in fewer experiments. Further, work may also include the use of regression models to inform future optimisations.

Chapter 6

Conclusions and Outlook

The implementation of self-optimisation algorithms in the pharmaceutical and small molecule industries has led to huge advances in the optimisation of APIs and commercial molecule synthesis. There has been a slight delay in material chemistry, but traction has increased in the last decade. The synthesis of defined homopolymers is discussed with the aim of optimisation of the reaction parameters for the resultant conversion and dispersity. Here, the aim was to take advantage of the benefits of continuous flow, such as efficient heat transfer, safer process conditions above solvent boiling points, automated analysis, and online analysis to optimise the synthesis of polymerisations under more extreme conditions. The platform has been successfully applied and adapted to the RAFT polymerisation of dimethylacrylamide, tert-butylacrylamide, and butylacrylate. The optimisation platform operates using a state-of-the-art Bayesian algorithm that provides rapid evaluation of complex reactions compared to traditional OVAT and DoE approaches.

In Chapter 2 the closed-loop autonomous Bayesian optimisation of several homopolymers was discussed, these included: PDMAm, PtBuAm, and PBuA. Orthogonal online analysis in the form of GPC and NMR and continuous liquid handling allowed high-throughput optimisation of the reaction in as little as 20 experiments, including the 10 training experiments. The surfaces fitted to the data allowed for qualitative depiction of the effect of temperature and residence time on the conversion and dispersity and highlighted the areas of the reaction parameter space of interest for precision polymer synthesis. RAFT agents for the polymerisation of tert-butylacrylamide including two trithiocarbonates that differed by Z group and a halogenated pyrazole dithiocarbonate. Subsequently, this allowed the RAFT agent that afforded superior precision to be identified by comparison of the surfaces and the Pareto fronts. The Pareto fronts of dimethylacrylamide and butylacrylate at temperatures at or above boiling points were also obtained, and non-dominated solutions that led to low $Đ$ and high conversion were identified. The validity of using an inline degasser for optimisation was also attempted; however, large internal volumes rendered this invalid. The optimisation platform was also applied to a statistical copolymerisation that was shown to only reach 48 % conversion, which was considered due to rate-retardation by acrylate and the presence of an aprotic solvent. Prior to the work in this thesis, the novelty lies in the way in which the optimisations have been carried out, here the polymerisation optimisations are conducted in continuous flow and not plug flow; which improves the productivity. In addition, previously, a fully closed-loop optimisation platform had not been reported for polymerisation, and the work in this thesis uses a fully autonomous platform that only requires the press of a button to optimise due to the use of online analytics. This work has defined a starting point for intelligent synthesis of materials in a user-independent fashion that may be applied to other types of polymerisation and nano object formation. Further work to improve this platform could involve using the MVMOO algorithm to include categorical variables (i.e., solvent or RAFT agent), allowing identification of the optimum reaction system leading to the lowest Pareto front. Furthermore, work to optimise the protocol for the conversion of fluorinated monomers would be an interesting step toward a completely closed-loop continuous self-optimisation of the activity of the MRI agent ^{19}F.

Chapter 3 addressed the challenges of expanding the reaction space through the inclusion of additional pumps, allowing for autonomous variation in initiator equivalence. The main objective of this thesis was to develop a platform capable of precision; therefore, it was important to design the reactor to reduce the effects of laminar flow regimes, inefficient mixing, and unreliable pumps. Ultra-fast RAFT polymerisation of DMAm using VA044 was selected as a model system and molecular weight distributions determined by GPC/SEC were used to characterise mixing, with $Đ$ indicating the efficiency of mixing. Rapid kinetics afforded poor mixing in the system that relied on diffusion; a home-made packed bed offered the best mixing compared to 2 commercially available micromixers. The packed bed was then used on the expanded platform. A larger coil was also used for further experiments because of the reliability of the flow rates of the HPLC pumps used. Contrary to the literature, the packed bed did not cause asymmetry of the RTD that had been shown in Chapter 1 for a static mixer. The effect of temperature on RTD was also characterised here for the viscous $PDMAm_{200}$ tracer, which had not been done before for polymerisation and showed an expected narrowing of the RTD which is possibly due to temperature dependence of viscosity. The value of this chapter came in useful in Chapter 4 and 5 where the RTD was superimposed onto batch MWDs to identify a broadening factor; that was used to account for the effects of laminar flow regimes.

With the aim of using modelling to train the TS-EMO algorithm used in Chapter 2, an accessible model was developed for RAFT. In the search for identifying a computationally inexpensive model that could accurately predict conversion and $Đ$, it was observed that a complete explicit dispersity equation that accounts for terminative events was not available for RAFT. In Chapter 4, an explicit equation for dispersity was proposed as a function of conversion for RAFT polymerisation and validated against the literature and experimental data. Validation against experimental data from the literature for batch polymerisations of AAm, AA, and MA and experimentally in this work for DMAm. This was compared with existing equations for dispersity as a function of the conversion, where only terms one to three accounting for "livingness" and chain transfer to CTA were solved and found to fit the experimental data better. RTD associated with flow was taken into account by superimposing the RTD on each bin in the MWDs, and the convolution of these MWDs was used to obtain the dispersity and obtain the relative broadening factor, which is added onto the dispersity equation. The conversion obtained by NMR from the flow setup was shown to exhibit ideal heat transfer; indicated by the fit to the isothermal simulation. Semi-empiral simulation and validation of the batch experiment were also performed using the temperature trace, showing the expected induction period. Further improvements to the model could include accounting for transfer to the solvent or be used to fit approximate addition/fragmentation rate constants. The work in chapter 4 is useful not only for implementation in a self-optimising experimental platform, as discussed in chapter 5 but also for the wider polymer community. The IUPAC polymer division has significant interest in the bench-marking of rate constants due to the errors associated with the measurement and variation between different groups. The model may provide additional validation of these experiments, as well as, the ability to fit the model to elucidate transfer rate coefficients. The application and spreadsheet provides two accessible open-access routes to modelling RAFT polymerisation without the need for extensive coding; therefore, this could provide synthetic polymer chemists with the ability to predict outcomes of batch or flow reactions, reducing the time, money, and environmental impact of their work.

Typically, modelling is not a replacement for experimental work due to the nature of assumptions made to reduce computational expense and/or availability of rate coefficients. Following model validation, the conversion and dispersity model was augmented in the flow reactor software interface and used in conjunction with TS-EMO to provide an *in-silico* LHC training data set. Since the model may not provide the best fit in some monomer circumstances, the *in-silico* LHC data set was only used to train the initial TSEMO iteration 1. The digitally augmented platform performed the best for the polymerisation of N,N-dimethylacrylamide, reducing the number of experiments required to trace the pareto front by 40 % while also reducing the number of wasted experiments by more than 100 %, this data is shown in Table 6.1, highlighting the improvement in sustainability of the process. The model-assisted platform was unexpectedly useful in reducing the number of experiments for more challenging monomers using an ideal model. Multiple linear regression analysis shows a link between variables and effects on the objectives and was shown to work for small data sets after *in-silico* modelling. This area could be improved by using more complex modelling techniques, such as MoM or computationally inexpensive methods *kMC*. Improvements to the setup could also be made by introducing plug flow to reduce the effects of residence time distribution; however, this would require an efficient method of degassing before entering the GPC setup. Further work into incorporating categorical variables through inclusion of a multi-position switching valve could further diversify the platform to enable continuous screening of new RAFT agents. Chapter 5 offers a novel and unique approach to optimisation, which could be useful if a monomer with a challenging low-yielding synthesis is used, as there is a significant reduction in volumes of reagents required and, in theory, only a propagation rate constant of a certain monomer class is required. The modular approach to optimisation may also be applied to other chemistry such as small chemical industries, provided the reaction step in question has a relatively good model for both conflicting objectives, as the model can be switched for a different model with a few lines of code.

Table 6.1: Summary table showing the decrease in experimental time achieved using the digitally augmented platform for (a)DMAm and (b)nBuA

	Fully Experimental	Digitally Augmented
Number of experiments	$28^a/42^b$	$13^a/26^b$
Experimental training points	$15^a/15^b$	$5^a/5^b$
Volume of solution (mL)	$450^a/714^b$	$180^a/442^b$
Time taken to map Pareto front (h)	$17^a/36^b$	$7^a/22^b$

Fully autonomous self-optimisation applied to polymers is still in its early days. In the same way that the application of machine learning algorithms has enabled high-throughput optimisation of pharmaceuticals/fine chemicals, it could also be used to facilitate the optimisation of polymeric nano-objects. High-throughput experimentation can provide big data to feed into further machine learning algorithms to model and predict success outcomes when discovering new polymeric materials. However, this is not without potential challenges, including the availability of online monitoring techniques and reactor fouling. Work on scaling up and/or numbering up these types of polymerisation reactors could also improve the productivity of certain polymers. An algorithm such as MVMOO as mentioned in Chapter 1 could facilitate self-optimisation of the reactor geometries of different 3D printed microfluidic reactors by selecting the reactor used. Identifying rate constants by feeding data into machine learning algorithms would also be an interesting opportunity to predict values, which would be useful for all polymer chemists, whether synthetic or computational.

References

(1) Morawetz, H. In *Encyclopedia of Polymer Science and Technology*, 2014, pp 1–30.

(2) Berzelius, J. J. *Annalen der Physik* **1832**, *102*, 320–322.

(3) Staudinger, H. *Reports of the German Chemical Society (A and B Series)* **1920**, *53*, 1073–1085.

(4) Berthelot, M. *Société de Paris* **1866**.

(5) Carothers, W. H. *Journal of the American Chemical Society* **1929**, *51*, 2548–2559.

(6) Odian, G., *Principles of Polymerization*, 2004.

(7) Bhanu, V. A.; Kishore, K *Chemical Reviews* **1991**, *91*, 99–117.

(8) Li, N.; Pan, X.-C. *Chinese J. Polym. Sci* **2021**, *39*, 1084–1092.

(9) Jenkins, A. D.; Stepto, R. F.; Kratochvíl, P.; Suter, U. W. *Pure and Applied Chemistry* **1996**, *68*.

(10) Szwarc, M.; Levy, M.; Milkovich, R. Polymerization initiated by electron transfer to monomer. A new method of formation of block polymers, 1956.

(11) Szwarc, M.; Litt, M. *Journal of Physical Chemistry* **1958**, *62*, 568–569.

(12) Szwarc, M. *Journal of Polymer Science Part A: Polymer Chemistry* **1998**, *36*.

(13) Baskaran, D.; Müller, A. H. *Progress in Polymer Science (Oxford)* **2007**, *32*, 173–219.

(14) Takahashi, Y.; Nagaki, A. Anionic polymerization using flow microreactors, 2019.

(15) Stobbe H.; Posnjak, G. *Justus Liebigs Annalen der Chemie* **1909**, *371*, 259.

(16) Stobbe, H. *Justus Liebigs Annalen der Chemie* **1915**, *409*, 1–13.

(17) Lautenschlager, L *University of Karlsruhe* **1913**.

(18) Staudinger, H.; Brunner, M.; Frey, K.; Garbsch, P.; Signer, R.; Wehrli, S. *Reports of the German Chemical Society (A and B Series)* **1929**, *62*, 241–263.

(19) Staudinger, H. *Reports of the German Chemical Society (A and B Series)* **1926**, *59*, 3019–3043.

(20) Staudinger, H.; Kohlschütter, H. W. *Reports of the German Chemical Society (A and B Series)* **1931**, *64*, 2091–2098.

(21) Schulz, G. *Zeitschrift für physikalische Chemie* **1935**, *30*, 379–398.

(22) Flory, P. J. *Journal of the American Chemical Society* **1937**, *59*, 241–253.

(23) Brandrup, J; Immergut, E. H.; Grulk, E. A., *Polymer Handbook fouth edition*, 1999, p 2366.

(24) Buback, M.; Schroeder, H.; Kattner, H. Detailed Kinetic and Mechanistic Insight into Radical Polymerization by Spectroscopic Techniques, 2016.

(25) Beuermann, S.; Buback, M. *Progress in Polymer Science (Oxford)* **2002**, *27*, 191–254.

(26) Buback, M.; Kattner, H. *Molecular Physics* **2021**, *119*, DOI: `10.1080/00268976.2021.1939452`.

(27) Buback, M.; Müller, E.; Russell, G. T. *Journal of Physical Chemistry A* **2006**, *110*, 3222–3230.

(28) Drawe, P.; Buback, M. *Macromolecular Theory and Simulations* **2016**, *25*, 74–84.

(29) Perrier, S. 50th Anniversary Perspective: RAFT Polymerization - A User Guide, 2017.

(30) Trommsdorff, V. E.; Köhle, H.; Lagally, P. *Die Makromolekulare Chemie* **1948**, *1*, 169–198.

(31) NORRISH, R. G. W.; SMITH, R. R. *Nature* **1942**, *150*, 336–337.

(32) Jenkins, A. D.; Jones, R. G.; Moad, G. *Pure and Applied Chemistry* **2010**, *82*, 483–491.

(33) Moad, G.; Rizzardo, E. In *RSC Polymer Chemistry Series*; 19, 2016; Vol. 2016-Janua, pp 1–44.

(34) Wang, J. S.; Matyjaszewski, K. *Macromolecules* **1995**, *28*, 7901–7910.

(35) Dworakowska, S.; Lorandi, F.; Gorczyński, A.; Matyjaszewski, K. Toward Green Atom Transfer Radical Polymerization: Current Status and Future Challenges, 2022.

(36) Solomon, D. H.; Rizzardo, E.; Cacioli, P. *European Patent Application* **1985**, *1985.*

(37) Marić, M. *Canadian Journal of Chemical Engineering* **2021**, *99*, 832–852.

(38) Chiefari, J.; Chong, Y. K.; Ercole, F.; Krstina, J.; Jeffery, J.; Le, T. P.; Mayadunne, R. T.; Meijs, G. F.; Moad, C. L.; Moad, G.; Rizzardo, E.; Thang, S. H. *Macromolecules* **1998**, *31*, 5559–5562.

(39) Tian, X.; Ding, J.; Zhang, B.; Qiu, F.; Zhuang, X.; Chen, Y. Recent advances in RAFT polymerization: Novel initiation mechanisms and optoelectronic applications, 2018.

(40) Opiyo, G.; Jin, J. Recent progress in switchable RAFT agents: Design, synthesis and application, 2021.

(41) Braunecker, W. A.; Matyjaszewski, K. *Progress in Polymer Science* **2007**, *32*, 93–146.

(42) Truong, N. P.; Jones, G. R.; Bradford, K. G.; Konkolewicz, D.; Anastasaki, A. *Nature Reviews Chemistry 2021 5:12* **2021**, *5*, 859–869.

(43) Solomon, D. H.; Waverley, G. *European Patent* **1984**, *581*, 429.

(44) Kato, M.; Kamigaito, M.; Sawamoto, M.; Higashimura, T. Polymerization of Methyl Methacrylate with the Carbon Tetrachloride/Dichlorotris-(triphenylphosphine)ruthenium(II)/ Methylaluminum Bis(2,6-di-tert-butylphenoxide) Initiating System: Possibility of Living Radical Polymerization, 1995.

(45) Krys, P.; Matyjaszewski, K. Kinetics of Atom Transfer Radical Polymerization, 2017.

(46) Pan, X.; Fantin, M.; Yuan, F.; Matyjaszewski, K. *Chemical Society Reviews* **2018**, *47*, 5457–5490.

(47) Barner-Kowollik, C., *Handbook of RAFT Polymerization*, 2008, pp 1–543.

(48) Keddie, D. J.; Moad, G.; Rizzardo, E.; Thang, S. H. RAFT agent design and synthesis, 2012.

(49) Donald, M. K.; Bon, S. A. *Polymer Chemistry* **2020**, *11*, 4281–4289.

(50) Benaglia, M.; Chiefari, J.; Chong, Y. K.; Moad, G.; Rizzardo, E.; Thang, S. H. *Journal of the American Chemical Society* **2009**, *131*, 6914–6915.

(51) Enikolopyan, N. S.; Smirnov, B. R.; Ponomarev, G. V.; Belgovskii, I. M. *Journal of polymer science. Part A-1, Polymer chemistry* **1981**, *19*, 879–889.

(52) Engelis, N. G.; Anastasaki, A.; Nurumbetov, G.; Truong, N. P.; Nikolaou, V.; Shegiwal, A.; Whittaker, M. R.; Davis, T. P.; Haddleton, D. M. *Nature Chemistry* **2017**, *9*, 171–178.

(53) Engelis, N. G.; Anastasaki, A.; Whitfield, R.; Jones, G. R.; Liarou, E.; Nikolaou, V.; Nurumbetov, G.; Haddleton, D. M. *Macromolecules* **2018**, *51*, 336–342.

(54) Wang, Y.; Fantin, M.; Park, S.; Gottlieb, E.; Fu, L.; Matyjaszewski, K. *Macromolecules* **2017**, *50*, 7872–7879.

(55) J. Monteiro, M.; de Brouwer, H. *Macromolecules* **2001**, *34*, 349–352.

(56) Kwak, Y.; Goto, A.; Tsujii, Y.; Murata, Y.; Komatsu, K.; Fukuda, T. *Macromolecules* **2002**, *35*, 3026–3029.

(57) Barner-Kowollik, C.; Quinn, J. F.; Morsley, D. R.; Davis, T. P. *Journal of Polymer Science, Part A: Polymer Chemistry* **2001**, *39*, 1353–1365.

(58) Vana, P. In *Macromolecular Symposia*, 2007; Vol. 248, pp 71–81.

(59) Coote, M. L. *Macromolecules* **2004**, *37*, 5023–5031.

(60) Zapata-Gonzalez, I.; Hutchinson, R. A.; Buback, M.; Rivera-Magallanes, A. *Chemical Engineering Journal* **2021**, *415*, 128970.

(61) Bradford, E.; Schweidtmann, A. M.; Lapkin, A. *Journal of Global Optimization* **2018**, *71*, 407–438.

(62) Veloso, A.; García, W.; Agirre, A.; Ballard, N.; Ruipérez, F.; De La Cal, J. C.; Asua, J. M. *Polymer Chemistry* **2015**, *6*, 5437–5450.

(63) Junkers, T.; Barner-Kowollik, C. *Journal of Polymer Science, Part A: Polymer Chemistry* **2008**, *46*, 7585–7605.

(64) Reyhani, A.; McKenzie, T. G.; Ranji-Burachaloo, H.; Fu, Q.; Qiao, G. G. *Chemistry - A European Journal* **2017**, *23*, 7221–7226.

(65) Chapman, R.; Gormley, A. J.; Herpoldt, K. L.; Stevens, M. M. *Macromolecules* **2014**, *47*, 8541–8547.

(66) Gody, G.; Maschmeyer, T.; Zetterlund, P. B.; Perrier, S. *Nature Communications 2013 4:1* **2013**, *4*, 1–9.

(67) Gody, G.; Barbey, R.; Danial, M.; Perrier, S. *Polym. Chem* **2015**, *6*, 1502.

(68) Leuchs, H. *Berichte der deutschen chemischen Gesellschaft* **1906**, *39*, 857–861.

(69) Grubbs, R. B. Nitroxide-mediated radical polymerization: Limitations and versatility, 2011.

(70) Grubbs, R. B.; Grubbs, R. H. 50th Anniversary Perspective: Living Polymerization - Emphasizing the Molecule in Macromolecules, 2017.

(71) Overberger, C. G.; O'shaughnessy, T; Shalit, H *Trans. Faraday Sac* **1949**, *71*, 2027.

(72) Idage, B. B.; Vernekar, S. P.; Ghatge, N. D. *Journal of polymer science. Part A-1, Polymer chemistry* **1983**, *21*, 2145–2156.

(73) Gillespie, D. T. *Journal of Computational Physics* **1976**, *22*, 403–434.

(74) Rego, A. S.; Brandão, A. L. *Industrial and Engineering Chemistry Research* **2021**, *60*, 8396–8408.

(75) Al-Harthi, M. A.; Masihullah, J. K.; Abbasi, S. H.; Soares, J. B. *Macromolecular Theory and Simulations* **2009**, *18*, 307–316.

(76) He, J.; Li, L.; Yang, Y. *Macromolecular Theory and Simulations* **2000**, *9*, 463–468.

(77) He, J.; Zhang, H.; Chen, J.; Yang, Y. *Macromolecules* **1997**, *30*, 8010–8018.

(78) Drache, M.; Schmidt-Naake, G.; Buback, M.; Vana, P. *Polymer* **2005**, *46*, 8483–8493.

(79) Pintos, E.; Sarmoria, C.; Brandolin, A.; Asteasuain, M. *Industrial and Engineering Chemistry Research* **2016**, *55*, 8534–8547.

(80) Brandão, A. L.; Soares, J. B.; Pinto, J. C.; Alberton, A. L. When Polymer Reaction Engineers Play Dice: Applications of Monte Carlo Models in PRE, 2015.

(81) Tripathi, A. K.; Sundberg, D. C. *Macromolecular Theory and Simulations* **2015**, *24*, 52–64.

(82) Mohammadi, Y.; Pakdel, A. S.; Saeb, M. R.; Boodhoo, K. *Chemical Engineering Journal* **2014**, *247*, 231–240.

(83) Gibson, M. A.; Bruck, J. *Journal of Physical Chemistry A* **2000**, *104*, 1876–1889.

(84) Chaffey-Millar, H.; Stewart, D.; Chakravarty, M. M.; Keller, G.; Barner-Kowollik, C. *Macromolecular Theory and Simulations* **2007**, *16*, 575–592.

(85) Drache, M.; Drache, G. *Polymers* **2012**, *4*, 1416–1442.

(86) Mastan, E.; Zhu, S. *European Polymer Journal* **2015**, *68*, 139–160.

(87) D'hooge, D. R.; Reyniers, M. F.; Marin, G. B. *Macromolecular Reaction Engineering* **2009**, *3*, 185–209.

(88) D'Hooge, D. R.; Konkolewicz, D.; Reyniers, M. F.; Marin, G. B.; Matyjaszewski, K. *Macromolecular Theory and Simulations* **2012**, *21*, 52–69.

(89) Toloza Porras, C.; D'Hooge, D. R.; Reyniers, M. F.; Marin, G. B. *Macromolecular Theory and Simulations* **2013**, *22*, 136–149.

(90) Riazi, H.; Shamsabadi, A. A.; Grady, M. C.; Rappe, A. M.; Soroush, M. *Processes* **2019**, *7*, 656.

(91) Dorschner, D.; Jung, W.; Riahinezhad, M.; Duever, T. A.; Penlidis, A. *Journal of Macromolecular Science, Part A: Pure and Applied Chemistry* **2017**, *54*, 339–371.

(92) Asteasuain, M. *International Journal of Polymer Science* **2018**, *2018*, ed. by Roghani-Mamaqani, H., 7803702.

(93) Veregin, R. P.; Odell, P. G.; Michalak, L. M.; Georges, M. K. *Macromolecules* **1996**, *29*, 3346–3352.

(94) Bonilla, J.; Saldívar, E.; Flores-Tlacuahuac, A.; Vivaldo-Lima, E.; Pfaendner, R.; Tiscareño-Lechuga, F. *Polymer Reaction Engineering* **2002**, *10*, 227–263.

(95) Wang, A. R.; Zhu, S. *Journal of Polymer Science, Part A: Polymer Chemistry* **2003**, *41*, 1553–1566.

(96) Jiang, J.; Wang, W. J.; Li, B. G.; Zhu, S. *Macromolecular Reaction Engineering* **2017**, *11*, 1700029.

(97) Wulkow, M. *Macromolecular Theory and Simulations* **1996**, *5*, 393–416.

(98) Wulkow, M. *Macromolecular Reaction Engineering* **2008**, *2*, 461–494.

(99) Vana, P.; Davis, T. P.; Barner-Kowollik, C. *Macromolecular Theory and Simulations* **2002**, *11*, 823–835.

(100) Zetterlund, P. B.; Gody, G.; Perrier, S. *Macromolecular Theory and Simulations* **2014**, *23*, 331–339.

(101) Corrigan, N.; Boyer, C. *Macromolecules* **2022**, *55*, 8960–8969.

(102) Wang, A. R.; Zhu, S. *Macromolecular Theory and Simulations* **2003**, *12*, 663–668.

(103) Mastan, E.; Zhu, S. *Macromolecules* **2015**, *48*, 6440–6449.

(104) Wang, T. T.; Wu, Y. Y.; Luo, Z. H.; Zhou, Y. N. *Macromolecules* **2020**, *53*, 10813–10822.

(105) Figini, V. R. V. *Die Makromolekulare Chemie* **1964**, *71*, 193–197.

(106) Figini, V. R. V. *Die Makromolekulare Chemie* **1967**, *107*, 170–187.

(107) Coleman, B. D.; Fox, T. G. *Journal of the American Chemical Society* **1963**, *85*, 1241–1244.

(108) Zhu, S. *Macromolecular Theory and Simulations* **1999**, *8*, 29–37.

(109) H. E. Mueller, A.; Yan, D.; Litvinenko, G.; Zhuang, R.; Dong, H. *Macromolecules* **2002**, *28*, 7335–7338.

(110) Kearns, M. M.; Morley, C. N.; Parkatzidis, K.; Whitfield, R.; Sponza, A. D.; Chakma, P.; De Alwis Watuthanthrige, N.; Chiu, M.; Anastasaki, A.; Konkolewicz, D. *Polymer Chemistry* **2022**, *13*, 898–913.

(111) Heuts, J. P.; Russell, G. T.; Smith, G. B.; Van Herk, A. M. In *Macromolecular Symposia*, 2007.

(112) H. E. Mueller, A. et al. Kinetic Analysis of "Living" Polymerization Processes Exhibiting Slow Equilibria. 1. Degenerative Transfer (Direct Activity Exchange between Active and "Dormant" Species). Application to Group Transfer Polymerization.

(113) Harrisson, S. *Polymers* **2018**, *10*, 887.

(114) Zhou, Y.-n.; Li, J.-j.; Wang, T.-t.; Wu, Y.-y.; Luo, Z.-h. *Progress in Polymer Science* **2022**, *130*, 101555.

(115) Beers, K. L.; Boo, S.; Gaynor, S. G.; Matyjaszewski, K. *Macromolecules* **1999**, *32*, 5772–5776.

(116) Gromada, J.; Spanswick, J.; Matyjaszewski, K. *Macromolecular Chemistry and Physics* **2004**, *205*, 551–566.

(117) Plutschack, M. B.; Pieber, B.; Gilmore, K.; Seeberger, P. H. The Hitchhiker's Guide to Flow Chemistry â¥, 2017.

(118) Wegner, J.; Ceylan, S.; Kirschning, A. Ten key issues in modern flow chemistry, 2011.

(119) Zhang, J.; Wang, K.; Teixeira, A. R.; Jensen, K. F.; Luo, G. Design and scaling up of microchemical systems: A review, 2017.

(120) Nagy, K. D.; Shen, B.; Jamison, T. F.; Jensen, K. F. *Organic Process Research and Development* **2012**, *16*, 976–981.

(121) Gobert, S. R.; Kuhn, S.; Braeken, L.; Thomassen, L. C. *Organic Process Research and Development* **2017**, *21*, 531–542.

(122) Fogler, H. S. *Elements of Chemical Reaction Engineering* **2006**, 867–944.

(123) Reis, M. H.; Varner, T. P.; Leibfarth, F. A. *Macromolecules* **2019**, *52*, 3551–3557.

(124) *Flow Chemistry – Fundamentals*, 2021.

(125) Peres, J. C. G.; Herrera, C. d. C.; Baldochi, S. L.; de Rossi, W.; dos Santos Vianna, A. *Canadian Journal of Chemical Engineering* **2019**, *97*, 594–603.

(126) Patel, *No Title No Title No Title*; De Gruyter: 2019, pp 9–25.

(127) UNDRR UNDRR - Terminology, 2017.

(128) Kockmann, N.; Thenée, P.; Fleischer-Trebes, C.; Laudadio, G.; Noël, T. *Cite this: React. Chem. Eng* **2017**, *2*, 258.

(129) Mastronardi, F.; Gutmann, B.; Oliver Kappe, C. *Organic Letters* **2013**, *15*, 5590–5593.

(130) Dallinger, D.; Gutmann, B.; Kappe, C. O. *Cite This: Acc. Chem. Res* **2020**, *53*, 1330–1341.

(131) Borukhova, S.; Noël, T.; Metten, B.; Devos, E.; Hessel, V. *ChemSusChem* **2013**, *6*, 2220–2225.

(132) Woitalka, A.; Kuhn, S.; Jensen, K. F. *Chemical Engineering Science* **2014**, *116*, 1–8.

(133) Zhao, F.; Cambié, D.; Janse, J.; Wieland, E. W.; Kuijpers, K. P.; Hessel, V.; Debije, M. G.; Noël, T. *ACS Sustainable Chemistry and Engineering* **2018**, *6*, 422–429.

(134) Merrifield, R. B. *Science* **1965**, *150*, 178–185.

(135) Houben, C.; Peremezhney, N.; Zubov, A.; Kosek, J.; Lapkin, A. A. *Organic Process Research and Development* **2015**, *19*, 1049–1053.

(136) Dragone, V.; Sans, V.; Henson, A. B.; Granda, J. M.; Cronin, L. *Nature Communications* **2017**, *8*, 1–8.

(137) Chatterjee, S.; Guidi, M.; Seeberger, P. H.; Gilmore, K. *Nature* **2020**, *579*, 379–384.

(138) Holmes, N.; Akien, G. R.; Blacker, A. J.; Woodward, R. L.; Meadows, R. E.; Bourne, R. A. *Reaction Chemistry and Engineering* **2016**, *1*, 366–371.

(139) Jeraal, M. I.; Holmes, N.; Akien, G. R.; Bourne, R. A. *Tetrahedron* **2018**, *74*, 3158–3164.

(140) Ingham, R. J.; Battilocchio, C.; Hawkins, J. M.; Ley, S. V. *Beilstein Journal of Organic Chemistry* **2014**, *10*, 641–652.

(141) Van Herck, J.; Abeysekera, I.; Buckinx, A.-L.; Cai, K.; Hooker, J.; Thakur, K.; Van de Reydt, E.; Voorter, P.-J.; Wyers, D.; Junkers, T. *Digital Discovery* **2022**, *1*, 519–526.

(142) Gilmore, K.; Kopetzki, D.; Lee, J. W.; Horváth, Z.; McQuade, D. T.; Seidel-Morgenstern, A.; Seeberger, P. H. *Chemical Communications* **2014**, *50*, 12652–12655.

(143) Brocklehurst, C. E.; Lehmann, H.; La Vecchia, L. *Organic Process Research and Development* **2011**, *15*, 1447–1453.

(144) McMullen, J. P.; Jensen, K. F. *Annual Review of Analytical Chemistry* **2010**, *3*, 19–42.

(145) Lange, H.; Carter, C. F.; Hopkin, M. D.; Burke, A.; Goode, J. G.; Baxendalea, I. R.; Ley, S. V. *Chemical Science* **2011**, *2*, 765–769.

(146) Moore, J. S.; Jensen, K. F. *Organic Process Research and Development* **2012**, *16*, 1409–1415.

(147) Rodriguez-Zubiri, M.; Felpin, F. X. *Organic Process Research and Development* **2022**, *2022*, 1766–1793.

(148) Benito-Lopez, F.; Verboom, W.; Kakuta, M.; Gardeniers, J. G.; Egberink, R. J.; Oosterbroek, E. R.; Van Den Berg, A.; Reinhoudt, D. N. *Chemical Communications* **2005**, 2857–2859.

(149) Ahmed-Omer, B.; Sliwinski, E.; Cerroti, J. P.; Ley, S. V. *Organic Process Research and Development* **2016**, *20*, 1603–1614.

(150) Czitrom, V. *American Statistician* **1999**, *53*, 126–131.

(151) Eckert, T.; Klein, F. C.; Frieler, P.; Thunich, O.; Abetz, V. *Polymers* **2021**, *13*, 3137.

(152) Nieuwland, P. J.; Segers, R.; Koch, K.; Van Hest, J. C.; Rutjes, F. P. *Organic Process Research and Development* **2011**, *15*, 783–787.

(153) Sans, V.; Porwol, L.; Dragone, V.; Cronin, L. *Chemical Science* **2015**, *6*, 1258–1264.

(154) Clayton, A. D.; Manson, J. A.; Taylor, C. J.; Chamberlain, T. W.; Taylor, B. A.; Clemens, G.; Bourne, R. A. *Reaction Chemistry and Engineering* **2019**, *4*, 1545–1554.

(155) Holmes, N.; Akien, G. R.; Savage, R. J.; Stanetty, C.; Baxendale, I. R.; Blacker, A. J.; Taylor, B. A.; Woodward, R. L.; Meadows, R. E.; Bourne, R. A. *Reaction Chemistry and Engineering* **2016**, *1*, 96–100.

(156) Krishnadasan, S.; Brown, R. J.; DeMello, A. J.; DeMello, J. C. *Lab on a Chip* **2007**, *7*, 1434–1441.

(157) Rasmussen, C. E.; Williams, C., *Gaussian Processes for Machine Learning*; MIT Press: 2006.

(158) Schweidtmann, A. M.; Clayton, A. D.; Holmes, N.; Bradford, E.; Bourne, R. A.; Lapkin, A. A. *Chemical Engineering Journal* **2018**, *352*, 277–282.

(159) Knowles, J. *IEEE Transactions on Evolutionary Computation* **2006**, *10*, 50–66.

(160) Emmerich, M. Single-and multi-objective evolutionary design optimization assisted by gaussian random field metamodels, Ph.D. Thesis, 2005.

(161) Deb, K.; Jain, H. *IEEE Transactions on Evolutionary Computation* **2014**, *18*, 577–601.

(162) Müller, P.; Clayton, A. D.; Manson, J.; Riley, S.; May, O. S.; Govan, N.; Notman, S.; Ley, S. V.; Chamberlain, T. W.; Bourne, R. A. *Reaction Chemistry & Engineering* **2022**, *7*, 987–993.

(163) Clayton, A. D.; Schweidtmann, A. M.; Clemens, G.; Manson, J. A.; Taylor, C. J.; Niño, C. G.; Chamberlain, T. W.; Kapur, N.; Blacker, A. J.; Lapkin, A. A.; Bourne, R. A. *Chemical Engineering Journal* **2020**, *384*, 123340.

(164) Manson, J. A.; Chamberlain, T. W.; Bourne, R. A. *Journal of Global Optimization* **2021**, *80*, 865–886.

(165) Kershaw, O. J.; Clayton, A. D.; Manson, J. A.; Barthelme, A.; Pavey, J.; Peach, P.; Mustakis, J.; Howard, R. M.; Chamberlain, T. W.; Warren, N. J.; Bourne, R. A. *Chemical Engineering Journal* **2023**, *451*, 138443.

(166) Hicks, J. A.; Melville, H. W. *Nature* **1953**, *171*, 300–301.

(167) Geacintov, C.; Smid, J.; Szwarc, M. *Journal of the American Chemical Society* **1962**, *84*, 2508–2514.

(168) Meira, G. R.; Johnson, A. F. *Polymer Engineering & Science* **1981**, *21*, 415–423.

(169) Cortese, B.; Noel, T.; de Croon, M. H. J. M.; Schulze, S.; Klemm, E.; Hessel, V. *Macromolecular Reaction Engineering* **2012**, *6*, 507–515.

(170) Iida, K.; Chastek, T. Q.; Beers, K. L.; Cavicchi, K. A.; Chun, J.; Fasolka, M. J. *Lab on a Chip* **2009**, *9*, 339–345.

(171) Zaquen, N.; Kadir, A. M.; Iasa, A.; Corrigan, N.; Junkers, T.; Zetterlund, P. B.; Boyer, C. *Macromolecules* **2019**, *52*, 1609–1619.

(172) Baeten, E.; Haven, J. J.; Junkers, T. *Polymer Chemistry* **2017**, *8*, 3815–3824.

(173) Chan, N.; Cunningham, M. F.; Hutchinson, R. A. *Macromolecular Reaction Engineering* **2010**, *4*, 369–380.

(174) Chan, N.; Boutti, S.; Cunningham, M. F.; Hutchinson, R. A. *Macromolecular Reaction Engineering* **2009**, *3*, 222–231.

(175) Chan, N.; Cunningham, M. F.; Hutchinson, R. A. *Macromolecular Rapid Communications* **2011**, *32*, 604–609.

(176) Chan, N.; Cunningham, M. F.; Hutchinson, R. A. *Journal of Polymer Science, Part A: Polymer Chemistry* **2013**, *51*, 3081–3096.

(177) Enright, T. E.; Cunningham, M. F.; Keoshkerian, B. *Macromolecular Rapid Communications* **2005**, *26*, 221–225.

(178) Rosenfeld, C.; Serra, C.; Brochon, C.; Hadziioannou, G. *Chemical Engineering Science* **2007**, *62*, 5245–5250.

(179) Iwasaki, T.; Yoshida, J. I. *Macromolecules* **2005**, *38*, 1159–1163.

(180) Iwasaki, T.; Kawano, N.; Yoshida, J. I. *Organic Process Research and Development* **2006**, *10*, 1126–1131.

(181) Wang, H.; Jin, Z.; Hu, X.; Jin, Q.; Tan, S.; Reza Mahdavian, A.; Zhu, N.; Guo, K. *Chemical Engineering Journal* **2022**, *430*, 132791.

(182) Diehl, C.; Laurino, P.; Azzouz, N.; Seeberger, P. H. *Macromolecules* **2010**, *43*, 10311–10314.

(183) Hornung, C. H.; Guerrero-Sanchez, C.; Brasholz, M.; Saubern, S.; Chiefari, J.; Moad, G.; Rizzardo, E.; Thang, S. H. *Organic Process Research and Development* **2011**, *15*, 593–601.

(184) Hornung, C. H.; Nguyen, X.; Kyi, S.; Chiefari, J.; Saubern, S. *Australian Journal of Chemistry* **2013**, *66*, 192–198.

(185) Kottisch, V.; Gentekos, D. T.; Fors, B. P. *ACS Macro Letters* **2016**, *5*, 796–800.

(186) Zhou, Y.; Gu, Y.; Jiang, K.; Chen, M. *Macromolecules* **2019**, *52*, 5611–5617.

(187) Corrigan, N.; Zhernakov, L.; Hashim, M. H.; Xu, J.; Boyer, C. *Reaction Chemistry and Engineering* **2019**, *4*, 1216–1228.

(188) Wenn, B.; Junkers, T. T. *Macromolecules* **2016**, *49*, 6888–6895.

(189) Chen, M.; Johnson, J. A. *Chemical Communications* **2015**, *51*, 6742–6745.

(190) Melker, A.; Fors, B. P.; Hawker, C. J.; Poelma, J. E. *Journal of Polymer Science, Part A: Polymer Chemistry* **2015**, *53*, 2693–2698.

(191) El Achi, N.; Bakkour, Y.; Adhami, W.; Molina, J.; Penhoat, M.; Azaroual, N.; Chausset-Boissarie, L.; Rolando, C. *Frontiers in Chemistry* **2020**, *8*, 1–10.

(192) Huang, W.; Zhai, J.; Hu, X.; Duan, J.; Fang, Z.; Zhu, N.; Guo, K. *European Polymer Journal* **2020**, *126*, 109565.

(193) Parkinson, S.; Hondow, N. S.; Conteh, J. S.; Bourne, R. A.; Warren, N. J. *Reaction Chemistry and Engineering* **2019**, *4*, 852–861.

(194) S.Parkinson *University of Leeds* **2020**.

(195) Ilare, J.; Sponchioni, M.; Storti, G.; Moscatelli, D. *React. Chem. Eng* **2020**, *5*, 2081.

(196) Qi, G.; Jones, C. W.; Schork, J. F. *Industrial and Engineering Chemistry Research* **2006**, *45*, 7084–7089.

(197) Chan, N.; Meuldijk, J.; Cunningham, M. F.; Hutchinson, R. A. *Industrial and Engineering Chemistry Research* **2013**, *52*, 11931–11942.

(198) Payne, K. A.; Debling, J.; Nesvadba, P.; Cunningham, M. F.; Hutchinson, R. A. *European Polymer Journal* **2016**, *80*, 186–199.

(199) Walsh, D. J.; Schinski, D. A.; Schneider, R. A.; Guironnet, D. *Nature Communications* **2020**, *11*, 3094.

(200) Kandelhard, F.; Schuldt, K.; Schymura, J.; Georgopanos, P.; Abetz, V. *Macromolecular Reaction Engineering* **2021**, *15*, 2000058.

(201) Alb, A. M.; Drenski, M. F.; Reed, W. F. *Polymer International* **2008**, *57*, 390–396.

(202) Pasquale, A. J.; Long, T. E. *Macromolecules* **1999**, *32*, 7954–7957.

(203) Reis, M. M.; Araújo, P. H.; Sayer, C.; Giudici, R. *Macromolecular Symposia* **2004**, *206*, 165–178.

(204) Lu, L.; Zhang, H.; Yang, N.; Cai, Y. *Macromolecules* **2006**, *39*, 3770–3776.

(205) Alb, A. M.; Serelis, A. K.; Reed, W. F. *Macromolecules* **2008**, *41*, 332–338.

(206) Lauterbach, F.; Abetz, V. *Macromolecular Rapid Communications* **2020**, *41*, 2000029.

(207) Haven, J. J.; Junkers, T. *Polymers* **2018**, *10*, 1228.

(208) Mirau, P. A. *Polymer Characterisation* **1993**, 37–68.

(209) Atkins, P.; Paula, J. d. **2009**, 1008.

(210) Castaing-Cordier, T.; Bouillaud, D.; Farjon, J.; Giraudeau, P. *Annual Reports on NMR Spectroscopy* **2021**, *103*, 191–258.

(211) Knox, S. T.; Parkinson, S.; Stone, R.; Warren, N. J. *Polymer Chemistry* **2019**, *10*, 4774–4778.

(212) Rubens, M.; Van Herck, J.; Junkers, T. *ACS Macro Letters* **2019**, *8*, 1437–1441.

(213) Groves, P. *Polymer Chemistry* **2017**, *8*, 6700–6708.

(214) Vrijsen, J. H.; Thomlinson, I. A.; Levere, M. E.; Lyall, C. L.; Davidson, M. G.; Hintermair, U.; Junkers, T. *Polymer Chemistry* **2020**, *11*, 3546–3550.

(215) Levere, M. E.; Willoughby, I.; O'Donohue, S.; De Cuendias, A.; Grice, A. J.; Fidge, C.; Becer, C. R.; Haddleton, D. M. *Polymer Chemistry* **2010**, *1*, 1086–1094.

(216) Hiller, W.; Hehn, M.; Hofe, T.; Oleschko, K. *Analytical Chemistry* **2010**, *82*, 8244–8250.

(217) Cudaj, M.; Guthausen, G.; Hofe, T.; Wilhelm, M. *Macromolecular Rapid Communications* **2011**, *32*, 665–670.

(218) Haven, J. J.; Zaquen, N.; Rubens, M.; Junkers, T. *Macromolecular Reaction Engineering* **2017**, *11*, 1700016.

(219) Rubens, M.; Vrijsen, J. H.; Laun, J.; Junkers, T. *Angewandte Chemie - International Edition* **2019**, *58*, 3183–3187.

(220) Gu, Y.; Lin, P.; Zhou, C.; Chen, M. *Science China Chemistry* **2021**, *64*, DOI: `10.1007/s11426-020-9969-y`.

(221) Reis, M.; Gusev, F.; Taylor, N. G.; Chung, S. H.; Verber, M. D.; Lee, Y. Z.; Isayev, O.; Leibfarth, F. A. *Journal of the American Chemical Society* **2021**, *143*, 17677–17689.

(222) Agboluaje, M.; Kaur, G.; Hutchinson, R. A. *Macromolecular Reaction Engineering* **2022**, 2200026.

(223) Wako *Wako Catalog* **2016**.

(224) Gardiner, J.; Martinez-Botella, I.; Kohl, T. M.; Krstina, J.; Moad, G.; Tyrell, J. H.; Coote, M. L.; Tsanaktsidis, J. *Polymer International* **2017**, *66*, 1438–1447.

(225) Willemse, R. X.; Van Herk, A. M.; Panchenko, E.; Junkers, T.; Buback, M. *Macromolecules* **2005**, *38*, 5098–5103.

(226) Valdebenito, A.; Encinas, M. V. *Polymer International* **2010**, *59*, 1246–1251.

(227) Lacík, I.; Chovancová, A.; Uhelská, L.; Preusser, C.; Hutchinson, R. A.; Buback, M. *Macromolecules* **2016**, *49*, 3244–3253.

(228) Zhong, F.; Zhou, Y.; Chen, M. *Polymer Chemistry* **2019**, *10*, 4879–4886.

(229) Gody, G.; Barbey, R.; Danial, M.; Perrier, S. *Polymer Chemistry* **2015**, *6*, 1502–1511.

(230) Zapata-González, I.; Saldívar-Guerra, E.; Ortiz-Cisneros, J. *Macromolecular Theory and Simulations* **2011**, *20*, 370–388.

(231) Barth, J.; Buback, M.; Russell, G. T.; Smolne, S. *Macromolecular Chemistry and Physics* **2011**, *212*, 1366–1378.

(232) Konkolewicz, D.; Hawkett, B. S.; Gray-Weale, A.; Perkier, S. *Journal of Polymer Science, Part A: Polymer Chemistry* **2009**, *47*, 3455–3466.

(233) Desmet, G. B.; De Rybel, N.; Van Steenberge, P. H.; D'hooge, D. R.; Reyniers, M. F.; Marin, G. B. *Macromolecular Rapid Communications* **2018**, *39*, 1700403.

(234) Lacík, I.; Beuermann, S.; Buback, M. *Macromolecules* **2003**, *36*, 9355–9363.

(235) Lacík, I.; Učňova, L.; Kukučková, S.; Buback, M.; Hesse, P.; Beuermann, S. *Macromolecules* **2009**, *42*, 7753–7761.

(236) Kattner, H.; Buback, M. *Macromolecules* **2015**, *48*, 7410–7419.

(237) Brandrup, J; Immergut, E. H.; Grulke, E. A.; Abe, A.; Bloch, D. R. Table 7. Miscellaneous Initiators, 2005.

(238) Lin, C. Y.; Coote, M. L. *Australian Journal of Chemistry* **2009**, *62*, 1479–1483.

(239) Convertine, A. J.; Lokitz, B. S.; Lowe, A. B.; Scales, C. W.; Myrick, L. J.; McCormick, C. L. *Macromolecular Rapid Communications* **2005**, *26*, 791–795.

(240) Schrooten, J.; Lacík, I.; Stach, M.; Hesse, P.; Buback, M. *Macromolecular Chemistry and Physics* **2013**, *214*, 2283–2294.

(241) Moad, G.; Barner-Kowollik, C. In *Handbook of RAFT Polymerization*, 2008, pp 51–104.

(242) Mastan, E.; Zhou, D.; Zhu, S. *Journal of Polymer Science, Part A: Polymer Chemistry* **2014**, *52*, 639–651.

(243) Liang, J.; Shan, G. r.; Pan, P. j. *Chinese Journal of Polymer Science (English Edition)* **2017**, *35*, 123–129.

(244) Ji, J.; Jia, L.; Yan, L.; Bangal, P. R. *Journal of Macromolecular Science, Part A: Pure and Applied Chemistry* **2010**, *47*, 445–451.

(245) Wood, M. R.; Duncalf, D. J.; Findlay, P.; Rannard, S. P.; Perrier, S. *Australian Journal of Chemistry* **2007**, *60*, 772–778.

(246) Haehnel, A. P.; Wenn, B.; Kockler, K.; Bantle, T.; Misske, A. M.; Fleischhaker, F.; Junkers, T.; Barner-Kowollik, C. *Macromolecular Rapid Communications* **2014**, *35*, 2029–2037.

(247) Alberti, A.; Benaglia, M.; Fischer, H.; Guerra, M.; Laus, M.; Macciantelli, D.; Postma, A.; Sparnacci, K. *Helvetica Chimica Acta* **2006**, *89*, 2103–2118.

(248) Kattner, H.; Buback, M. *Macromolecules* **2018**, *51*, 25–33.

Appendix A

Appendix Chapter 2

A.1 Data Tables for Optimisations

Table A.1: Raw data for the optimisation shown in Figure 2.7 in chapter 2

Residence Time (min)	Temperature ($^\circ C$)	Conversion (%)	M_n(g/mol)	M_p(g/mol)	Đ
6	70	0.534813	5116.686	1587.195	2
19	76	72.15371	10916.14	11852.8	1.218754
17	78	77.82843	11624.13	13039.39	1.231365
9	80	51.56274	8380.179	9698.214	1.203652
14	84	91.78376	13220.8	15927.33	1.270214
12	86	92.59817	12936.49	14394.26	1.253644
16	90	100.3107	12105.79	13518.99	1.454678
18	92	99.14615	12405.91	17142.69	1.461576
8	96	97.66148	13418.97	15221.37	1.560631
11	100	100.3384	12844.99	15970.52	1.717995
8	86	77.96727	12031.29	14685.96	1.205846
16	80	84.86235	12153.32	13681.1	1.243831
19	92	101.6823	12162.63	16292.75	1.637773
8	90	91.17132	13654.08	16346.88	1.253367
17	82	92.41907	13252.81	16452.18	1.293193
10	86	87.52309	13264.98	16676.6	1.256869
7	90	88.07786	13186.47	15444.23	1.288086
20	82	96.16675	13022.4	15418.51	1.283992

Table A.2: Raw Data from the optimisation shown in figure 2.11 in chapter 2.

Residence Time (min)	Temperature ($^{\circ}C$)	Conversion (%)	M_n(g/mol)	M_n(g/mol)	Đ
4	80	3.47944	2168.239	3667.011	2
19	86	2.318654	869.3861	452.6513	2
16	90	17.59924	3600.332	5106.321	1.434877
8	92	3.818404	2153.091	364.0313	2
13	98	64.01589	14482.49	15233.02	1.158882
10	100	56.88997	12830.12	13957.85	1.164647
15	102	78.21673	17982.76	21077.49	1.178914
18	106	83.81856	18423.15	21160.17	1.19102
7	112	67.90622	14260.55	16055.01	1.21399
10	116	74.4174	14117.67	18025.21	1.223956
18	110	81.83042	16324.45	18141.01	1.205766
19	112	80.83997	15596.4	18572.92	1.244677
20	114	79.89302	14121.01	17569.23	1.224357
17	100	79.73149	16801.48	21057.87	1.197548
17	108	81.65298	16633.5	20950.33	1.206256
19	110	82.16035	17359.64	20008	1.255447
14	98	65.21042	15259.11	18545.98	1.184912
16	98	72.84364	15534.91	18292.44	1.170222
12	112	76.82003	15511.53	18397.02	1.213937
15	114	76.98287	16347.7	18932.59	1.227047
17	100	77.81387	16929.64	19897.75	1.199976
19	100	81.39355	19098.66	21075.54	1.170927
19	102	83.10512	15887.59	19980.38	1.194063
16	106	82.16608	16164.2	18299.06	1.181429
20	110	83.14362	16228.07	21063.75	1.238441

Table A.3: Raw data for the optimisation shown in figure 2.10 in chapter 2

Residence Time (min)	Temperature ($^\circ C$)	Conversion (%)	M_n(g/mol)	M_p(g/mol)	Đ
4	80	3.189619	1054.864	299.0134	2
19	86	64.3955	13892.91	16893.94	1.183513
16	90	71.02265	15007.22	16927.02	1.171423
8	92	48.38241	10154.09	13132.7	1.207345
13	98	78.88167	15619.52	18930.89	1.199679
10	100	75.86065	15485.43	19730.1	1.223243
15	102	83.06429	14107.83	17986.26	1.247149
18	106	83.8646	13879.61	17159.29	1.272565
7	112	76.42956	12868.6	16441.79	1.235132
10	116	74.74776	13058.53	17364.35	1.302446
20	98	85.35131	15250.2	21028.48	1.279918
17	100	82.15479	14989.89	19383.94	1.229178
18	100	83.72044	14985.53	20152.45	1.268557
20	100	85.23079	14239.04	18442.05	1.298283
19	110	80.84406	15441.14	19533.7	1.270305
19	112	78.54612	14001.77	20048.63	1.28641
20	112	78.86738	13959.63	19352.04	1.290413
11	106	80.59662	13990.09	18908.48	1.274681
12	106	79.954	14920.47	18317.28	1.244205
12	108	80.5702	13609.18	16346.22	1.310491
20	88	72.78658	15923.05	19494.35	1.191201
20	94	82.72962	16416.85	21504.85	1.236481
18	96	82.85109	14371.4	18944.69	1.206448

Table A.4: Raw data for the optimisation shown in figure 2.13 in chapter 2

Residence Time (min)	Temperature ($^\circ C$)	Conversion (%)	M_n(g/mol)	M_p(g/mol)	Đ
4	80	2.291687	2100.643	7848.829	2
19	86	72.72325	10748.16	15022.88	1.260242
16	90	75.7733	11514.36	15002.05	1.248978
8	92	54.30836	6835.76	10102.79	1.356105
13	98	82.15361	12084.58	15913.18	1.288943
10	100	77.6591	11736.44	14929.47	1.283685
15	102	84.09318	12780.77	17319.38	1.334201
18	106	85.50641	12764.39	18190.23	1.384661
7	112	76.28054	11131.26	15978.98	1.361198
10	116	73.85091	10532.71	15050.26	1.342572
13	96	78.64464	11459.52	15846.31	1.318954
16	96	82.25012	13250.25	18201.73	1.332569
15	100	84.00659	12060.07	15039.83	1.359282
6	116	73.1012	9547.724	13835.86	1.347619
15	92	76.3763	11218.46	15113.07	1.309989
14	98	81.63686	13594.76	18740.65	1.30788
8	108	77.71394	11628.23	16128.64	1.286388
13	108	81.59189	11155.06	16495.68	1.384421
18	94	82.88324	13336.92	17049.51	1.290669
18	96	84.26513	13121.58	17035.84	1.305732
16	98	82.58453	12362.15	16402.61	1.330758
17	98	83.74156	12113.07	16892.41	1.316172
18	90	77.89126	11659.41	16460.7	1.343342

Table A.5: Raw data for the optimisation shown in figure 2.13 in chapter 2

Residence Time (min)	Temperature ($^\circ C$)	Conversion (%)	M_n(g/mol)	M_p(g/mol)	Đ
4	80	2.297626	1954.449	7138.098	2
19	86	64.40301	9035.301	12193.05	1.237165
16	90	71.59781	10457.63	13203.69	1.262359
8	92	50.07341	5552.335	8434.534	1.348699
13	98	80.0163	11427.28	15069.85	1.309244
10	100	77.24948	10537.37	12177.9	1.298188
15	102	84.82699	12283.25	17274.55	1.309283
18	106	85.29163	12342.91	17199.14	1.325596
7	112	76.86056	11042.61	15812.99	1.36411
10	116	76.8	10062.41	13867.7	1.375444
16	94	79.19	11129.32	15039.81	1.304871
16	100	84.39	11444.66	15203.92	1.320174
17	100	84.82	11802.64	15851.86	1.332022
16	108	84.3	11721.74	17327.11	1.366091
17	88	74.59	11050.63	13947.13	1.25586
16	106	85.08	12341.49	17150.1	1.331689
19	108	84.08	11595.39	15835.19	1.393255
16	110	81.38	10907.48	15274.15	1.312069
8	114	77.62	10362.34	14572.84	1.348411

Table A.6: Raw data for the optimisation shown in figure 5.8 in chapter 2

Residence Time (min)	Temperature ($^{\circ}C$)	Conversion (%)	M_n(g/mol)	M_p(g/mol)	Đ
3	64	2.678779	1588.026	425.0318	2
27	76	63.20847	17241.56	19574.03	1.224444
24	80	69.16396	17872.49	21612.27	1.226586
9	84	49.48268	12485.16	16336.56	1.238372
18	96	75.49783	12379.05	19924.5	1.522059
15	102	67.99333	11701	18837.84	1.449882
21	106	69.00637	11865.69	19915.61	1.484438
27	112	68.38827	9453.018	15254.93	1.576055
9	122	54.71901	7644.253	11785.6	1.494619
12	128	57.69707	4587.59	10704.56	2
27	86	81.12579	20288.03	28035.47	1.335616
21	88	77.592	19137.49	23541.29	1.291658
24	80	75.16483	20057.17	23890.49	1.246697
30	86	82.21025	19631.64	26479.68	1.356665
27	90	80.53557	18960.89	24239.05	1.284264
30	102	74.82191	11213.38	17203.93	1.542546
18	82	71.9799	18003.23	24102.96	1.342506
30	92	80.72185	16110.74	24074.05	1.491561
21	80	73.69827	18539.42	23717.32	1.254105
27	80	81.55837	18422.33	23649.8	1.313914

Appendix B

Appendix Chapter 3

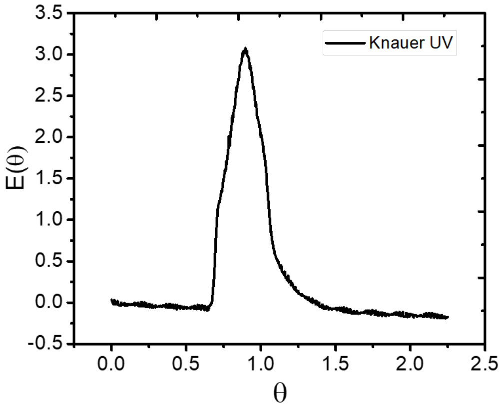

Figure B.1: Example of a UV/vis from the Knauer UV using the PDMA as a tracer

Appendix C

Appendix Chapter 4

C.1 Rate constant tables for Experimental and literature validation

Table C.1: Rate constants for the RAFT polymerisation of DMAm in the presence of TTC2 using VA044 in water at 30 w / w %, where the rate coefficients are given at 80 $°C$.

	E_a		A		$k(80°C)$		ref
k_p	14.1	$kJmol^{-1}$	1.10×10^7	$M^{-1}s^{-1}$	9.03×10^4	$M^{-1}s^{-1}$	240
k_t	25.0	$kJmol^{-1}$	2.00×10^{11}	$M^{-1}s^{-1}$	4.00×10^7	$M^{-1}s^{-1}$	236
$k_a^\dagger$	0.00	$kJmol^{-1}$	6.00×10^6	$M^{-1}s^{-1}$	6.00×10^6	$M^{-1}s^{-1}$	247
$k_\beta^\dagger$					2.00×10^4	s^{-1}	247
k_d	108.2	$kJmol^{-1}$	1.28×10^{12}	s^{-1}	5.48×10^{-5}	s^{-1}	223
f	0.5				$\alpha_s^\dagger$	0.40	236
k_{ct}	$0.25k_t$				$\alpha_l^\dagger$	0.18	236
$K^\dagger$	300				$L_c^\dagger$	50	236

Table C.2: Rate constants for the RAFT polymerisation of DMAm in the presence of TTC1 using ACVA in water at 30 w/w %, where rate coefficients are given at 85 and 90 $°C$.

	E_a		A		$k(85°C)/k(90°C))$		ref
k_p	14.1	$kJmol^{-1}$	1.10×10^7	$M^{-1}s^{-1}$	$9.66 \times 10^4/1.03 \times 10^5$	$M^{-1}s^{-1}$	240
k_t	25.0	$kJmol^{-1}$	2.00×10^{11}	$M^{-1}s^{-1}$	$4.52 \times 10^7/5.07 \times 10^7$	$M^{-1}s^{-1}$	236
$k_a^\dagger$	0.00	$kJmol^{-1}$	7.00×10^6	$M^{-1}s^{-1}$	7.00×10^6	$M^{-1}s^{-1}$	247
$k_\beta^\dagger$					7.00×10^4	s^{-1}	247
k_d	132.4	$kJmol^{-1}$	1.37×10^{15}	s^{-1}	$6.69 \times 10^{-5}/1.23 \times 10^{-4}$	s^{-1}	223
f	0.70				$\alpha_s^\dagger$	0.40	236
k_{ct}	$0.25k_t$				$\alpha_l^\dagger$	0.18	236
$K^\dagger$	100				$L_c^\dagger$	50	236

Table C.3: Rate constants for the RAFT polymerisation of AAm in the presence of TTC3 using VA044 in water at 15 w/w %, where rate coefficients are given at 45 $°C$.

	E_a		A		$k(45°C)$		ref
k_p	18.1	$kJmol^{-1}$	1.47×10^7	$M^{-1}s^{-1}$	1.27×10^5	$M^{-1}s^{-1}$	227
k_t	19.1	$kJmol^{-1}$	5.30×10^{11}	$M^{-1}s^{-1}$	3.88×10^8	$M^{-1}s^{-1}$	236
$k_a^\dagger$	0.00	$kJmol^{-1}$	7.00×10^7	$M^{-1}s^{-1}$	7.00×10^7	$M^{-1}s^{-1}$	247
$k_\beta^\dagger$					1.67×10^2	s^{-1}	247
k_d	108.2	$kJmol^{-1}$	1.28×10^{12}	s^{-1}	1.93×10^{-5}	s^{-1}	223
f	0.55				$\alpha_s^\dagger$	0.50	236
k_{ct}	$0.25k_t$				$\alpha_l^\dagger$	0.15	236
$K^\dagger$	25000				$L_c^\dagger$	30	236

Table C.4: Rate constants for the RAFT polymerisation of AA in the presence of TTC4 using ACVA in water at 13 w/w %, where rate coefficients are given at 69 $°C$.

	E_a		A		$k(69°C)$		ref
k_p	15.0	$kJmol^{-1}$	6.60×10^7	$M^{-1}s^{-1}$	3.89×10^5	$M^{-1}s^{-1}$	234
k_t	15.0	$kJmol^{-1}$	1.60×10^{12}	$M^{-1}s^{-1}$	8.20×10^9	$M^{-1}s^{-1}$	236
$k_a^\dagger$	0.00	$kJmol^{-1}$	2.00×10^7	$M^{-1}s^{-1}$	2.00×10^7	$M^{-1}s^{-1}$	247
$k_\beta^\dagger$					6.66×10^4	s^{-1}	238
k_d	132.8	$kJmol^{-1}$	3.62×10^{15}	s^{-1}	2.19×10^{-5}	s^{-1}	223
f	0.70				$\alpha_s^\dagger$	0.80	236
k_{ct}	$0.25k_t$				$\alpha_l^\dagger$	0.16	236
$K^\dagger$	3000				$L_c^\dagger$	30	236

Table C.5: Rate constants for the RAFT polymerisation of MA in the presence of TTC5 using AIBN in toluene at 30 w/w %, where rate coefficients are given at 50 $°C$.

	E_a		A		$k(50°C)$		ref
k_p	17.4	$kJmol^{-1}$	1.87×10^7	$M^{-1}s^{-1}$	2.82×10^5	$M^{-1}s^{-1}$	248
k_t	10.0	$kJmol^{-1}$	2.30×10^{10}	$M^{-1}s^{-1}$	5.56×10^8	$M^{-1}s^{-1}$	248
$k_a^\dagger$	0.00	$kJmol^{-1}$	7.00×10^6	$M^{-1}s^{-1}$	7.00×10^6	$M^{-1}s^{-1}$	247
$k_\beta^\dagger$					7×10^3	s^{-1}	247
k_d	132.4	$kJmol^{-1}$	2.37×10^{15}	s^{-1}	2.16×10^{-6}	s^{-1}	223
f	0.70				$\alpha_s^\dagger$	0.74	248
k_{ct}	$0.25k_t$				$\alpha_l^\dagger$	0.15	248
$K^\dagger$	1000				$L_c^\dagger$	30	248

Table C.6: Rate constants for the RAFT polymerisation of MA in the presence of TTC5 using AIBN in toluene at 30 w/w %, where rate coefficients are given at 50 $°C$.

Appendix D

Appendix Chapter 5

Table D.1: Raw data used in the optimisation seen in Figure 5.4.a in Chapter 5

[I]:[CTA]	Temperature ($^{\circ}C$)	Residence Time(min)	Đ	Conversion(%)
0.06	52	18	1.151	78.5
0.075	54	15	1.199	86.1
0.05	54	6	2.000	10.9
0.065	58	13	1.213	92.9
0.08	58	20	1.236	99.4
0.07	60	7	1.164	76.9
0.055	64	9	1.182	90.9
0.045	66	11	1.242	96.6
0.09	68	8	1.229	100.4
0.06	70	18	1.297	101.4
0.065	70	11	1.263	100.5
0.05	72	12	1.243	101.5
0.08	74	14	1.309	101.7
0.04	78	8	1.282	100.1
0.085	78	17	1.348	101.3
0.085	62	15	1.243	102.2
0.06	64	11	1.234	97.3
0.09	76	10	1.367	100.6
0.055	76	16	1.333	102.0
0.06	80	19	1.369	100.7
0.06	64	15	1.232	101.5
0.04	50	10	2.000	0.1
0.08	58	6	1.154	64.3
0.085	70	11	1.372	100.1
0.075	72	8	1.328	98.5
0.04	72	18	1.406	102.8
0.09	64	6	1.176	94.0
0.06	72	5	1.243	97.5

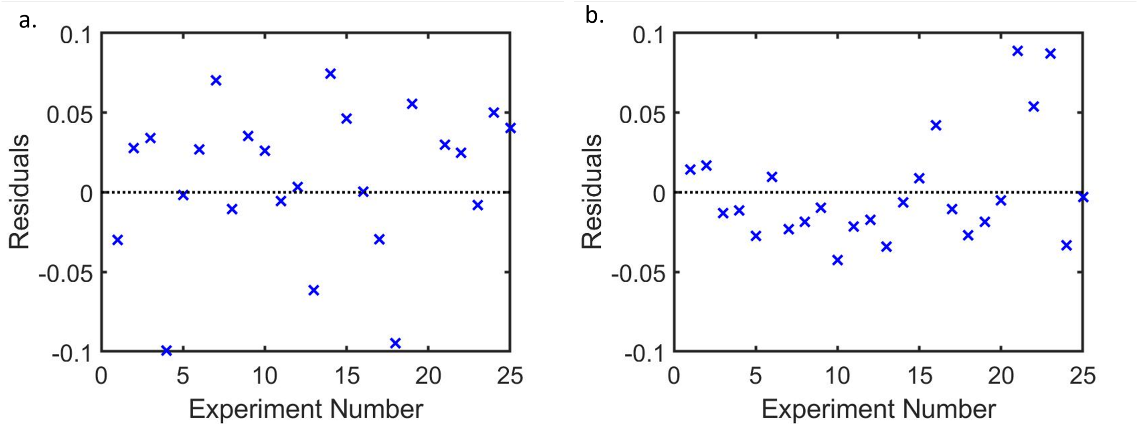

Figure D.1: (a) residuals analysis for the regression shown in Figure 5.5.a in Chapter 5.(b)residuals analysis for the dispersity objective regression shown in Figure 5.5.a in Chapter 5.

Table D.2: Arrhenius and rate parameters used in digitally augmented optimisation of DMAm at 30 w / w %

	E_a		A		ref
k_p	14.1	$kJmol^{-1}$	1.10×10^7	$M^{-1}s^{-1}$	240
k_t	25.0	$kJmol^{-1}$	2.00×10^{11}	$M^{-1}s^{-1}$	236
$k_a^\dagger$	0.00	$kJmol^{-1}$	6.00×10^6	$M^{-1}s^{-1}$	247
k_d	108.2	$kJmol^{-1}$	1.28×10^{12}	s^{-1}	223
f	0.6		$\alpha_s^\dagger$	0.40	236
k_{ct}	$0.25k_t$		$\alpha_l^\dagger$	0.18	236
$K^\dagger$	300		$L_c^\dagger$	50	236

Table D.3: Raw data used in the optimisation seen in Figure 5.6.a in Chapter 5

[I]:[CTA]	Temperature (°C)	Residence Time(min)	Đ	Conversion(%)
0.06	52	18	1.196	90.6
0.075	54	15	1.197	92.2
0.05	54	6	1.171	44.0
0.065	58	13	1.198	93.2
0.08	58	20	1.196	99.6
0.07	60	7	1.208	77.0
0.055	64	9	1.202	91.0
0.045	66	11	1.200	96.0
0.09	68	8	1.202	98.0
0.06	70	18	1.201	100.0
0.065	70	11	1.202	99.6
0.05	72	12	1.202	99.8
0.08	74	14	1.205	100.0
0.04	78	8	1.206	99.3
0.085	78	17	1.209	100.0
0.08	50	16	1.185	77.7
0.06	56	8	1.142	58.1
0.06	56	20	1.239	102.8
0.04	78	11	1.315	101.1
0.06	56	6	1.138	26.1
0.055	56	11	1.164	68.0
0.075	68	19	1.398	104.6
0.065	60	20	1.306	101.8
0.05	50	14	2.000	0.6
0.04	58	18	1.194	89.8
0.065	54	18	1.184	85.4
0.085	74	17	1.383	100.4
0.08	80	20	1.481	99.5
0.07	56	18	1.197	92.4
0.065	78	11	1.318	100.2

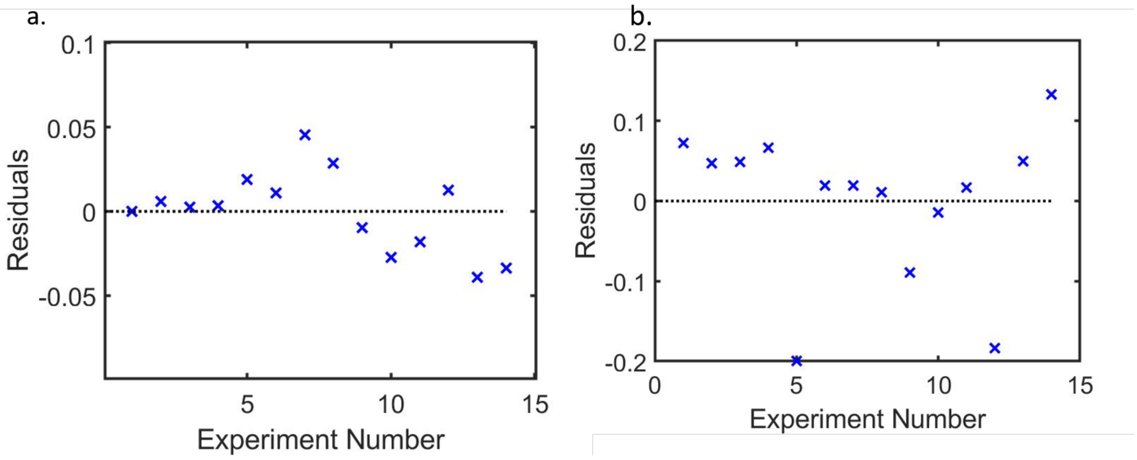

Figure D.2: (a) residuals analysis for the conversion objective regression shown in Figure 5.7.a in Chapter 5. (b)residuals analysis for the dispersity objective regression shown in Figure 5.7.b in Chapter 5.

Table D.4: Raw data used in the optimisation seen in Figure 5.8.a in Chapter 5

[I]:[CTA]	Temperature ($^\circ C$)	Residence Time(min)	Đ	Conversion(%)
0.075	74	15	1.412	30.5
0.05	74	6	2.000	6.7
0.065	78	13	1.266	32.1
0.08	78	20	1.203	47.4
0.07	80	7	1.089	18.9
0.055	84	9	1.205	33.1
0.045	86	11	1.230	36.7
0.09	88	8	1.310	42.8
0.06	90	18	1.376	63.1
0.065	90	11	1.340	50.3
0.05	92	12	1.325	51.6
0.08	94	14	1.421	64.0
0.04	98	8	1.361	50.1
0.085	98	17	1.997	73.7
0.045	90	20	1.326	56.7
0.045	84	20	1.335	50.0
0.06	100	14	1.430	67.8
0.04	100	19	1.371	65.6
0.06	96	17	1.339	64.3
0.045	98	10	1.378	54.7
0.085	86	16	1.441	54.6
0.09	86	18	1.376	64.8
0.08	88	20	1.409	70.0
0.045	88	18	1.337	54.2
0.055	96	20	1.451	68.5
0.09	90	16	1.484	57.9
0.065	96	15	1.422	67.9
0.055	92	16	1.365	59.9
0.09	84	20	1.390	60.2
0.065	94	20	1.416	70.1
0.065	98	18	1.393	72.2
0.06	82	18	1.384	51.6
0.07	80	19	1.329	50.2
0.085	76	20	1.277	37.4
0.075	88	18	1.462	69.1
0.065	100	20	1.339	73.0
0.05	86	16	1.228	36.5
0.08	80	17	1.309	44.6
0.06	100	19	1.477	76.0
0.065	100	9	1.410	61.4

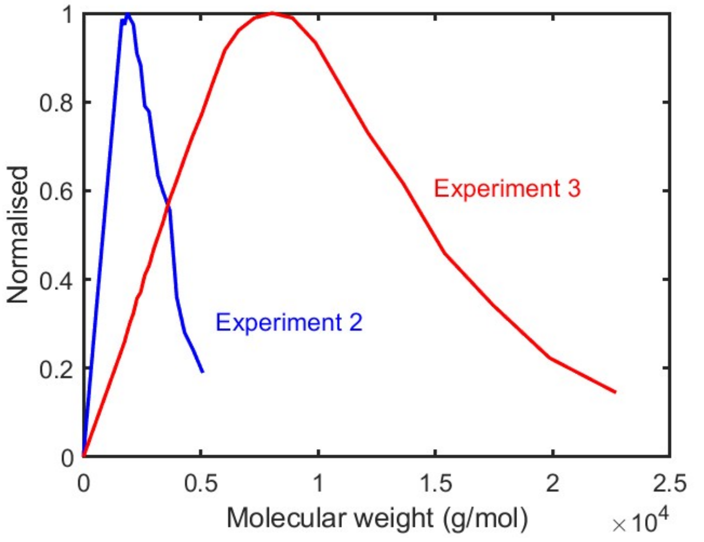

Figure D.3: Comparison of GPC traces associated with a low and high Đ polymer for experiment 2 and 3 from the RAFT polymerisation of nBUA shown in Figure 5.8, respectively.

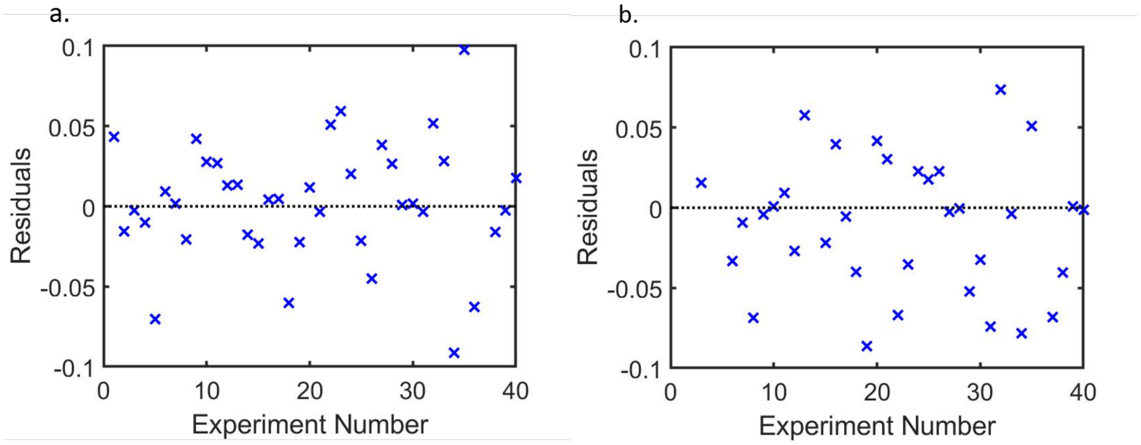

Figure D.4: (a) residuals analysis for the conversion objective regression shown in Figure 5.9.a in Chapter 5. (b)residuals analysis for the dispersity objective regression shown in Figure 5.9.b in Chapter 5.

Table D.5: Arrhenius and rate parameters used in digitally augmented optimisation of nBuA at 30 w / w %

	E_a		A		ref
k_p	17.9	$kJmol^{-1}$	2.24×10^7	$M^{-1}s^{-1}$	240
k_t	10.0	$kJmol^{-1}$	1.3×10^{10}	$M^{-1}s^{-1}$	236
$k_a^\dagger$	0.00	$kJmol^{-1}$	6.00×10^6	$M^{-1}s^{-1}$	247
k_d	132.2	$kJmol^{-1}$	1.28×10^{12}	s^{-1}	223
f	0.42		$\alpha_s^\dagger$	0.56	236
k_{ct}	$0.25k_t$		$\alpha_l^\dagger$	0.16	236
$K^\dagger$	100		$L_c^\dagger$	33	236

Table D.6: Raw data used in the optimisation seen in Figure 5.10.a in Chapter 5

[I]:[CTA]	Temperature ($^\circ C$)	Residence Time(min)	Đ	Conversion(%)
0.06	72	18	1.228	20.7
0.075	74	15	1.218	23.1
0.05	74	6	1.627	5.5
0.065	78	13	1.211	25.9
0.08	78	20	1.161	46.4
0.07	80	7	1.299	15.3
0.055	84	9	1.222	26.0
0.045	86	11	1.193	34.5
0.09	88	8	1.183	41.7
0.06	90	18	1.182	77.9
0.065	90	11	1.166	55.6
0.05	92	12	1.163	60.6
0.08	94	14	1.191	85.5
0.04	98	8	1.176	55.8
0.085	98	17	1.204	97.9
0.09	92	17	1.292	67.3
0.09	92	19	1.352	70.5
0.09	92	20	2.000	91.0
0.09	94	18	1.250	63.5
0.085	94	10	1.356	58.2
0.055	72	19	1.094	29.0
0.09	98	11	1.383	65.4
0.07	80	5	2.000	12.4
0.085	78	10	1.184	28.1
0.085	92	8	1.322	50.0
0.085	78	16	1.313	43.0
0.045	82	19	1.283	45.3
0.085	100	18	1.387	74.2
0.09	100	18	1.438	75.4
0.09	100	13	1.477	71.9
0.075	94	7	1.322	48.2
0.04	86	16	1.317	46.4
0.045	96	19	1.416	67.6
0.055	100	16	1.451	71.4
0.04	98	17	1.466	66.7
0.085	100	8	1.395	61.0
0.09	98	18	1.474	77.6
0.09	92	15	1.487	67.8
0.08	92	12	1.396	65.2
0.075	98	18	1.463	77.7

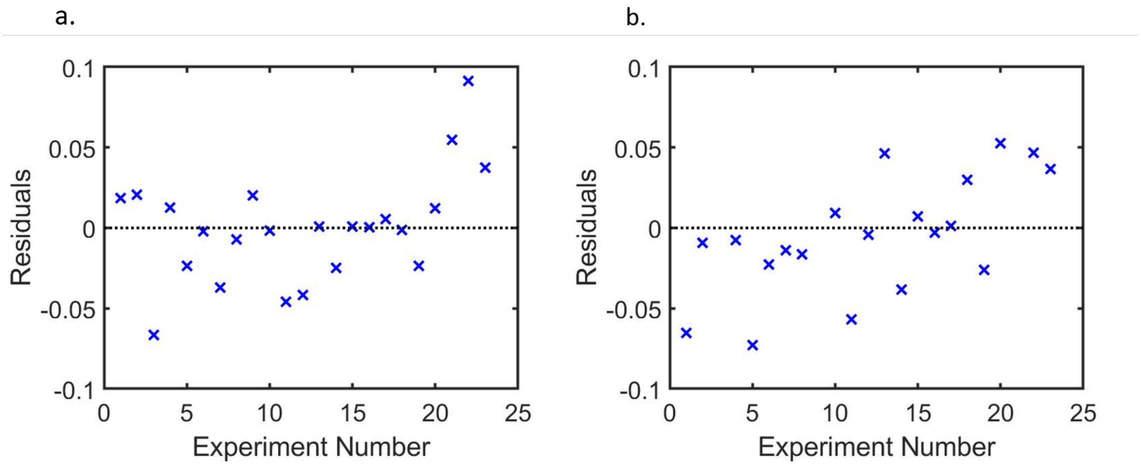

Figure D.5: (a) residuals analysis for the conversion objective regression shown in Figure 5.11.a in Chapter 5. (b)residuals analysis for the dispersity objective regression shown in Figure 5.11.b in Chapter 5.

Table D.7: Arrhenius and rate parameters used in digitally augmented optimisation of tBuAm at 20 w / w %

	E_a		A		ref
k_p	14.7	$kJmol^{-1}$	8.68×10^{6}	$M^{-1}s^{-1}$	240
k_t	13.6	$kJmol^{-1}$	1.88×10^{10}	$M^{-1}s^{-1}$	236
$k_a^{\dagger}$	0.00	$kJmol^{-1}$	6.00×10^{6}	$M^{-1}s^{-1}$	247
k_d	132.2	$kJmol^{-1}$	1.28×10^{12}	s^{-1}	223
f	0.48		$\alpha_s^{\dagger}$	0.52	236
k_{ct}	$0.25k_t$		$\alpha_l^{\dagger}$	0.16	236
$K^{\dagger}$	300		$L_c^{\dagger}$	33	236

Table D.8: Raw data used in the optimisation seen in Figure 5.12.a in Chapter 5

[I]:[CTA]	Temperature ($°C$)	Residence Time(min)	Đ	Conversion(%)
0.06	72	18	1.152	31.2
0.08	74	15	1.147	35.1
0.05	74	6	1.300	8.9
0.07	78	13	1.146	37.9
0.09	78	20	1.157	63.2
0.08	80	7	1.176	24.2
0.06	84	9	1.151	36.8
0.045	86	11	1.142	44.7
0.1	88	8	1.137	54.7
0.065	90	18	1.156	87.4
0.07	90	11	1.161	67.8
0.055	92	12	1.160	72.4
0.09	94	14	1.160	92.7
0.04	98	8	1.167	63.8
0.095	98	17	1.165	99.3
0.09	90	18	1.342	70.2
0.095	90	18	1.293	74.0
0.095	92	17	1.352	73.3
0.065	100	16	1.408	72.7
0.075	100	16	1.490	79.1
0.08	70	7	2.000	54.6
0.1	90	18	1.350	67.7
0.045	100	20	1.362	74.3
0.095	76	20	2.000	52.2
0.04	90	20	1.350	65.6
0.09	100	20	1.450	81.2
0.04	96	8	1.367	64.5
0.08	94	13	1.713	69.8
0.07	92	17	1.366	73.2
0.1	98	12	1.552	76.7
0.09	92	5	1.308	59.2
0.04	86	15	1.280	50.0
0.075	96	17	1.384	73.3
0.09	96	15	1.438	74.3

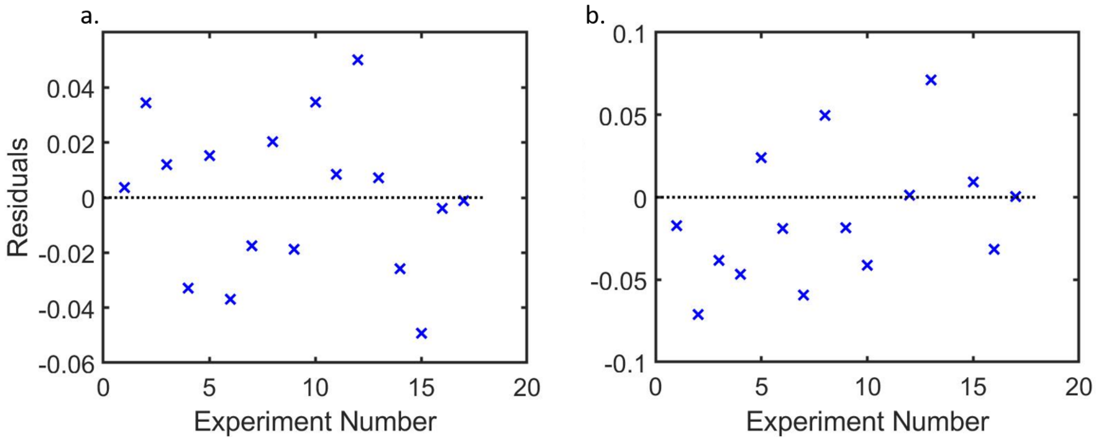

Figure D.6: (a) residuals analysis for the conversion objective regression shown in Figure 5.13.a in Chapter 5. (b)residuals analysis for the dispersity objective regression shown in Figure 5.13.b in Chapter 5.